

Liquid argon time projection chamber calibration using cosmogenic muons,
and measurement of neutrino induced charged kaon production in argon in
the charged current mode (MicroBooNE experiment)

by

Varuna Crishan N Meddage

B.S., University of Kelaniya, Sri Lanka, 2012

AN ABSTRACT OF A DISSERTATION

submitted in partial fulfillment of the
requirements for the degree

DOCTOR OF PHILOSOPHY

Department of Physics
College of Arts and Sciences

KANSAS STATE UNIVERSITY
Manhattan, Kansas

2019

Abstract

The MicroBooNE experiment at Fermilab uses the novel LArTPC technology to reconstruct neutrino interactions with liquid argon. The experiment consists of a detector having an active mass of 85 tons of liquid argon, where the operational electric field of the TPC is 0.273 kV/cm. While BNB neutrino beam at Fermilab is the main source for neutrinos for the experiment having an average energy of ~ 0.8 GeV, the NUMI neutrino beam at Fermilab also provides high energy neutrinos to perform different physics analyses. The MicroBooNE experiment has been in operation since October 2015. Its major physics goals include investigating into the anomalous production of electron neutrino like events as observed by MiniBooNE and LSND experiments and detail studies of neutrino-argon cross sections at lower neutrino energies. Moreover, the experiment will also serve as R&D for future LArTPC experiments like the already proposed SBN and DUNE programs. One of the major operational requirements of any LArTPC experiment including MicroBooNE is to achieve a high liquid argon purity keeping the electronegative contaminants like H₂O and O₂ at low concentration levels. This dissertation first describes how to perform an electron attenuation measurement using cosmogenic muons, which provides a handle over the amount of electronegative impurities inside our detector medium. Likewise this measurement also serves as the first step towards reconstruction of particle energies as MicroBooNE must compensate for the loss of ionization electrons due to capture by electronegative contaminants. Secondly, the discussion is about how to calibrate any LArTPC detector in removing any spatial and temporal variations of the dQ/dx (charge deposited per unit length) spectrum using cosmogenic muons and then how to calculate correct energies of particle interactions with these calibrated out dQ/dx values. The translation of dQ/dx to particle energies (dE/dx - energy deposited per unit length) makes use of the stopping muons coming from neutrino interactions as the standard candle. The final discussion is about the neutrino induced charged

kaon production at charged current mode in the lower neutrino energies of MicroBooNE experiment. This measurement is crucial as there is no such measurement so far on argon at the scale of neutrino energies used for MicroBooNE while already existing measurements on lighter nuclear targets are also sparse. This dissertation presents the first identified neutrino induced kaon candidates in MicroBooNE.

Liquid argon time projection chamber calibration using cosmogenic muons,
and measurement of neutrino induced charged kaon production in argon in
the charged current mode (MicroBooNE experiment)

by

Varuna Crishan N Meddage

B.S., University of Kelaniya, Sri Lanka, 2012

A DISSERTATION

submitted in partial fulfillment of the
requirements for the degree

DOCTOR OF PHILOSOPHY

Department of Physics
College of Arts and Sciences

KANSAS STATE UNIVERSITY
Manhattan, Kansas

2019

Approved by:

Major Professor
Glenn A. Horton-Smith

Copyright

© Varuna Crishan N Meddage 2019.

Abstract

The MicroBooNE experiment at Fermilab uses the novel LArTPC technology to reconstruct neutrino interactions with liquid argon. The experiment consists of a detector having an active mass of 85 tons of liquid argon, where the operational electric field of the TPC is 0.273 kV/cm. While BNB neutrino beam at Fermilab is the main source for neutrinos for the experiment having an average energy of ~ 0.8 GeV, the NUMI neutrino beam at Fermilab also provides high energy neutrinos to perform different physics analyses. The MicroBooNE experiment has been in operation since October 2015. Its major physics goals include investigating into the anomalous production of electron neutrino like events as observed by MiniBooNE and LSND experiments and detail studies of neutrino-argon cross sections at lower neutrino energies. Moreover, the experiment will also serve as R&D for future LArTPC experiments like the already proposed SBN and DUNE programs. One of the major operational requirements of any LArTPC experiment including MicroBooNE is to achieve a high liquid argon purity keeping the electronegative contaminants like H₂O and O₂ at low concentration levels. This dissertation first describes how to perform an electron attenuation measurement using cosmogenic muons, which provides a handle over the amount of electronegative impurities inside our detector medium. Likewise this measurement also serves as the first step towards reconstruction of particle energies as MicroBooNE must compensate for the loss of ionization electrons due to capture by electronegative contaminants. Secondly, the discussion is about how to calibrate any LArTPC detector in removing any spatial and temporal variations of the dQ/dx (charge deposited per unit length) spectrum using cosmogenic muons and then how to calculate correct energies of particle interactions with these calibrated out dQ/dx values. The translation of dQ/dx to particle energies (dE/dx - energy deposited per unit length) makes use of the stopping muons coming from neutrino interactions as the standard candle. The final discussion is about the neutrino induced charged

kaon production at charged current mode in the lower neutrino energies of MicroBooNE experiment. This measurement is crucial as there is no such measurement so far on argon at the scale of neutrino energies used for MicroBooNE while already existing measurements on lighter nuclear targets are also sparse. This dissertation presents the first identified neutrino induced kaon candidates in MicroBooNE.

Table of Contents

List of Figures	xiii
List of Tables	xxi
Acknowledgements	xxii
Dedication	xxiii
Preface	xxiv
1 Introduction	1
1.1 Electron Attenuation	2
1.2 Detector Calibration	4
1.3 Neutrino Induced Kaon Production In Argon	5
2 MicroBooNE Experiment	8
2.1 LArTPC Technology	8
2.2 MicroBooNE Detector	10
2.2.1 Liquid Argon Purification System	13
2.2.2 Light Collection System	15
2.2.3 UV Laser System	16
2.2.4 PMT and TPC Electronics	17
2.2.5 Readout Electronics	18
2.2.6 Data Acquisition System (DAQ)	20
2.2.7 Slow Monitoring and Control System	20

3	Booster Neutrino Beam (BNB)	22
3.1	Booster	23
3.2	Beam Monitoring	25
3.3	Target	26
3.4	Focusing-Defocusing Horn	26
3.5	Collimator	28
3.6	Decay Pipe	29
3.7	Neutrino Beam	30
4	Neutrinos	32
4.1	The Standard Model (SM)	32
4.2	The Weak Nuclear Force (Weak Interaction)	35
4.3	Neutrinos in General	39
4.4	Neutrino Oscillations	42
4.4.1	Solar Neutrino Oscillations	49
4.4.2	Experimental Search for Solar Neutrino Oscillations	51
4.4.3	Atmospheric Neutrino Anomaly	57
4.4.4	Accelerator Long Baseline Neutrino Experiments	60
4.4.5	Reactor Neutrino Experiments	64
4.4.6	Short Baseline Neutrino Experiments	67
4.4.7	The MicroBooNE Experiment	71
4.4.8	Upcoming Neutrino Experiments	72
4.4.9	Neutrino Oscillation Parameters (Current Knowledge)	74
5	Electron Attenuation (Electron Lifetime)	75
5.1	Introduction	75
5.2	MicroBooNE Purification System	78
5.3	Event Samples	78

5.4	Reconstruction	79
5.4.1	Reconstructing the Arrival Times of Cosmic-Ray Tracks	80
5.5	Event Selection	80
5.6	Extracting Charge Dependency from Drift Time	82
5.6.1	Space Charge in Liquid Argon	85
5.6.2	Effect of Space Charge on dQ/dx	86
5.6.3	Space Charge Corrections	88
5.6.4	Comparison between Data and Simulation	90
5.7	Location Dependence of Q_A/Q_C	93
5.8	Systematic Uncertainties	96
5.8.1	Space Charge Correction	97
5.8.2	Recombination Model	97
5.8.3	Diffusion	99
5.8.4	Systematics Summary	100
5.9	Results	101
5.10	Future Plans	101
5.11	Summary and Conclusions	103
6	Detector Calibration	104
6.1	Introduction	104
6.2	Calibrating the MicroBooNE Detector	105
6.2.1	dQ/dx Calibration	106
6.2.2	Misconfigured or Cross-Connected TPC Channels	106
6.2.3	Space Charge Effects	107
6.2.4	Electron Attenuation	108
6.2.5	Diffusion	109
6.2.6	Recombination	110
6.2.7	Temporal Variations	110

6.2.8	dQ/dx Variation	110
6.2.9	dE/dx Calibration	111
6.3	Event Selection	112
6.3.1	Selection Cuts (dQ/dx Calibration)	112
6.3.2	Selection Cuts (dE/dx Calibration)	113
6.4	Data Sample	115
6.5	Analysis Method	116
6.5.1	Detector Calibration in YZ Plane	116
6.5.2	Drift Direction Calibration of the Detector	118
6.5.3	Time Dependent Calibration of the Detector	119
6.5.4	dE/dx Calibration of the Detector	122
6.6	Results	124
6.6.1	dQ/dx Calibration (Monte Carlo)	124
6.6.2	dQ/dx Calibration (Data)	125
6.6.3	dE/dx Calibration	127
6.6.4	Validation of Calorimetric Energy Reconstruction	128
6.7	Angular Dependence Study	129
6.8	Conclusions	131
7	Neutrino Induced Kaons	136
7.1	Strong Nuclear Force	136
7.2	Neutrino Induced Kaons	139
7.3	Proton Decay	147
7.4	Proton Decay Searches	149
7.5	Strange Particle Production (Early Measurements)	151
8	Event Selection of Charged Current Neutrino Induced Kaon Events in MicroBooNE	164
8.1	MC and Data Samples	164

8.2	Simulation	165
8.3	Truth Level and Reconstructed Level Information	166
8.4	Calorimetry Based Particle Identification for Kaons/Muons	169
8.5	Event Selection	172
8.6	Background Estimation	184
8.7	Data Monte Carlo Comparison	190
8.8	Kaon Candidate Events in MicroBooNE Data	192
8.9	Cross Section	193
8.10	Future Plans	200
	Bibliography	201
A	Electron Attenuation	218
B	Event Selection of Charged Current Neutrino Induced Kaon Events in MicroBooNE	229

List of Figures

2.1	A cartoon showing the basic working principle of a LArTPC detector.	11
2.2	Components of the MicroBooNE detector.	13
2.3	Real image of the MicroBooNE cryostat sitting inside the LArTF.	13
2.4	Purification system of MicroBooNE	14
2.5	PMT system of MicroBooNE.	16
2.6	UV laser system of MicroBooNE	17
2.7	Image of front end CMOS ASIC used in the MicroBooNE electronics and a graph showing the noise level of MicroBooNE ASICs under different temperature conditions	19
2.8	MicroBooNE slow monitoring and control system display.	21
3.1	Booster Neutrino Beam at Fermilab	23
3.2	Beam structure of the output of the Booster	25
3.3	BNB target	27
3.4	Booster Neutrino Beam horn structure	28
3.5	A cartoon showing all the major components of the Booster Neutrino Beam line	29
3.6	Beam composition of the Booster Neutrino Beam in neutrino and anti neutrino modes	31
4.1	Fundamental particles in the standard model	34
4.2	Possible coupling states of neutrinos in the charged current weak interaction	36
4.3	Feynman diagrams of K^- and π^- decays	37
4.4	Feynman diagrams of neutrino couplings in the neutral current weak interaction	39

4.5	Feynman diagrams of FCNC processes	39
4.6	Natural and man-made neutrino sources	42
4.7	Neutrino oscillations	47
4.8	Neutrino mass hierarchy	48
4.9	Neutrino production channels in the Sun	50
4.10	The direction of the neutrinos reconstructed by the SuperK experiment	54
4.11	Measurements of the solar neutrino flux by different experiments	57
4.12	ν_e like and ν_μ like events recorded in SuperK atmospheric data	60
4.13	Zenith angle definition	61
4.14	ν_μ disappearance channel search by MINOS 2013	63
4.15	$\bar{\nu}_\mu$ disappearance channel search by T2K experiment in 2016	64
4.16	KamLAND $\bar{\nu}_e$ disappearance channel search	66
4.17	Daya Bay θ_{13} measurement results 2016	68
4.18	LSND $\bar{\nu}_\mu \rightarrow \bar{\nu}_e$ search	69
4.19	MiniBooNE low energy excess	70
4.20	Separation of the electron and photon induced showers in Argoneut LArTPC using shower energy	72
4.21	Schematic diagram of Fermilab's SBN program	73
4.22	Schematic diagram of the DUNE experiment	74
5.1	Electron attenuation as a function of drift parth	76
5.2	Graphs of number of reconstructed tracks per event & 3D reconstructed track length in data	80
5.3	Graphs of X -projected track length & number of hits per crossing track in data	81
5.4	Definition of θ_{XZ} & θ_{YZ} angles	83
5.5	dQ/dx distributions as a function of θ_{XZ} & θ_{YZ}	83
5.6	dQ/dx vs drift time scatter plot & most probable value for dQ/dx extracted from Landau convolved Gaussian fits to each drift bin	85

5.7	Landau convolved Gaussian fits to the dQ/dx distributions	86
5.8	dQ/dx vs drift time curves for isotropic single muons with various space charge settings in simulation	88
5.9	Space charge corrections with drift time fitted with a third order polynomial	89
5.10	dQ/dx vs drift time plots for data before and after space charge corrections	91
5.11	Variation of Q_A/Q_C over 56 days of data before and after applying space charge corrections only with statistical uncertainties	92
5.12	Comparison of track hit X , Y and Z coordinates between data and isotropic single muons with the shorted channels cut	93
5.13	2-D and 1-D representations of dQ/dx variation w.r.t. the median dQ/dx	94
5.14	2-D map of Q_A/Q_C for non-drift (Y and Z) directions	95
5.15	Variation in dQ/dx with drift time for isotropic single muons for different parameter settings of modified box recombination model	99
5.16	dQ/dx vs drift time distributions for isotropic single muons with and without diffusion	100
5.17	Variation of Q_A/Q_C over 56 days of data before and after applying space charge corrections with both statistical and systematic uncertainties	102
6.1	Plots of dQ/dx vs drift distance for different space charge settings in Monte Carlo	108
6.2	Change of dQ/dx as a function of drift distance in low purity data	109
6.3	Variation of dQ/dx in data in the drift direction and in YZ plane under the influence of various detector effects	111
6.4	Presence of cosmic muons in MicroBooNE's 4.8 ms wide read out window and anode-cathode crossing tracks in data	113
6.5	Definition of angle θ_{XZ} and θ_{YZ}	114
6.6	Variation of average dQ/dx values in the phase space of θ_{XZ} and θ_{YZ} in the collection plane	114

6.7	Variation of the global median dQ/dx over time in the collection plane . . .	121
6.8	YZ and drift direction correction factors derived for collection plane in Monte Carlo	125
6.9	Calibrated dQ/dx vs Residual range for stopping muons and stopping protons in Monte Carlo (collection plane information)	126
6.10	The variation of YZ correction factors in the collection plane for the combined time period from February to May in 2016 in data	126
6.11	The variation of the time correction $C(t)$ over time in the collection plane . .	127
6.12	Comparison of calibrated and uncalibrated dQ/dx spectra in Monte Carlo and data using collection plane information	128
6.13	Distributions of $\chi^2 - \chi_{Min}^2$ vs calibration constant C for the collection plane in Monte Carlo and data	129
6.14	Comparison between the prediction and the fitted MPV dE/dx for stopping muons in Monte Carlo and data using collection plane information	130
6.15	Calibrated dE/dx vs Residual range for true stopping muons and protons in Monte Carlo using collection plane information	131
6.16	Fractional difference in range vs. calorimetric kinetic energy for selected stopping muons	132
6.17	Percentage differences in YZ correction factors in all YZ cells between different subsamples and all samples combined	133
6.18	Percentage differences in X correction factors between different subsamples and all samples combined	134
7.1	Neutrino, anti neutrino cross sections per nucleon for different processes in the charged current interaction	141
7.2	Feynman diagram of QE interaction in the neutino mode	141
7.3	A Feynman diagram of single pion production by resonance in the charged current mode	143

7.4	Possible final state interactions for pion produced in a neutrino interaction	143
7.5	Feynman diagrams of neutrino induced kaon production	145
7.6	Energy distributions of neutrinos for different kaon production mechanisms using GENIE simulations in the MicroBooNE	147
7.7	Single kaon production modes	148
7.8	Feynman diagram for the charged current coherent kaon production	148
7.9	Feynman diagram of $p \rightarrow e^+ + \pi^0$ in a non SUSSY GUT model	150
7.10	Limits set for proton lifetime by SuperK in the decay channel $p \rightarrow e^+ + \pi^0$ as a function of time	151
7.11	Feynman diagram of $p \rightarrow K^+ + \nu$ with the participation of supersymmetric particles in SUSSY GUT models	152
7.12	Limits set for proton lifetime by SuperK in the decay channel $p \rightarrow K^+ + \nu$ as a function of time	153
7.13	Constraints on proton lifetime by different experiments on different decay modes and predictions on proton lifetime by different GUT and SUSSY GUT models	154
7.14	Bubble chamber image of the channel $\nu + n \rightarrow \nu + \Lambda + K^0$	158
7.15	Differential cross section of charged kaon production in charged current and neutral current modes in the MINERVA experiment	161
7.16	Charged current K^+ event observed in the MINERVA data	162
7.17	Neutral current K^+ event observed in the MINERVA data	162
7.18	Kinetic energy of charged current coherent K^+ events observed in the MIN- ERVA data	163
8.1	Monte Carlo event display showing neutrino induced kaon decaying to muon in MicroBooNE	167
8.2	Monte Carlo event display showing neutrino induced kaon decaying to pion	168
8.3	Fiducial volume defined for the neutrino interactions	168

8.4	Kinetic energy and track length distributions of muons and pions coming from kaon decay at rest	170
8.5	Reconstructed track length of kaons	171
8.6	Reconstructed calorimetric kinetic energy of kaons	172
8.7	Reconstructed polar angle (θ) of kaons	173
8.8	Reconstructed azimuth angle (ϕ) of kaons	174
8.9	Reconstructed track length of muons coming from kaon decay at rest	175
8.10	Reconstructed calorimetric kinetic energy of muons coming from kaon decay at rest	176
8.11	Reconstructed polar angle (θ) of muons coming from kaon decay at rest	177
8.12	Reconstructed polar angle (ϕ) of muons coming from kaon decay at rest	178
8.13	Standard dE/dx energy profiles for different particle types calculated using Bethe-Bloch formula in liquid argon	179
8.14	Comparison of χ^2 values calculated under proton/kaon hypotheses for kaon tracks that decay at rest with other particle tracks	180
8.15	Comparison of χ^2 value calculated under proton hypothesis for muon tracks coming from kaon that decay at rest with other particle tracks	181
8.16	Signal/Background ratios for different combinations of the the two free parameters A and B	181
8.17	Distribution of signal and background events in the signal band of the χ_P^2 - χ_K^2 phase space	182
8.18	Purity and efficiency curves for muon candidate variables coming from kaon decay at rest	183
8.19	Schematic diagram showing the distribution of some arbitrary variable named X to be used to define efficiencies and purities	184
8.20	Event display showing proton-proton scattering event in MicroBooNE Monte Carlo	185

8.21	Event display found in MicroBooNE data, which resembles proton-proton scattering	185
8.22	Event display showing pion-pion scattering event in MicroBooNE Monte Carlo	186
8.23	Event display found in MicroBooNE data, which resembles pion-pion scattering	186
8.24	Distribution of signal and background kaon candidate events in the side band 1 in the phase space of χ_P^2 - χ_K^2 of kaon candidate tracks	187
8.25	Distribution of signal and background kaon candidate events in the side band 2 in the phase space of χ_P^2 - χ_K^2 of kaon candidate tracks	187
8.26	Data-Monte Carlo comparison of track length variable of kaon candidate tracks in side band 1 and side band 2	188
8.27	Background scale factors ($W_i^{Background}$) derived for each bin in kaon candidate track length distributions in side band 1 and 2	189
8.28	Data-Monte Carlo comparison for the track length of kaon and decay muon candidates	192
8.29	Data-Monte Carlo comparison for the calorimetric kinetic energy of kaon and decay muon candidates	193
8.30	Data-Monte Carlo comparison for the number of hits registered in the collection plane of kaon and decay muon candidates	194
8.31	Data-Monte Carlo comparison for the angle θ of kaon and decay muon candidates	195
8.32	Data-Monte Carlo comparison for the angle ϕ of kaon and decay muon candidates	196
8.33	Data-Monte Carlo comparison for the variable χ_P^2 (χ^2 value calculated under proton hypothesis) of kaon and decay muon candidates	197
8.34	Data-Monte Carlo comparison for the variable χ_K^2 (χ^2 value calculated under kaon hypothesis) of kaon candidates	198
8.35	Event display showing charged current neutrino induced kaon candidate event in MicroBooNE data	198

8.36 Event display showing charged current neutrino induced kaon candidate event in MicroBooNE data	199
A.10 Plots of dQ/dx Vs. drift time for all 56 days of data analyzed in the electron attenuation measurement.	228
B.1 Data-Monte Carlo comparison for the track length of kaon and decay muon candidates (area normalized)	230
B.2 Data-Monte Carlo comparison for the calorimetric kinetic energy of kaon and decay muon candidates (area normalized)	231
B.3 Data-Monte Carlo comparison for the number of hits registered in the collec- tion plane of kaon and decay muon candidates (area normalized)	232
B.4 Data-Monte Carlo comparison for the angle θ of kaon and decay muon candi- dates (area normalized)	233
B.5 Data-Monte Carlo comparison for the angle ϕ of kaon and decay muon can- didates (area normalized)	234
B.6 Data-Monte Carlo comparison for variable χ_P^2 (χ^2 value calculated under pro- ton hypothesis) of kaon and decay muon candidates (area normalized)	235
B.7 Data-Monte Carlo comparison for variable χ_K^2 (χ^2 value calculated under kaon hypothesis) of kaon candidates (area normalized)	236

List of Tables

2.1	Properties of inert gases	10
4.1	Ratio between $(\# \nu_\mu)/(\# \nu_e)$ in data to $(\# \nu_\mu)/(\# \nu_e)$ in simulation measured by different experiments in atmospheric neutrino sector	59
4.2	Latest neutrino oscillation parameters	74
5.1	Impact of individual cuts on track statistics	84
5.2	Space charge dQ/dx corrections in the 22 drift bins	90
5.3	Systematic uncertainties for space charge corrections on the Q_A/Q_C values for all 56 datasets	98
5.4	Summary of systematic uncertainties in percentages on the final Q_A/Q_C value	101
6.1	Tabulated values of CSDA Residual range vs Kinetic energy for stopping muons in liquid argon	124
6.2	Calibration constants and $\chi^2_{Min}/d.o.f$ for the collection plane in Monte Carlo and data	129
7.1	Different single pion production channels in the resonance production for neu- tral current interaction and charged current interaction	142
7.2	Coherent single pion production in the charged current and the neutral current interactions	144
7.3	Possible associated kaon production channels in both charged current inter- action and neutral current interaction	146
7.4	Possible single kaon production channels in the charged current interaction .	146
7.5	Proton lifetime measured on different decay channels by SuperK experiment	152

7.6	Number of events observed for different neutral strange particle species in the neutrino and anti neutrino modes at BEBC, CERN	154
7.7	Inclusive production rates observed for different neutral strange particle species in the interactions $\bar{\nu} - p$, $\bar{\nu} - n$, $\nu - p$, and $\nu - n$ at BEBC, CERN	154
7.8	Different production rates for neutral strange particles coming from anti neutrino-neon interactions in the charged current mode (at BEBC, CERN)	156
7.9	Different production rates and number of events observed for strange particles coming from neutrino-neon interactions in the charged current mode at Fermilab bubble chamber	156
7.10	Different production rates for different individual strange particles in the charged current mode at neutrino energies of 150 GeV on a $H_2 - Ne$ target at Fermilab bubble chamber	157
7.11	Number of events observed for different production channels listed in both charged current and neutral current interactions in the ANL bubble chamber	157
7.12	Cross sections for the reaction $\nu + n \rightarrow \mu^- + \Lambda + K^+$ at different neutrino energies in Fermilab bubble chamber	160
8.1	Data set information in the kaon analysis	165
8.2	Kaon production rates of MicroBooNE at charged current mode by looking into truth level information at a POT equivalent to 6.6×10^{20}	167
8.3	K^+ decay modes and branching fractions	169
8.4	Selection cuts to isolate kaon tracks originating from neutrino interaction vertices	179
8.5	Selection cuts to isolate muon tracks coming from kaons that decay at rest	182
8.6	Background scaling factors ($W_i^{Background}$) in different track length bins	190
8.7	Cross sections for kaon production calculated using ON-Beam data	199
8.8	Cross sections for kaon production calculated using Monte Carlo	199

Acknowledgments

First of all I would like to thank Kansas State University for selecting me for the Ph.D program in physics to pursue my higher education goals. The time, I spent in the university was really fruitful in the sense that the diversity of the experiences, I had in all aspects of my life. The department of physics in KSU is the ideal place to do physics and a special note of thank should go to all my professors and supporting staff for their immense support for me to come so far. The time I spent with my thesis advisor professor Glenn A. Horton-Smith was memorable and fruitful in all possible ways. The support, he rendered to climb the ladder was so helpful. So I would like to make a special note of thank to my professor here. The time, I had with professor Tim Bolton, was once again memorable and really helpful in expanding the horizons of knowledge in the subject of particle physics. I feel really privileged, honored and specially lucky to have spent three complete years in one of the world's leading particle physics national laboratories, the Fermi national accelerator. The Fermi lab offered me the rare opportunity of working with people, best in the business and collected wealth of experience to carve myself to be a modern day particle physicist. So here I would like to make a note of thank to Fermilab as well. The time, I spent with the MicroBooNE collaboration is a very fruitful period in my life which I really cherished. The collaboration offered me the opportunity to deal with real research and tons of knowledge, I earned there is really prolific. Here I would like to make a special note of thank to my three mentors at Fermi lab professor Sowjanya Gollapinni, Dr. Tingjun Yang and professor David Martinez for their immense help and guidance in different research programs. Moreover, I would also like to thank Dr. Christopher Marshall from Lawrence Berkeley National Laboratory (Berkeley, California) and Dr. Alex Higuera from university of Houston, Texas for their expertise knowledge outside the collaboration. In the final note of thank, I like to thank the spoke persons, the physics conveners, the working group conveners and all the fellow collaborators of the MicroBooNE experiment for their immense support to me in various aspects.

Dedication

Here I would like to dedicate this work to all my professors, all my mentors, parents, all my friends and those who helped me in various ways without whom this wouldn't have been possible.

Preface

The detector calibration studies presented here with cosmogenic muons will be helpful to many of the upcoming neutrino experiments who are planning to use LArTPC technology. The second discussion about the neutrino induced charged kaons in argon was primarily motivated due to the facts that there is no such measurement at the moment while already existing measurements are so sparse and most of them are only on lighter nuclear targets. Moreover, in the neutrino energy regime, we are probing is so low such that strange particle production is suppressed making this analysis specially challenging. The information we are presenting here on this particular production channel will specifically be helpful for proton decay searches in LArTPC detectors to mitigate background and better model-building in neutrino generators. Here I would like to thank all those who helped me in various aspects in making this work successful without whom this wouldn't have been possible.

Chapter 1

Introduction

In the standard model neutrinos are predicted to be massless, chargeless, and weakly interacting particles. But the discovery of neutrino oscillations by several experiments in the last decade has given indirect evidence that the neutrino may not be actually massless leading to some *Beyond Standard Model (BSM)* physics. For instance this observation can have an impact on the large scale structure of our universe and its expansion rate. Ever since this discovery, neutrino physics is one of the hottest topics not only within the physics community but also to the general public as well, and there have been several dedicated efforts to thoroughly understand the properties of neutrinos. In the discussion of impact of neutrinos in our day today life, there is an ongoing effort to use neutrinos to monitor the illegal production of nuclear weapons in nuclear non-proliferation efforts, scan the Earth's crust in search of hidden oil and mineral deposits, develop technologies for fast global communication and inter-planetary communication in search of extra-terrestrial life, etc. In the aspect of physics, these neutrinos are nicknamed as **messengers of the universe** and can carry so much information about different cosmological activities happening in the far away universe. Nonetheless, still there are many unsolved puzzles about these mysterious particles. The following is a list of questions yet to be answered:

- Are there sterile neutrino states other than the already accepted neutrino flavors ?
- What is the exact mass hierarchy of mass square splittings ? Is it inverse mass hierarchy

or normal mass hierarchy ?

- Are neutrinos Majorana particles or Dirac particles ?
- Is there any asymmetry between neutrino and anti neutrino oscillations ?
- Can neutrinos be dark matter candidates ?

Answering these questions could ultimately be rewarded with solving long existing mysteries in the physics like matter-antimatter asymmetry in the universe and evidence for elusive dark matter candidates. To overcome this challenge one needs to collect more and more data and focus on more novel detector technologies while having better understanding of neutrino interaction models. A crucial aspect of novel particle detection technologies is the ability to reconstruct neutrino energies with very high precision, which is important in accurately measuring neutrino oscillation parameters. The *Liquid Argon Time Projection Chamber (LArTPC)* technology has already shown promise as the technology for the next generation of neutrino experiments. A more detailed discussion about LArTPC technology will be given in the Chapter 2. In this dissertation one of the topics we talk about is how to precisely calibrate a LArTPC detector to attain a better energy resolution and how to measure the electron attenuation (electron lifetime) using cosmic ray muons. The discussion is specific to the MicroBooNE detector, but can be used by other LArTPC experiments with modifications.

1.1 Electron Attenuation

One of the most fundamental operational requirements of any LArTPC is to have sufficiently large electron drift paths. Contaminants like oxygen and water, which are also known as the *electronegative contaminants* can capture the ionization electron on their drift path. So it is of utmost importance to keep these electronegative contaminants at low concentrations inside the detector. Equation 1.1 governs how a cloud of ionization electrons gets depleted due to capture by electronegative contaminants on their drift path. The attenuation of the

ionization electron cloud can directly impact the energy and track reconstruction. Hence, measuring electron lifetime is one the most fundamental measurements that any LArTPC detector should do, in order to compensate for the loss of ionization electrons. Moreover, the electron lifetime is inversely proportional to the amount of electronegative contaminants present in liquid argon. Thus, any prior knowledge about electron lifetime gives some insight into the purity of liquid argon. In reality, it is hard to find liquid argon, 100% free of electronegative contaminants. There is always a ppm (parts per million) level oxygen contamination present in the commercially available liquid argon. Moreover, due to the out-gassing of warm walls, cables, other detector components, ... etc and leakages through detector feedthroughs, these contaminants can leak into the detector. Other contaminant of interest is nitrogen, which can quench and absorb the scintillation light produced by neutrino-argon interactions. The maximum tolerable level of nitrogen that can be present in the detector, should be less than 2 parts per million (ppm) for proper detector operations. In the MicroBooNE, the desired level of liquid argon purity is achieved by continually operating liquid argon purification and re-circulation system, which consists of dedicated filters to remove mostly water and oxygen.

$$\frac{n_e(t_{\text{drift}})}{n_e(t_0)} = \exp\left(\frac{-(t_{\text{drift}} - t_0)}{\tau}\right) \quad (1.1)$$

Here $n_e(t_0)$ stands for the initial number of electrons whereas $n_e(t_{\text{drift}})$ is the number of electrons after a time t_{drift} . An important parameter in this equation is τ , which stands for the electron lifetime. The electron lifetime contains information about the amount of electronegative contaminants present in the detector where a higher electron lifetime is indicative of low levels of contamination. If liquid argon is 100% pure, then τ should ideally be infinite.

We can deploy different techniques to measure liquid argon purity inside the MicroBooNE detector and following lists some of the possible methods:

- Using dedicated devices called purity monitors.
- Using long minimum ionizing cosmic ray muon tracks.

- Using laser tracks.

But the discussion here is only restricted to the measurement of liquid argon purity using long cosmic ray muon tracks collected by the MicroBooNE detector. A more detailed discussion about this measurement will be given in the Chapter 5.

1.2 Detector Calibration

The first step of reconstructing particle's energy of any LArTPC detector is to use the charge information registered in the anode wire plane signals (waveforms). But the charge extracted in this way normally doesn't reconstruct the particle's energy in correct way due to a number of reasons. Among those reasons:

- Distortions in detector response due to misconfigured or cross-connected TPC channels.
- Space Charge Effects.
- Electron attenuation.
- Diffusion.
- Recombination.

are the most significant. So to reconstruct particle's energy properly, we need to correct for these effects. In the detector calibration, first we correct the dQ/dx (charge deposited per unit track pitch) values for these detector effects where this procedure is known as the *dQ/dx calibration* or the *relative calibration* of the detector. Next we move to calculate the energy loss of particle due to ionization starting from the corrected dQ/dx values. This second step of the detector calibration is termed as the *dE/dx calibration* or the *absolute calibration* of the detector. More details of this detector calibration study will be presented in the Chapter 6.

1.3 Neutrino Induced Kaon Production In Argon

As LArTPC technology is a relatively novel technology, there has been very little known about different particle production rates in argon compared to other commonly used detector media like carbon and water. Specially there has been no measurement at the moment for rare processes like neutrino induced strange particle (kaons and hyperons) production in argon. The only available data at the moment for this kind of exotica search is from bubble chamber data, which has very limited statistics and kaon production rates on carbon by MINERVA experiment at Fermilab. In this dissertation one of the other topics we are focusing on is neutrino induced charged kaon production in argon in the intermediate energy regime (~ 1 GeV neutrino energy). The information will be useful for other upcoming LArTPC neutrino detectors and better understand different nuclear effects in argon.

The kaons are born as eigenstates of the strong Hamiltonian and characterized by a strange quark in its content. They manifest themselves as neutral kaons ($K^0(d\bar{s}), \bar{K}^0(s\bar{d})$) and charged kaons ($K^+(u\bar{s}), K^-(s\bar{u})$) where the mass of charged type is ~ 493 MeV while neutral kaons are relatively heavier having a mass of ~ 498 MeV. The charged kaons can live up to 12 ns before their decay into other lighter elements where the decay of neutral kaon systems is of particular interest. The weak interaction decay eigenstates of neutral kaons are different to their strong interaction production eigenstates. The two weak interaction eigenstates of neutral kaons are known as $K_S(K_{short})$ and $K_L(K_{long})$, which are characterized by distinct decay modes and lifetimes. The K_S component can stay upto $\sim 0.9 \times 10^{-10}$ seconds and ultimately decays into two pions while K_L component can live up to $\sim 5.1 \times 10^{-8}$ seconds and decays into three pions. So one consequence of this two distinct decay components is that a neutral kaon beam consisting of 50% of K_L and 50% of K_S components would ultimately end up with a pure beam of only K_L component in the same manner, a ν_μ neutrino beam completely oscillating into a ν_e neutrino beam as K_S component becomes exhausted due to its low lifetime. The measurement of kaon production in argon would primarily help to better understand the strange quark content of the nucleus and in turn it

would help to better understand:

- Neutrino oscillation parameters
- Cabbibo and V-A theories

In the last 50 years or so, one of the major quest of physics was to come up with a single theory that would explain everything in the universe in a form of one single equation. We would call this the infamous *Theory of Everything*. While theories like *SUSY (Super Symmetry)*, *GUT (Grand Unified Theory)* etc are possible candidates for this ultimate theory, one specific model named *SUSY GUT (Super Symmetric Grand Unified Theory)* has incorporated many features expected. All of these exotic models predicts some beyond standard model physics where one of the striking predictions of the SUSY GUT is that proton is no longer a stable particle. We already know that the neutron, the counter part of the proton is not a stable particle and has a lifetime of only ~ 15 minutes and finally decays to a proton by β emission. According to this new model, one of the golden decay channels of proton is $p^+ \rightarrow K^+ + \nu$. The current established limit for the lifetime of proton is 10^{33} years, which is way beyond the age of our own universe. One of the forerunners of proton decay search is the SuperKamiokande experiment in Japan, which is a multi kilo ton water cherenkov detector. The upcoming experiments like DUNE (Deep Under ground Neutrino Experiment), a multi kilo ton liquid argon time projection chamber, is also focusing on looking into this rare process. All these experiments would keep an eye on a bunch of protons (ideally it should be over 10^{33} protons) until one of them decays to a charged kaon. Eventually this charged kaon would decay to a muon and if the detector is sensitive enough, we can see the michel electron coming from that muon decay as well. As this is a very rare process it is of utmost importance that this kind of nucleon decay experiment fully understand its background processes, which could mimic the same topology as their signal events. The main background of concern for this particular proton decay channel is that an atmospheric neutrino sneaking into the detector medium and producing a secondary charged kaon, which would follow the same decay pattern as our signal. Prior knowledge about neutrino induced charged kaon production will aid in mitigating background for ongoing nucleon decay experiments.

The work presented in this dissertation was performed while I was a member of Micro-BooNE collaboration. I used many tools produced by others in the collaboration and by me. During the course of this work, I produced several technical notes, public notes, and a proceedings paper. The work described in the Chapter 5 is largely derived from^[1] and Chapter 6 from^[2], which I co-authored.

Chapter 2

MicroBooNE Experiment

In this chapter, we give an overview picture about LArTPC technology and MicroBooNE experiment followed by a detail discussion about different sub systems of the MicroBooNE detector.

2.1 LArTPC Technology

The concept of LArTPC detectors dates back to the early 1970s. C. Rubbia suggested their use for neutrino detection in 1977^[3] referencing earlier work by Nygren on TPCs^[4] and Derenzo, et al, on liquid argon wire chambers^[5]. The technology really began to boom in the ICARUS program^[6] where the worlds first large scale LArTPC neutrino detector named T600 was built in 2010 in the Gran Sasso laboratory, Italy. The detector was filled with approximately 600 tons of liquid argon. Going in the foot steps of the ICARUS experiment, the two experiments at Fermilab ArgoNeuT^[7] and MicroBooNE^[8], which are comparatively smaller, also used the LArTPC technology. Once all these experiments proved that this novel technology was feasible, the upcoming large scale neutrino experiments SBN^[9] (Short Baseline Neutrino Program) at Fermilab and DUNE^[10] (Deep Underground Neutrino Experiment) laid plans to use this technology for their massive neutrino detectors.

The major component of any LArTPC detector is the Time Projection Chamber (TPC),

which comprises an anode and a cathode kept at certain voltages so as to introduce a uniform electric field between them. The TPC is completely filled with ultra pure liquid argon. Ideally the detector medium could be any inert element such as He, Ne, Xe, etc. Liquid argon is the superior choice for neutrino detector for several reasons:

- Argon is dense - Density of argon is 1.4 g/cm^3 and that makes it an ideal target medium for any neutrino experiment.
- Argon has relatively high boiling point and is very abundant in nature - The boiling point of argon is 87.3 K which is higher than that of nitrogen. So liquid argon comes as a by product of mass scale production of liquid nitrogen. Moreover, argon is naturally abundant in the atmosphere compared to the other rare elements like Kr or Xe. Because of these reasons liquid argon is readily available in the market for a cheaper price.
- Argon has a higher electron mobility - Argon does not attach ionization electrons easily, so it permits for long drift distances.
- Argon is a bright scintillator - It copiously produces scintillation light in the neutrino interactions. Moreover, liquid argon is transparent to its own scintillation light.
- Liquid argon has good dielectric properties - Even at very high voltages, liquid argon remains stable and does not suffer any breakdowns.

Table [2.1](#) shows some interesting properties of inert gases.

Property	He	Ne	Ar	Kr	Xe
Boiling point at 1 atm (K)	4.2	27.1	87.3	120.0	165.0
Density (g/cm^3)	0.125	1.2	1.4	2.4	3.0
Radiation Length (cm)	755.2	24.0	14.0	4.9	2.8
dE/dx (MeV/cm)	0.24	1.4	2.1	3.0	3.8
Scintillation (γ /MeV)	19000	30000	40000	25000	42000
Scintillation λ (nm)	80	78	128	150	175

Table 2.1: Properties of inert gases^[11].

When a charged particle traverses through liquid argon, it produces clouds of ionization electrons by knocking out loosely bound outermost electrons of argon atoms. In this process UV photons are also copiously produced. The production mechanism of UV photons in liquid argon will be discussed in more detail in the Section 2.2.2. Due to the applied electric field between anode and the cathode, ionization electron are propelled to travel to the anode where sense wires in the anode planes will ultimately collect these electrons. The UV photons isotropically produced are collected by Photo Multiplier Tubes (PMTs) sitting inside the detector. Thus, one can retrieve the information recorded in both PMTs and anode sense wires to reconstruct particle tracks and their energies with very high precision. The images reconstructed by LArTPC detectors have such a high resolution that only the bubble chamber images are comparable with them. Figure 2.1 shows the basic working principle of a LArTPC detector and how the tracks are reconstructed using the information registered in the anode wire planes.

2.2 MicroBooNE Detector

The main component of the MicroBooNE detector is its Time Projection Chamber (TPC). The active volume of the MicroBooNE TPC defined to be the maximum volume, which can be used for any physics analysis, is a box with 2.3 m high, 2.5 m wide, and 10.4 m long.

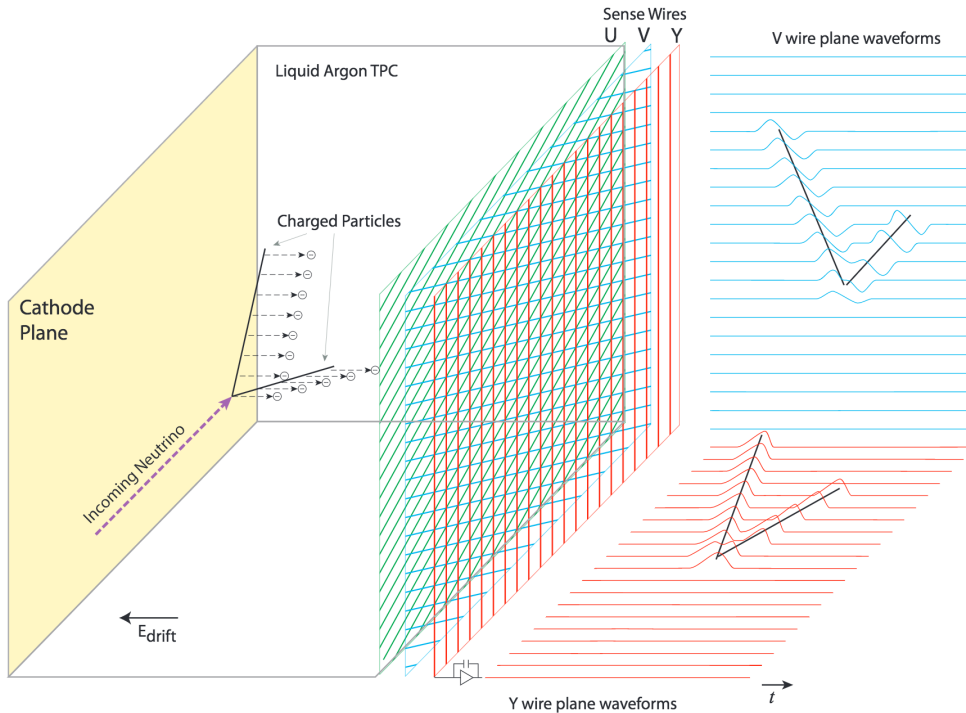


Figure 2.1: A cartoon showing the basic working principle of a LArTPC detector^[8]. The charged particles ionize the liquid argon and these ionization electrons drift to the anode wire planes (here U,V, and Y planes). The information registered in the anode wire planes combined with timing information is then used to reconstruct both particle energies and 3-D trajectories.

Once the active volume is completely filled with liquid argon, the active mass of the TPC is estimated to be approximately 85 tons. There are three major components, which comprise the MicroBooNE LArTPC, namely 1) Cathode 2) Anode 3) Field Cage. The cathode is made up of stainless steel sheets, which are fixed to a supporting frame and is kept at a negative voltage of -70 kV. This voltage is supplied through a high voltage feedthrough connected to a high voltage power supply. The anode consists of three separate anode wire planes (two induction planes U & V, and one collection plane Y) where each wire plane is made up of highly tensioned electrically connected stainless steel wires having a spacing of 3 mm. The two induction planes are slanted $\pm 60^\circ$ to the vertical, whereas the collection plane wires are completely vertical. The three planes are also separated from each other by a 3 mm gap.

The entire anode frame consists of a total of 8256 sense wires where the two induction planes have 2400 sense wires in each while the collection plane is made up of 3456 wires. The three anode planes (U, V & Y) are kept at bias voltages of -200 V, 0 V & +440 V respectively in order to make sure that ionization electrons are collected only by the collection plane but not by any of the two induction planes. Furthermore, these bias voltages also provide the necessary shielding to isolate each plane from others. The field cage defines the perimeter of the active volume and houses both cathode and anode wire planes. The structure of the field cage is made up of 64 stainless steel tubes where each tube is shaped into form a rectangular loop. Each rectangular loop of this structure is electrically connected to the neighboring loop via a resistor divider chain in order to have a uniform electric field from anode to cathode. The operational electric field of the MicroBooNE TPC is known to be 0.273 kV/cm. Once a trail of ionization electrons are born inside the active volume, they travel towards the anode wire planes in the influence of the applied electric field. When the electron cloud passes by each of the two induction planes, they induce a bipolar electrical signal in both of the planes. At last the ionization electrons are collected by the collection plane and a unipolar signal is generated in the collection plane. By combining the information registered in any of the two anode planes and the time it took for the electron cloud to reach to the collection plane, one can pin point the 3-D location of the origin of the ionization electron cloud. Furthermore, by analyzing the shapes of the signals generated in each of the anode planes, the total energy of the ionization electron cloud can also be determined. The whole MicroBooNE TPC is lying inside a structure called cryostat, which is a cylindrical shaped stainless steel vessel having a capacity of 170 tons of liquid argon. The outer insulating foam layer of the cryostat is intended to prevent the influx of heat from surrounding environment into the detector, which can otherwise boil the liquid argon inside. The cryostat lies inside a 10 m deep pit called the Liquid Argon Test Facility (LArTF) inside Fermilab lab site (see Figures 2.2 & 2.3). The other subsystems, which make up the MicroBooNE detector will be discussed in coming sections.

Major Components in the MicroBooNE TPC

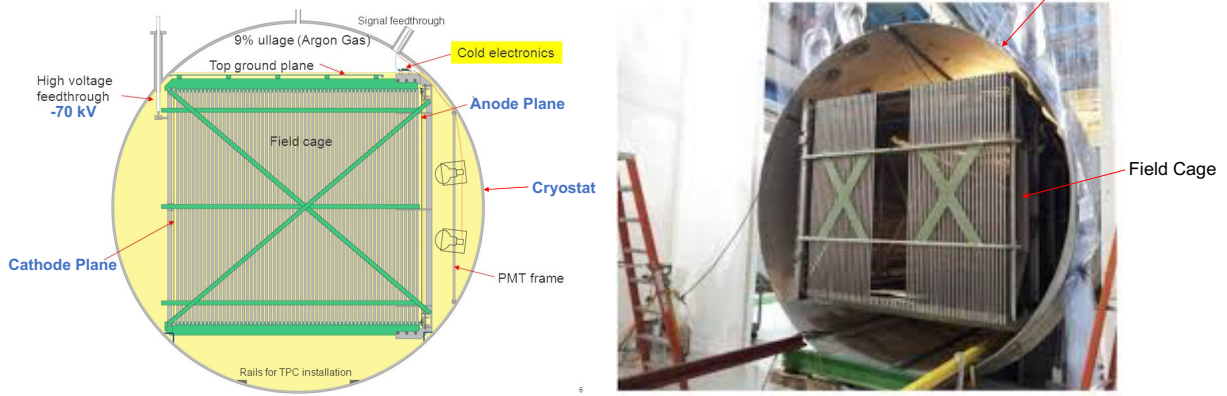


Figure 2.2: (Left) A cartoon showing the cross-sectional view of the MicroBooNE detector^[12]. This shows all the major components of the detector, which are sitting inside the cryostat. (Right) A real image of the MicroBooNE field cage sitting inside the cryostat before being filled with liquid argon^[13].



Figure 2.3: Real image of the MicroBooNE cryostat sitting inside the LArTF^[8]. The outer foam layer (white) of the cryostat prevents heat leaking inside from the surrounding environment.

2.2.1 Liquid Argon Purification System

The primary target of the MicroBooNE purification system is to keep the electronegative contaminant levels as low as possible (below 100 ppt). In MicroBooNE, the electronegative

contaminants are mainly made up of H_2O and O_2 , which can leak into the detector through the processes like out-gassing, diffusion, and detector leakages via detector walls and nozzles. The main disadvantage of the presence of electronegative contaminants is the attenuation of the ionization electron clouds where these contaminants tend to capture some of the ionization electrons along their drift path resulting a degradation of data, the experiment collects. Moreover, the system also helps to keep the elements like N_2 at bay, which would other wise quench the scintillation light yield. The purification system mainly consists of two sets of liquid argon pumps and filters where one set is always on standby while the other one is on operation. The two filters in each of the system are made up of different filter media, which serve for different purposes. Both liquid and gaseous argon is removed from the detector for purification and once argon passes through the first filter, it removes mostly H_2O while O_2 and N_2 to a lesser extent. The second filter helps mainly to get rid of O_2 while H_2O is also filtered out in small quantities. After the purification, argon is injected back into the detector in the form of liquid. The impurity levels of liquid argon is constantly monitored online to make sure the depletion of the ionization electron clouds is minimal (see Figure 2.4.).

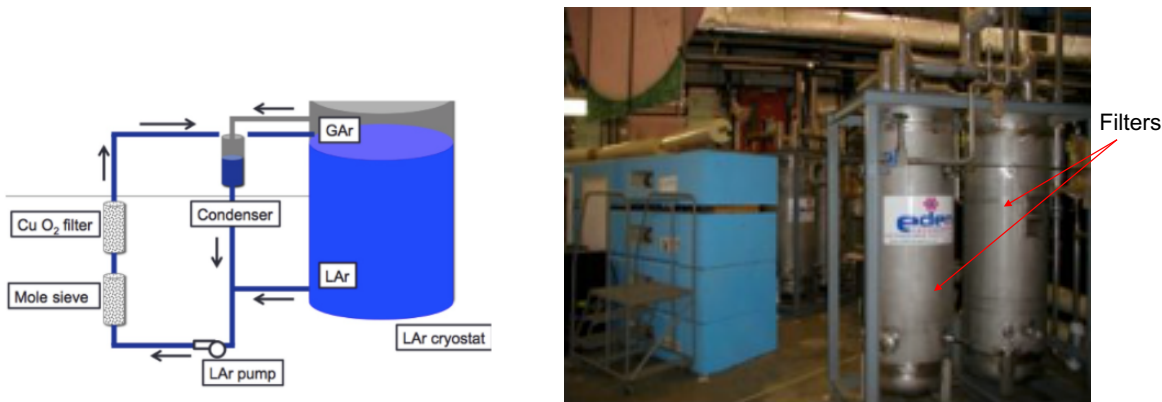


Figure 2.4: (Left) Cartoon of MicroBooNE purification system^[14]. Both liquid and gaseous argon is removed from the detector and passed through two filters to get rid of impurities. (Right) Real image of two filters in one of the MicroBooNE filter skid^[15].

2.2.2 Light Collection System

When a charged particle traverses liquid argon, it produces both scintillation light and cherenkov radiation. The cherenkov radiation is a well directed cone of light that is born as a result of a charged particle traveling higher than the speed of light in the detector medium. The mechanism of the formation of the scintillation light is as follows: An excited argon atom combines with an argon atom at its ground state forming an unstable dimer or an excimer state (Ar_2^+). Then the excimer or dimer radiatively decays producing an isotropic distribution of UV photons having a wavelength of 128 nm. The decay of the excimer state consists of two components where the prompt signal has a decay time of 6 ns whereas the longer component corresponds to a time constant of 1.6 μs . The scintillation light yield of the liquid argon is known to be 40000 photons/MeV under no electric field making it one of the brightest scintillator materials. The information of the light produced inside the detector is useful in a number of ways:

- it can be used as an event trigger in the beam spill window, which helps to significantly reduce the amount of data that should be recorded.
- it can be used to estimate the start time (t_0) of particle tracks, which helps to suppress the background contamination by cosmics.
- it can be used to identify specific non beam physics events like supernovae bursts.
- it can be used to distinguish between specific topologies like through going and stopping muons.

The light collection system of MicroBooNE is intended to record all the information related to the light produced inside the detector and consists of two units called the primary system and the secondary system. The secondary system, which is made up of light guide paddles is mainly for R&D purposes. The primary system is made up of 32 8-inch (20 cm) Hamamatsu photo multiplier tubes, which sit behind the anode wire planes covering the YZ plane of the detector. As the PMTs are not sensitive to UV light, each PMT is supplied with

an acrylic plate coated with *Tetraphenylbutadiene* (*TPB*) to convert UV light into photons having a peak wavelength of 425 nm before the detection. Figure 2.5 (Left) shows a PMT used in the MicroBooNE light collection system.

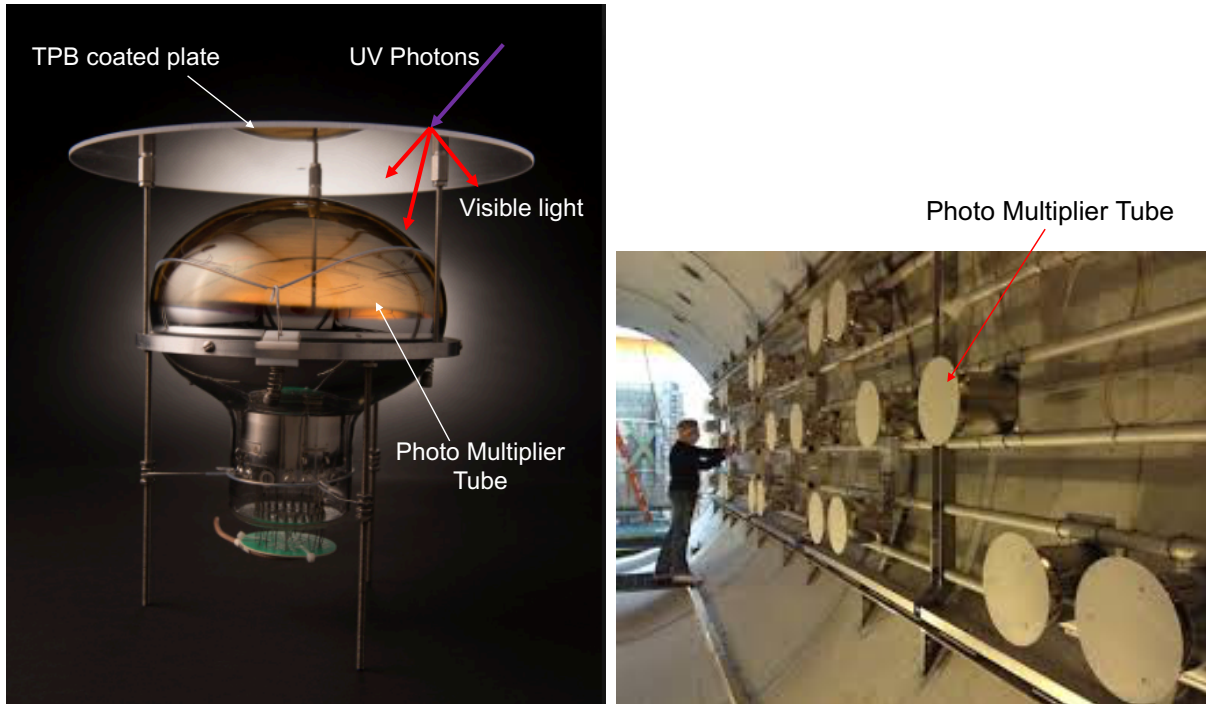


Figure 2.5: (Left) Image of a photo multiplier tube used in the MicroBooNE light collection system^[16]. (Right) The PMT system of the MicroBooNE sitting inside the cryostat before being filled with liquid argon^[8].

2.2.3 UV Laser System

As MicroBooNE is a surface detector, there is a high rate of cosmic ray activity inside the detector. Quantitatively speaking, it has been estimated that in every 4.8 ms wide readout window, there are roughly 25 cosmic criss-crossing the detector volume. This leads to a build up of slow moving, positively charged argon ions inside the detector, which results in distortions in the uniformity of the electric field vector. The distortions in the electric field can badly affect the reconstructions of particle trajectories, which would then propagate to the momentum estimation based on Multiple Coulomb Scattering (MCS) and other track range based methods. So it is of utmost importance to map out electric field

distortions and introduce corrections for proper track reconstruction. The UV laser system in the experiment was introduced for this purpose. The system consists of two steerable lasers installed in either side of the detector in the beam direction. The lasers are capable of emitting a collimated beam of UV photons having a wavelength 266 nm at a preferred direction. The tracks generated by shooting the lasers are found to be straight, less ionizing than minimum ionizing particles (leading to less electron-ion recombination), and free of δ -rays. Because of this, the E-field corrections generated by laser tracks are thought to be more accurate over the corrections derived using other alternative methods like the use of cosmic muons (see Figure 2.6).

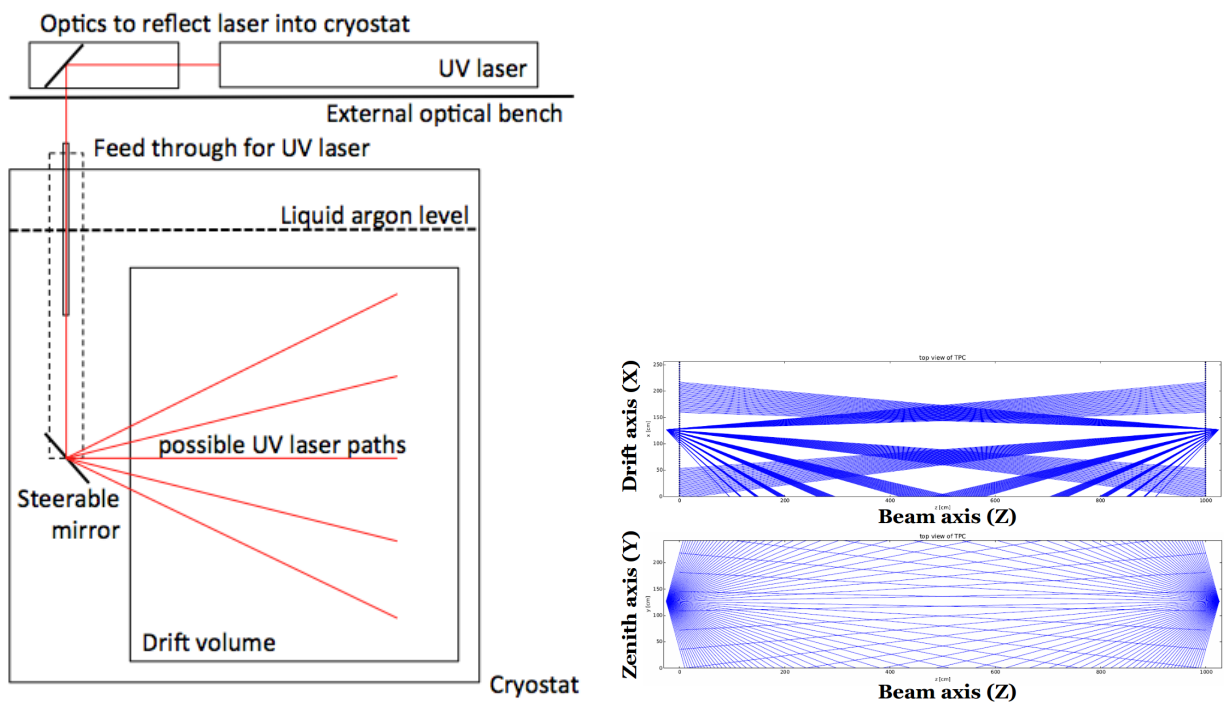


Figure 2.6: (Left) Cartoon of MicroBooNE steerable UV laser^[17]. (Right) Diagram showing the laser tracks produced by two lasers installed at upstream and downstream ends of the MicroBooNE detector by shooting at different angles^[18]. (Top) XZ plane view. (Bottom) YZ plane view.

2.2.4 PMT and TPC Electronics

The MicroBooNE electronic system can be divided into two main categories: 1) TPC electronics 2) PMT electronics. The TPC electronics consists of cold electronics immersed in

the liquid argon and warm electronics lying outside the cryostat. The main component of the cold electronic system is the analog front end CMOS ASIC mounted on a motherboard. Each ASIC is connected to 16 anode wires and responsible for preamplifying and shaping the analog signals generated in sense wires before passing them to the warm electronics. The ASICs were designed in such a way that they can be configured to operate in any of four possible gain settings (4.7, 7.8, 14, 25 mV/fC) and in any of four peaking time settings (0.5, 1.0, 2.0, 3.0 μ s). There are a total of 516 CMOS ASICs deployed in MicroBooNE to handle the signals generated in a total of 8256 anode plane sense wires. These ASICs, which sit close to the anode plane wires, have high signal to noise ratios and high gains compared to ASICs operating at room temperatures, which is crucial for the detection of low threshold signals (see Figure 2.7 (Bottom)). The main components of the TPC warm electronics are the intermediate preamplifier, which amplifies the signal from cold electronics for the long distance transmission to the readout electronics, service boards, which regulate and monitor the signals from front end ASICs, and the readout electronics, which digitizes and compresses the data before being handed over to the DAQ. The electronics used in the PMTs are quite different to that of the TPC electronics design. There is only one cold cable dedicated for the both purposes of supplying the high voltage and transmitting the read-back signals for each PMT. A custom designed splitter circuit is deployed to decompose the two signals at the bottom of the chain. The output signal of the splitter circuit consists of two components called the High-Gain(HG) signal and Low-Gain(LG) signal. These signals are shaped by dedicated preamp/shaper boards into unipolar signals with a peaking time of 60 ns and sent to the PMT readout electronics for digitization.

2.2.5 Readout Electronics

The MicroBooNE readout electronic system can also be separated into: 1) TPC readout electronics 2) PMT readout electronics. In the TPC readout system, the first step is the transmission of shaped and amplified signals of all the 8256 anode sense wires to the ADC and Front End read-out Modules (ADC/FEMs) through warm cables. There are a total

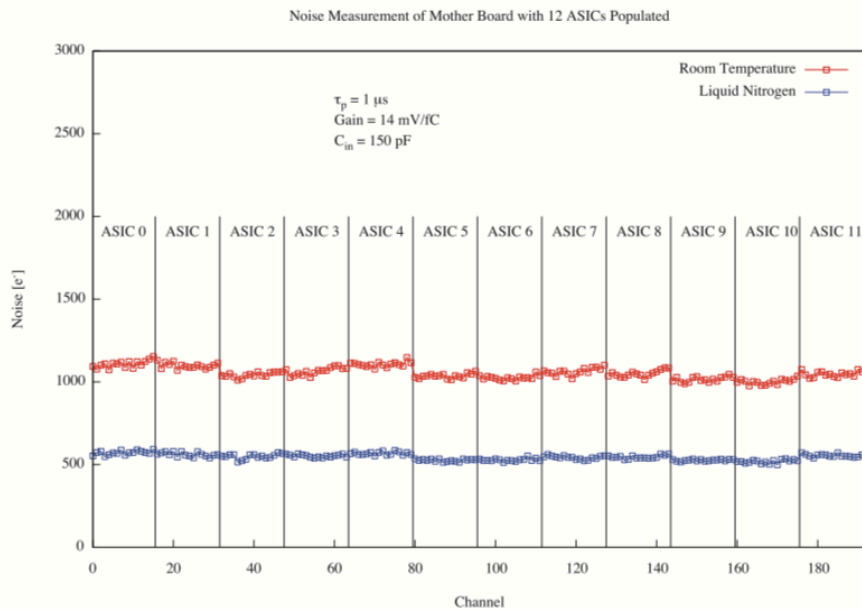
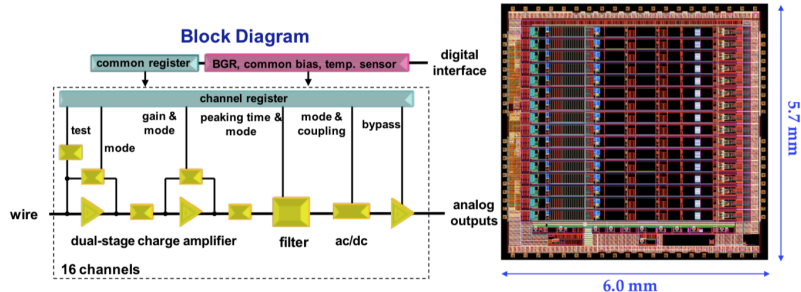


Figure 2.7: (Top) Image of a front end CMOS ASIC used in the MicroBooNE cold electronics^[19]. (Bottom) Noise level of ASICs under different temperature conditions. It is clearly obvious that under cryogenic temperatures noise levels are so low^[8].

of 130 ADC/FEMs in the TPC readout system, which are evenly distributed among nine readout crates where all the nine crates are synchronized to each other using a 16 MHz clock. The ADC modules digitize the analog signals generated by anode sense wires continuously at a rate of 16 MHz and pass the output to FEMs. The FPGAs housed in FEMs then reduce the sampling rate from 16 MHz to 2 MHz and data is Huffman compressed by a factor of 4.5 before being transferred to the XMIT modules for temporary storage. In the PMT readout system there are 3 ADC/FEM readout boards which digitize all the PMT analog signals at a rate of 64 MHz and then hand over the signal to the XMIT modules as in the TPC readout.

2.2.6 Data Acquisition System (DAQ)

The MicroBooNE DAQ system primarily involves in writing data to the local disks passed from the readout crates, configuring readout electronics, and close observation of data flow and detector conditions during data taking period. In the first place, data from crates in the readout system is passed to a server called sub-event buffer (SEB) via optical fibers. In the next step, an application collects all the information related to a TPC event and constructs the sub-event fragments. In the MicroBooNE readout there exist two data streams called *NU* stream and *SN* stream. In the *NU* stream, the aforementioned sub-events fragments are directly passed to the Event Building Machine (EVB), next in the chain which builds up the complete event. Next the consistency of those events are checked based on a high-level software trigger to determine whether to keep the event or discard. Once an event passes the software trigger, it is stored in the local disk and copied to another server for compressing and then transferred to the Fermilab central data management system for long term storage. The data in the *SN* stream is written directly to the local disk from SEBs without going through the EVB. The maximum data writing speed in either *NU* or *SN* streams to the local disk is expected to be 300 MB/s.

2.2.7 Slow Monitoring and Control System

The MicroBooNE slow monitoring and control system is responsible for controlling and monitoring devices, which are important to the experiment, observing the detector and environmental conditions, archiving data, status displaying, and issuing alarms if needed. The system keeps eye on approximately 4500 different variables where power supply controls, temperatures of different detector components, fan speeds, rack protection interlock status are of high importance. The system is primarily based on EPICS where applications from *Control System Studio Software Collection* is used for providing necessary displays, alarm notifications, and data archiving. The Data Acquisition System (DAQ), cryogenic and beam monitoring systems operate partially independent of the slow monitoring system but coor-

dinate in exporting data for archiving and status displays (see Figure 2.8).

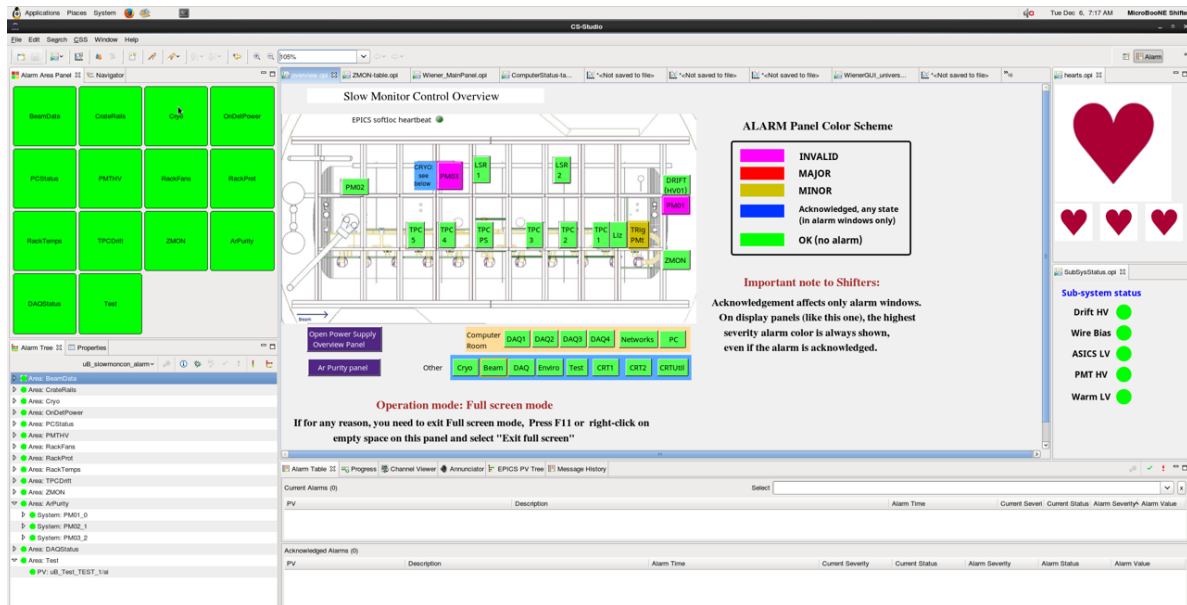


Figure 2.8: Screen shot of the MicroBooNE slow monitoring and control system display. (Top Left) Alarms dedicated for different subsystems of the detector. (Bottom Left) Alarm tree, which shows the status of specific variables, (Middle Top) Overview panel, which gives access to the different subsystems of the detector, (Middle Bottom) Alarm table, which gives specific information about variables in alarm status, (Top Right) Heart beat, which confirms the programs dedicated for different subsystems such as cryogenics, high voltage etc are properly running, (Bottom Right) Alarms dedicated for different power supplies of the detector [8].

Chapter 3

Booster Neutrino Beam (BNB)

It is of utmost importance to have a clear understanding about the kinematics of the neutrino beams used in doing neutrino related physics when it comes to making strong statements in any of the cross section or oscillation analysis. MicroBooNE makes use of both of the two neutrino beams produced in Fermilab, namely the BNB and the NuMI (Neutrinos from Main Injector). But the experiment is heavily dependent on the BNB beam as the majority of its main analyses are based on it. The BNB is a well understood neutrino beam, which is rich in ν_μ s ($\sim 93\%$) having an energy spectrum peaking at ~ 0.8 GeV. The beam is born in the form of H^- ions, which are then accelerated by the Linear Accelerator (LINAC) at Fermilab up to the energies of 400 MeV before being injected into the Booster ring. The output of the Booster is 8 GeV (8.89 GeV/c momentum) protons, which are then directed to the beryllium target. The secondary meson beams, which mainly consist of π^\pm , K^\pm and K^0 produced in collisions, are then passed through the focusing-defocusing magnetic horn to get rid of unnecessary particles and keep the secondary beams focused. Ultimately these pions and kaons decay inside the decay pipe giving birth to well collimated beams of neutrinos, which would finally reach the detector sitting very last in the chain. In this chapter we discuss all the stages of the Booster Neutrino Beam in detail, followed by a discussion about the composition of the neutrino beams (see Figure 3.1).

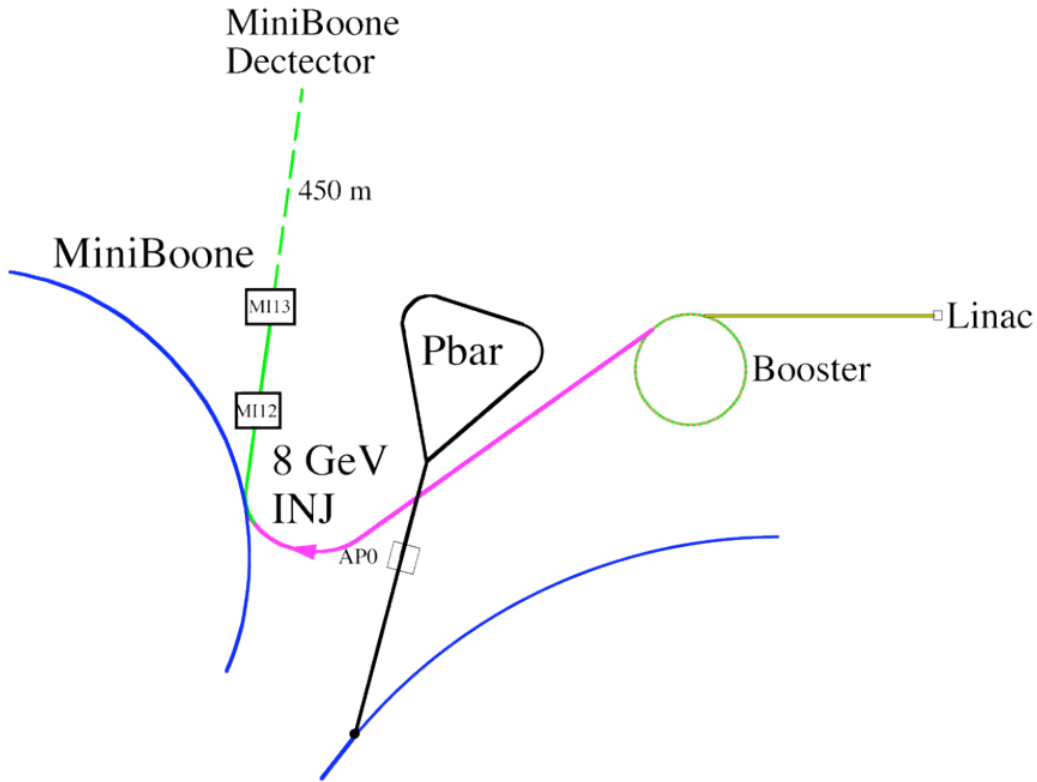


Figure 3.1: Booster Neutrino Beam at Fermilab^[20]. The beam starts with H^- ions accelerated by the LINAC up to 400 MeV. Then these H^- ions are injected into the Booster, which further accelerates things and out comes the 8 GeV protons. Protons are directed on to a beryllium target and the resultant secondary meson beams are passed through magnetic horn (Green line). Mesons decay giving birth to neutrinos and these neutrinos would reach to the MicroBooNE detector which is ~ 470 m away from the target hall.

3.1 Booster

As mentioned earlier, the Booster Neutrino Beam starts with a H^- source. The production mechanism of these H^- ions is of particular interest. Here a H_2 -filled bottle is supplied with some very high voltage (-35 kV) to form electric arcs in between anode and the cathode. These electric discharges can easily ionize the hydrogen gas inside and form a plasma in the process. Once positively charged hydrogen atoms drift to the cathode to get neutralized, some of these H^+ ions can grab a pair of electrons from the plasma giving birth to H^- ions. To extract these H^- ions out of the source, the voltage applied between the anode and the cathode is pulsed and the result is a 35 keV beam of H^- ions. When the H^- beam is ready, the first

stage of the acceleration is provided by the *RFQ (Radio Frequency Quadrupole)* cavities. But before this acceleration happens, there is some processing going on to the beam, as described below. First the beam is better focused using some solenoids and corrector magnets. Here the corrector magnets are basically responsible for adjusting the horizontal and vertical position of the beam. At this stage, steps are taken to sandwich H^+ ions in the beam to minimize the repulsive forces between negatively charged hydrogen atoms, which would otherwise force the beam to diffuse. Next to match the frequency of the beam to that of RFQ cavities, an *Einzel* lens is used which provides a pulse structure to the beam having a pulse rate of 15 Hz and 100 μs beam width. The RFQ cavities can speed up the beam up to 750 keV and hand over to the LINAC. The acceleration in the LINAC happens in two separate steps again by RFQ cavities. In the first stage, the beam is accelerated up 116 MeV with an RF frequency of ~ 201 MHz, followed by acceleration to a beam energy of 400 MeV (the corresponding RF frequency in the second step is ~ 805 MHz). Next in the chain is the Booster. The beam coming out of the LINAC is propelled towards the Booster by a *chopper* equipped with two electrodes placed along the beam line in both sides. A pulsed potential difference is introduced in between electrodes once the Booster is required to be filled with beam. A kicker magnet would then bend the H^- beam to the full curvature of the ring and *stripping foils* on the way strip off the two electrons attached to hydrogen atoms resulting a pure beam of protons. The FNAL Booster has a circumference of 474 m and a synchrotron frequency of 15 Hz. The maximum time it takes for a proton beam to circumnavigate the whole distance is 2.2 μs . The RFQ cavities are used here to accelerate the beam, which has an initial operating frequency of 37.8 MHz. But once the beam acquires more and more speed the RF frequency also needs to be adjusted. By the time the accelerated proton beam leaves the Booster, the period (time per one revolution of the Booster) drops from 2.2 μs to 1.6 μs forcing the RF frequency to range between 37.8 MHz to 52.8 MHz. A single complete revolution of the beam inside the Booster is technically termed as a *Turn* while several turns of the beam make up the *Batch*. The number of turns per batch is not fixed but is decided by the preferred intensity of the beam. The same kicker magnet, which steered the H^- beam into the Booster is used to extract the beam out of the Booster. As this kicker magnet has

a significant ramp-up time, to avoid any out of focus beam during the extraction, a *Notch* in the beam is deliberately built up. Here the term notch refers to one full revolution of the beam inside the Booster with no protons in it. The beam is extracted from the Booster in bunch form, where in one go, a total of 84 bunches are extracted from a $1.6 \mu\text{s}$ wide batch having a spacing of 18 ns in between two consecutive bunches and 2 ns bunch width. But the notch formed corresponds to three bunches with no protons in it. So the net output beam corresponds to a total of 81 filled buckets having a proton kinetic energy of 8 GeV with a corresponding momentum of $8.89 \text{ GeV}/c$ (see Figure 3.2).

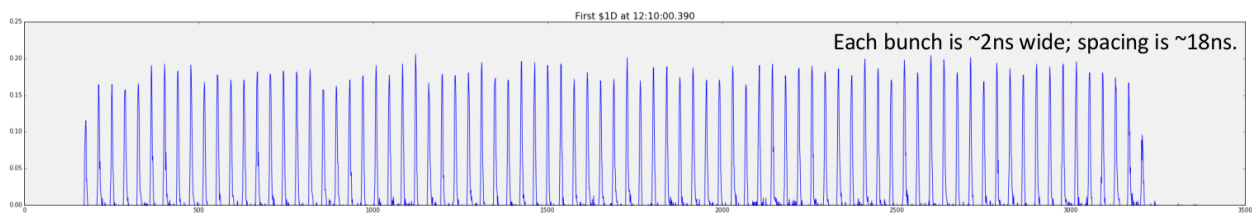


Figure 3.2: Beam structure of the output of the Booster^[20] (Image courtesy of Tom Kobilarcik). A $1.6 \mu\text{s}$ Booster batch consists 84 bunches, out of which 81 buckets are filled having a 18 ns spacing and 2 ns beam width.

3.2 Beam Monitoring

Before the Booster beam reaches the target, the beam is monitored by several dedicated systems:

Toroids: The two toroids deployed, measure the flux of the incoming proton beam.

Beam Position Monitors (BPMs): The BPMs are made up two plates, which calculates the difference of charge induced on the two plates once the beam passes through. The beam position is monitored using these devices at several locations in the beam line to see any deviations in the beam direction.

Multi Wire Chamber: The Multi Wire Chamber is dedicated to pin-point the horizontal and vertical position of the beam while measuring beam width. This device is made up of 48 horizontal and 48 vertical wires having a wire pitch of 0.5 mm in both planes. The measurement is done using the charge induced on individual wires once the beam passes

through the wire planes.

Resistive Wall Monitor (RWM): This measures the timing and intensity of the proton pulse just before it hits the target. The information collected by the RWM is really useful in matching neutrino interactions inside the detector with beam timing.

3.3 Target

The target of the Booster Neutrino Beam is made up beryllium. The choice of beryllium was motivated mainly due to two reasons:

- To minimize the radio activity in the target area in case of a target replacement.
- Energy losses are at minimum levels once the proton beam hits the target.

The target is made up of seven cylindrical shaped beryllium slugs where each individual slug has a radius of 0.51 cm. The whole seven slugs has a total length of 71.1 cm. The target is sitting inside another cylindrical container, which is also made up of beryllium having an inner radius of 1.37 cm and thickness equivalent to 0.9 cm. The air circulating inside this container is used for cooling the target where each slug is connected with the container via metal fins, which are also made up of beryllium (see Figure 3.3).

3.4 Focusing-Defocusing Horn

The focusing-defocusing horn of the Booster Neutrino Beam serves for two purposes:

- Keep the secondary meson beam well focused to make sure the neutrinos born after decay are also well focused.
- Switch from neutrino mode to anti neutrino mode as desired by focusing preferred mesons while defocusing the unwanted mesons.

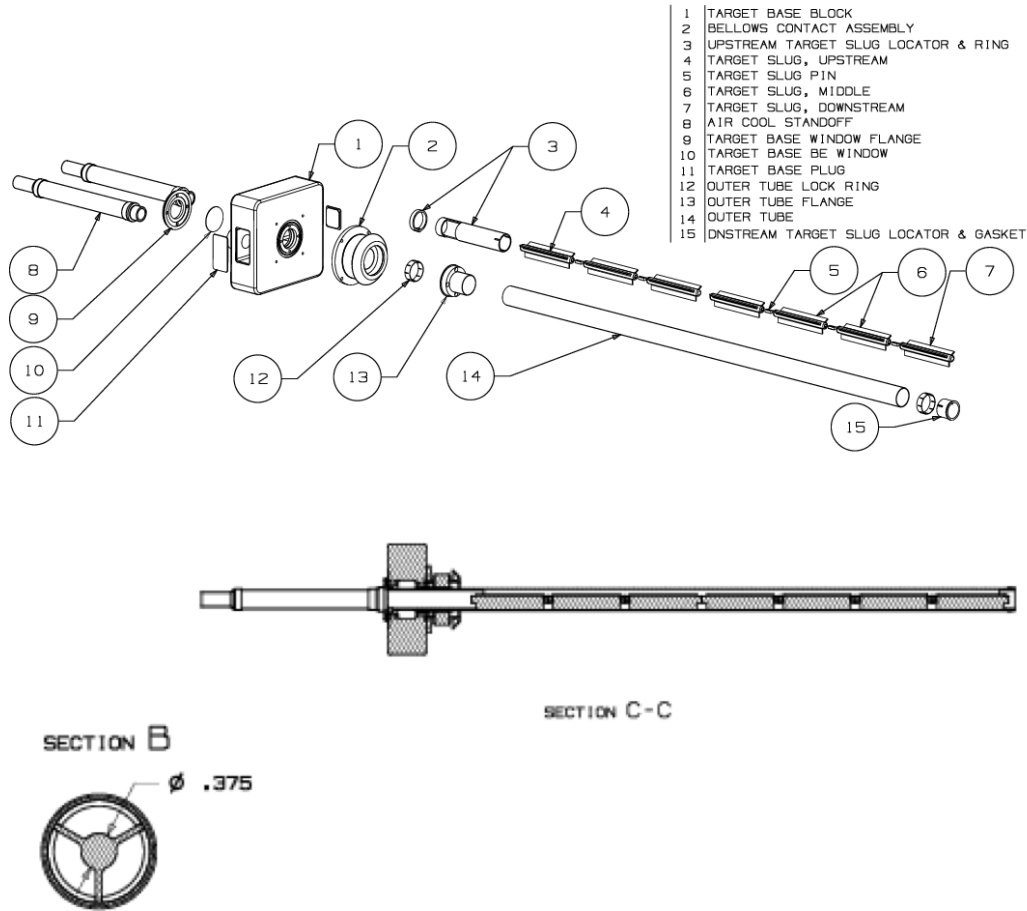


Figure 3.3: (Top) All the components of the BNB target^[21]. (Bottom) The seven beryllium slugs sitting inside the cylindrical container and the cross sectional view of each slug connected to the enclosure via beryllium fins^[21].

The structure is made up of steel alloy and consists of inner and outer cylinders. The total length of the horn is ~ 185 cm where the target lies inside the inner cylinder in the upstream end of the beam. The horn is supplied with a pulsed signal, which is coincidental with the arrival of the beam and signal peaks at ~ 174 kA in both neutrino and anti neutrino modes. Steps are taken to electrically isolate the target from the horn. Once pulsed, a current flows from the inner cylinder to the outer surface resulting a magnetic field in the region defined by the outer and inner surfaces. The magnetic field thus generated has a $1/R$ dependence where the field reaches to a maximum of 1.5 Tesla closest to the inner cylinder. The preferred sign (neutrino & anti neutrino) of the neutrinos can be determined easily by

switching the polarity of the horn current. The heat generated inside the system is removed away by a dedicated water cooling system (see Figure 3.4).

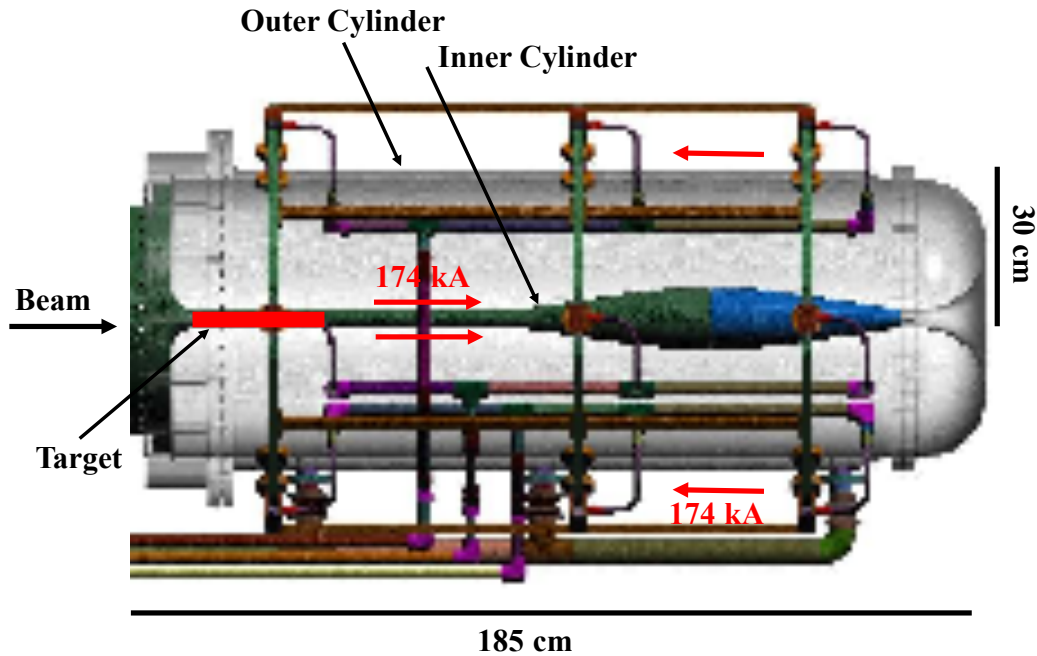


Figure 3.4: Booster Neutrino Beam horn structure^[21]. The two main components of the horn are its inner and outer cylinders. A 174 kA current flows from inner cylinder to the outer surface, once the beam is incident on the target to get rid of unwanted mesons while keeping the preferred particles well focused. By switching the direction of the current flow, one can change sign of the neutrino beam coming out.

3.5 Collimator

The secondary meson beams, after being focused by the horn, enter into the decay region where first to encounter is the collimator, which is located 259 cm away from the upstream end of the target. The main purpose of the collimator is to absorb the unnecessary particles, which would otherwise contaminate the neutrino beam. The structure is made up of pure concrete having a total length of 214 cm. The upstream end of the collimator has an opening with a radius of 30 cm, which gradually grows to a radius of 35.5 cm at the other extreme.

3.6 Decay Pipe

After the collimator, next in the chain is the decay pipe. The decay pipe has an effective length of 49.47 m including the collimator region and an opening of three feet radius. The whole decay pipe region is filled with air and all the walls are made up of corrugated steel pipe. For further protection the pipe is also surrounded by a tightly packed layer of dolomite gravel, which stops any radiation leaking outside. All the secondary mesons decay in this region giving birth to the neutrino beam. The decay region ends with the *Beam Stop* made up steel and concrete with in which sits the *Gas Proportional Counters*, to measure the contamination of muons in the beam. The main purpose of the beam stop, is to block any charged particles, which have not yet decayed to neutrinos inside the decay pipe. Furthermore, the decay region is also equipped with another maneuverable absorber made up of ten steel plates sitting 25 m along the decay pipe, to absorb any contaminants in the beam (mainly muons, which would ultimately decay to ν_e). See Figure 3.5.

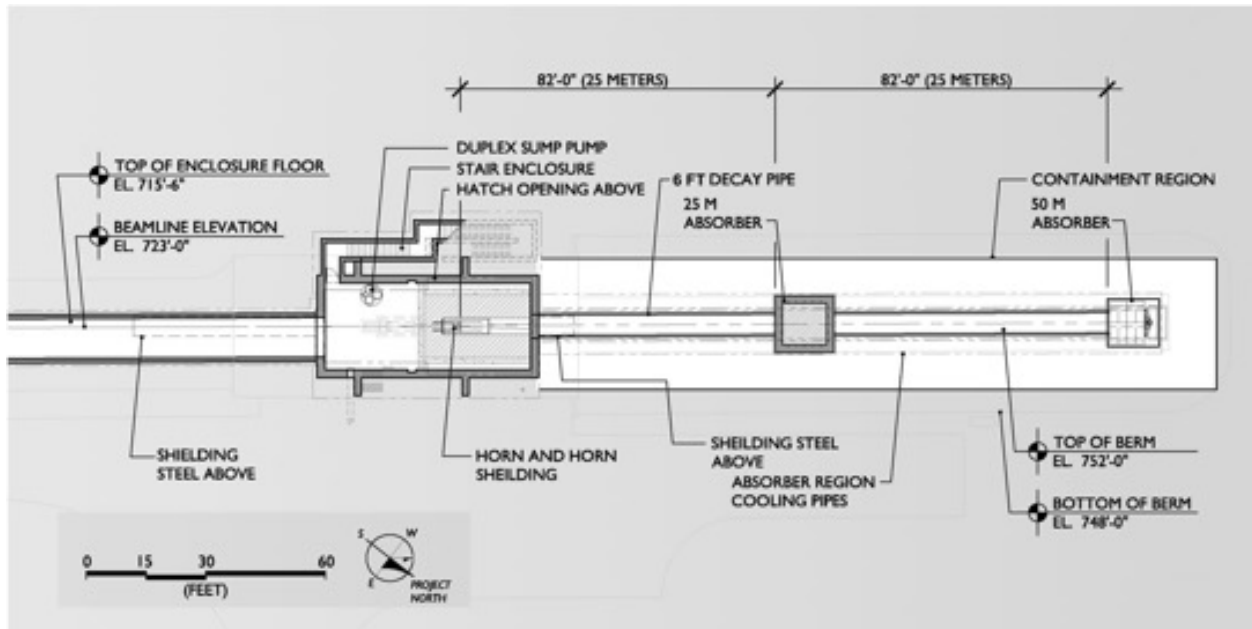


Figure 3.5: A cartoon showing all the major components of the Booster Neutrino Beam line^[21].

3.7 Neutrino Beam

The Booster neutrino beam can be switched between neutrinos and anti neutrinos depending on the horn current polarity. When the horn is operating at positive polarity, the resultant neutrino beam is primarily composed of ν_μ s ($\sim 93\%$) while there is smaller contamination coming from $\nu_{\bar{\mu}}$ s ($\sim 5\%$), ν_e s ($\sim 0.5\%$), and $\nu_{\bar{e}}$ s ($\sim 0.05\%$). The main decay channel, which contributes for the ν_μ flux below ~ 2.5 GeV is the $\pi^+ \rightarrow \mu^+ + \nu_\mu$ (most π^+ s decay on flight). The neutrinos above this threshold are mainly coming from kaon (K^+ and K_L^0) decays. The contaminant ν_e s are mainly coming from two sources:

- The decay of μ^+ s born from pion decays ($\mu^+ \rightarrow e^+ + \bar{\nu}_\mu + \nu_e$).
- Kaon decays (Ex : $K^+ \rightarrow \pi^0 + e^+ + \nu_e$, $K_L^0 \rightarrow \pi^- + e^+ + \nu_e$).

The more energetic and forward going π^- s, which are undeflected by the horn's magnetic field, are mixing some $\nu_{\bar{\mu}}$ s to the neutrino beam, once they decay while the main contributor for the $\bar{\nu}_e$ contamination is from K_L^0 decays. In the anti neutrino mode, the beam is $\sim 83\%$ pure from $\bar{\nu}_\mu$ s while there is $\sim 15\%$ contamination of ν_μ s coming from π^+ decays. For more details of the composition of the Booster Neutrino Beam, MiniBooNE flux paper^[21] is a good source of information (see Figure 3.6).

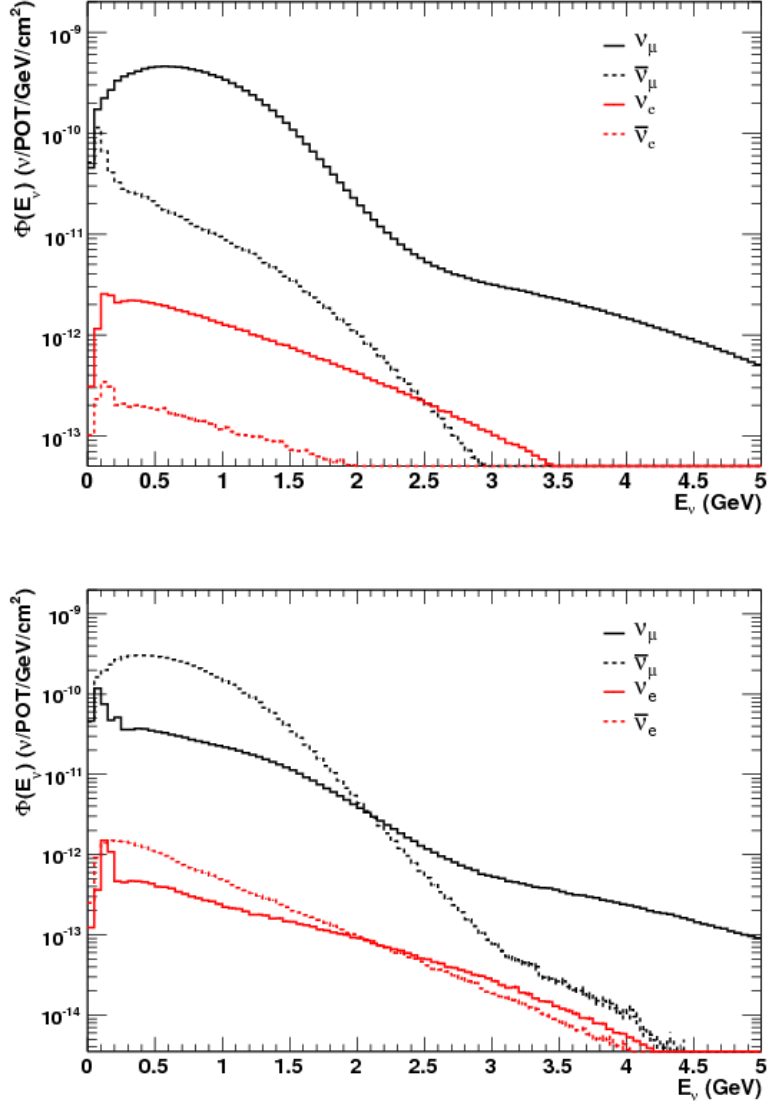


Figure 3.6: (Top) Flux prediction of the Booster Neutrino Beam in the neutrino mode^[21]. (Bottom) Flux prediction of the Booster Neutrino Beam in the anti neutrino mode^[21]. In the neutrino mode, the beam is pure over $\sim 93\%$ from ν_μ s while in the anti neutrino mode, the beam consists of over $\sim 83\%$ from $\bar{\nu}_\mu$ s.

Chapter 4

Neutrinos

In this chapter, we give a detailed discussion of the role played by the neutrinos in the *Standard Model*, followed by a description about different neutrino types (e.g., solar neutrinos, atmospheric neutrino etc.), neutrino oscillations, different neutrino experiments, and the major physics goals of MicroBooNE as a short baseline neutrino experiment. Most of the information is based on the material listed in the References^{[20] [22] [23] [24] [25]}.

4.1 The Standard Model (SM)

The standard model of particle physics tries to explain the fundamental interactions of matter at very minute scales. The theory is composed of different theoretical explanations put consistently, which are motivated by current experimental results. The four corner stones of the theory are:

- Dirac Equation: Explains the behavior of fermions using the relativistic quantum mechanics.
- Quantum Field Theory: Explains interactions of particles via different forces.
- Local Gauge Symmetry: Explains nature of different interactions.
- Higgs Mechanism: Explains how the particle masses are generated.

The standard model comprises two categories of particle types called *bosons* and *fermions* where, by definition, the bosons have integer spin values while fermions have half integer spins. All the interactions in this universe are supposed happen via only four fundamental forces namely, the strong nuclear force, weak nuclear force, electromagnetic force, and gravity, in descending order of how powerful they are. The forces are interpreted in terms of exchange of particles called *force carriers* (also known as *gauge bosons*) in between objects in the SM. Here each force is characterized by its own distinct gauge boson and there exist altogether six of them, as listed below.

- Gluon (g): Force carrier of the strong nuclear force.
- W and Z bosons: Force carriers of the weak nuclear force.
- Photon (γ): Force carrier of the electromagnetic force.
- Graviton (G): Force carrier of the gravitational force.
- Higgs boson (H): Exchange particle of the Higgs field, which generates particle masses; this is a scalar boson as its spin is zero.

The fundamental fermions in the SM belong to two separate families called *leptons* and *quarks* where each family can further be subdivided into three more families. The main difference between two generations of particles in both lepton and quark sectors is the particle masses. The quark sector consists of a total of six particles (12 particles if the anti particle states are also counted) while lepton sector also has six different particles (12 particles with their antiparticles). One of the most fundamental differences between quarks and leptons is that quarks can feel both the strong and the electromagnetic forces but not the weak nuclear force, whereas leptons can feel only the weak nuclear force and the electromagnetic forces but not the strong nuclear force (since neutrinos are chargeless, they feel only the weak nuclear force). A notable feature of all the quarks is that they all have non-integer charges (+2/3 & -1/3) and none of the quarks can be isolated individually in nature, due to a phenomenon known as *color confinement*, which will be discussed in the Section 7.1 of Chapter 7. So all

the quarks found in nature exist as bound states of two quark combinations (mesons - quark and anti quark combination) and three quark combinations (hadrons). Even though there are some hints from some experiments about the existence of tetra- and penta-quark states^[26], nothing has yet been conclusively demonstrated (see Figure 4.1 for the fundamental particles in the SM).

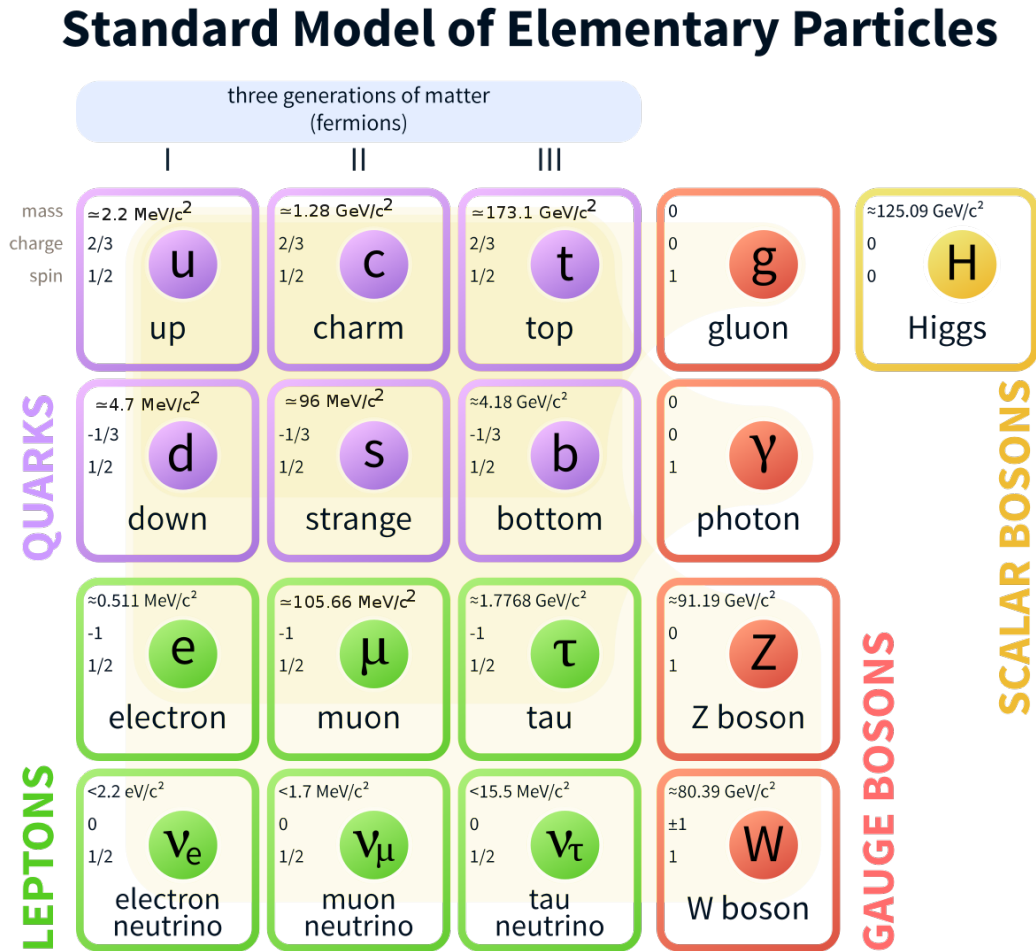


Figure 4.1: Fundamental particles of the standard model^[27]. The SM contains two categories of particles known as fermions (leptons and quarks) and bosons (force carrier gauge bosons and Higgs particle). The Lepton family and the quark family can further be divided into three more families called first generation, second generation, and third generation of particles.

4.2 The Weak Nuclear Force (Weak Interaction)

The formal formulation of the *Weak Interaction* dates back as long as 1934 where in the famous *Fermi Theory*^[28] by Enrico Fermi, introduced a new fundamental short range force known as *Weak Nuclear Force* to explain the β decay. In the world of particle physics, this weak interaction is of particular interest, as many of the particle decays happen through the weak force both in leptonic and quark sectors (e.g., $\mu^- \rightarrow e^- + \bar{\nu}_e + \nu_\mu$, $n \rightarrow p^+ + e^- + \bar{\nu}_e$). In the standard model, the weak interaction manifests itself in two forms known as *Charged Current Weak Interaction* and *Neutral Current Weak Interaction*. Both of the interactions are characterized by the exchange of very heavy bosons where the charged current interaction is mediated by W^\pm bosons having a mass of ~ 80 GeV while the mediator of the neutral current interaction is the neutral Z^0 boson with a mass of ~ 90 GeV. Initially only the charged current interaction was observed in particle interactions. But due to the pioneering work by Glashow, Salam, and Weinberg in unifying electromagnetic and weak nuclear forces in 1960 s, the theory^[29] predicted the existence of the neutral current weak interaction, which was finally observed sometime later in the *Gargamelle Bubble Chamber*^[30] neutrino interactions at CERN. One of the most striking features of the charged current weak interaction, which differs from QED and QCD, is that parity is no longer conserved, which was experimentally proven in 1957 in the Cobalt-60 β decay experiment led by Wu^[31]. As the charged current weak interaction violates the parity conservation, the weak interaction vertex doesn't share the same vector current form as QED or QCD vertices, but shows V-A (Vector minus Axial Vector) interaction form depicted in the Equation 4.1

$$j^\mu = \frac{g_W}{\sqrt{2}} \bar{u}(p') \frac{1}{2} \gamma^\mu (1 - \gamma^5) u(p) \quad (4.1)$$

γ - Gamma matrices, u and \bar{u} - Spinors, p and p' - 4-Momentum, g_W - Weak coupling constant

Later this V-A nature of the weak interaction was experimentally demonstrated by the *TWIST* experiment^[32] by looking into the angular distributions of decaying polarized muons.

As a consequence of this particular structural form of the interaction vertex, the charged current interaction is sensitive to the chiral states of the particles. So only the left-handed chiral particle states and the right handed chiral anti particle states are allowed to participate in the charged current weak interaction. But when it comes to the energy regime where particle's energy is much higher compared to that of particle's mass ($E \gg m$), the helicity and the chiral states would overlap and the previous statement would take the revised form, **only left-handed helicity particles and right-handed helicity anti particles are allowed in the charged current weak interaction.**

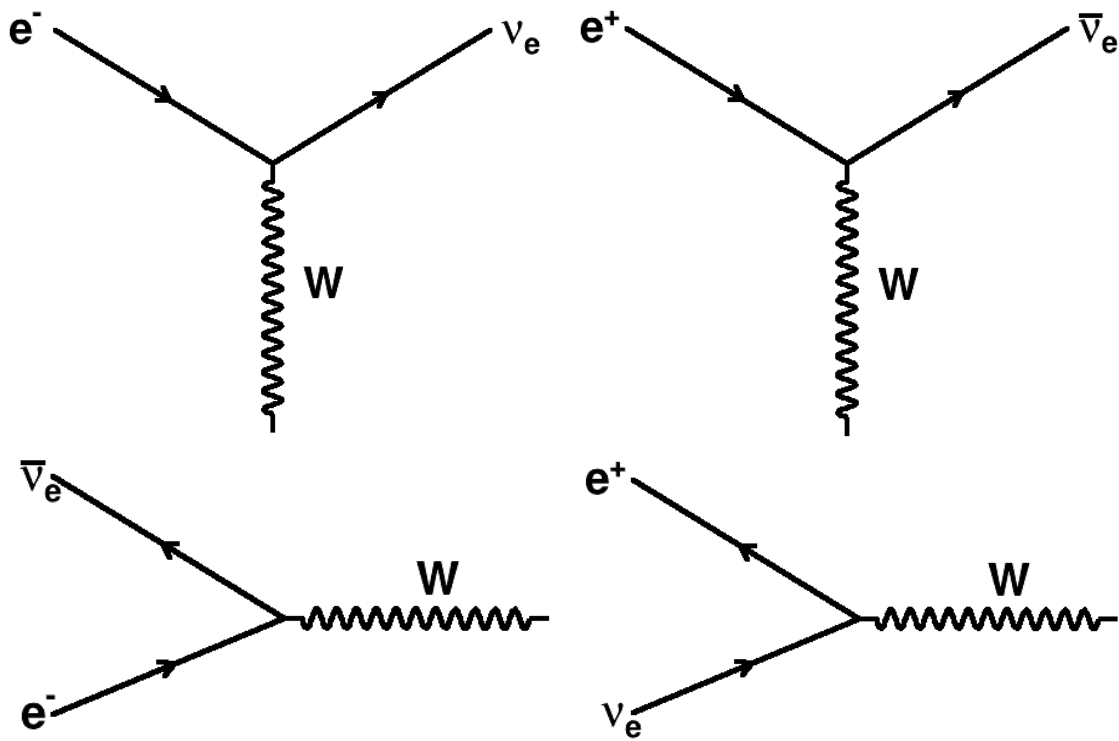


Figure 4.2: Possible coupling states of neutrinos in the charged current weak interaction^[23]. (Top Left) Left handed neutrino-Left handed lepton. (Top Right) Right handed anti neutrino-Right handed anti lepton. (Bottom Left) Right handed anti neutrino-Left handed lepton. (Bottom Right) Left handed neutrino-Right handed anti lepton.

The implications of the weak interaction can separately be studied in the quark sector and the leptonic sector. The charged current weak interaction only couples up type quarks (quarks with charge $+2/3$) with the down type quarks (quarks with charge $-1/3$) where in the leptonic sector, left handed neutrinos are coupled with their counter part leptons (see

Figure 4.2). These doublets of particles, both in quark and leptonic sectors form the eigenstates of the charged current weak interaction. The following lists some of the possible pair of doublets in the charged current weak interaction.

$$\begin{pmatrix} e \\ \nu^e \end{pmatrix}, \begin{pmatrix} \mu \\ \nu^\mu \end{pmatrix}, \begin{pmatrix} \tau \\ \nu^\tau \end{pmatrix}, \begin{pmatrix} u \\ d \end{pmatrix}, \begin{pmatrix} c \\ s \end{pmatrix}, \begin{pmatrix} t \\ b \end{pmatrix}$$

It has been observed that the coupling strength of the charged current weak interaction is independent on the neutrino flavor involved in the leptonic sector. But there is strong evidence in nature that this is no longer true in the quark sector when quarks from different generations are coupled together. For instance, the decay rate of $K^\pm \rightarrow \mu^\pm + \nu_\mu(\bar{\nu}_\mu)$ (see Figure 4.3 (Left)) where $\bar{u}(u)$ and $s(\bar{s})$ couple with a W^\pm , is suppressed by a factor of ~ 20 compared to the decay rate of the process $\pi^\pm \rightarrow \mu^\pm + \nu_\mu(\bar{\nu}_\mu)$ (see Figure 4.3 (Right)) where a pair of $\bar{u}(u)$ and $d(\bar{d})$ is coupled to a W^\pm . The interpretation for this lies in the *Cabbibo Hypothesis*^[33] where mass eigenstates of the quarks are distinguished from the weak eigenstates as in the explanation of the *Neutrino Oscillations*, which will be discussed in the Section 4.4. In this theory, the weak eigenstates and mass eigenstates are related to each other by a unitary matrix named *CKM (Cabbibo-Kobayashi-Masaka)* matrix as indicated in the Equation 4.2. Here the coupling probability amplitude between any two of the quark flavors is given by $|V_{ij}|^2$.

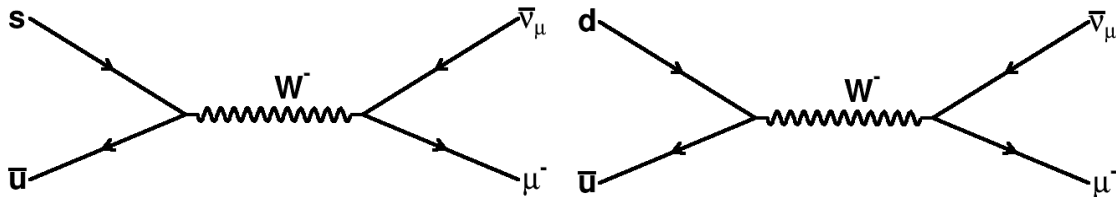


Figure 4.3: (Left) Feynman diagram of K^- decay in the charged current weak interaction. (Right) Feynman diagram of π^- decay in the charged current weak interaction.

$$\begin{pmatrix} d' \\ s' \\ b' \end{pmatrix} = \begin{pmatrix} V_{ud} & V_{us} & V_{ub} \\ V_{cd} & V_{cs} & V_{cb} \\ V_{td} & V_{ts} & V_{tb} \end{pmatrix} \begin{pmatrix} d \\ s \\ b \end{pmatrix} \quad (4.2)$$

Assuming just two quark flavors, the Equation 4.2 can be rewritten in the following simplified form. Here the parameter θ_c is referred to as the *Cabbibo Angle*, which was experimentally measured to be $\sim 13^\circ$.

$$\begin{pmatrix} d' \\ s' \end{pmatrix} = \begin{pmatrix} \cos\theta_c & \sin\theta_c \\ -\sin\theta_c & \cos\theta_c \end{pmatrix} \begin{pmatrix} d \\ s \end{pmatrix} \quad (4.3)$$

According to Equation 4.3, $|V_{ud}|^2 \propto \cos^2\theta_c$ while $|V_{us}|^2 \propto \sin^2\theta_c$. So the ratio between two probability amplitudes yields $\tan^2\theta_c$, which would result a factor of ~ 20 , once the Cabbibo angle is substituted. This way the Cabbibo hypothesis is capable of explaining the different probability amplitudes of different quark flavor couplings. Thus, the enhanced quark couplings are aptly called *Cabbibo favored* processes while lower probability amplitude couplings are tagged as *Cabbibo suppressed*.

The neutral current weak interaction behaves somewhat similar to the way the electromagnetic interaction as both couple fermions and anti fermions in the vertex. In addition, as in the charged weak current interaction, the neutral current interaction is also sensitive to the chiral states of the fermions involved where the electromagnetic interaction does not distinguish the particle's chirality. In consequence, only the left handed neutrinos and right handed anti neutrinos are allowed to participate in the neutral current weak interaction as also observed in the charged current scenario (see Figure 4.4). Moreover, in the case of charged particles, the strength of the neutral weak coupling is dependent on the electric charge where the particles having same electric charge share the same coupling strengths. One of the interesting topics popped up in the context of neutral current interaction is the *Flavor Changing Neutral Current (FCNC)* processes. The *GIM* mechanism^[34] (proposed by Glashow, Illiopoulos, and Maiani in 1970) almost rules out the possibility of these FCNC interactions, which would otherwise allow for the coupling of fermions and anti fermion of different flavors both in quark and leptonic sectors (see Figure 4.5). The importance of these FCNC interactions is mostly relevant to the models like SUSY^[35], which looks for beyond standard model physics. Moreover, if we were to observe these rare processes in nature, then

it would create more chances of observing new massive particle states.

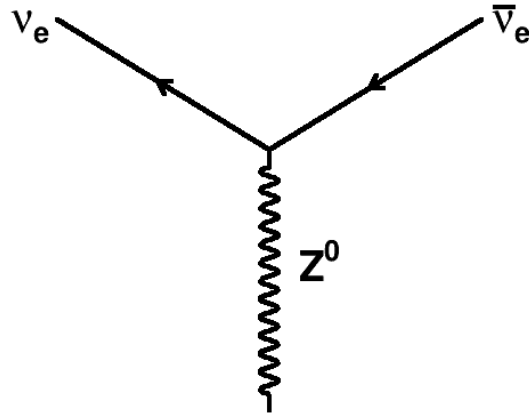


Figure 4.4: Left handed neutrinos and right handed anti neutrino are coupled in the neutral current weak interaction.

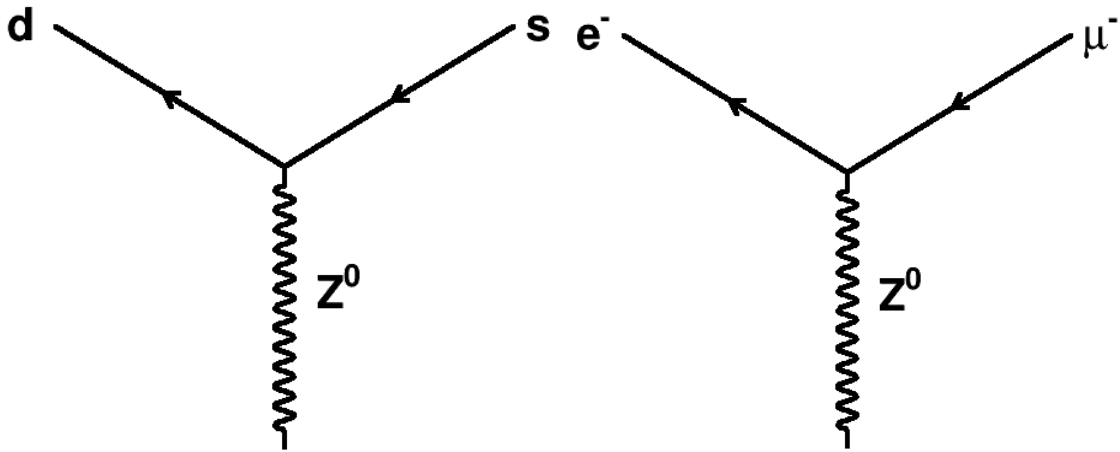


Figure 4.5: Forbidden couplings of flavor changing neutral current interaction^[36]. (Left) FCNC in quark sector. (Right) FCNC in leptonic sector.

4.3 Neutrinos in General

Neutrino physics is arguably one of the most discussed topics in the modern day physics as it has already laid the path for several Nobel prizes in the field, with many more surprises yet to be unveiled. It was as early as 1930 that the famous theoretician Wolfgang Pauli predicted the existence of a massless, chargeless, and spin 1/2 particle, which he never believed to

be experimentally detectable, to explain the controversial continuous energy spectrum of electrons coming from atomic beta decay. It was in 1933 that Enrico Fermi extensively made use of Pauli's hypothetical particle in his weak theory (Fermi Theory) to explain the nature of β decays, and aptly named the particle *neutrino*, which means in Latin *the smaller neutral particle* not to be confused with the neutron. Despite Pauli had no faith on seeing neutrinos in his life, the challenge was overcome by Frederick Reines and Clyde L. Cowan in 1956 by detecting anti electron neutrinos coming from a reactor core in the famous *Savannah River Experiment* in South Carolina^[37]. Later two more flavors of neutrino, ν_μ ^[38] and ν_τ ^[39] were identified by different experiments in 1962 and 1975 respectively. Measurements of the Z decay width at the LEP collider at CERN has confirmed that there exists only ν_e , ν_μ and ν_τ neutrino flavors in nature^[40]. By today, so many details of these mysterious particles have been unveiled, but more effort is needed to complete the picture.

Even though neutrinos are relatively abundant in the nature compared to other types of elementary particles, observing them in the detector is a big challenge due to their low interaction rate with matter. All three flavors of neutrinos in the standard model are supposed to interact only through the weak force. The only way of identifying the presence of neutrinos inside the detector is to see the trail generated by its accompanying lepton counterpart in the charged current interaction. Neutrinos are produced both by natural and man-made sources. Natural sources include;

- Solar neutrinos produced in the Sun's core: The fusion of protons inside the sun gives birth to $\sim 2 \times 10^{38}$ ν_e s per second, which would cause an influx of roughly 6.5×10^{10} neutrinos per second on Earth's atmosphere.
- Relic neutrinos: These neutrinos are supposed to originate from the *Big-Bang*^[41], which happened around 13.6 billion years ago giving birth to the current universe. The detection of the relic neutrinos can unravel some hidden information about the early universe and the Big-Bang itself. These neutrinos pervade through space with a density of ~ 330 neutrinos per cm^3 .
- Supernovae neutrinos: Cosmological activities like supernovae bursts can also produce

neutrinos in great quantities. The estimated flux of neutrinos produced in a supernova burst is $\sim 10^{58}$ neutrinos per second.

- Atmospheric neutrinos: High energy cosmic rays can bombard the outer layer of Earth's atmosphere giving rise to secondary mesons. These mesons travel downwards and ultimately decay to lighter elements giving birth to neutrinos as by products. The atmospheric neutrino spectrum mainly consists of ν_μ s having energies ranging from a few GeVs up to the energies of the highest cosmic rays^[42].
- Geo neutrinos: Neutrinos produced by different decay chains inside the Earth's crust.

There exist two major man-made neutrino sources: reactor neutrinos and the accelerator neutrinos. The reactor neutrinos, which consists of $\bar{\nu}_e$ s, are born inside large cores of reactors due to the decay of different radioisotopes (e.g., ^{235}U , ^{238}U , ^{239}Pu , ^{241}Pu). These are very feeble neutrinos having an energy of ~ 3 MeV. On the contrary, accelerator neutrinos are very energetic and have well understood energy spectra. These neutrino beams are mainly composed of a desired flavor of neutrinos (e.g., ν_μ , $\bar{\nu}_\mu$) and born from the decay of secondary meson beams artificially produced. One of the most intense and highly energetic man-made neutrino beams in the world is the NUMI beam at Fermilab, which mainly consists of ν_μ ($\bar{\nu}_\mu$) in its neutrino (anti neutrino) mode having an energy spectrum tailing up to 10 GeV. See Figure 4.6 for different sources of neutrinos.

In the context of recent developments in the field of neutrino physics, the discovery of *Neutrino Oscillations*, which suggests that neutrinos can change their flavor as they travel through space, is worthy of mentioning. One of the major implications of this finding is that this indirectly suggests that all neutrino flavors should have non-zero masses opening door ways for some new rules of physics. The most up to date upper limit set on the lightest possible neutrino mass by the *KATRIN* experiment is 2 eV^[23] while the recent cosmological measurements predicts $\sum_{i=1}^3 m_{\nu_i} \lesssim 1\text{eV}$ ^[23], despite the fact that neutrinos are massless in the SM. Moreover, the recent observations in the short baseline neutrino experiments hint to the possible existence of more exotic flavors of neutrinos such as *Sterile neutrinos*, which do not interact with matter via weak force like ordinary neutrinos.

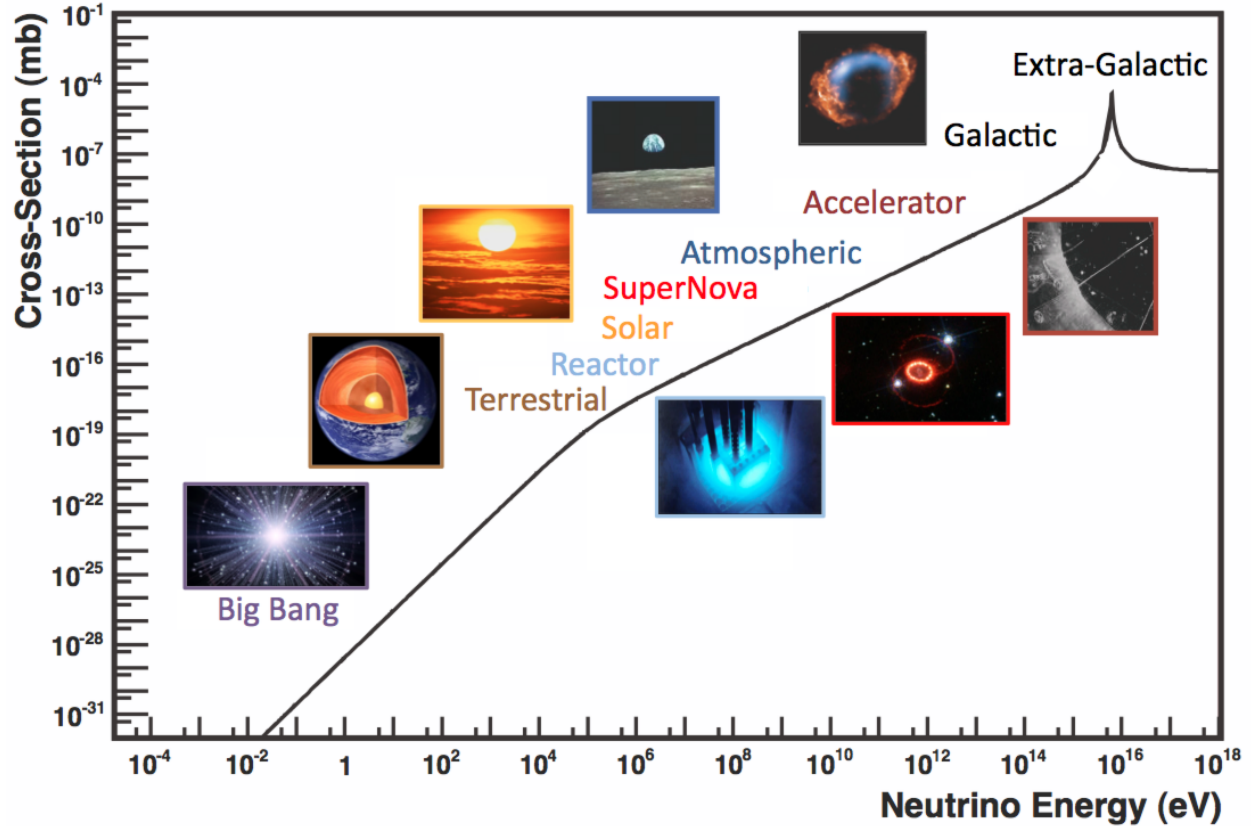


Figure 4.6: Natural and man-made neutrino sources as function of neutrino energy and their interaction probabilities with matter^[43].

4.4 Neutrino Oscillations

It is now well established that neutrinos change their flavor as they travel through space. The explanation of the phenomenon lies in the most fundamental concepts of the quantum mechanics. The theory of neutrino oscillations^[44], which was originally developed by Bruno Pontecorvo in 1957, is analogous in all the aspects to the Cabbibo theory to explain the mixing of different quark flavors in the weak interaction. Here the weak and mass eigenstates of the neutrinos are treated differently and, related to each other using a unitary matrix named *PMNS* (*PonteCorvo-Maki-Nakagawa-Sakata*) matrix as indicated in the Equation 4.4.

$$\begin{pmatrix} \nu_e \\ \nu_\mu \\ \nu_\tau \end{pmatrix} = \begin{pmatrix} U_{e1} & U_{e2} & U_{e3} \\ U_{\mu1} & U_{\mu2} & U_{\mu3} \\ U_{\tau1} & U_{\tau2} & U_{\tau3} \end{pmatrix} \begin{pmatrix} \nu_1 \\ \nu_2 \\ \nu_3 \end{pmatrix} \quad (4.4)$$

Here ν_e , ν_μ , and ν_τ are known as the weak eigenstates, which are the observable neutrino flavors inside the detector in the weak interaction. On the other hand ν_1 , ν_2 , and ν_3 are eigenstates of the free Hamiltonian and also known mass eigenstates. According to the Equation 4.4, a particular neutrino flavor can be expressed in terms of the superposition of three mass eigenstates as in the Equation 4.5.

$$|\nu_e\rangle = U_{e1}^* |\nu_1\rangle + U_{e2}^* |\nu_2\rangle + U_{e3}^* |\nu_3\rangle \quad (4.5)$$

As the neutrino travels, the different mass eigenstates propagate in space with different velocities due the difference in the masses. In consequence, a phase difference can develop over time in between different mass components. The Equation 4.6 shows the time evolution of the neutrino wave function.

$$|\psi\rangle = U_{e1}^* |\nu_1\rangle e^{i(\vec{p}_1 \cdot \vec{x} - E_1 t)} + U_{e2}^* |\nu_2\rangle e^{i(\vec{p}_2 \cdot \vec{x} - E_2 t)} + U_{e3}^* |\nu_3\rangle e^{i(\vec{p}_3 \cdot \vec{x} - E_3 t)} \quad (4.6)$$

Now due to the non-zero phase difference between mass components, the next time neutrino interacts inside the detector in the weak interaction, will in general be a superposition of more than one flavor, resulting in a lower probability of observing the original flavor again and an enhanced probability of seeing a new flavor.

Now to derive an explicit expression for a neutrino oscillation probability, for simplicity, let us restrict only to two neutrino flavors. Then the Equation 4.4 can be simplified to,

$$\begin{pmatrix} \nu_e \\ \nu_\mu \end{pmatrix} = \begin{pmatrix} \cos\theta & \sin\theta \\ -\sin\theta & \cos\theta \end{pmatrix} \begin{pmatrix} \nu_1 \\ \nu_2 \end{pmatrix} \quad (4.7)$$

Time evolution of any arbitrary state can be written,

$$|\psi\rangle = \cos\theta |\nu_1\rangle e^{i(\vec{p}_1 \cdot \vec{x} - E_1 t)} + \sin\theta |\nu_2\rangle e^{i(\vec{p}_2 \cdot \vec{x} - E_2 t)} \quad (4.8)$$

Taking $\phi_i = (E_i t - \vec{p}_i \cdot \vec{x})$, the Equation 4.8 can be rewritten,

$$|\psi\rangle = \cos\theta |\nu_1\rangle e^{-i\phi_1} + \sin\theta |\nu_2\rangle e^{-i\phi_2} \quad (4.9)$$

Using the fact that,

$$\begin{pmatrix} \cos\theta & -\sin\theta \\ \sin\theta & \cos\theta \end{pmatrix} \begin{pmatrix} \cos\theta & \sin\theta \\ -\sin\theta & \cos\theta \end{pmatrix} = \begin{pmatrix} 1 & 0 \\ 0 & 1 \end{pmatrix} \quad (4.10)$$

The Equation 4.7 can be inverted,

$$\begin{pmatrix} \nu_1 \\ \nu_2 \end{pmatrix} = \begin{pmatrix} \cos\theta & -\sin\theta \\ \sin\theta & \cos\theta \end{pmatrix} \begin{pmatrix} \nu_e \\ \nu_\mu \end{pmatrix} \quad (4.11)$$

$$|\nu_1\rangle = \cos\theta |\nu_e\rangle - \sin\theta |\nu_\mu\rangle \quad (4.12)$$

$$|\nu_2\rangle = \sin\theta |\nu_e\rangle + \cos\theta |\nu_\mu\rangle \quad (4.13)$$

Replacing $|\nu_1\rangle$ and $|\nu_2\rangle$ in the Equation 4.9,

$$\begin{aligned} |\psi\rangle &= \cos\theta [\cos\theta |\nu_e\rangle - \sin\theta |\nu_\mu\rangle] e^{-i\phi_1} + \cos\theta [\sin\theta |\nu_e\rangle + \cos\theta |\nu_\mu\rangle] e^{-i\phi_2} \\ &= \cos^2\theta |\nu_e\rangle e^{-i\phi_1} - \cos\theta \sin\theta |\nu_\mu\rangle e^{-i\phi_1} + \sin^2\theta |\nu_e\rangle e^{-i\phi_2} + \cos\theta \sin\theta |\nu_\mu\rangle e^{-i\phi_2} \\ &= |\nu_e\rangle [\cos^2\theta e^{-i\phi_1} + \sin^2\theta e^{-i\phi_2}] + |\nu_\mu\rangle \sin\theta \cos\theta [e^{-i\phi_2} - e^{-i\phi_1}] \end{aligned}$$

$$|\psi\rangle = e^{-i\phi_1} \{ [\cos^2\theta + \sin^2\theta e^{i(\phi_1-\phi_2)}] |\nu_e\rangle - \sin\theta\cos\theta [1 - e^{i(\phi_1-\phi_2)}] |\nu_\mu\rangle \} \quad (4.14)$$

When there is no phase difference (i.e $\phi_1 - \phi_2 = 0$), $|\psi\rangle$ is equivalent to $|\nu_e\rangle$. So, the probability $P(\nu_e \rightarrow \nu_\mu)$ of ν_e oscillating to ν_μ is,

$$\begin{aligned} P(\nu_e \rightarrow \nu_\mu) &= |\langle \nu_\mu | \psi \rangle|^2 \\ &= \langle \nu_\mu | \psi \rangle \langle \nu_\mu | \psi \rangle^* \\ &= \sin^2\theta \cos^2\theta [1 - e^{i(\phi_1-\phi_2)}] [1 - e^{-i(\phi_1-\phi_2)}] \\ &= \left(\frac{\sin^2 2\theta}{4}\right) [2 - (e^{i(\phi_1-\phi_2)} + e^{-i(\phi_1-\phi_2)})] \\ &= \left(\frac{\sin^2 2\theta}{4}\right) [2 - 2\cos(\phi_1 - \phi_2)] \\ &= \left(\frac{\sin^2 2\theta}{4}\right) [2[1 - \cos(\phi_1 - \phi_2)]] \\ &= \left(\frac{\sin^2 2\theta}{4}\right) [2[1 - (1 - 2\sin^2(\frac{\phi_1 - \phi_2}{2}))]] \end{aligned}$$

$$P(\nu_e \rightarrow \nu_\mu) = \sin^2 2\theta \sin^2\left(\frac{\phi_1 - \phi_2}{2}\right) \quad (4.15)$$

$$\begin{aligned} \phi_1 - \phi_2 &= [E_1 t - \vec{p}_1 \cdot \vec{x}] - [E_2 t - \vec{p}_2 \cdot \vec{x}] \\ &= (E_1 - E_2)t - (\vec{p}_1 - \vec{p}_2) \cdot \vec{x} \end{aligned}$$

Assuming $\vec{p}_1 = \vec{p}_2 = \vec{p}$ and using $t = \frac{L}{c}$ where $c = 1$ (in natural units),

$$\phi_1 - \phi_2 = (E_1 - E_2)L$$

Using the relation $E = \sqrt{p^2 + m^2}$,

$$\begin{aligned}\phi_1 - \phi_2 &= (\sqrt{p^2 + m_1^2} - \sqrt{p^2 + m_2^2})L \\ &= [p(1 + \frac{m_1^2}{p^2})^{\frac{1}{2}} - p(1 + \frac{m_2^2}{p^2})^{\frac{1}{2}}]L \\ &= p[(1 + \frac{m_1^2}{p^2})^{\frac{1}{2}} - (1 + \frac{m_2^2}{p^2})^{\frac{1}{2}}]L\end{aligned}$$

Using the relation $p = \frac{E_\nu}{c}$ and setting $c = 1$,

$$\phi_1 - \phi_2 = E_\nu[(1 + \frac{m_1^2}{E_\nu^2})^{\frac{1}{2}} - (1 + \frac{m_2^2}{E_\nu^2})^{\frac{1}{2}}]L \quad (4.16)$$

Assuming $m \ll E_\nu$,

$$(1 + \frac{m_i^2}{E_\nu^2})^{\frac{1}{2}} \approx 1 + \frac{m_i^2}{2E_\nu^2} \quad (4.17)$$

From the Equations 4.16 and 4.17,

$$\phi_1 - \phi_2 = (\frac{m_1^2 - m_2^2}{2E_\nu})L \quad (4.18)$$

Substituting for $\phi_1 - \phi_2$ in the Equation 4.15,

$$P(\nu_e \rightarrow \nu_\mu) = \sin^2 2\theta \sin^2(\frac{(m_1^2 - m_2^2)L}{4E_\nu}) \quad (4.19)$$

Converting the natural units into SI units and taking $\Delta m^2 = m_1^2 - m_2^2$, the Equation 4.19 can be rewritten,

$$P(\nu_e \rightarrow \nu_\mu) = \sin^2 2\theta \sin^2\left(\frac{1.27\Delta m^2(eV^2)L(km)}{4E_\nu(GeV)}\right) \quad (4.20)$$

Where θ – Mixing angle, L – The distance, neutrino beam traveled, E_ν – Average energy of the neutrino beam, and Δm^2 – Mass squared difference between two mass eigenstates considered. Figure 4.7 shows the variation of oscillation probability as a function of distance assuming only two neutrino flavors. The derivation of the Equation 4.20 is guided by the pages 338-341 of the Reference^[23].

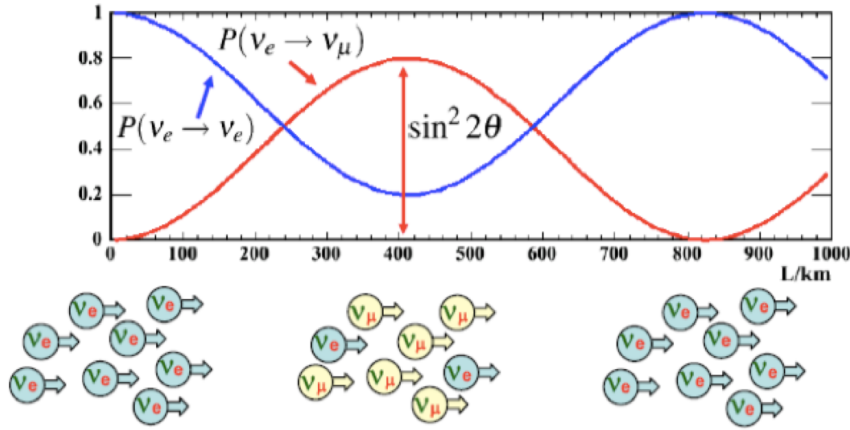


Figure 4.7: The survival probability $P(\nu_e \rightarrow \nu_e)$ of ν_e s and appearance probability $P(\nu_e \rightarrow \nu_\mu)$ of ν_μ s as a function of distance L . Here $\Delta m^2 = 3 \times 10^{-3} eV^2$, $\sin^2 2\theta = 0.8$ and $E_\nu = 1 GeV$ ^[25].

Since we observe neutrino oscillations, the Equation 4.20 implies that the term Δm^2 should be non-zero. This implies that mass eigenstates should be different to each other and at least one of them should be non-zero. Thus, the observation of neutrino oscillation indirectly suggests that neutrinos are not massless.

In the treatment of three neutrino flavor oscillations, the Equation 4.20 can be generalized to the following form using the matrix elements of PMNS matrix,

$$P(\nu_e \rightarrow \nu_\mu) = |U_{e1}^* U_{\mu 1} e^{-i\phi_1} + U_{e2}^* U_{\mu 2} e^{-i\phi_2} + U_{e3}^* U_{\mu 3} e^{-i\phi_3}|^2 \quad (4.21)$$

Here the PMNS matrix can alternatively be written,

$$\begin{pmatrix} U_{e1} & U_{e2} & U_{e3} \\ U_{\mu1} & U_{\mu2} & U_{\mu3} \\ U_{\tau1} & U_{\tau2} & U_{\tau3} \end{pmatrix} = \begin{pmatrix} c_{12}c_{13} & s_{12}c_{13} & s_{13}e^{-i\delta} \\ -s_{12}c_{23} - c_{12}s_{23}s_{13}e^{i\delta} & c_{12}c_{23} - s_{12}s_{23}s_{13}e^{i\delta} & s_{23}c_{13} \\ s_{12}s_{23} - c_{12}c_{23}s_{13}e^{i\delta} & -c_{12}s_{23} - s_{12}c_{23}s_{13}e^{i\delta} & c_{23}c_{13} \end{pmatrix} \quad (4.22)$$

Here $s_{ij} = \sin\theta_{ij}$ and $c_{ij} = \cos\theta_{ij}$.

So in summary, the three flavor neutrino oscillation can be explained in terms three mixing angles ($\theta_{12}, \theta_{23}, \theta_{13}$), three mass squared splittings ($\Delta m_{21}^2, \Delta m_{31}^2, m_{32}^2$ - here only 2 mass squared splittings are independent), and CP violating factor δ . The current knowledge about the neutrino mass eigenstates is not complete and have two possibilities for the mass hierarchies as indicated in the Figure 4.8.

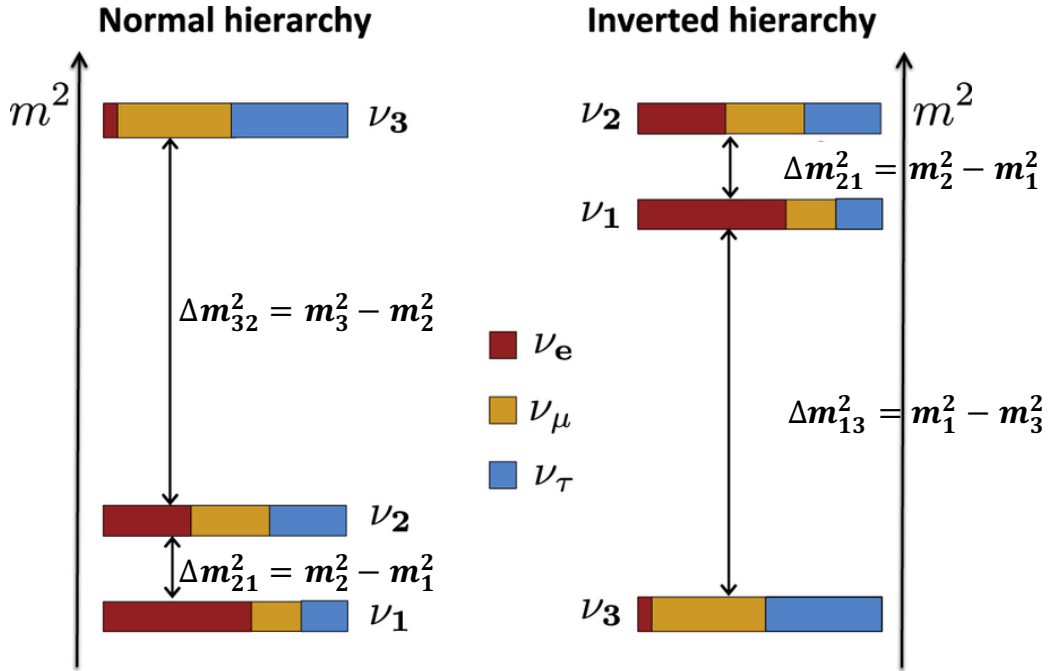
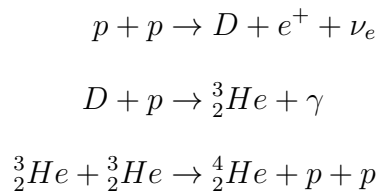


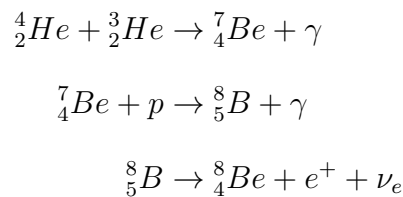
Figure 4.8: (Left) Normal mass hierarchy ($\Delta m_{31}^2 = \Delta m_{32}^2 + \Delta m_{21}^2$). (Right) Inverted mass hierarchy ($\Delta m_{23}^2 = \Delta m_{21}^2 + \Delta m_{13}^2$)^[45].

4.4.1 Solar Neutrino Oscillations

The *Standard Solar Model (SSM)*^[46] predicts the flux of neutrinos produced in the core of the Sun by various fusion processes. The model is mainly driven by *helioseismologic* data to predict the chemical composition, temperature, and various other dynamics for any star. According to the model, the Sun produces 2×10^{38} ν_e s in each second via number of fusion processes and radio active decays. The main fusion process of the Sun is *pp cycle* as indicated below.



The neutrinos produced in this process are very feeble ($E_\nu < 0.5 \text{ MeV}$), so detecting them inside the detector is very hard. The other channel of interest is the ${}^8\text{B}$ radio active decay, which gives rise to higher energy solar neutrinos. Most of the solar neutrino experiments are sensitive this particular channel as the ${}^8\text{B}$ neutrino energy spectrum can span up to 15 MeV. The following steps list the production mechanism of the neutrinos in this channel. See Figure 4.9 for the different sources of neutrinos inside the Sun as SSM predicts.



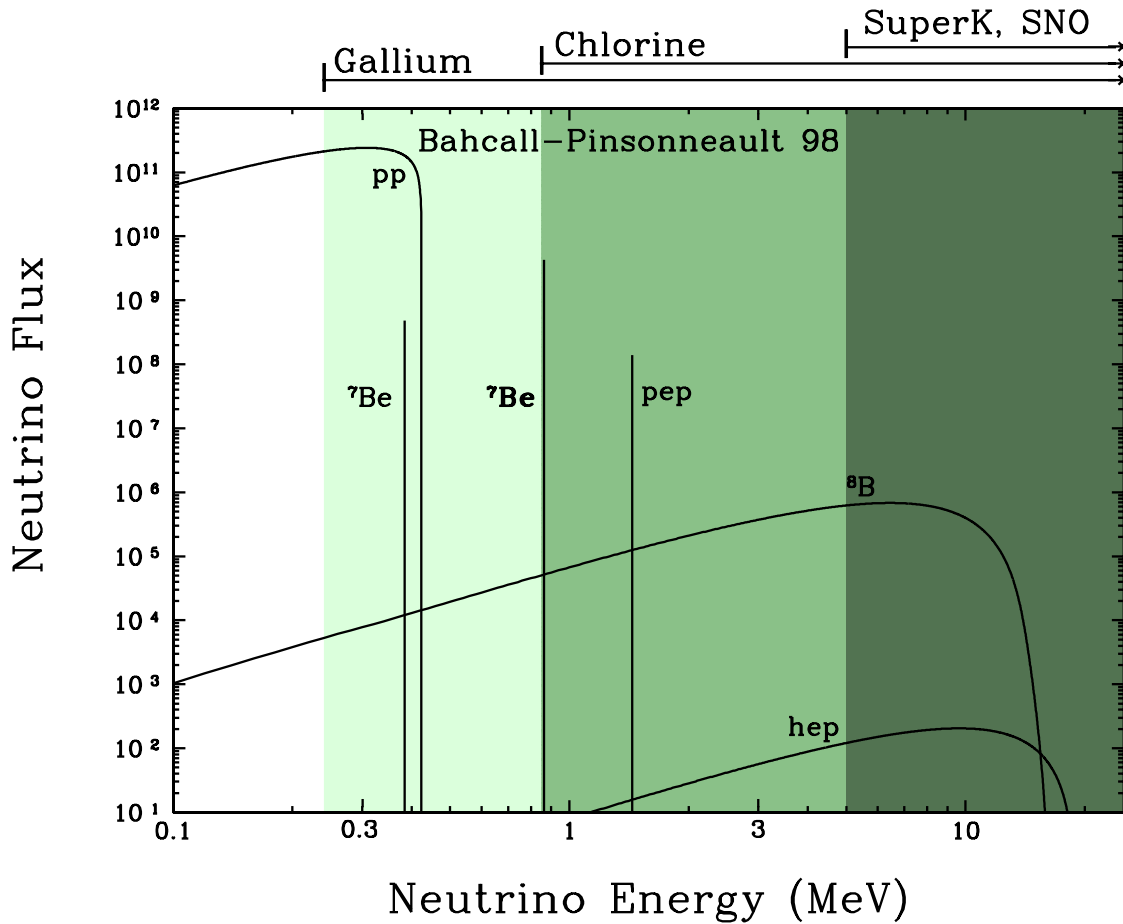


Figure 4.9: Different neutrino production channels in the Sun according to the standard solar model^[47]. The lowest energy neutrinos are produced in the pp cycle having an energy $E_\nu < 0.5$ MeV. The ${}^8\text{B}$ radio active decay produces neutrinos having energies up to 15 MeV. Radio chemical neutrino detectors are sensitive to much lower energy neutrino channels, whereas the water cherenkov detectors like SuperK^[48] are only sensitive to the higher energy tail.

The neutrino oscillations can be studied under two different categories. Namely,

- Neutrino oscillations in the vacuum.
- Neutrino oscillations in the matter.

As so far discussed, the neutrino oscillations in vacuum is a direct consequence of the non-zero phase difference developed over different neutrino mass eigenstates due to their

different propagation speeds in the vacuum. But in the context of neutrino oscillations in matter, the story becomes a bit complicated. When a beam of neutrinos passes through some electron dense medium, different neutrino flavors interact with the medium differently. In consequence, the phase difference between different mass eigenstates is completely determined by the total energy of the state. Here the term total energy refers to the sum of energy (E) of the mass eigenstate itself and interaction potential (V) between neutrinos and the medium. Assuming only two neutrino flavors, we can derive an oscillation probability for oscillations in matter as well having the same form as in the Equation 4.20. But it should be noted that, in the presence of matter effects, the mixing angles and mass squared splittings get redefined compared to that of the neutrino oscillations in the vacuum. As this phenomenon was well understood due to the pioneering work of Mikheyev, Smirnov, and Wolfenstein, the effect is also known as the *MSW effect*^[49].

So in the context of solar neutrino oscillations, once a beam of electron neutrinos born at the core of the Sun propagates outward, it should pass through some electron dense region satisfying some resonance conditions (if the matter density is too high, neutrino oscillations are suppressed. So to observe oscillations in matter, the matter density of the region should satisfy some resonance conditions). Once in the ideal conditions, some of ν_e s begin to oscillate to ν_μ s. So by the time neutrinos arrive to the surface of the Sun, a significant fraction of the ν_e s are already transformed into ν_μ s. Here onward on their journey to the Earth, if there exist any ν_e s that transform into ν_μ s, that could only happen via oscillations through vacuum as matter effects become sub dominant due to lower matter densities.

4.4.2 Experimental Search for Solar Neutrino Oscillations

The very first solar neutrino experiment to have measured the solar neutrino flux was the Homestake experiment^[50] at Homestake mine in South Dakota, USA. The experiment was initially invented by Ray Davis in 1965. It used some radio chemical techniques to confirm the presence of neutrinos. The initial experimental setup consisted of large tank filled with 615 tons of dry cleaning fluid C_2Cl_4 . Once neutrinos entered into the detector, they inter-

acted with the detector medium through the process $\nu_e + {}^{37}_{17}\text{Cl} \rightarrow {}^{37}_{18}\text{Ar} + e^-$ producing the radioactive isotope ${}^{37}_{18}\text{Ar}$. Then these rare ${}^{37}_{18}\text{Ar}$ atoms were isolated out very meticulously using radio chemical methods and, counted to determine the number of neutrino interactions that occurred inside the detector. After years of data taking, they published their results claiming that the capture rate of solar neutrinos in their detector to be 2.56 ± 0.25 SNU (1 SNU = 10^{-36} neutrino interactions per target atom per second). But the standard solar model predicted this number to be 8.1 ± 1.2 SNU (numbers are quoted from the Reference^[25]). This was the first evidence for neutrino oscillations observed in the solar neutrino sector as there was a clear deficit of neutrinos in the measurement. But as nothing was known about neutrino oscillation by the time Homestake experiment was operational, the discrepancy observed between measurement and the prediction was attributed to some mis-modeling in the solar model.

The next stage of the radio chemical neutrino experiments was SAGE^[51] and GALLEX^[52] experiments. Both of these experiments used gallium as their detector medium to capture solar neutrinos. The main advantage of using gallium as the detector medium instead of chlorine is that, these two experiments were sensitive to lower energy neutrinos as indicated in the Figure 4.9. In their final result GALLAX experiment reported a rate of 77.5 ± 8 SNU^[25] where the SAGE observed a rate of 70.8 ± 5 SNU^[25]. Even though the two results were comparable with each other within their uncertainties, there was again clear deficit in the observed rates in both of the experiments compared to the prediction of 129 ± 9 SNU^[25]. But it has been observed that this time the deficit between measurement and prediction has been narrowed down significantly compared to the results obtained by the Homestake experiment.

Another experiment which played an important role in the search for solar neutrinos is the giant Super-Kamiokande (SuperK) experiment. The experiment uses the water cherenkov detector technology to hunt down solar neutrinos, which is completely different to the radio chemical techniques deployed by Homestake, GALLEX, and SAGE experiments. The detector consists of large cylindrical vessel filled with approximately 50000 tons of ultra pure water. The walls of the vessel are fitted with close to 11000 units of Photo Multiplier Tubes

(PMTs) to pick up the tell-tale signs of different particles. If an elementary particle happens to have enough energy that it can travel faster than the speed of light inside the detector medium, then a well-directed cone of light known as cherenkov radiation, is produced along the trajectory of the particle. This light information is collected by the PMTs, and using the information recorded in these PMTs, one can trace back different kinematic information of the particle like kinetic energy, direction, etc. As the solar neutrinos are so feeble, the only permitted interaction inside the SuperK is the *Elastic Scattering* through the process $\nu_e + e^- \rightarrow \nu_e + e^-$. SuperK is capable of reconstructing neutrinos energies with a threshold of 5 MeV as below this energy, the contamination introduced by different radio active elements is significant. One of the most powerful tools that SuperK has is that it can reconstruct the original direction of the neutrino by looking into the kinematics of the scattering electrons (see Figure 4.10). In this way the SuperK experiments reconfirmed the measured flux deficit by previous radio chemical experiments in solar neutrino sector with very high confidence. The SuperK result revealed a factor of almost two discrepancy between the measured rate and the observed rate.

Even though all radio chemical experiments and SuperK clearly observed a deficit between measured and predicted solar neutrino fluxes, all of them lacked the ability to uncover the real reason behind this. It was finally the Sudbury Neutrino Observatory (SNO) experiment^[54] in Canada, which clearly demonstrated to the world that it is due to the ν_e s oscillating into ν_μ s and ν_τ s that all previous experiments observed a clear deficit in their measured fluxes. The setup of the SNO comprises a huge vessel filled with 1000 tons of heavy water (D_2O) where 9600 PMT units are always on the look out to catch any signs of interactions inside the detector. As D_2O is highly unstable, even a very low energy neutrino having an energy of ~ 2 MeV, can break apart the molecule releasing a proton and a neutron in the final state. This final state neutron undergoes the following interaction releasing a 6.25 MeV final state photon.

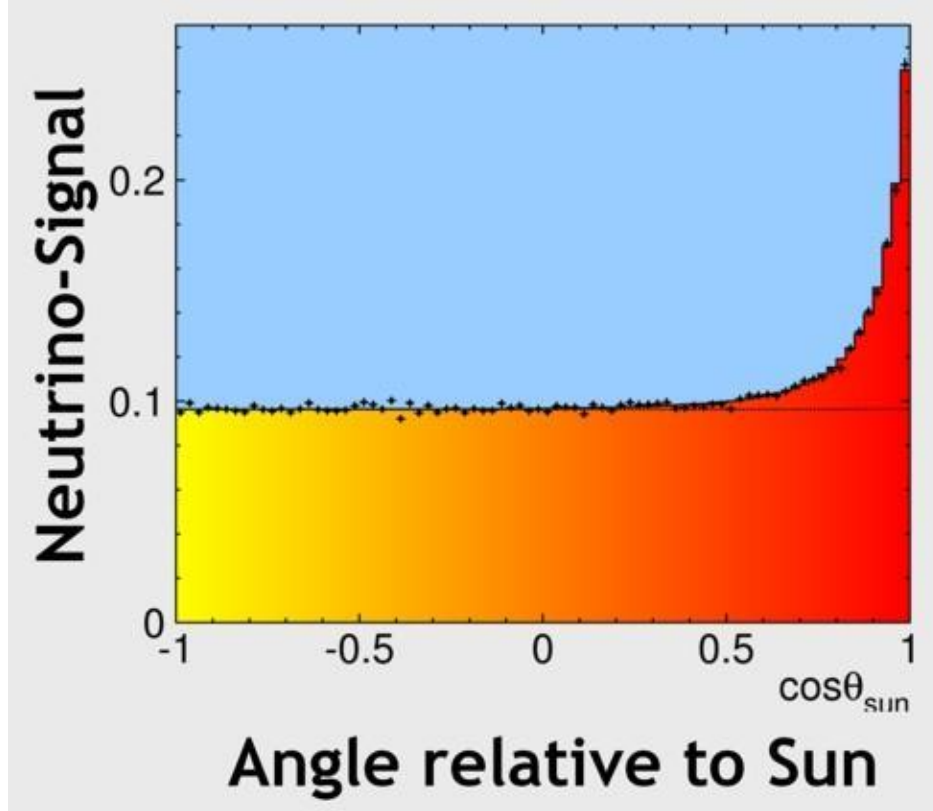
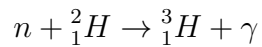


Figure 4.10: The direction of the neutrinos reconstructed by the SuperK experiment looking into the kinematics of scattered electrons^[53]. Here $\cos\theta = 1$ refers to the direction of the Sun.



The high energy 6.25 MeV photon interacts with the detector medium to produce an electromagnetic shower of energetic electrons and positrons, which produce many low energy photons of cherenkov light, which in turn are detected by the PMTs. Thus, by using the information in PMTs, the kinematics of the final state neutron can be reconstructed. One of the major handicaps that all previous solar neutrino experiments commonly shared was that they were only dependent on the charged current interaction in identifying neutrino interactions inside their detectors. But as the solar neutrino energy spectrum spans up to only ~ 30 MeV identifying a ν_μ or ν_τ in charged current mode in their detectors is an

impossible task due to the higher energy threshold. But inside the SNO detector, as it has the ability to reconstruct neutrons, the experiment is sensitive to the presence to all three neutrino types in the neutral current mode. The following discussion involves how SNO experiment solved the *Solar Neutrino Problem* by separating out individual neutrino flavor fluxes via different interaction processes.

The experiment focused on three main interaction channels namely,

- Elastic scattering.
- Charged current interaction.
- Neutral current interaction.

The elastic scattering channel involves the process $\nu + e^- \rightarrow \nu + e^-$ where in the final state always there is an electron. This final state electron is always going to be reconstructed by the PMTs using the cherenkov ring it produces. The electron neutrinos can elastically be scattered both in charged current and neutral current modes while for other two types it is only the neutral current mode. Using the information in this channel, one can calculate the flux ϕ_{ES} to be,

$$\phi_{ES} = \phi(\nu_e) + 0.15(\phi(\nu_\mu) + \phi(\nu_\tau))$$

As mentioned previously, it is only the electron neutrinos that can undergo the charged current interaction in the SNO detector. The complete charged current interaction involves, $\nu_e + D_2O \rightarrow e + p + p$. Here also the final state electron is reconstructed using the cherenkov light it produces. As both charged current interaction and elastic scattering are characterized by the final state electron, they produce, the separation between two process was done in the following manner in the SNO detector. The direction of the electron in the elastic scattering is correlated with direction of its mother neutrino, which is coming from the Sun. But in the latter case, the direction of the electron is isotropic and there is hardly and correlation to

the direction of the Sun. Thus using the directional information of the final state electrons, SNO can distinguish between two processes. The flux ϕ_{CC} in this channel can be expressed,

$$\phi_{CC} = \phi(\nu_e)$$

The neutral current interaction can be undergone by all the three neutrino flavors with equal probabilities due its low threshold. The full process involves $\nu + D_2O \rightarrow n + p + \nu$. The ϕ_{NC} flux of the interaction can be expressed,

$$\phi_{NC} = \phi(\nu_e) + \phi(\nu_\mu) + \phi(\nu_\tau)$$

The following lists measured and predicted fluxes in the SNO experiment.

$$\begin{aligned}\phi(\nu_e) &= (1.76 \pm 0.10) \times 10^{-6} cm^{-2} s^{-1} [23] \\ \phi(\nu_\mu) + \phi(\nu_\tau) &= (3.41 \pm 0.63) \times 10^{-6} cm^{-2} s^{-1} [23] \\ \phi(\nu_e)_{Predicted} &= (5.1 \pm 0.9) \times 10^{-6} cm^{-2} s^{-1} [23]\end{aligned}$$

As it is obvious the measured total flux of ν_e , ν_μ , and ν_τ components is in very good agreement with the SSM prediction. In addition, the measurement further revealed that there is a large flux of ν_μ s and ν_τ s ($\sim 2/3$ of the total measured flux), which is consistent with the missing fraction of ν_e s in the previous experiments. Thus, the SNO experiment conclusively solved the long existed solar neutrino puzzle by experimentally demonstrating the evidence for neutrino oscillations in the solar sector. This finding was ultimately rewarded with a joint Nobel prize between Super-Kamiokande and SNO experiments in 2015. Figure 4.11 shows the measured solar neutrino flux by different experiments.

Total Rates: Standard Model vs. Experiment
Bahcall–Serenelli 2005 [BS05(OP)]

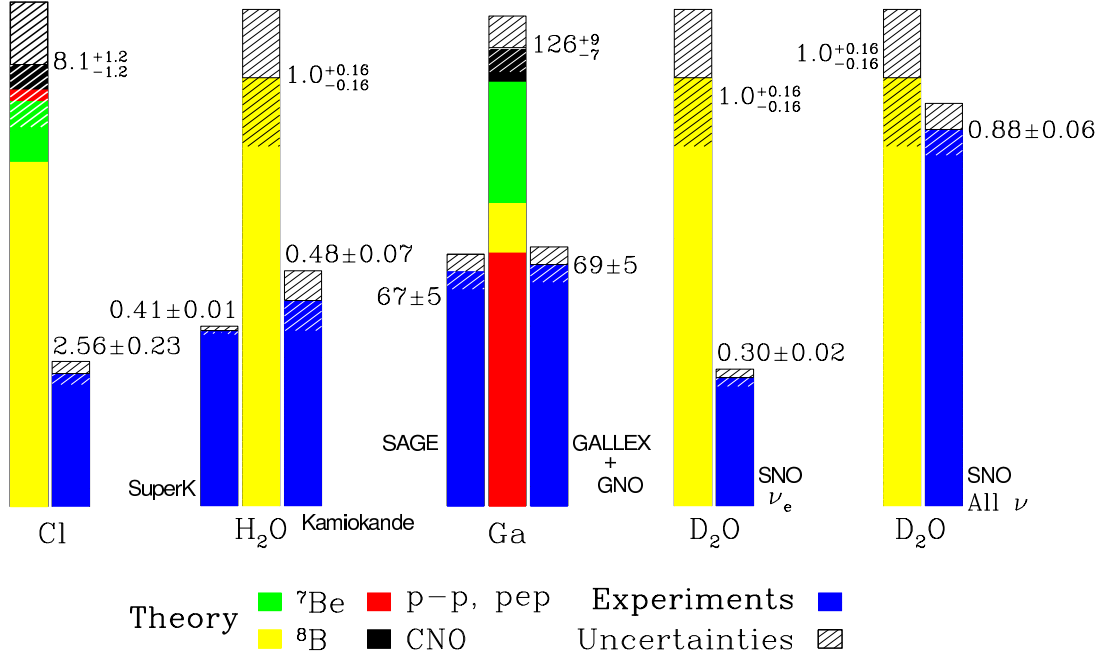


Figure 4.11: This shows the measurements of the solar neutrino flux by different experiments. All experiments observed a clear deficit in ν_e flux compared to the SSM prediction. The SNO experiment, once it measured all three components of the neutrino flux, concluded that it is due to the neutrino oscillations that all experiments observed a clear discrepancy between the measured and the predicted ν_e fluxes^[55]^[46].

4.4.3 Atmospheric Neutrino Anomaly

The production mechanism of atmospheric neutrinos is as follows. When cosmic rays (mainly consisting of protons 95%, Alpha nuclei 5%, and other heavy nuclei 1%) hit the Earth's atmosphere, they produce showers of secondary hadronic beams. Mostly these hadronic beams consist of pions while there is some contribution coming from strange and charm mesons as well. The secondary pions mostly decay on flight giving birth to neutrinos and muons where these tertiary muon beams further decay producing more neutrinos. The following decay channels show how neutrinos are produced in the secondary pion beams.

$$\pi^+ \rightarrow \nu_\mu + \mu^+ \rightarrow e^+ + \nu_e + \bar{\nu}_\mu$$

$$\pi^- \rightarrow \bar{\nu}_\mu + \mu^- \rightarrow e^- + \bar{\nu}_e + \nu_\mu$$

The energy spectrum of these neutrinos can span up to a few 100 GeVs while it has a peak energy of ~ 1 GeV. In the atmospheric neutrino sector, the model suggests with some uncertainty that at few GeV energy regime, the following ratio R ,

$$R = \frac{\nu_\mu + \bar{\nu}_\mu}{\nu_e + \bar{\nu}_e}$$

should remain close to 2, as it is already obvious in the decay channels of pions. The experiments that focus on atmospheric neutrinos always try to measure the ratio R to establish the validity of the model. But rather than exactly measuring R , all experiments measure the alternative quantity R' ,

$$R' = \frac{(N_\mu/N_e)_{Data}}{(N_\mu/N_e)_{Simulation}}$$

with the purpose of canceling out different systematics and interpreting different results by different experiments in a coherent manner. In this new variable, the numerator has the ratio between number of ν_μ s to number of ν_e s in data while the denominator got the same ratio as the model predicts. There were several dedicated experiments to measure the atmospheric neutrino flux. Table 4.1 lists the measurements for R' done by these different experiments.

The measurements of almost all experiments reveal that the quantity R' is significantly lower than 1 indicating a serious disagreement between data and the model prediction. To

Experiment	Detector Technology	R'
Super-Kamiokande (sub-GeV)	Water Cherenkov	$0.658 \pm 0.016 \pm 0.035$
Super-Kamiokande (multi-GeV)	Water Cherenkov	$0.702_{-0.030}^{+0.032} \pm 0.101$
Soudan2	Ion Tracking Calorimeter	$0.69 \pm 0.10 \pm 0.06$
IMB	Water Cherenkov	$0.57_{-0.07}^{+0.08} \pm 0.07$
Kamiokande (sub-GeV)	Water Cherenkov	$0.60_{-0.05}^{+0.06} \pm 0.05$
Kamiokande (multi-GeV)	Water Cherenkov	$0.57_{-0.07}^{+0.08} \pm 0.05$
Frejus	Ion Tracking Calorimeter	$0.69 \pm 0.10 \pm 0.08$

Table 4.1: Measurement of R' by different experiments^[56].

explain these results, one could assume that there is lower number of ν_μ s in data than the model prediction or there is more ν_e s in reality or finally it could be a combination of both reasons. As an exact cause wasn't known by that time, this observation was famously known as the *Atmospheric Neutrino Anomaly* in the neutrino community.

This time it was the SuperK experiment, which played the major role in understanding this anomaly. The SuperK experiment is capable of distinguishing between ν_μ interactions and ν_e interactions inside their detector by looking into the cherenkov light produced by the final state muons and electrons. Moreover, the experiment is capable of inferring neutrino energies and direction by looking into the kinematics of final state particles. The Figure 4.12 shows the ν_μ and ν_e interactions recorded in the SuperK detector.

Looking into the plots in the Figure 4.12, it is clearly obvious that there is a deficit of ν_μ events compared to the prediction in all energies, whereas the number of ν_e interactions are in good agreement with the model. So the only possible explanation for the disappearance of some ν_μ interactions is that, some of ν_μ s may have oscillated into ν_τ s on their way to the detector. Even though the SuperK was incapable of reconstructing ν_τ events in their detector to back up this logic, they have paved the way for the next generations of neutrino experiments as how to fully solve the atmospheric neutrino anomaly.

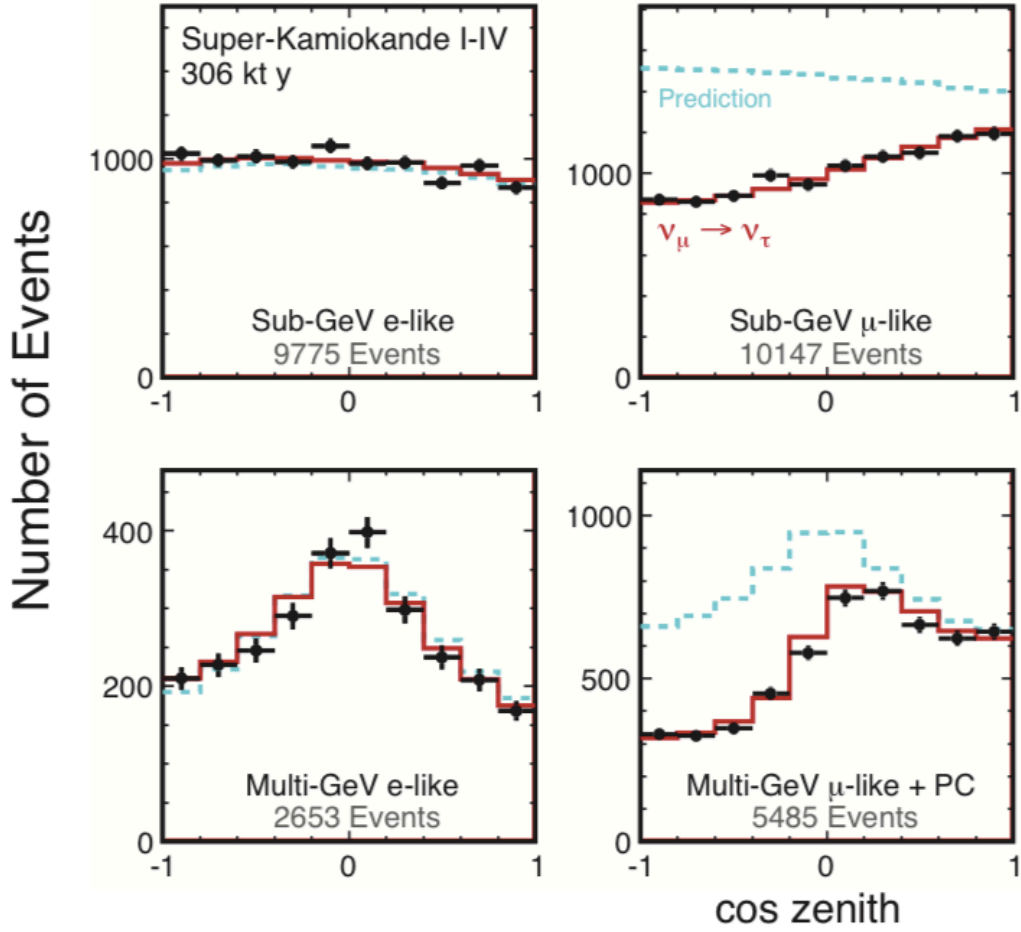


Figure 4.12: ν_e like and ν_μ like events recorded in SuperK atmospheric data^[56]. (Left Column) ν_e like events. (Right Column) ν_μ like events. Multi-GeV implies events having visible energies greater than 1.33 GeV while sub-GeV events have visible energies less than 1.33 GeV. (Dotted Line) Non-Oscillation hypothesis. (Solid Line) $\nu_\mu \rightarrow \nu_\tau$ oscillation best fit. In all plots X-axis represents cosine value of the zenith angle as shown in the Figure 4.13. Here the zenith angle 0° represents neutrinos coming from straight up whereas angle 180° is for neutrinos coming from straight down.

4.4.4 Accelerator Long Baseline Neutrino Experiments

Even though SuperK couldn't directly identify ν_τ events inside their detector, in an indirect way, they confirmed that the atmospheric neutrino anomaly is mainly due to ν_μ s oscillating into ν_τ s. So with that assumption, by analyzing their atmospheric neutrino data, they went onto determine the parameters Δm_{32}^2 and $\sin^2(2\theta_{23})$ to be $2.2 \times 10^{-3} eV^2$ and 1.0^[58] respectively. Compared to atmospheric neutrino observations, the accelerator neutrino ex-

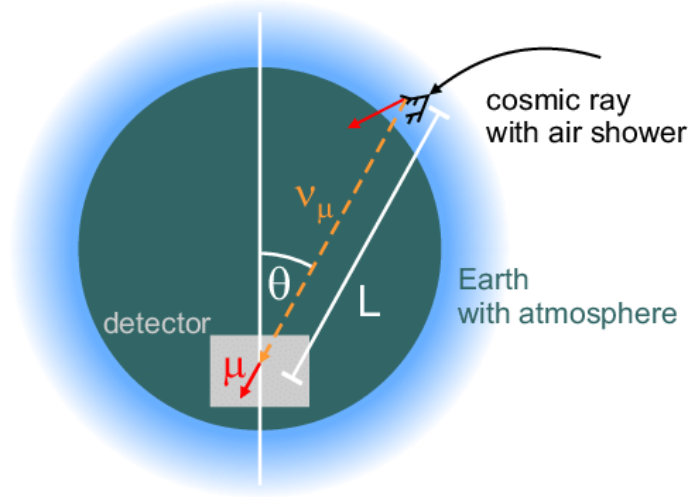


Figure 4.13: Zenith angle of neutrinos^[57].

periments give us more control over experimental conditions, since we design and build the neutrino source. Therefore, accelerator experiment can be more precise with enough data. Because of that, most of the accelerator based long baseline neutrino experiments cross-check these neutrino oscillation parameters derived using atmospheric neutrino data. Most of the long baseline neutrino experiment consists of two detectors, commonly known as the near detector and the far detector. But, there are some exceptions to this general rule. For example, the OPERA experiment^[59] used the CNGS beam, which had muon detectors at the near site but no neutrino detector. The KamLAND experiment^[60] had a long-baseline (180 km average) but had no near detectors at the neutrino sources. As the average energy for any man-made neutrino beam hovers around ~ 1 GeV and to be sensitive to the above mentioned Δm^2 value, the far and the near detectors of any long baseline experiment should roughly be separated by 400 km. But this really depends on the energy spectrum of the neutrinos and what the experiment wants to achieve. For instance the NOVA experiment^[61] at Fermilab has a far and near detector separation of ~ 810 km where in the MINOS experiment^[62] the far detector was ~ 735 km away from the near detector. The near detector is intended to gather the information of the neutrino beam before the oscillation happens while far detector measures the number of neutrinos that have oscillated or survived after their long journey. Conventionally both near and far detectors are made using the same detector

technology in order to smear out any systematic uncertainties. Meanwhile, the far detector of any long baseline experiment is always larger than the near detector by a large factor in order to account for the spreading up of the neutrino beam as it travels. In any long baseline project, the neutrino oscillations could be studied in two different channels namely,

- Appearance search.
- Disappearance search.

In an appearance search, people are looking for a flavor change in the original neutrino beam where in this kind of search, it is of an utmost importance to understand any beam contamination and other background processes. The disappearance channel basically looks for the survival probability of a given neutrino flavor. So just by taking the ratio between number of events observed in the near detector and far detector of a given neutrino flavor, one can easily find information about neutrino oscillations in the disappearance channel. Here onwards the discussion will be about the role played by two long baseline experiments MINOS and T2K^[63] in understanding the neutrino oscillation parameters in the atmospheric sector.

The MINOS was one of the long baseline experiments at Fermilab. The experiment was operational in the time period of 2005 to 2016 in two stages. Experimental setup of the MINOS consisted of two detectors with the near detector placed roughly 1 km away from the target hall while the far detector was ~ 735 km away from the near detector in the Soudan mine, Northern Minnesota. Both of the detectors were made up of thick iron plates where scintillator bars were sandwiched in between consecutive plates. Once a charged particle travels through these scintillator bars, the scintillation light produced from the interaction is transmitted through optical fibers to the PMT units. Thus, the presence of neutrino interactions inside two MINOS detectors can be detected. The near detector had a total mass of ~ 980 tons while the far detector sitting ~ 716 m underground weighed ~ 5.4 ktons. One of the notable features of the MINOS detectors is that both of its detectors were fully magnetized, which allowed the experiment to distinguish between negatively and

positively charged particles. The experiment made use of Fermilab's most intense neutrino beam, NUMI, which got a spectrum peaking around ~ 3 GeV and largely composed of ν_μ s. The 2013 results of the MINOS in ν_μ and $\bar{\nu}_\mu$ disappearance channels explained in the Reference^[64] reveals that $\Delta m^2 = 2.41_{-0.10}^{+0.09} \times 10^{-3} eV^2$, $\sin^2 2\theta = 0.950_{-0.036}^{+0.035}$ in the neutrino mode and $\Delta m^2 = 2.50_{-0.25}^{+0.23} \times 10^{-3} eV^2$, $\sin^2 2\theta = 0.970_{-0.08}^{+0.03}$ in its anti neutrino mode (see Figure 4.14).

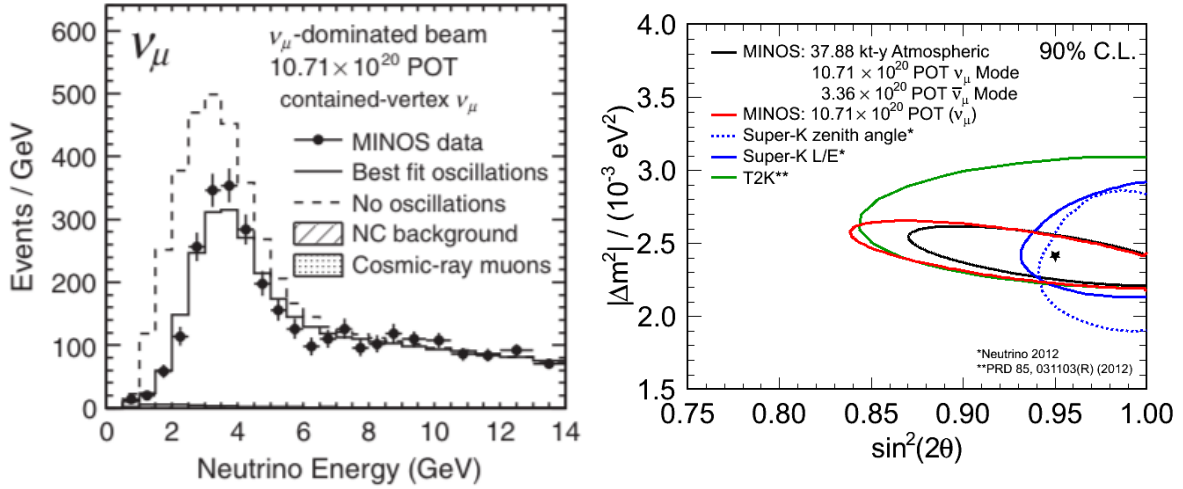


Figure 4.14: ν_μ disappearance channel search by MINOS 2013^[64]. (Left) Dashed line is for number of events that can be observed in the far detector if no oscillation are there. Solid black line is the best fit if oscillation happens. The data points clearly reveal that some ν_μ s have disappeared in the far detector due to oscillations. (Right) The allowed regions of $\sin^2 2\theta$ and Δm^2 with 90% confidence level. Different contours are for different experiments and different data taking modes of the MINOS as indicated in the plot. The best fit point in this plot is $\Delta m^2 = 2.41_{-0.10}^{+0.09} \times 10^{-3} eV^2$, $\sin^2 2\theta = 0.950_{-0.036}^{+0.035}$.

The T2K experiment in Japan, which is still running, is another long baseline neutrino experiment having a near to far detector separation of ~ 295 km. The T2K ND280 near detector, which is placed ~ 280 m away from its target, makes use of the neutrinos produced by the J-PARC accelerator facility at Tokai in east coast of Japan. Neutrino beam used by T2K is found to be $\sim 99\%$ pure in ν_μ s where beam is initially measured in the near detector to know the initial number of ν_μ s as in all other long baseline experiments. The experiment uses the famous SuperKamiokande detector in the west coast of Japan as its far detector, which is placed $\sim 2.5^0$ off axis of the beam line and ~ 1000 m underground. 2017 results of

the T2K experiment in its ν_μ disappearance channel found Δm^2 to be $2.53_{-0.13}^{+0.15} \times 10^{-3} eV^2$ while $\sin^2\theta$ is $0.51_{-0.07}^{+0.08}$ [65] in the atmospheric sector. The respective values for anti neutrino mode are $\Delta m^2 = 2.55_{-0.27}^{+0.33} \times 10^{-3} eV^2$ and $\sin^2\theta = 0.47_{-0.07}^{+0.25}$ [65]. Figure 4.15 shows the T2K 2016 results in the disappearance channel.

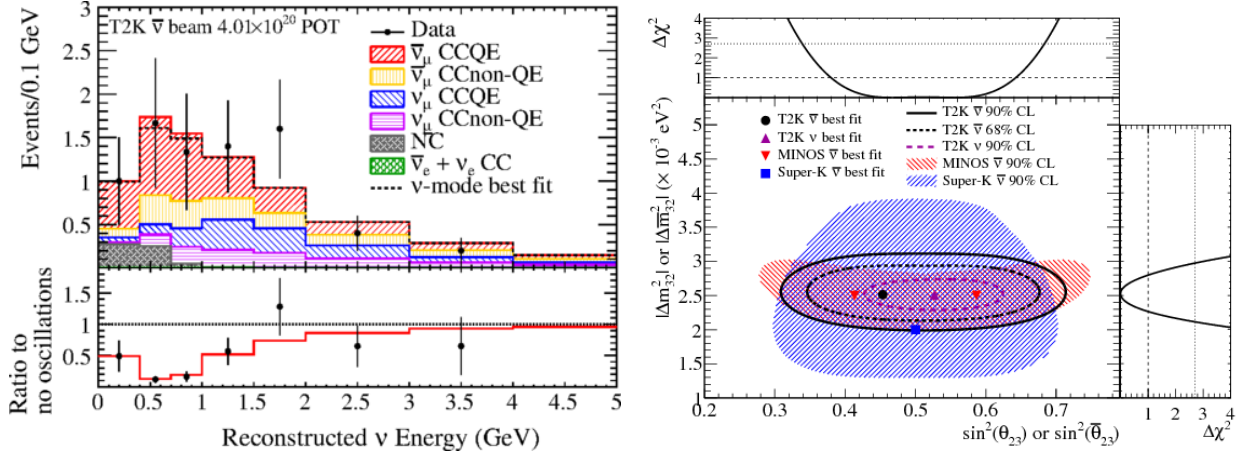


Figure 4.15: $\bar{\nu}_\mu$ disappearance channel search by T2K experiment in 2016 [66]. (Left) The ratio plot (number of events observed in the far detector to the expected number of events with no oscillation hypothesis). Here in the bottom panel it clearly shows that some $\bar{\nu}_\mu$ s have disappeared due to oscillations. (Right) Δm^2 vs $\sin^2\theta$ sensitivity plot in both neutrino and anti neutrino modes. Different contours show different confidence levels for different experiments in both neutrino and anti neutrino modes as indicated in the legend. The best fit values for $\bar{\nu}_\mu$ disappearance channel in T2K are $\Delta m^2 = 2.51 \times 10^{-3} eV^2$ and $\sin^2\theta = 0.45$.

4.4.5 Reactor Neutrino Experiments

The global dataset analysis by the SNO experiment in the solar sector explained in the Reference [67], reveals that Δm_{sol}^2 or Δm_{21}^2 to be $\sim (7.46_{-0.19}^{+0.20}) \times 10^{-5} eV^2$ while $\tan^2(2\theta_{sol})$ or $\tan^2(2\theta_{12})$ is $0.443_{-0.025}^{+0.030}$ suggesting that mixing angle θ_{sol} (θ_{12}) in the solar sector to be $\sim 32^\circ$. If we were to use a long baseline neutrino experiment again to verify these results as in the case of atmospheric neutrinos, then we would need to build an experiment having a baseline length of $\sim 10^6$ km to be sensitive to this particular mass squared splitting. As this is not pragmatic by any means, we need to come up with an alternative solution. One possible solution is to make use of $\bar{\nu}_e$ s, which are produced in abundance in larger commercial reactor cores. As the energies of these very feeble neutrinos are around 5 MeV, which is pretty much

similar to the solar neutrino energy spectrum, the baseline length of the experiments are reduced to manageable distances. Here the discussion is about the KamLAND experiment in the Kamioka mines, Honshu islands in Japan in verifying solar neutrino results, which is operational since 2002. The experiment made use of a cumulative $\bar{\nu}_e$ flux generated by a total of 53 Japanese commercial nuclear reactors where the detector is located at an average flux-weighted distance of ~ 180 km away from all reactor cores. KamLAND would still make use of antineutrinos from Japanese reactors, except that all reactors in Japan have been shut down since the Fukushima Daiichi nuclear disaster in 2011. The KamLAND experimental setup consists of three major components namely, the outermost cylindrical water cherenkov detector, the intermediate inner spherical vessel, and the innermost nylon balloon. Here the outermost water cherenkov detector, which has a total mass of 3.2 ktons, acts as a cosmic veto region while providing shield against any radio activity produced in the nearby rock. The next inner container is a 18 m diameter spherical vessel whose inner wall is fitted with a total of 1879 photo multiplier tubes. This vessel is completely filled with non-scintillating ultra pure oil, which absorbs radioactivity emitted by uranium and thorium in the cavern rock, veto water, and PMT glass without making any scintillation light. In addition, oil provides the necessary buoyancy for the inner most nylon balloon. This nylon balloon with a diameter of 13 m is completely filled with a mixture of 1000 tons of mineral oil, benzene, and a fluorescent chemical, which acts as the detector medium to identify the presence of $\bar{\nu}_e$ s in the detector. When an anti electron neutrino happens to interact inside the detector, it undergoes the reaction $\bar{\nu}_e + p \rightarrow e^+ + n$, which is famously known as the *Inverse Beta Decay*. The positron produced in the final state immediately pair produces and ejects out photons while the final state recoiling neutron is going to be captured sometime later (after $\sim 200 \mu\text{s}$) by hydrogen in the medium releasing a 2.2 MeV mono energetic photon. This prompt signal by the pair production and the delayed neutron capture signal generate the characteristic inverse beta decay signal in any of the reactor neutrino experiment. The combined analysis of data collected by KamLAND and other solar neutrino experiments documented in the Reference^[68] found Δm_{sol}^2 (Δm_{21}^2) and $\tan^2\theta_{sol}$ ($\tan^2\theta_{12}$) to be $7.9_{-0.5}^{+0.6} \times 10^{-5} eV^2$ and $0.40_{-0.07}^{+0.10}$ respectively (see Figure 4.16).

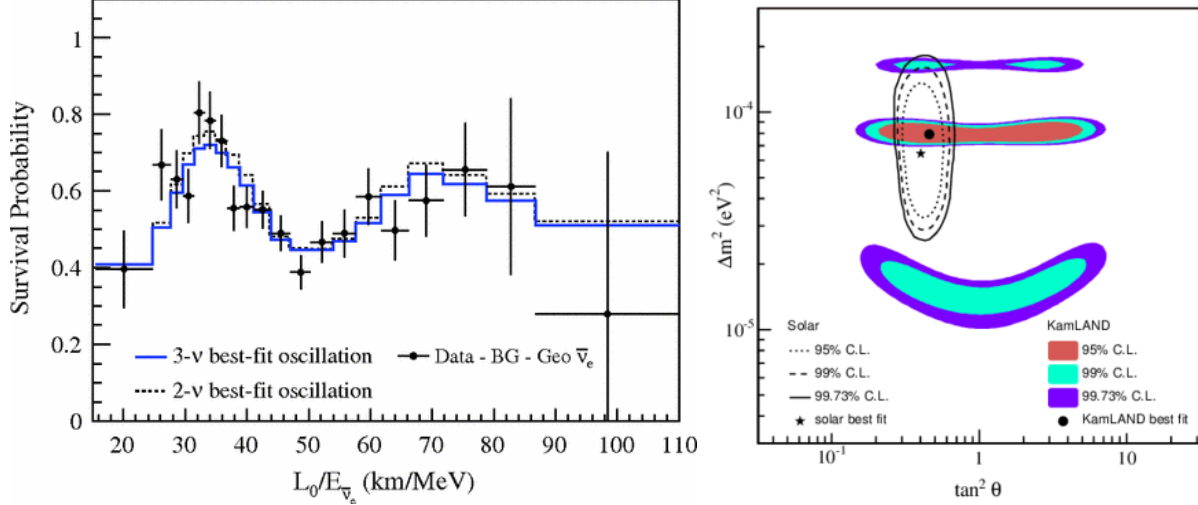


Figure 4.16: KamLAND $\bar{\nu}_e$ disappearance channel search. (Left) The ratio of observed $\bar{\nu}_e$ events to the no-oscillation hypothesis^[69]. The data points below one is a clear evidence for the $\bar{\nu}_e$ oscillations. (Right) The allowed regions of Δm^2 and $\tan^2 \theta$ in KamLAND data and other solar neutrino experiments^[68]. The best fit for the global dataset of KamLAND plus other solar neutrino experiments is $\Delta m^2 = 7.9_{-0.5}^{+0.6} \times 10^{-5} eV^2$ and $\tan^2 \theta = 0.40_{-0.07}^{+0.10}$ with the assumption of CPT (Charge-Parity-Time) invariance. A description about CPT invariance is provided in pages 347-349 of the Reference^[23].

As reactor neutrino experiments play a major role in verifying oscillation parameters in the solar sector (Δm_{21}^2 and $\sin \theta_{12}$), they also help to determine the θ_{13} mixing angle, independent of other oscillation parameters. The channel people are looking in this context is the survival probability of $\bar{\nu}_e$ s in short baseline oscillations. It has been long believed that the mixing angle θ_{13} is so small that short baseline neutrino oscillations does not exist. But, the Double Chooz experiment^[70] saw an indication of non-zero θ_{13} for the first time at 90% confidence level using one far detector and no near detector. Daya Bay^[71] was the first to conclusively demonstrate non-zero θ_{13} at the 5-sigma confidence level, which is generally accepted as the standard for discovery in high energy physics. The Daya Bay experiment in China is located at 52 km northeast of Hongkong and 45 km east of Shenzhen. The experiment consists of six separate neutrino detectors, which make use of $\bar{\nu}_e$ s produced by six commercial purpose reactor cores each having a total power of 2.9 GW. All six detectors are strategically placed at different places where two are placed at mean flux weighted distance of 470 m, one at 576 m and remaining three at 1.65 km away from all six reactor cores.

All six detectors share some features in common where each detector is filled with roughly 20 tons of some liquid scintillator material doped with gadolinium. The photo multiplier tubes sitting inside the detector will catch any of the scintillation photons or cherenkov light to reconstruct the neutrino interactions inside the detector. Here the gadolinium atoms are supposed to capture the recoiling neutrons produced in the inverse beta decay reaction, finally releasing a mono energetic photon in the delayed signal. The Daya Bay experiment relies on two metrics to observe neutrino oscillations where first one is to look for a change of $\bar{\nu}_e$ events as a function of distance while the second method being comparison of e^+ energy spectrum in near and far detectors (see Figure 4.17). The value for $\sin^2\theta_{13}$ obtained by the analysis described in the Reference^[72] is 0.071 ± 0.011 indicating that mixing angle θ_{13} is small ($\sim 7^\circ$). In addition reactor experiments like RENO^[73] (South Korea) also played a crucial role in making this measurement where upcoming experiments like JUNO^[74] (China) will go for better measurements with very high precision.

4.4.6 Short Baseline Neutrino Experiments

The LSND experiment^[75] at Los Alamos national lab is the first experiment to have reported the evidence for short baseline neutrino oscillations. The experiment, which was designed to see the oscillation $\bar{\nu}_\mu \rightarrow \bar{\nu}_e$ through the appearance channel, was operational from 1993 to 1998. LSND detector consisted of a large tank filled with 167 tons of a mixture of mineral oil and some scintillating material. The anti electron neutrinos produced due to oscillations along the path from source to detector, cause the inverse beta decay reaction ($\bar{\nu}_e + p \rightarrow e^+ + n$) on protons producing final state neutrons, which are captured by mineral oil releasing a 2.2 MeV photons in consequence. Here also the detector relies on prompt and delayed signals produced by the inverse beta decay to reconstruct the $\bar{\nu}_e$ events. To collect the scintillation light and cherenkov radiation produced inside the detector due to a variety of interactions, the detector is fitted with a total of 1220 PMT units. The experiment made use of the pion beam produced in the Los Alamos Meson Physics Facility (LAMPF) to get the $\bar{\nu}_\mu$ s. These pions are produced inside a water target where they decay at rest inside the target itself

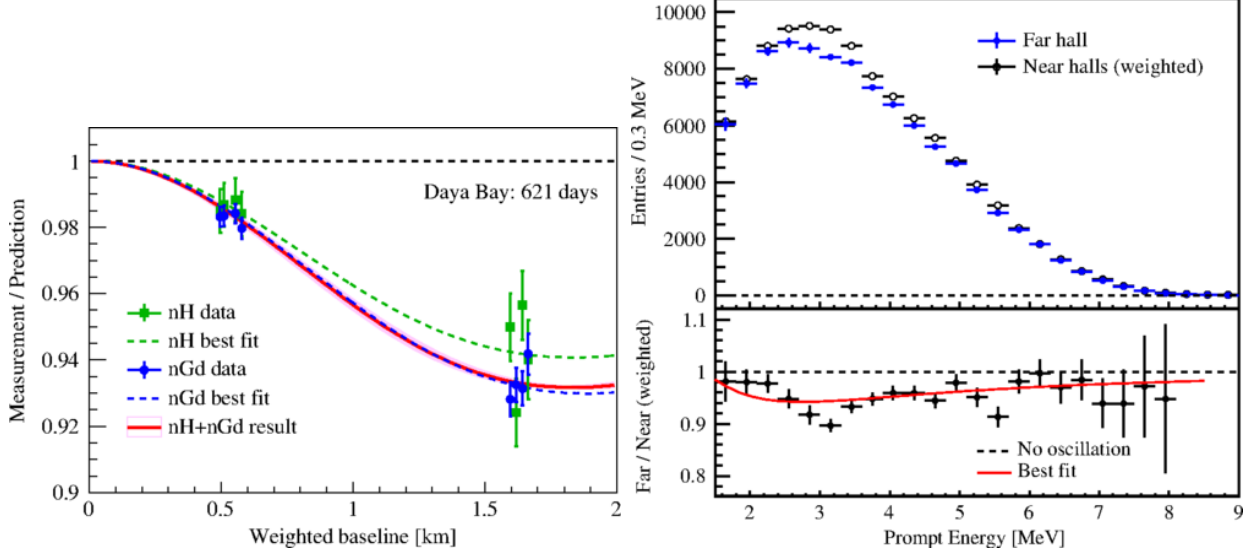


Figure 4.17: Daya Bay θ_{13} measurement results 2016^[72]. (Left) Ratio of measurement vs no-oscillation hypothesis for all six detectors. Each blue and green point represent individual detectors where green data points represent delayed signal coming from neutron captured by hydrogen while blue data points represent delayed signal reconstructed using neutrons captured by gadolinium. Data points reveal that all six detectors observe a deficit in $\bar{\nu}_e$ s in both gadolinium and hydrogen analysis due to oscillations. (Right) The energy spectrum of the prompt signal (e^+) in the far detectors and the same scaled distribution in the two near detectors. The ratio between number of events observed in the far and the near detectors in the bottom panel of this plot clearly indicates the deficit in $\bar{\nu}_e$ events in the far detectors due to oscillations.

giving birth to $\bar{\nu}_\mu$ beams as indicated in the below reaction.

$$\pi^+ \rightarrow \nu_\mu + \mu^+ \rightarrow e^+ + \nu_e + \bar{\nu}_\mu$$

Then these $\bar{\nu}_\mu$ s whose energy spectrum can span up to a maximum value of 52.8 MeV, start their journey to the LSND detector, which is located ~ 30 m away from the water target. After analyzing 5 years of data collected, the LSND experiment reported that they have observed an excess of $87.9 \pm 22.4 \pm 6.0$ $\bar{\nu}_e$ like events after subtracting all possible background. Moreover, they concluded that this excess is the result of a mass squared splitting in the range of 0.2 - 10 eV^2 (see Reference^[76]), which far exceeds the values obtained for Δm_{32}^2 and Δm_{21}^2 by any of long baseline or reactor experiment. See Figure 4.18 for LSND

results.

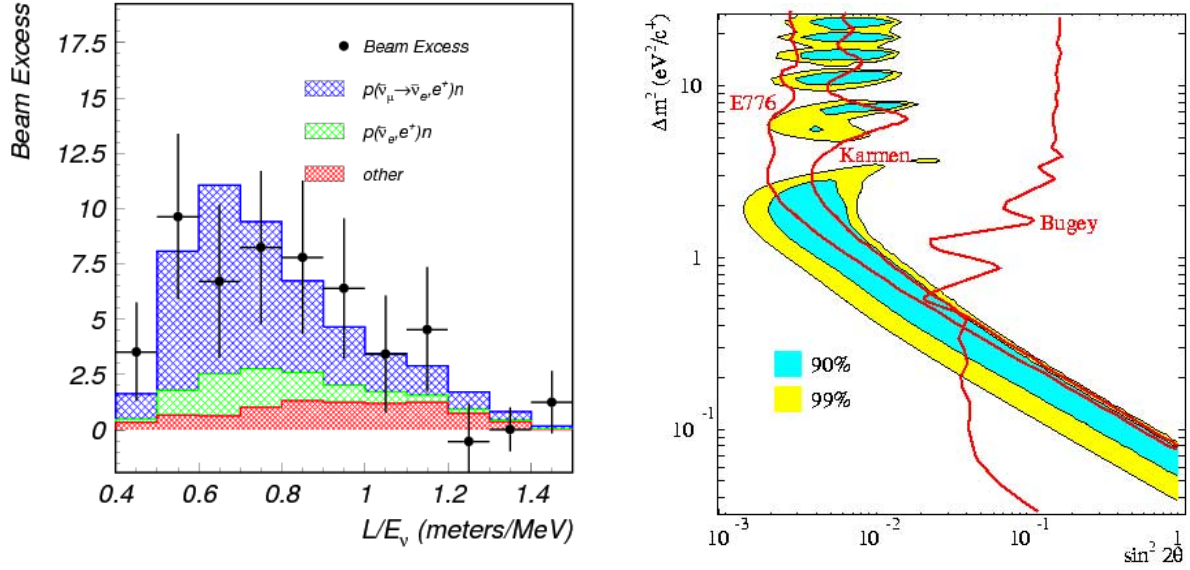


Figure 4.18: LSND $\bar{\nu}_\mu \rightarrow \bar{\nu}_e$ search^[76]. (Left) Number of $\bar{\nu}_e$ like events observed as a function of L/E_ν in the neutrino energy range of $20 \text{ MeV} < E_\nu < 60 \text{ MeV}$. (Right) the 90% and 99% favored regions for LSND^[77]. The regions dedicated for E776, Karmen, and Bugey are at 90% confidence level. The LSND excess is consistent with $0.2 \text{ eV}^2 < \Delta m^2 < 10 \text{ eV}^2$.

To solve the controversial result obtained by the LSND experiment, the importance of a new experiment was first discussed by the BooNE collaboration^[78] led by Janet Conrad (then at Columbia) and Bill Louis (Los Alamos). Then a new experiment was designed, named MiniBooNE^[79] at Fermilab, which was operational from 2003 to the recent past. The experiment is made up of a large spherical tank filled with ~ 800 tons of mineral oil mixed with a scintillator material. Cherenkov radiation and scintillation light produced by particle interactions is collected by an array of photo multiplier tubes, which is made up of total of 1280 individual units. Here the whole detector is buried underground to shield it against showers of cosmic muons. MiniBooNE made use of the Booster Neutrino Beam produced in the Fermilab, which is over 95% pure in ν_μ s having an average neutrino energy of $\sim 0.7 \text{ GeV}$. Moreover, the beam is switchable between neutrino mode and anti neutrino mode as preferred. The detector is located $\sim 540 \text{ m}$ away from the neutrino source to have the same L/E ratio in the LSND experiment. The MiniBooNE results published

so far reveals that MiniBooNE experiment also observed a significant excess of ν_e and $\bar{\nu}_e$ events in its both neutrino and anti neutrino runnings as in LSND. MiniBooNE's combined analysis of $\nu_\mu \rightarrow \nu_e$ and $\bar{\nu}_\mu \rightarrow \bar{\nu}_e$ documented in the Reference^[80], claims that they observed a total of excess events $240.3 \pm 34.5 \pm 52.6$ in the energy region of $200 \text{ MeV} < E_\nu^{QE} < 1250 \text{ MeV}$ (see Figure 4.19). The results obtained by MiniBooNE is consistent with LSND, and improves upon LSND by reducing the uncertainty in the LSND result as claimed in their latest results^[81].

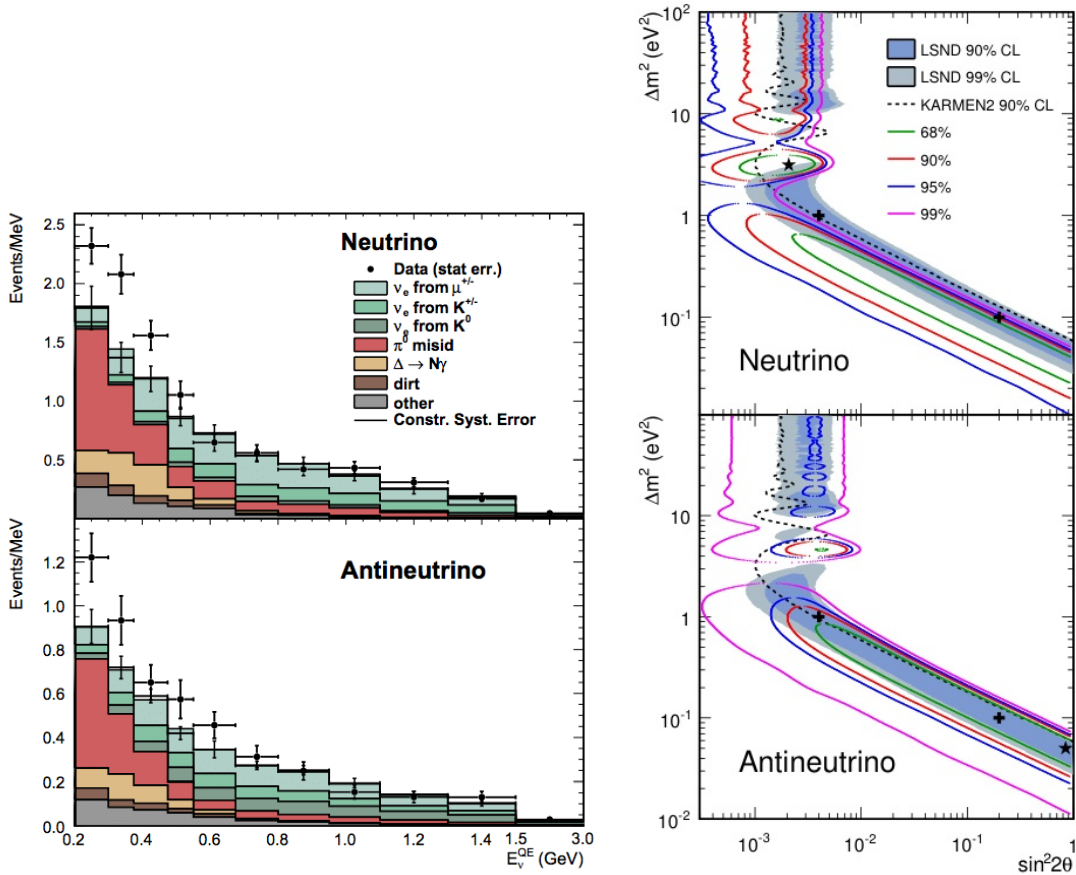


Figure 4.19: MiniBooNE low energy excess^[80]. (Left) The low energy excess observed by the MiniBooNE experiment in its neutrino and anti neutrino modes separately, after subtracting all possible backgrounds. The combined analysis of $\nu_\mu \rightarrow \nu_e$ and $\bar{\nu}_\mu \rightarrow \bar{\nu}_e$ is claiming a total excess of $240.3 \pm 34.5 \pm 52.6$ events. (Right) Allowed regions of MiniBooNE for events $E_\nu^{QE} > 200 \text{ MeV}$ with different confidence level as indicated in both neutrino and anti neutrino modes. The allowed region for both LSND and MiniBooNE are consistent with each other.

4.4.7 The MicroBooNE Experiment

The major physics goal behind the MicroBooNE experiment is to investigate further into the low energy excess observed by the MiniBooNE experiment. One of the major criticisms of both MiniBooNE and LSND results is that both experiments lack the ability to distinguish between photons and electrons with high confidence level. As a result the electron like excess observed by MiniBooNE/LSND could in reality be from an unknown background process. As MicroBooNE uses a fine-grained LArTPC detector, it has the potential to separate out photon and electron induced showers as explained below. One of the main feature of an electron induced shower is that electron begins to deposit energy in the detector right from the moment it is born. In other words, there is no separation between the point where electron shower begins and the vertex point where the electron is born. But on the contrary, there is a clear separation between vertex point where the photon is originally born and the origin of the photon shower. Furthermore, in the very beginning of an electron induced shower, it is only the electron, which mostly deposits its energy before the shower develops. But in a photon induced shower, due to pair production, a pair of electron and positron is responsible in depositing energy at the start. So typically a photon induced shower has more energy at the start compared to that of an electron induced shower. So relying on these two features, MicroBooNE can easily distinguish between photons and electrons and ultimately will reveal the truth behind MiniBooNE and LSND results. Moreover, as MicroBooNE can reconstruct very low threshold particle interactions, it has the ability to explore into much lower energy regions in search of short baseline neutrino oscillations where MiniBooNE could not reach. See Figure 4.20 for the separation of electron and photon induced showers based on their energy by Argoneut experiment.

In addition to the investigation into the MiniBooNE signal, MicroBooNE will help to understand the neutrino argon interactions in the energy regime of ~ 1 GeV. As LArTPC technology is still novel and argon atoms are very complicated, very little is known about the neutrino argon interactions so far. So all the information that MicroBooNE is going to learn through its variety of cross section measurements, will reveal many hidden information about

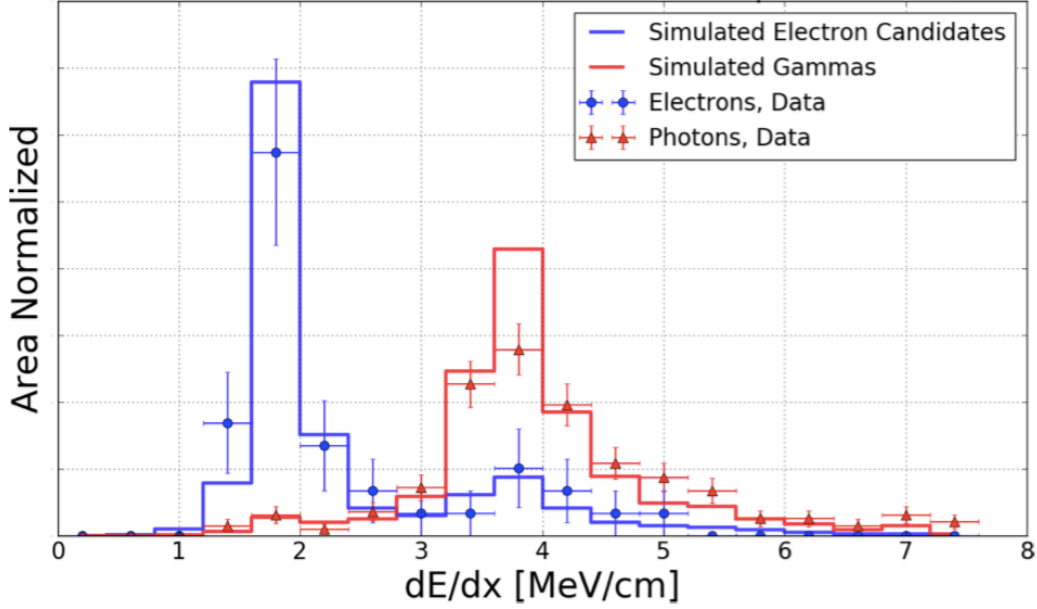


Figure 4.20: Separation of the electron and photon induced showers in Argoneut LArTPC using shower energy^[82]. It is clear that a photon induced shower is more energetic compared to that of an electron induced shower.

neutrino argon interactions and will be very useful specially for different neutrino generators in model building. Apart from its major physics goals, MicroBooNE would also serve as R&D for upcoming neutrino experiments, which are also planning to use the LArTPC technology.

4.4.8 Upcoming Neutrino Experiments

In the discussion of upcoming neutrino experiments, Fermilab’s SBN (Short Baseline Neutrino) and long baseline neutrino programs are of the highest importance. Under the SBN program, the plan is to come up with a three detector arrangement in search of a fourth type of neutrino called sterile neutrino. In this three detector arrangement, MicroBooNE is going to play the role of the intermediate detector while the ICARUS T600 detector has been imported from CERN to be used as the far detector. For the near detector, which is going to measure composition of the neutrino beam beforehand the neutrino oscillations, a new detector is going to be built closer to the BNB beam line in the Fermilab site. Here all three detectors will be using LArTPC technology to reconstruct low threshold neutrino interactions with impeccable accuracy (see Figure 4.21). In the appearance channel of $\nu_\mu \rightarrow \nu_e$,

the SBN will cover the 90% confidence level allowed region of the LSND experiment at $> 5\sigma$ level above $\Delta m^2 = 0.1 \text{ eV}^2$ and $> 4.5\sigma$ level everywhere. Meanwhile, In the disappearance channel of ν_μ , the SBN will be the most sensitive experiment of all time in the region of $\Delta m^2 \sim 1 \text{ eV}^2$ ^[9]. The whole program is supposed to kick start in early 2019 while MicroBooNE detector is already in operation.

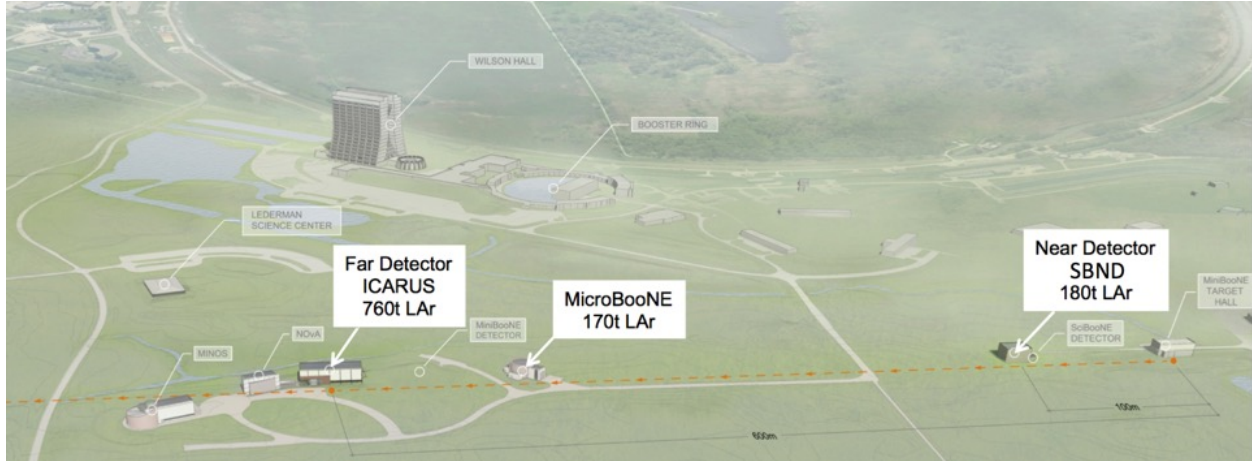


Figure 4.21: Schematic diagram of Fermilab’s SBN program^[83].

The next ambitious project in the Fermilab’s long baseline neutrino program is the DUNE (Deep Underground Neutrino Experiment) experiment, which is mainly aimed at resolving the mass hierarchy issue and CP violation in neutrinos. The experiment will also be looking into the rare proton decay as well. As a typical long baseline project, the whole experiment is going to consist of a near detector and a far detector where the far detector is scheduled to be located in the Sanford underground research facility at Lead, South Dakota, nearly 1300 km away from the near detector. Plans have already been laid down to use the LArTPC technology for the far detector, which is going to be comprised four 10 kton individual modules making it the world’s largest neutrino detector ever to be built so far. The design of the near detector of this project is yet to be finalized. The LBNF program (Long Baseline Neutrino Facility) at Fermilab will be producing the world’s most intense neutrino beams with an average energy of $\sim 2 \text{ GeV}$, specifically for this project where the whole DUNE project is supposed to come to a completion by the year 2026. Figure 4.22 is a cartoon of proposed DUNE experiment.

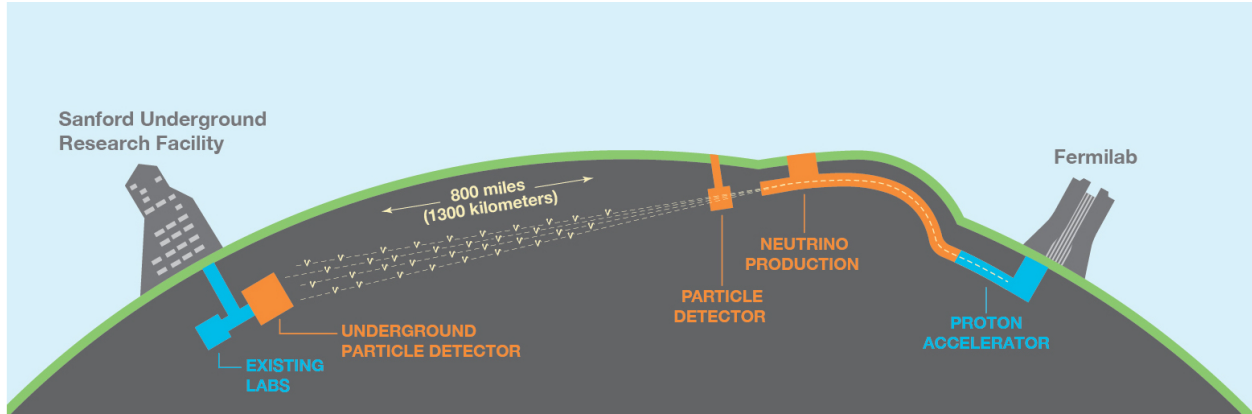


Figure 4.22: Schematic diagram of the DUNE experiment [84].

4.4.9 Neutrino Oscillation Parameters (Current Knowledge)

Table 4.2 lists the current knowledge about neutrino oscillation parameters.

Oscillation Parameter	Value
$\sin^2\theta_{12}$	0.307 ± 0.013
Δm_{21}^2	$(7.53 \pm 0.18) \times 10^{-5} eV^2$
$\sin^2\theta_{23}$	$0.421^{+0.033}_{-0.025}$ (Inverted Order, Quadrant 1)
$\sin^2\theta_{23}$	$0.592^{+0.023}_{-0.030}$ (Inverted Order, Quadrant 2)
$\sin^2\theta_{23}$	$0.417^{+0.025}_{-0.028}$ (Normal Order, Quadrant 1)
$\sin^2\theta_{23}$	$0.0597^{+0.024}_{-0.030}$ (Normal Order, Quadrant 2)
Δm_{32}^2	$(-2.56 \pm 0.04) \times 10^{-3} eV^2$ (Inverted Order)
Δm_{32}^2	$(2.51 \pm 0.05) \times 10^{-3} eV^2$ (Normal Order)
$\sin^2\theta_{13}$	2.12 ± 0.08

Table 4.2: Latest neutrino oscillation parameters [56].

Chapter 5

Electron Attenuation (Electron Lifetime)

In this chapter, we discuss about the MicroBooNE purification system, event samples, reconstruction, event selection, analysis method, impact of space charge effects, comparison between data and simulation, location dependence of liquid argon purity, systematic uncertainties, results and, future plans. The text in this chapter follows closely the MicroBooNE public note^[1], which I co-authored.

5.1 Introduction

One of the important operational requirements of a LArTPC is to keep electronegative impurities such as oxygen and water at extremely low concentrations. These contaminants¹ capture the drifting ionization electrons (signal) and thereby reduce the size of the recorded TPC signals. This can affect both energy measurements and track reconstruction, particularly for events far from the anode wires. The electron lifetime is inversely proportional

¹Another impurity of concern is nitrogen (N_2), which can quench as well as absorb the scintillation light produced in neutrino-argon interactions. The concentration of N_2 is required to be less than 2 parts per million (ppm). But, liquid argon cannot be efficiently purified for N_2 , hence the required low contamination level for N_2 has to come from the manufacturer. Note that even multi-ppm levels of nitrogen do not affect the ionization charge.

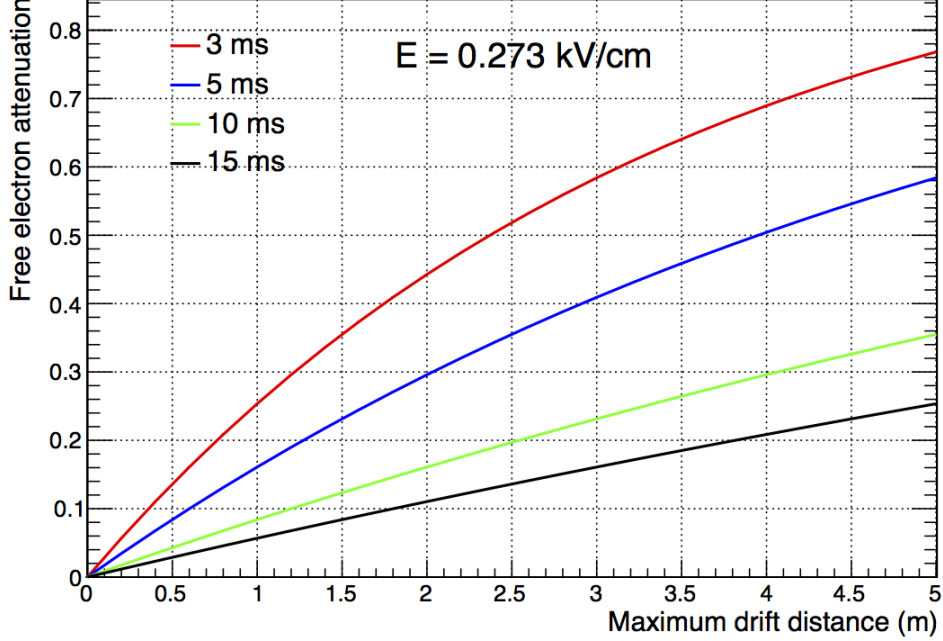


Figure 5.1: Drift electron attenuation as a function of maximum drift path (in m) for an electric field of $\sim 0.273 \text{ kV/cm}$ ^[1]. The colored curves correspond to different values of the detector parameter, electron drift-lifetime (τ). In 100% pure liquid argon, electrons will drift forever resulting in infinite lifetime.

to the impurity concentration^{[85][86]} and hence provides a direct measurement of the liquid argon impurity content. As an example, Figure 5.1 shows the drift-electron attenuation as a function of maximum drift path for a uniform electric field of 0.273 kV/cm and a drift velocity of 114 cm/ms for different electron drift-lifetimes. To achieve less than 36% signal loss for a drift distance of 2.56 m (equivalent to a 5-ms lifetime in an electric field of 0.273 kV/cm), the O_2 equivalent contamination is required to be as low as 60 parts per trillion (ppt). Similarly, to achieve a signal loss of less than 20% (or a lifetime of 10 ms at 0.273 kV/cm), the O_2 equivalent concentration is required to be less than 30 ppt. Commercial liquid argon typically contains parts per million (ppm) oxygen concentration levels. Liquid argon can also become contaminated inside the cryostat due to the out-gassing of the warm walls, cables, and other TPC components present in the gaseous argon volume. Additionally, virtual leaks (such as from the parts located close to the feedthroughs) can also become a constant source of impurities. The desired purity is therefore achieved using

a continuous liquid-argon recirculation system and dedicated filters to remove oxygen and water.

In general, the level of purity inside a liquid argon volume can be measured in four ways:

- Using gas analyzers^[87].
- Using purity monitors^{[87] [88]}.
- Using laser tracks^[89].
- Using long minimum-ionizing cosmic-ray muon tracks^[90].

This note will only discuss the measurement of liquid argon purity using cosmic-ray muon tracks in the MicroBooNE detector. As MicroBooNE is located only a few meters below the surface, a large flux of cosmic-ray muons enter the detector volume. Using long tracks from minimum ionizing particles such as cosmic ray muons to determine the drift-electron lifetime, has several advantages over the other techniques. For example, the use of purity monitors has practical advantages in terms of speed of measurement and the ability to measure low electron drift-lifetimes before tracks can be reconstructed. The technique of using tracks has the statistical and systematic advantage that one can use the charge information over the full range of electron drift-times on each track to measure the electron drift-lifetime thereby allowing for internal consistency checks and the measurement of long electron drift-lifetimes. If there is indeed a variation of the electron drift-lifetime over the cryostat volume, the tracks (if they are distributed uniformly) will give an appropriate average value for electron drift-lifetime while a purity monitor gives the value in one location. Tracks also have the potentially important systematic advantage that one is measuring the effect of the contaminants at the relevant electric field while the purity monitor typically measures the effect of the contaminants at a lower electric field. In fields above about 200 V/cm, the drift-field increases the speed of the drift electrons and this can lead to a different electron capture cross section on the contaminants for the purity monitor and the drift-electrons in the TPC.

5.2 MicroBooNE Purification System

The purification of liquid argon in MicroBooNE is achieved by two pairs of filters with each pair consisting of two filter vessels, one for filtering water and the other for oxygen. The water filter vessels are filled with 4\AA molecular sieves supplied by Sigma-Aldrich^[91]. The oxygen filter vessels are filled with BASF CU-0226 S, a dispersed copper oxide impregnated on a high surface area alumina^[92]. The MicroBooNE argon recirculation system is designed to extract argon in two places and sent back into the cryostat from a single port. Liquid argon is extracted from the bottom upstream end of the cryostat whereas the gaseous argon from the very top of the cryostat is condensed and extracted from the cryostat. Argon from both of these paths is sent to the purification system. The clean argon that enters the cryostat from the top downstream end is brought to the bottom of the cryostat via a pipe that lies within the cryostat.

5.3 Event Samples

Cosmic-ray muon data taken between 02/16/2016 and 04/21/2016 are used for this analysis. LArSoft^[93] was used to reconstruct the data. Approximately 5000 total events per day of data-taking were processed in order to study the variation in electron lifetime on a daily basis during the time period 02/16/2016 – 04/21/2016. Data corresponding to 03/05/2016 and 03/17/2016 – 03/25/2016 are not included in the analysis due to problems in processing the data. Also, the datasets were chosen such that there is approximately 24 hour difference in time between consecutive runs. The data during the selected run period include both high- and low-purity conditions. On 03/02/2016, the liquid argon circulation pump tripped as a result of oxygen deficiency hazard (ODH) system test resulting in a drop of lifetime from 9 ms to 5 ms, according to the purity monitor data. On 03/04/2016, due to power outage from 10 a.m. to midnight, lower lifetime was recorded. During 03/29/2016 – 03/31/2016

the electron lifetime dropped due to liquid argon top-off².

Monte Carlo (MC) simulation samples were also used in this analysis for systematic error studies. All the simulation samples used in this analysis are single muons generated isotropically in the detector with start positions at the center of the TPC ($X=128.0$ cm, $Y=0.0$ cm, and $Z=518.5$ cm). The muon momentum ranges from 0 to 2.0 GeV. The muon angle with respect to the X - Z plane ranges from 0° to 180° and the angle with respect to the Y - Z plane ranges from 0° to 90° . The same reconstruction chain used in data was also used in simulation.

5.4 Reconstruction

The raw signal recorded on the wires, first passes a noise filter^[94] before hits (ionization signals) are extracted from the observed waveforms on each wire. Reconstructed hits that are connected in space and time are then grouped into clusters. Clusters are merged between planes based on temporal and spatial information in order to create three-dimensional reconstructed objects (tracks and showers). The calorimetric reconstruction^{[95][96]} of tracks starts by converting the hit amplitude (in units of ADC counts) to charge (in units of electrons) using an electronics calibration factor. In the next step, a correction is made for ionization charge loss along the drift due to electronegative impurities in liquid argon. This measured charge dQ is then normalized for the track pitch length dx to obtain the charge deposited per unit track length dQ/dx . Finally, dQ/dx is converted to energy released per unit track length dE/dx by accounting for ionization charge loss due to argon-ion recombination process using the modified-box model^[96].

Figure 5.2 shows example distributions of the average number of cosmic-ray tracks per event (Left) and corresponding 3-D reconstructed track length distributions (Right) using a cosmic-ray data sample before any event selection is applied. On an average, about 15 cosmic-ray muons enter the TPC active volume per recorded event (Figure 5.2 (Left)).

²The gas analyzers^[87] constantly draw a small amount of gas from the cryostat so periodically argon gas is sent from the dewar to the condenser to maintain argon levels in the cryostat. This procedure is called liquid argon top-off.

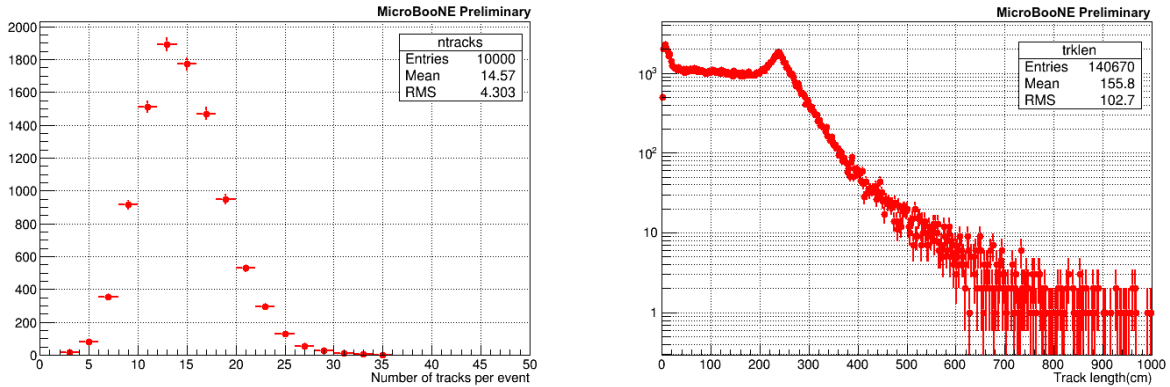


Figure 5.2: (Left) Distribution of the number of reconstructed tracks per event (for full read-out window) using a cosmic-ray data sample containing 10,000 cosmic-ray events (data runs 5411 and 5600)^[1]. (Right) 3D reconstructed track length distribution of all the tracks in the data sample^[1].

5.4.1 Reconstructing the Arrival Times of Cosmic-Ray Tracks

Since hits are treated independently from tracks in this analysis, we need to know how far the electrons associated with each hit drifted before arriving at the collection-plane. This is equivalent to knowing t_0 , the time that the muon traversed the chamber. One can extract the t_0 information by associating reconstructed TPC objects with the corresponding scintillation light objects recorded in the system of PMTs. At the time of this analysis, the light reconstruction of PMT data in MicroBooNE is not reliable for t_0 extraction. Here we use cosmic-ray muon tracks that cross both anode and cathode instead which does not require PMT information. For these crossing tracks, t_0 is associated with the minimum hit X (drift) coordinate. As one might expect, crossing tracks are rare with only about three tracks in a 100 event sample.

5.5 Event Selection

A series of selection cuts as listed below are applied to data to select a crossing track cosmic-muon sample.

- Require that the track length projected onto the X (drift) direction is be-

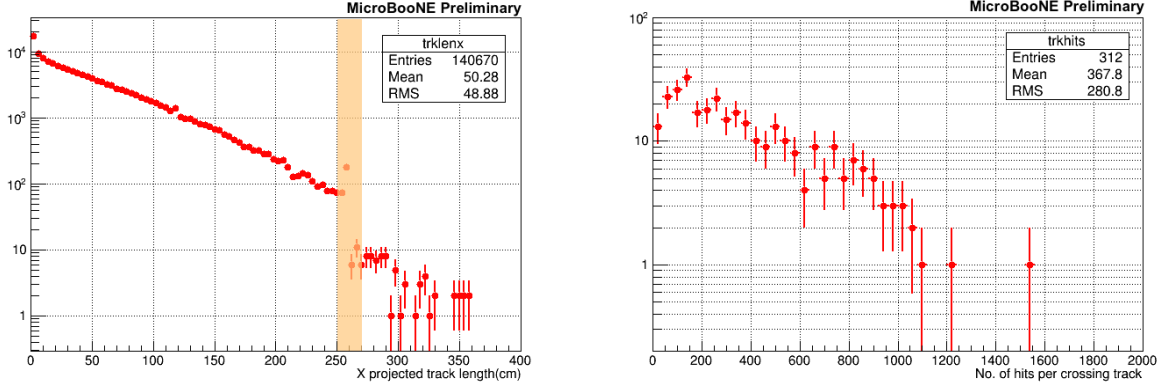


Figure 5.3: (Left) Distribution of the X -projected track length using 10,000 events from cosmic-ray data (runs 5411 and 5600)^[1]. The highlighted band shows the region used to select anode-cathode crossing tracks. (Right) Distribution of number of hits per crossing track for the sample used in the left plot^[1].

tween 250 cm and 270 cm. Crossing tracks are expected to have a sharp peak at 256 cm. A spread of a few centimeters around this value is observed in the data. The spread is likely due to spatial distortions caused by space charge effects^[97]. Figure 5.3 (Left) shows an example track length distribution in the drift direction using a cosmic-ray data sample containing 10,000 events. The highlighted region shows the selected crossing track band.

- **Exclude tracks with $75^\circ < \theta_{XZ} < 105^\circ$ and $85^\circ < \theta_{YZ} < 95^\circ$.** θ_{XZ} is the angle with respect to the X - Z plane and is defined as the inverse of the tangent of the ratio of track start in X and Z directions where track start represents the vertex direction. θ_{YZ} is the angle with respect to the Y - Z plane and is defined as the inverse of the tangent of the ratio of track start in Y and Z directions. Figure 5.4 shows an illustration of these angles in the MicroBooNE coordinate system. The θ_{XZ} (θ_{YZ}) cut eliminates tracks that are nearly perpendicular (parallel) to the collection plane wires. These tracks are difficult to reconstruct, and thus lower the quality of calorimetric reconstruction. Figure 5.5 shows dQ/dx of hits as a function of θ_{XZ} and θ_{YZ} angles before any angular cuts are applied.

- **Require that each selected crossing track contains at least 100 hits in the**

collection plane. This ensures uniform density of hits along the drift direction. Figure 5.3 (Right) shows an example distribution of number of hits per crossing track before any selection cuts using a cosmic-ray data sample containing 10,000 events. Table 5.1 shows the effect of each applied cut listed so far on track statistics using a cosmic-ray data sample of 50,000 events.

- **Exclude TPC regions associated with shorted channels.** Require that the hit Z and Y coordinates are in a region of the TPC that does not correspond to shorted channels^[94]: $(250 < Z < 675)$ cm and $(-100 < Y < 20)$ cm. In the other regions of the TPC, the collection plane response is altered due to shorted channels affecting the dQ/dx reconstruction. Since we know that the regions of modified response are not yet being properly reconstructed, we chose to exclude them from the analysis. Initial observations showed that this cut improves the dQ/dx reconstruction near the anode. Note that in the case of simulation, one usually does not require this cut as shorted channels are not implemented in MC simulation. However, we apply this cut for simulation samples with space charge and recombination simulation since space charge effect is a 3D effect and will result in position dependence.

We fit to the Landau peak of the hit dQ/dx distribution to extract dQ/dx relative to the MIP value in a given drift bin (see Section 5.6 for more details on the analysis method). Therefore, no explicit cuts are required to remove high-charge hits such as those produced by delta rays.

5.6 Extracting Charge Dependency from Drift Time

All collection plane hits associated with the tracks passing the selection are used. Each track-hit X position is corrected for the track t_0 . The resulting dQ/dx on the collection plane wires for all tracks is plotted as a function of (corrected) drift time as shown in Figure 5.6 (Left). The dQ/dx distribution is then split into 22 drift time bins of 100 μ s size each (full drift time 2200 μ s). In each drift time bin, a Landau convolved with Gaussian

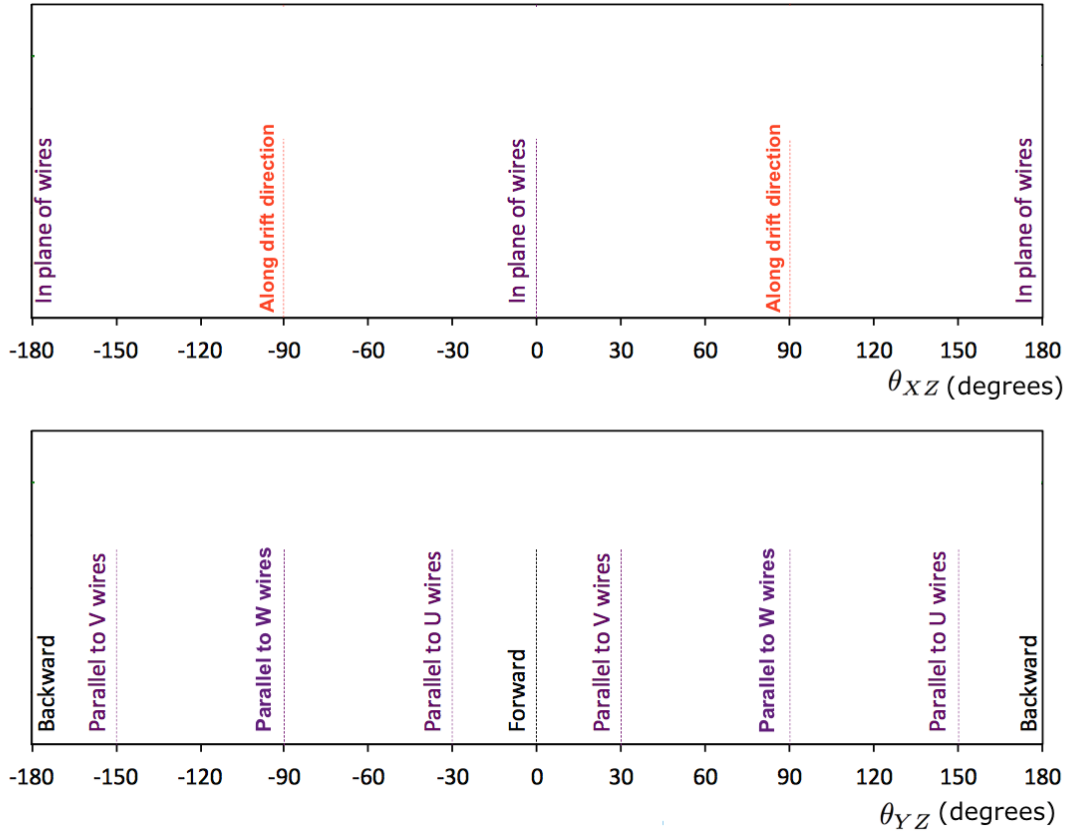


Figure 5.4: (Top) Definition of various θ_{XZ} angles^[1]. (Bottom) Definition of various θ_{YZ} angles^[1].

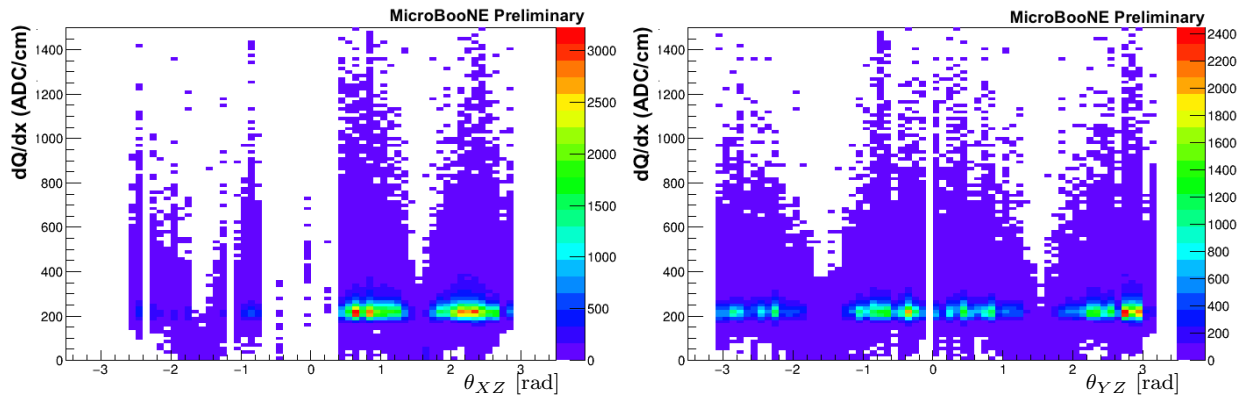


Figure 5.5: (Left) dQ/dx distribution as a function of angles θ_{XZ} ^[1]. (Right) dQ/dx distribution as a function of θ_{YZ} ^[1]. Plots are generated using crossing tracks before applying any angular cuts. Data set consists of 20,000 cosmic-ray events.

Applied cut	Number of tracks left	Percentage drop (%)
No cut	731093	
Crossing track	1652	99.8
Reject tracks with: $75^\circ < \text{abs}(\theta_{XZ}) < 105^\circ$, or $85^\circ < \text{abs}(\theta_{YZ}) < 95^\circ$	1180	28.6
Number of track hits > 100	1142	3.2

Table 5.1: Impact of each applied cut on the track statistics for a cosmic-ray data sample consisting of 50,000 events^[1].

function is fitted to the dQ/dx distribution (see Figure 5.7). The Landau function describes the signal charge distribution while the Gaussian function accounts for the effect of the electronics noise of the read-out system. Note that since the goal is to extract the peak value of the distribution, the fit range is restricted to the peak regions by scanning forward and backward in bin number from the most probable value (MPV) bin until the value of the bin (number of hits) has fallen below some threshold typically 50% of the MPV. This technique improves accuracy and ensures that we are selecting more MIP-like signals. The χ^2/ndf value of the Landau convolved Gaussian fit is required to be less than 5 to eliminate poor quality fits. After applying this criterion, the MPV of the fitted distribution in each bin is extracted and plotted as a function of average drift time (in μs) as shown in Figure 5.6 (Right). The amount of charge arriving at the anode (Q_A) after a drift time t_{drift} to that leaving the cathode (Q_C) can be extracted by fitting an appropriate functional form to this distribution. Q_C (Q_A) is extracted by substituting $t=0$ ($t=2.2$ ms) in the functional form. For an exponential functional form, the ratio of Q_A/Q_C can be interpreted as an electron lifetime (τ) using the relation,

$$\frac{Q_A}{Q_C} = \exp(-t_{\text{drift}}/\tau) \quad (5.1)$$

For non-exponential functional forms (exponential plus constant or polynomial of order 2 fits were used for some datasets), one cannot interpret Q_A/Q_C as an electron lifetime. For the example dataset shown in Figure 5.6 (Right) the positive slope in the plot shows that

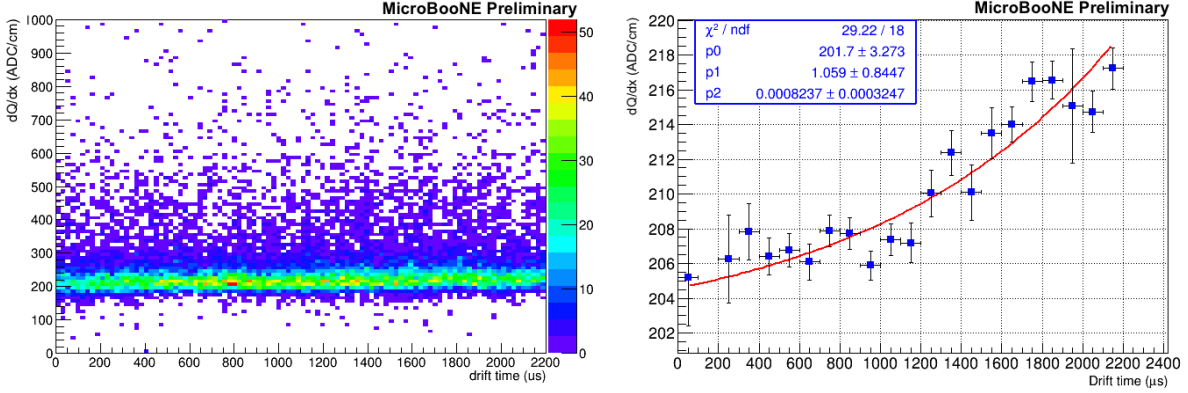


Figure 5.6: (Left) dQ/dx vs drift time scatter plot for Run 5411 using the event selection described in Section 5.5^[1]. (Right) The most probable value for dQ/dx extracted from Landau convolved Gaussian fits to each drift bin (see Figure 5.7) plotted as a function of drift time^[1]. In the example shown, an exponential plus constant function is used to fit the points.

there is more charge observed for longer drift times than at shorter drift times while one would expect more attenuation at longer drift times. This unexpected behavior resulting in $Q_A/Q_C > 1$, is observed for a majority of the runs analyzed. It is interesting to note that the LongBo experiment^[98] has also observed a similar scenario. A number of quantities were explored to understand this unexpected scenario. Among them, the most convincing explanation is provided by space charge.

5.6.1 Space Charge in Liquid Argon

Space charge^[97] refers to the build-up of slow-moving positive ions in the detector primarily due to ionization from cosmic rays leading to a distortion of the electric field (both in direction and magnitude) resulting in distortions in the reconstructed position of ionization electron clusters detected by the TPC wire planes. We will refer to this as *spatial SCE* where *SCE* stands for space charge effect. The presence of space charge also modifies the electron-ion recombination which is a function of electric field. We will refer to this as *recombination SCE*.

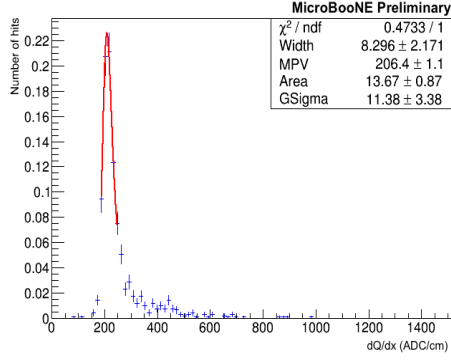
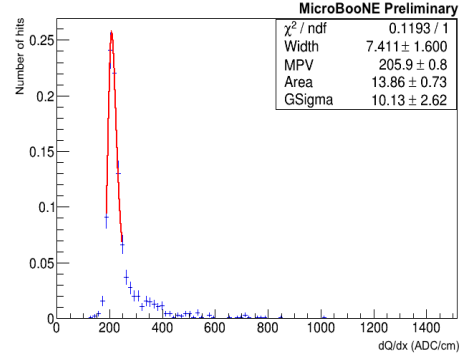
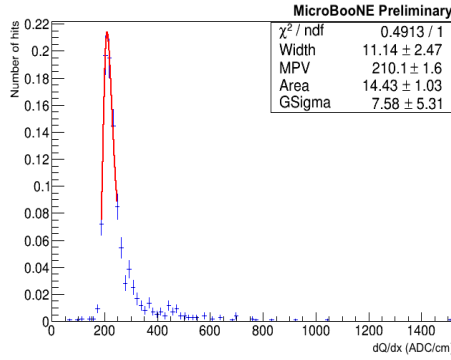
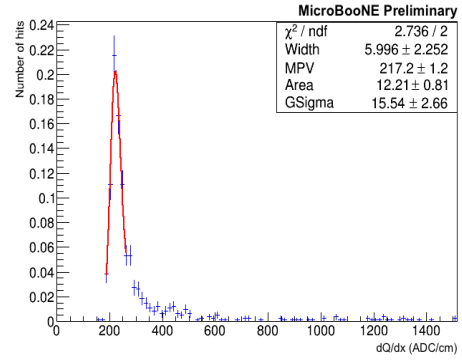
(a) $400 \mu\text{s} < \text{drift time} < 500 \mu\text{s}$ (b) $900 \mu\text{s} < \text{drift time} < 1000 \mu\text{s}$ (c) $1400 \mu\text{s} < \text{drift time} < 1500 \mu\text{s}$ (d) $2100 \mu\text{s} < \text{drift time} < 2200 \mu\text{s}$

Figure 5.7: Figure illustrating Landau convolved Gaussian fits to the dQ/dx distributions in four drift bins for run 5411^[1]. Fits are restricted to the peak region to extract the most probable value (MPV) more accurately and improve the χ^2/ndf of the fit.

5.6.2 Effect of Space Charge on dQ/dx

MicroBooNE is located near the Earth's surface with no overburden and the high influx of cosmic rays results in significant space charge effects^[97] leading to both spatial and recombination SCE. Because the space charge varies over the volume of the TPC, the resulting electric field varies in direction and magnitude affecting the drift trajectory and velocity. Following Reference^[97], the spatial SCE modifies the measured dQ/dx according to,

$$(dQ/dx)_{\text{measured}} = 1.15 \times (dQ/dx)_{\text{true}} \times \cos(\alpha) \quad (5.2)$$

where α is the angle of the track with respect to the wire planes. Reconstructed tracks with $\alpha=90^\circ$ (perpendicular to the wire planes) will be minimally distorted whereas tracks

with $\alpha=0^\circ$ (parallel to the wire planes) will be most distorted. As an example, if the angle with respect to the cathode (or anode plane) for crossing tracks is 45° , one would expect about 8% increase in charge near the cathode.

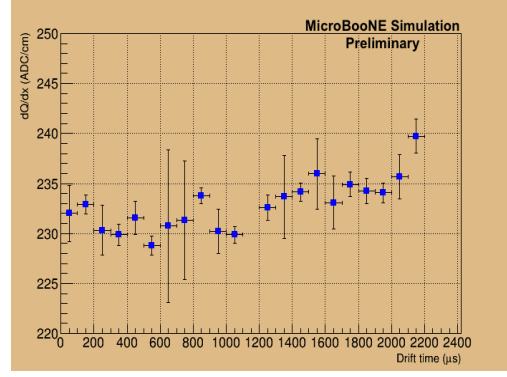
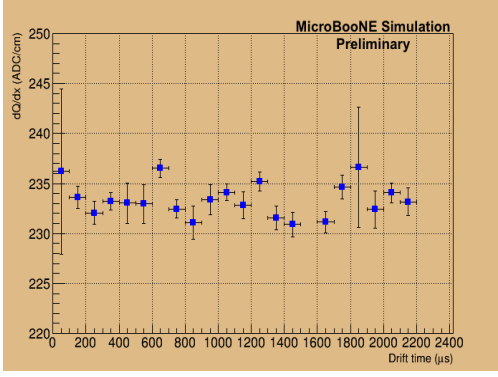
The electric-field increases by 12% at the cathode and decreases by 5% at the anode due to space charge. The electron-ion recombination is a function of electric field and following the Modified-box model^[96] is given by,

$$R_{\text{box}} = \frac{\ln\left(\alpha + \frac{\beta_p}{\rho\mathcal{E}} \cdot \frac{dE}{dx}\right)}{\frac{\beta_p}{\rho\mathcal{E}} \cdot \frac{dE}{dx}} \quad (5.3)$$

where \mathcal{E} is the electric field (0.273 kV/cm for MicroBooNE), ρ is the liquid argon density (1.38 gm/cm³ at a pressure of 18.0 psia), and parameters $\alpha=0.93\pm0.02$ and $\beta_p=0.212\pm0.002$ (kV/cm)(g/cm²)/MeV.

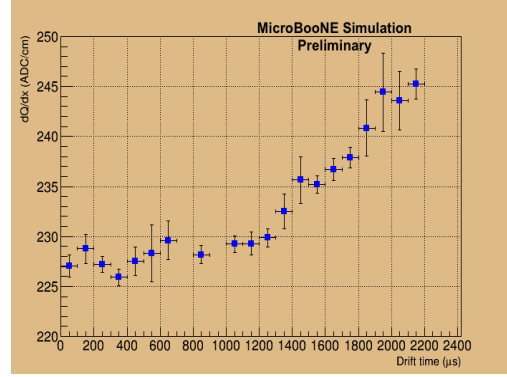
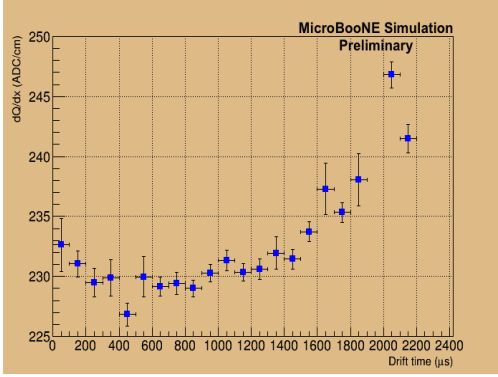
The values for α and β_p come from ArgoNeuT measurements^[96] corresponding to an electric field of 0.481 kV/cm. Recombination is suppressed at higher fields and enhanced at lower electric fields. Two commonly used models of electron-ion recombination are the Birks model and the Modified-box model^[96]. A feature of both of these models is that the recombination decreases with increasing electric field (because electrons drift faster in higher fields leaving less time to recombine). For MicroBooNE the electric field is largest at the cathode, therefore more ionization electrons present and thus a larger signal. A change in dQ/dx of -1.2% ($+3.55\%$) is expected at the anode (cathode) due to recombination SCE alone. The overall change in dQ/dx from cathode to anode is about 5%.

In order to study the unexpected $Q_A/Q_C > 1$ phenomenon in simulation, a 3D space charge model is implemented. The default recombination model used in simulation is the modified box model. In order to study effects due to space charge alone, other detector effects such as electron drift-lifetime and electron diffusion that can also produce attenuation in dQ/dx along the drift are turned off. Figure 5.8 shows the dQ/dx variation along the drift direction for isotropic single muons with and without space charge and recombination simulation. The positive slope in the plots indicates that the $Q_A/Q_C > 1$ phenomenon arises mainly from space charge effects.



(a) Spatial SCE=off, Recombination SCE=off

(b) Spatial SCE=off, Recombination SCE=on



(c) Spatial SCE=on, Recombination SCE=off

(d) Spatial SCE=on, Recombination SCE=on

Figure 5.8: dQ/dx vs drift time curves for isotropic single muons with various space charge settings in simulation^[1]. The full event selection listed in Section 5.5 is applied including the shorted channels cut. Also, the electron lifetime is set to 1000 seconds and both longitudinal and transverse diffusion coefficients are set to zero to exclude any attenuation in dQ/dx , caused by them.

5.6.3 Space Charge Corrections

In order to correct for the space charge effect, dQ/dx corrections in each drift bin (for the 22 bins used in the analysis) are extracted using simulated samples. The space charge correction C is obtained using the formula,

$$C = \frac{\left(\frac{dQ}{dx}\right)_{(SCE=on)} - \left(\frac{dQ}{dx}\right)_{(SCE=off)}}{\left(\frac{dQ}{dx}\right)_{(SCE=on)}} \quad (5.4)$$

Figure 5.8 shows the simulation samples used to extract the space charge corrections. Corrections were obtained by comparing samples (a) and (d) of Figure 5.8 where sample (d)

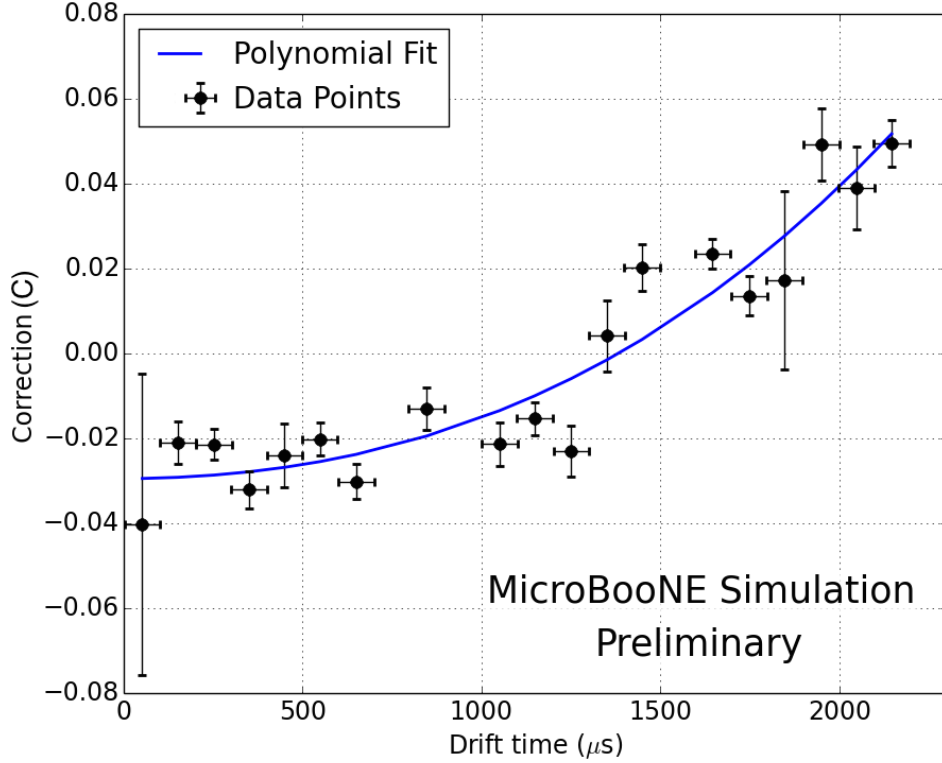


Figure 5.9: Space charge corrections with drift time fitted with a third order polynomial^[1]. Corrections C were extracted based on plots shown in Figure 5.8 and following Equation 5.4.

includes both spatial and recombination SCE. The extracted corrections C are plotted as a function of drift time (Figure 5.9) and a polynomial of order three is fitted to the distribution. The final corrections C' for each drift bin are obtained from the fitted function and are shown in Table 5.2. Uncertainties associated to the space charge effect and extracted corrections are discussed in Section 5.8.1. The space charge corrections are applied to the data using,

$$\left(\frac{dQ}{dx}\right)' = \frac{dQ}{dx}(1 - C') \quad (5.5)$$

where C' is listed in Table 5.2 and $(dQ/dx)'$ stands for space charge corrected dQ/dx . As an example, Figure 5.10 shows the individual dQ/dx vs drift time plots for six data runs before (Left) and after (Right) applying the space charge corrections. Figure 5.11 shows a comparison of the Q_A/Q_C charge ratio over the data taking period 02/16/2016 to 04/21/2016

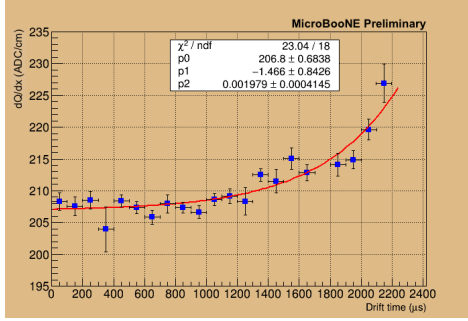
Drift bin (t)	Space Charge Correction (C') (%)
50 μs	-2.94
150 μs	-2.92
250 μs	-2.87
350 μs	-2.79
450 μs	-2.68
550 μs	-2.54
650 μs	-2.38
750 μs	-2.17
850 μs	-1.94
950 μs	-1.66
1050 μs	-1.35
1150 μs	-0.99
1250 μs	-0.59
1350 μs	-0.15
1450 μs	0.34
1550 μs	0.88
1650 μs	1.46
1750 μs	2.10
1850 μs	2.79
1950 μs	3.54
2050 μs	4.35
2150 μs	5.21

Table 5.2: Space charge dQ/dx corrections in the 22 drift bins obtained by comparing samples (a) and (d) of Figure 5.8 and using Equation 5.4^[1].

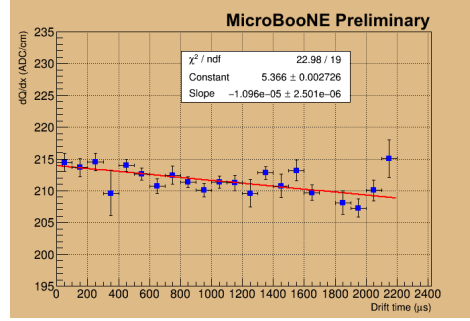
(as described in Section 5.3) with (black filled circles) and without (blue triangles) space charge corrections. After applying the corrections all of the measured Q_A/Q_C values are consistent with being 1.0 or less within statistical errors.

5.6.4 Comparison between Data and Simulation

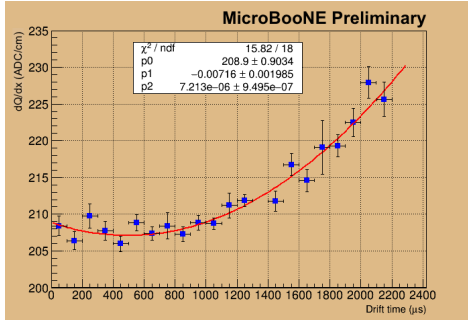
The analysis method described in the previous section is validated using isotropic single-muon samples (as described in Section 5.5). We found that for simulated electron drift-lifetimes of up to 8 ms, the extracted drift-lifetime values are within an accuracy of 1% to 2% of the input drift-lifetimes.



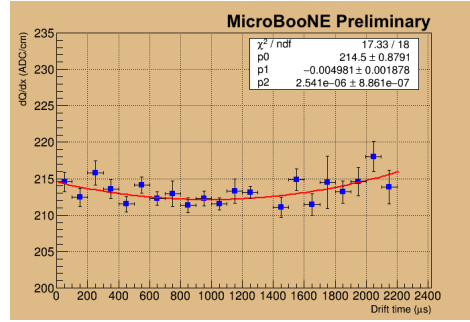
(a) 02/21/2016, day 6 (before),
Exponential plus constant fit



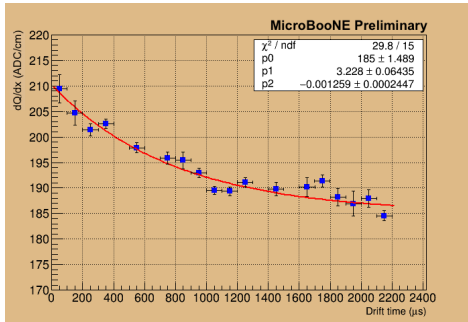
(b) 02/21/2016, day 6 (after),
Exponential fit



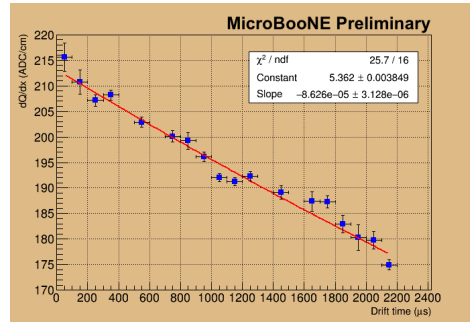
(c) 02/28/2016, day 13 (before),
Polynomial of order 2 fit



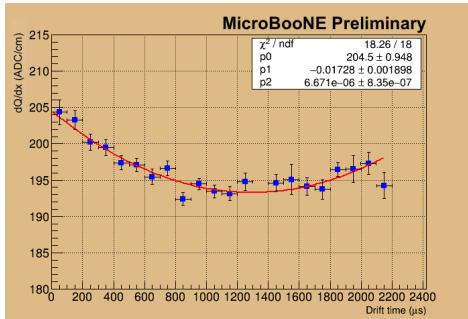
(d) 02/28/2016, day 13 (after),
Polynomial of order 2 fit



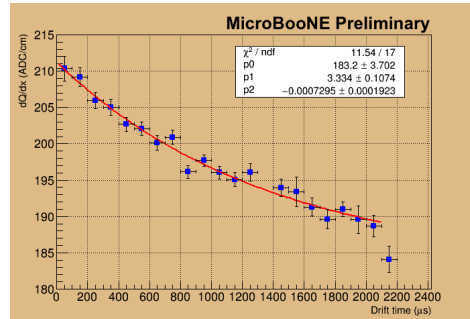
(e) 03/03/2016, day 17 (before),
Exponential plus constant fit



(f) 03/03/2016, day 17 (after),
Exponential fit



(g) 04/08/2016, day 43 (before),
Polynomial of order 2 fit



(h) 04/08/2016, day 43 (after),
Polynomial of order 2 fit

Figure 5.10: dQ/dx vs drift time plots for data before (Left) and after (Right) space charge corrections^[1].

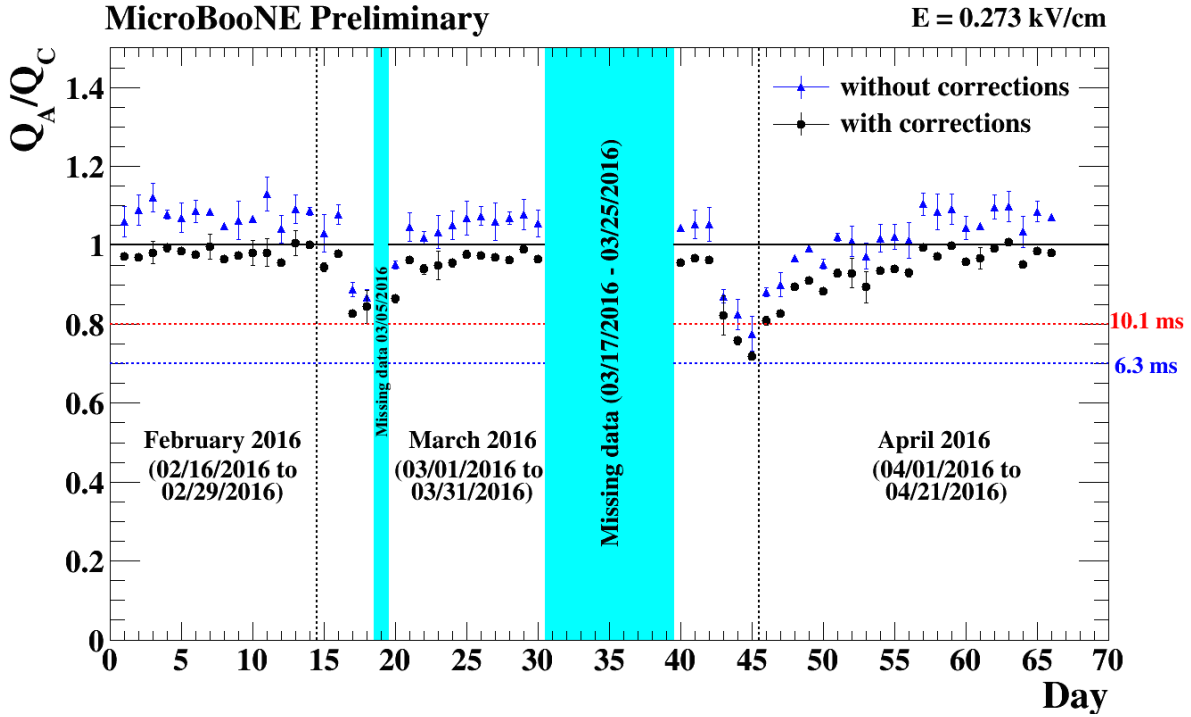
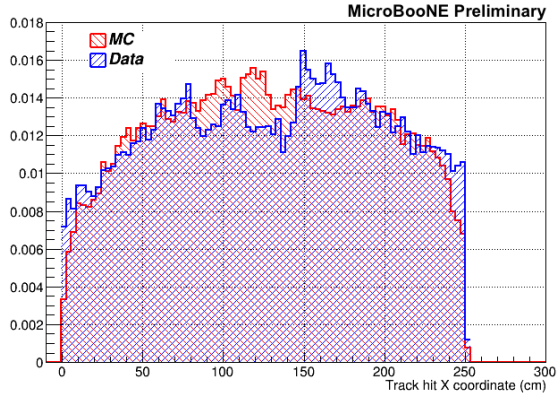
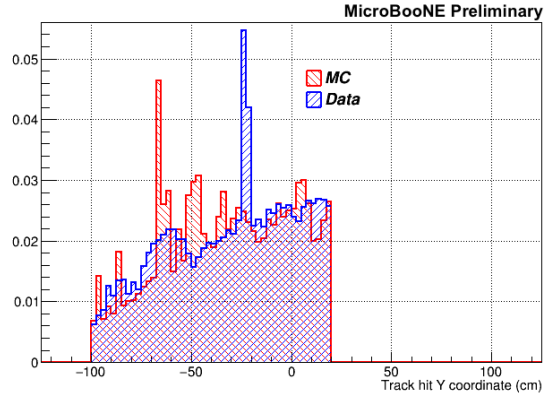


Figure 5.11: Variation of Q_A/Q_C over 56 days of data before (blue triangles) and after (black filled circles) applying space charge corrections^[1]. Error bars represent errors from the fitted function. The vertical cyan bands show missing data (see Section 5.3 for more details).

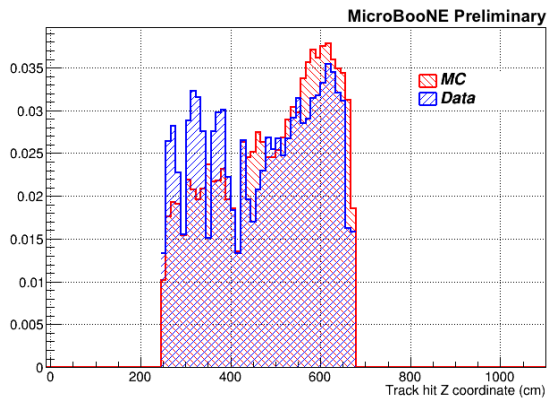
Since simulated samples are used to extract corrections (Section 5.6.3) and systematic uncertainties (Section 5.8) for the data, a comparison between data and simulation is performed. All the simulation samples used for comparison are isotropic single-muon samples (as defined in Section 5.3), which have different properties than cosmic-ray muons, for example in terms of number of tracks per event and track angular distributions. However, since hits are treated independently from tracks in this analysis, a comparison at the hit level shows that we are sampling the same coordinate space as data. Figure 5.12 shows the hit X , Y , and Z position comparison between data and simulation for all tracks with the shorted channels cut. All distributions are normalized to unity. For data, run 5910 is used with the full event selection applied. In the case of simulation, a single-muon isotropic sample is used with a electron drift-lifetime value of 1000 seconds. Simulated tracks with a minimum X projected length of 200 cm are used in the analysis along with all other selection cuts as data. Figure 5.12 shows that we are sampling the same coordinate space as data.



(a) Track hit X coordinate



(b) Track hit Y coordinate



(c) Track hit Z coordinate

Figure 5.12: Comparison of track hit X , Y and Z coordinates between data (run 5910) and isotropic single muons with the shorted channels cut^[1]. In the case of data, the drift (X) coordinate is corrected for t_0 . Both data and simulation are normalized to unity.

5.7 Location Dependence of Q_A/Q_C

The motivation to look for variations of Q_A/Q_C transverse to the drift direction comes mainly from the fact that such variations were observed in other experiments such as DUNE 35-ton prototype^[99] and ICARUS^[100]. The liquid argon purity was observed to vary along the vertical direction of these detectors. This observed non-uniformity mainly depends on the design of the argon recirculation system. For example, in the case of DUNE 35-ton prototype, the pump suction (where the liquid argon leaves the cryostat) was at the bottom as was the input (where the clean argon enters the cryostat). The circumstance that the

incoming argon was cold and came in at the bottom of the cryostat and that the pump suction was also low in the tank, meant that the clean argon did not circulate effectively throughout the cryostat resulting in the observed vertical dependence of electron drift-lifetime. Note that for both DUNE 35-ton prototype and ICARUS when this dependence was observed, the electron lifetime was very low around 3 ms and 2 ms respectively which made the effect more visible.

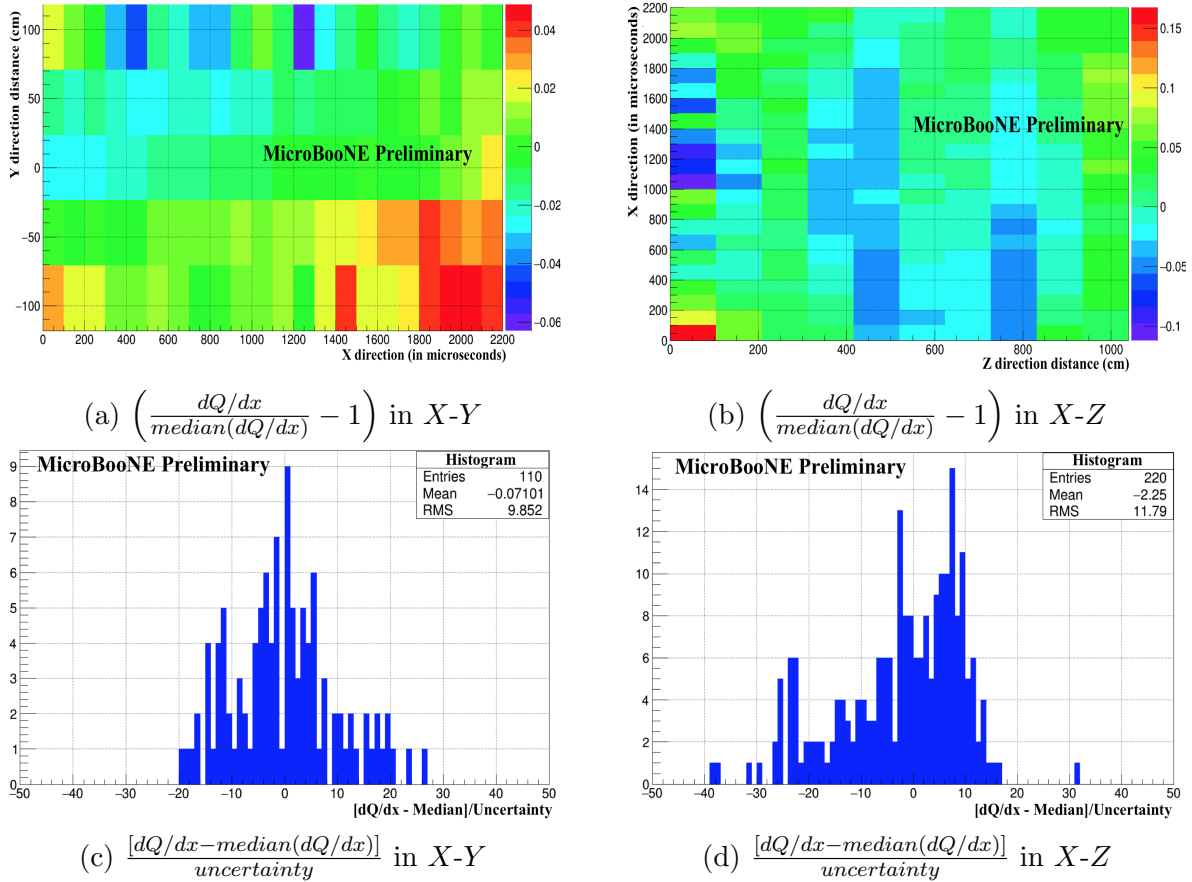


Figure 5.13: 2-D and 1-D representations of dQ/dx variation w.r.t. the median dQ/dx in top and bottom rows respectively^[1]. Plots are made using a 100,000 event sample with out the shorted channels cut.

In the case of MicroBooNE (as described in Section 5.2), the pump suction is on the upstream end about seven inches from the bottom of the cryostat and the input of clean argon is on the downstream end right at the top of the liquid level. This is a significant difference compared to the experiments mentioned earlier. Because of this, MicroBooNE need not exhibit the same effects as the other experiments.

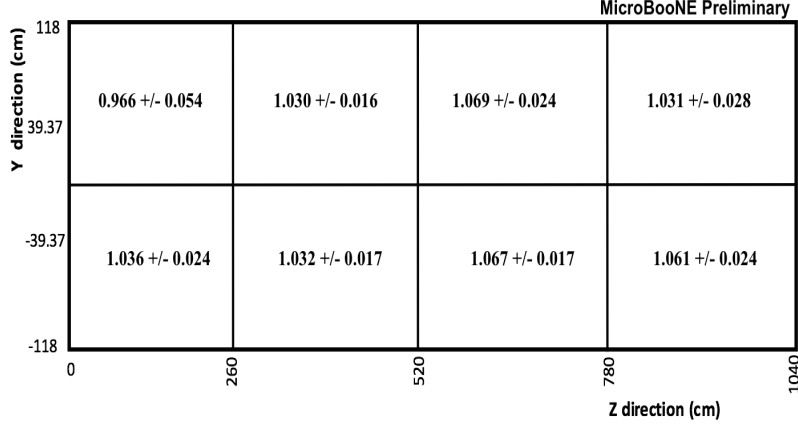


Figure 5.14: 2-D map of Q_A/Q_C for non-drift (Y and Z) directions using 100,000 cosmic-ray data events with the modified shorted channels cut but without space charge corrections^[1].

In order to estimate the location dependence of electron attenuation, a data-driven approach is used. As a first step, to illustrate how uniform our detector response is and how the combined magnitude of various effects such as space charge, recombination, lifetime, and wire-reponse uniformity affect the electron attenuation, the variation of dQ/dx across the detector is studied. The TPC is divided into ten (100 cm range) bins in the Z (beam) direction, five (50 cm range) bins in the Y (vertical) direction and twenty two drift time bins (100 μ s wide) along the X (drift) direction. In each X - Z and Y - Z bin the most probable dQ/dx value is extracted using a Landau convolved Gaussian fit (same as the method described in Section 5.6). This analysis was performed without the shorted channels cut to study the dQ/dx variation throughout the TPC. Figure 5.13 (Top Row) shows the dQ/dx variation with respect to the median dQ/dx in X - Y (Left) and X - Z (Right) coordinate space. Figure 5.13 (Bottom Row) shows the 1-D representations of the quantity shown in the top row for X - Y (Left) and X - Z (Right) coordinate space. From these plots, one can see that the dQ/dx varies by about 2% to 3% in the Y direction and about 2% to 5% in the Z direction.

To estimate the location dependence uncertainty, a 2-D Q_A/Q_C map in Y - Z is created by dividing the TPC into four bins, each with 260 cm range along the Z direction and two bins, each with 118 cm range along the Y direction. This binning is coarser compared to the binning used for studying the dQ/dx variation across the TPC (Figure 5.13). This is needed to obtain statistically adequate samples in each TPC sub-region. As we gain more

statistics, a more finer binning can be used. In extracting the Q_A/Q_C values in each TPC bin, a 10 cm fiducial cut from all TPC boundaries is applied along with a modified version of the shorted channels cut as follows (note that these cuts are different from the shorted channel cuts described in Section 5.5):

- Exclude *Shorted U* channel region: $Z < 400$ cm and $Y > [-120+Z/\tan(\pi/3)]$ cm and $Y < [20+Z/\tan(\pi/3)]$ cm.
- Exclude *Shorted W* channel region: 690 cm $< Z < 750$ cm.
- Exclude *Misconfigured U* channel region: $Z > 800$ cm and $Y < [-117+(Z-800)/\tan(\pi/3.0)]$ cm.

Using this along with the event selection and analysis method described in Sections 5.5 and 5.6, Q_A/Q_C values are obtained in each TPC bin as shown in Figure 5.14. Note that the extracted Q_A/Q_C values are not corrected for space charge effect in order to minimize the impact of the large errors associated with the space charge corrections. Also, space charge effect is expected to be similar in the selected TPC sub-regions by the symmetry of the detector. The RMS spread of the Q_A/Q_C distribution from the 8 TPC sub-regions is calculated to be 3.3%. In order to ensure that the observed variation in Q_A/Q_C for various regions of the TPC is not arising from statistical fluctuations, a fit to the hypothesis that the Q_A/Q_C values are consistent with a common average is performed. This test yielded a χ^2/ndf of 1.15 with $\text{ndf}=7$ and $(Q_A/Q_C)_{\text{average}} = 1.04$. This shows that there is no evidence of location dependence of Q_A/Q_C in MicroBooNE and hence is not included in our final results.

5.8 Systematic Uncertainties

A number of sources of systematic uncertainties are explored and presented here. While the list presented here may not be complete, we believe the most important systematics are addressed. Both data-driven and simulation based techniques are used to extract systematics

such as those coming from space charge corrections, recombination model and, diffusion. A brief summary of other sytematics not studied for this analysis that might effect dQ/dx but are expected to be small is presented in Section 5.10.

5.8.1 Space Charge Correction

The space charge correction is the single largest correction to the Q_A/Q_C ratio in this analysis. These preliminary corrections are extracted from the space charge models implemented^[97] in the simulation that are currently only valid for the central region of the TPC. To account for this, we conservatively assign a large uncertainty associated to this correction by comparing the Q_A/Q_C values before and after the space charge correction and taking 50% of their difference as systematic uncertainty. This is done for all 56 datasets used in the analysis. The resulting systematic uncertainty on each of the Q_A/Q_C value is listed in Table 5.3. The uncertainty associated to space charge corrections ranges from 1.4% to 7.5% with an average uncertainty around 4.6%. This may be reduced after space charge models are fully constrained.

5.8.2 Recombination Model

In the current default modified box model for recombination, the recombination effect is given by Equation 5.3. In order to account for recombination model systematic uncertainties, α and β_p in Equation 5.3 are maximally varied by 0.1 and 0.01 (kV/cm)(g/cm²)/MeV respectively. Two single-muon isotropic simulation samples were generated accordingly with only recombination SCE. Other effects such as electron drift-lifetime and electron diffusion that can alter dQ/dx were not included.

Figure 5.15 shows the dQ/dx variation with drift time. The red points are the result of using the default modified box model for recombination and the blue points using the same model but with changed parameters to estimate the systematic uncertainty. The full event selection (including the shorted channels cut) and analysis method described in Sections 5.5 and 5.6 are applied. Using an exponential plus constant (polynomial of second order) fit to

Day(s)	Q_A/Q_C after space charge correction	Space charge correction uncertainty	Space charge correction uncertainty (%)
1	0.972	0.044	4.5
2	0.969	0.060	6.2
3	0.981	0.069	7.1
4	0.994	0.042	4.2
5	0.985	0.042	4.3
6	0.976	0.055	5.6
7	0.997	0.044	4.4
8	0.964	0.042	4.4
9	0.974	0.045	4.6
10	0.980	0.043	4.4
11	0.981	0.074	7.5
12	0.956	0.043	4.4
13	1.006	0.043	4.3
14	1.000	0.043	4.3
15	0.944	0.043	4.6
16	0.978	0.050	5.1
17	0.827	0.031	3.7
18	0.844	0.012	1.4
19	0.865	0.043	5.0
20	0.963	0.042	4.3
21	0.939	0.040	4.3
22	0.949	0.042	4.4
23	0.955	0.048	5.0
24	0.977	0.047	4.8
25	0.973	0.051	5.2
26	0.970	0.045	4.6
27	0.962	0.054	5.6
28	0.989	0.045	4.5
29	0.965	0.045	4.7
30	0.955	0.044	4.6
31	0.967	0.043	4.4
32	0.962	0.045	4.7
33	0.823	0.024	2.9
34	0.758	0.034	4.4
35	0.719	0.029	4.0
36	0.808	0.037	4.5
37	0.827	0.037	4.4
38	0.894	0.037	4.1
39	0.911	0.040	4.4
40	0.884	0.034	3.8
41	0.929	0.046	5.0
42	0.929	0.041	4.4
43	0.894	0.039	4.4
44	0.936	0.041	4.3
45	0.939	0.041	4.4
46	0.930	0.041	4.4
47	0.995	0.055	5.5
48	0.972	0.057	5.8
49	0.999	0.047	4.7
50	0.958	0.043	4.5
51	0.967	0.041	4.2
52	0.993	0.052	5.2
53	1.008	0.045	4.5
54	0.952	0.041	4.3
55	0.985	0.050	5.1
56	0.980	0.046	4.6

Table 5.3: Systematic uncertainties for space charge corrections on the Q_A/Q_C values for all 56 datasets^[1].

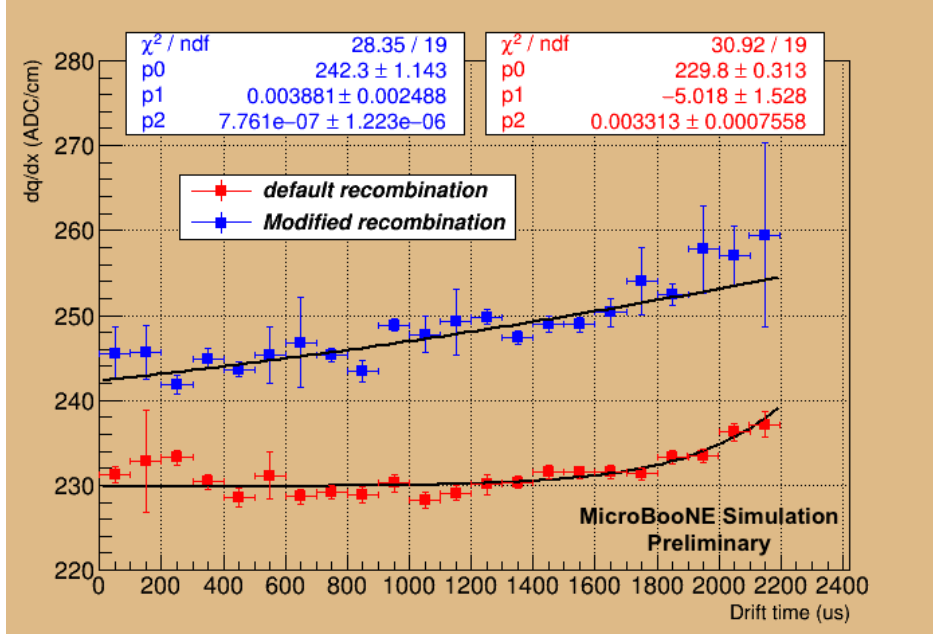
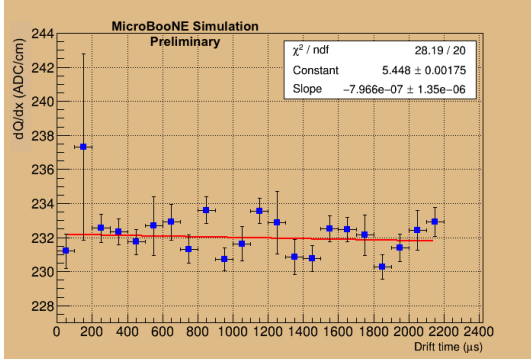


Figure 5.15: Variation in dQ/dx with drift time for isotropic single muons. The red points are the result of using the default modified box recombination model and the blue points using the same model but with changed parameters. An exponential plus constant (polynomial of second order) fit to the default (modified) model is used^[1].

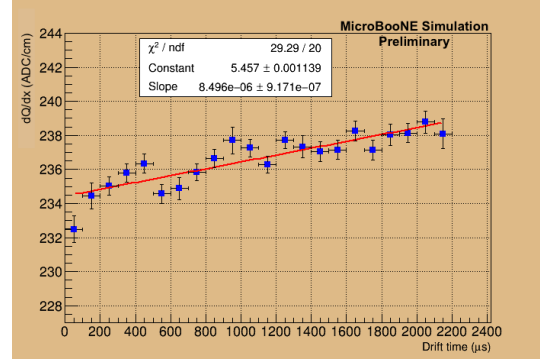
the default (modified) model as shown in the figure Q_A/Q_C values are extracted for both cases. Although a shift in the dQ/dx values was observed between the two models, the overall variation of dQ/dx from cathode to anode based on the fit is small. A Q_A/Q_C value of 1.042 ± 0.032 for the default model and 1.052 ± 0.039 for the varied parameter model are calculated. The difference between the two values w.r.t. the default model value is 1.0% and is taken as the systematic error on recombination in our final result.

5.8.3 Diffusion

Diffusion, especially transverse diffusion that is perpendicular to the drift direction can smear the charge distribution arriving at the anode to neighboring wires and affect the collected dQ/dx . In order to understand the effect of both longitudinal (along the drift direction) and transverse diffusion on electron attenuation, simulation samples with varied diffusion parameters are generated. Also, the effects from lifetime, space charge and, recombination are turned off in order to study the effect solely coming from diffusion. Figure 5.16 shows



(a) TD=off, LD=off



(b) TD=on, LD=on

Figure 5.16: dQ/dx vs drift time distribution for isotropic single muons with (Right) and without (Left) diffusion^[1]. The electron lifetime is set to 1000 seconds and the space charge and recombination effects are turned off. The full event selection described in Section 5.5 is applied except for the shorted channels cut. TD here refers to transverse diffusion with a nominal value of $16.2 \text{ cm}^2/\text{sec}$. LD here refers to longitudinal diffusion with a nominal value of $6.2 \text{ cm}^2/\text{sec}$.

the dQ/dx vs drift time curves with (Right) and without (Left) diffusion. Diffusion (mainly transverse component) modifies the lifetime in the same direction as does the space charge, but the effect is smaller. The Q_A/Q_C value is 0.998 ± 0.005 (1.019 ± 0.004) for the sample without (with) diffusion. As an estimate of the systematic error from this effect, we use 100% of the Q_A/Q_C difference between the results with and without diffusion (2.0%).

5.8.4 Systematics Summary

A summary of the systematic uncertainties calculated in this section is shown in Table 5.4. All the systematic uncertainties are added in quadrature to calculate the total systematic uncertainty, which is then added in quadrature to the statistical errors corresponding to the space charge corrected Q_A/Q_C values (black points in Figure 5.11). These final uncertainties are applied to the space charge corrected Q_A/Q_C values to arrive at the final results.

Systematic name	Uncertainty (%)
Space charge correction	5.0
Recombination model	1.0
Diffusion	2.0
Total	5.5

Table 5.4: Summary of systematic uncertainties in percentages on the final Q_A/Q_C value^[1]. In the case of space charge correction, the average uncertainty (from Table 5.3) is quoted. The total uncertainty is calculated by adding the individual uncertainties in quadrature.

5.9 Results

Figure 5.17 shows the variation in Q_A/Q_C as a function of time with both systematic and statistical uncertainties. It can be seen that even with systematic errors, the purity of liquid argon throughout the data period considered is very high during stable purity conditions with Q_A/Q_C values ranging from 0.88 ± 0.04 to 1.01 ± 0.05 . Following Equation 5.1 and using the full drift time for our TPC (2.2 ms to drift from cathode to anode), the lowest Q_A/Q_C charge ratio (0.88 ± 0.04) observed during stable purity period results in an electron drift-lifetime of 18.0 ms. This corresponds to a charge loss of 12% crossing the entire TPC at our nominal electric field of 0.273 kV/cm and an O₂ equivalent contamination of 17 ppt. The low purity regions also show relatively high Q_A/Q_C ratios ranging from 0.72 ± 0.03 to 0.87 ± 0.04 . The lowest Q_A/Q_C ratio (0.72 ± 0.03) over the entire data period analyzed corresponds to 6.8 ms, which corresponds to a charge loss of 28% over the full drift at our nominal field and an O₂ equivalent contamination of 44 ppt.

5.10 Future Plans

There are other effects in the detector that might impact the extracted dQ/dx , which are not currently accounted for. One comes from the induced charge on a given wire from electrons drifting to nearby wires. Here, the electrons drifting to wires near the target wire, also induce charge on the target wire. However this is expected to be a small effect for the

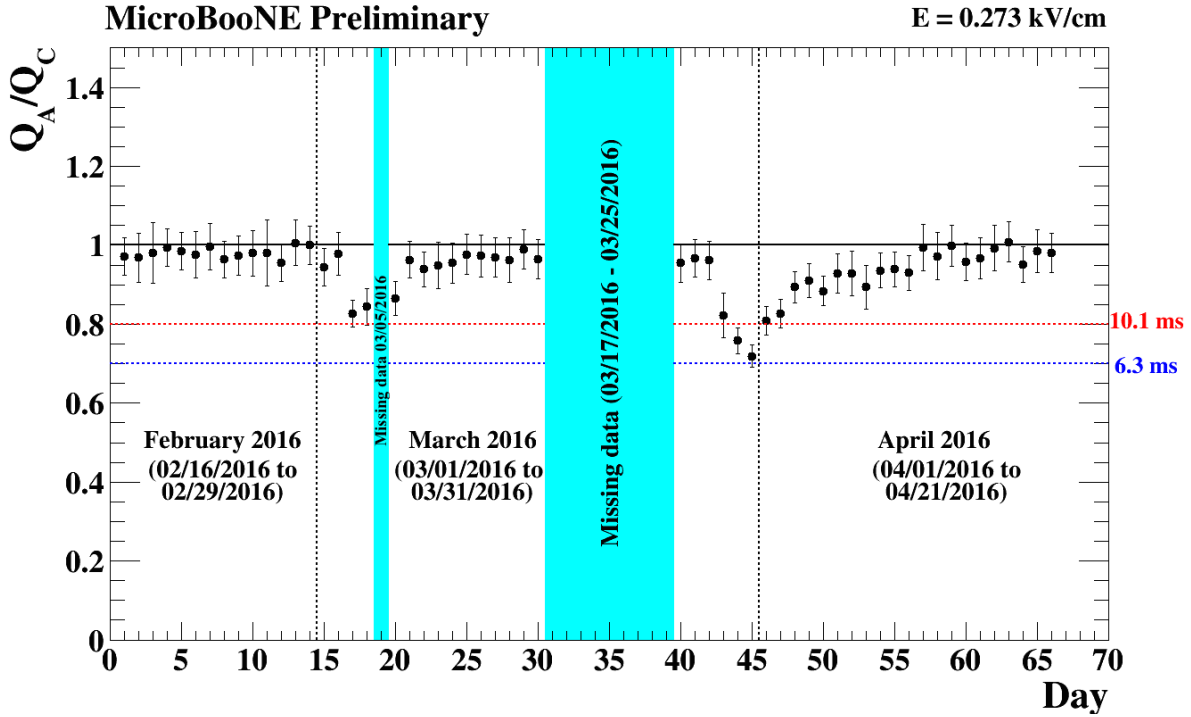


Figure 5.17: Variation in Q_A/Q_C as a function of time after space charge corrections and including both statistical and systematic uncertainties^[1]. The uncertainties are dominated by systematics and are expected to be largely correlated among all the points. The vertical cyan bands show missing data as explained in Section 5.3.

collection plane, which is what is used in the analysis. Also, the $2 \mu\text{s}$ electronics shaping time is expected to further reduce this effect. Another effect that is currently not considered for this analysis is the variation in the gain and shaping time of the electronics and how it affects the charge collection. Although a $2 \mu\text{s}$ shaping time is used in processing the signal at MicroBooNE, the actual shaping time of the electronics varies by about 2.5% across the detector. We plan to incorporate these in a future iteration of the analysis.

Another concern is that the space charge, recombination and, diffusion corrections and, related uncertainties are extracted from models implemented in simulation. In the case of recombination and diffusion, the effect is expected to be small as demonstrated in Sections 5.8.2 and 6.2.5 respectively. In the case of space charge as discussed in Section 5.6.2, the effects modeled in simulation correspond to the central Y/Z region of the TPC where the effects are expected to be maximal. Hence one can consider the modeled effects as the worst case

scenario. MicroBooNE is anticipating results on space charge, recombination and, diffusion measurements using TPC information in the near future and we plan to incorporate them in a future iteration of this analysis. Furthermore, a complete calibration of the space charge effect throughout the entire active TPC volume by utilizing a recently installed larger cosmic ray tagger system and/or a UV laser calibration system^{[8][101]} is planned for the future.

5.11 Summary and Conclusions

We report first measurements of liquid-argon purity in MicroBooNE expressed in terms of the ratio of collected charge to deposited charge Q_A/Q_C using cosmic-ray muons. Analysis of the runs during the time period 02/16/2016–04/21/2016 shows that the purity of liquid argon is very high with Q_A/Q_C values ranging from 0.72 ± 0.03 to 1.01 ± 0.05 . Systematic uncertainties dominate the measurement. The lowest electron drift-lifetime observed over the full data period analyzed is 6.8 ms corresponding to an O_2 equivalent contamination of 44 ppt and a charge loss of 28% at full drift and nominal electric field. During stable purity period the lowest electron drift-lifetime observed is 18.0 ms, which corresponds to a charge loss of 12% over the full drift distance at our nominal field and an O_2 equivalent contamination of 17 ppt. This is an indication that the argon purification and recirculation system of MicroBooNE is performing very well, substantially exceeding the MicroBooNE design goal of 3-ms electron drift-lifetime.

Chapter 6

Detector Calibration

In this chapter the discussion is about introduction to the detector calibration, calibrating the MicroBooNE detector, overview of dQ/dx calibration and different detector effects, temporal variations of detector response, dE/dx calibration, event selection, data sample, analysis method, results, validation of calorimetric energy reconstruction, angular dependence study, and conclusions. The text in this chapter follows closely the MicroBooNE public note^[2], which I co-authored.

6.1 Introduction

The first step of energy reconstruction in LArTPC detectors involves the extraction of charge information from the signals (waveforms) of the anode plane wires. The MicroBooNE experiment^[8] uses several signal processing techniques^{[102][103]} including noise filtering and deconvolution for charge extraction. However, the total charge extracted in this way normally does not reconstruct the total charge released from ionization due to a number of reasons. Among those reasons:

- Distortions in detector response due to misconfigured or cross-connected TPC channels^[94].
- Space charge effects^{[18][97]}.

- Electron attenuation^{[7] [1] [85] [86] [87] [88] [98]}.
- Diffusion.
- Recombination^[96].

are the most significant. So to trace back the exact amount of charge released from the original interaction, one has to correct for all of these effects starting from the dQ/dx ¹ values. Correcting the TPC signal for these effects is known as the dQ/dx calibration (relative calibration) of the detector. Once we have reliable charge information, we can calculate the exact amount of energy loss due to ionization and this process of determining energy is known as the dE/dx calibration (absolute calibration) of the detector. More details about dQ/dx and dE/dx calibration of the detector will be discussed in coming sections.

6.2 Calibrating the MicroBooNE Detector

The detector calibration applied consists of two steps. In the first step, we make the detector response to ionization charge uniform throughout the detector and in time. This process is known as the dQ/dx calibration of the detector. Once the detector response is uniform throughout the TPC and in time, calibration constant is determined to convert ionization charge per unit length dQ/dx to particle energy loss per unit length dE/dx . This process is known as the dE/dx calibration of the detector. In this analysis we focus on calibrating only the collection wire plane (plane 2) of the detector for both Monte Carlo and data. The calibration of induction planes is generally more difficult, in particular because of the large angular dependence of the detector response. New techniques are being developed to improve the reconstruction of the induction plane signals^{[102] [103]}, which will allow reliable dE/dx measurement on induction plane wires in the future. In addition, the forthcoming space charge effect calibration will address the residual angle dependence of dE/dx values on

¹Here and later in dE/dx & dQ/dx , the notation dx refers to the length of the particle track seen by a wire on a wire plane, which should not be confused with an infinitesimal distance in X (drift) direction of the TPC.

top of the improvements introduced by signal processing. The two-step calibration procedure is motivated by the similar calibration techniques developed for other calorimeters such as the MINOS detectors^[104].

6.2.1 dQ/dx Calibration

In the dQ/dx calibration step, we separate the detector non-uniformities into three categories and calibrate them in sequence:

- Detector non-uniformities in the YZ plane.
- Detector non-uniformities in the drift (X) direction.
- Variation of detector response over time.

Non-uniformities in the detector response in the YZ plane are primarily caused by misconfigured or cross-connected TPC channels, space charge effects, and transverse diffusion while the non-uniformities in the drift direction are mainly caused by electron attenuation, space charge effects (through both distortions of tracks and changes to the electric field), and longitudinal diffusion. It should be noted that the calibration scheme described here is an approximation, because effects such as space charge cannot be completely factorized in separating YZ plane and drift direction effects: for a given X value, the variations in the YZ plane are different. Ideally we should carry out this calibration by voxelizing the detector into small XYZ cubes and derive a calibration constant for each cube. But limited statistics makes this approach impractical. Moreover, spatial distortions introduced by space charge effects on track reconstruction are not addressed by this calibration scheme.

6.2.2 Misconfigured or Cross-Connected TPC Channels

There are several identified issues with the MicroBooNE electronics and wire planes that can affect the TPC response to the ionization signals. These effects include ASIC misconfiguration, which can change the gain of certain electronic channels and cross-connected or

touching wires, which can distort the electric field between wire planes. They affect roughly 10% of the channels. As a consequence, the TPC response has a dependence on the location of charge deposition in the TPC which needs to be calibrated out.

6.2.3 Space Charge Effects

Since MicroBooNE is a surface-based detector, we see many cosmic-ray induced tracks inside the detector. Because of this, there is a significant accumulation of slow-moving positive argon ions inside the detector, which is enough to distort the uniformity of the drift electric field. These distortions in the electric field inside the TPC have two significant effects:

- Distortions in the magnitude of the drift electric field.
- Distortions in the direction of the drift electric field.

When the magnitude of the electric field is distorted, the recombination of electrons and ions is affected. This recombination effect^[96] is very sensitive to the changes in the electric field. When the drift electric field is relatively low, recombination becomes dominant while at higher fields, the effect is suppressed. Moreover, space charge effects can lead to spatial distortions in the trajectories of reconstructed particle tracks and electromagnetic showers. The positive argon ions collected tend to drag ionization electrons closer to the middle of the detector: tracks that are reconstructed closer to the cathode suffer offsets in their start and end points closer to the detector edge. The space charge effects are expected to be stronger at the detector edges transverse to the drift direction. The cumulative effect of the space charge in track reconstruction leads to squeezing of the reconstructed track in transverse directions and bending towards the anode. Figure 6.1 shows how the SCE changes dQ/dx values over the entire drift distance of MicroBooNE^[1]. As seen in the right plot of the figure, the dQ/dx values closer to the cathode are much higher compared to that of the anode. The accumulation of positive ions causes the electric field closer to the cathode to be approximately 10% higher than at the anode. The higher field suppresses electron-ion recombination near the cathode. In addition, due to spatial distortions tracks reconstructed

closer to the cathode are bent and squeezed making reconstructed dx values smaller. Thus we observe a higher collected charge per unit of reconstructed length closer to the cathode.

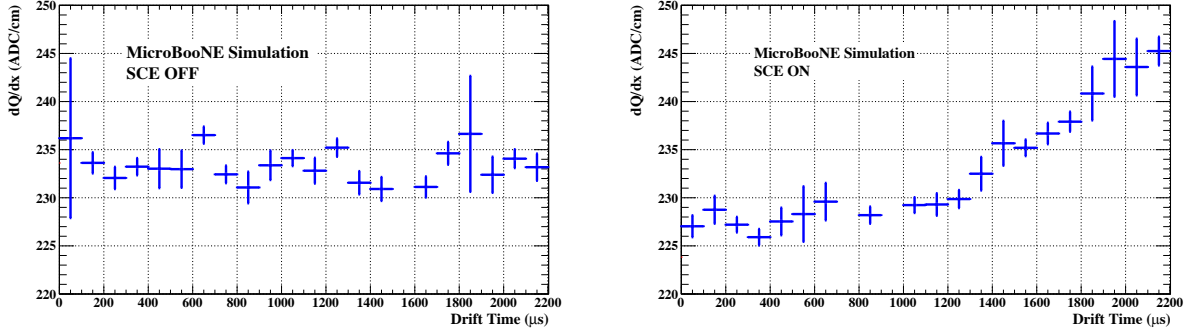


Figure 6.1: Plots of dQ/dx vs drift difference generated using Monte Carlo samples of isotropic single muons^[2]. In both of the samples diffusion is completely turned off and the electron lifetime is set very high. The plots show how dQ/dx changes over drift distance when a cloud of ionization electrons drifts from the cathode to the anode with and without space charge effects. In the left plot, space charge effects are turned off; in the right plot, space charge effects are turned on. Both plots are created using collection plane information.

6.2.4 Electron Attenuation

When a cloud of ionization electrons drifts from the cathode to the anode, electronegative contaminants such as H_2O and O_2 can capture some of the drifting electrons reducing the final dQ/dx measured at the wire planes.

Equation 6.1 governs how a cloud of ionization electrons gets depleted due to capture by electronegative contaminants as the electrons drift towards the anode.

$$\frac{n_e(t_{\text{drift}})}{n_e(t_0)} = \exp\left(\frac{-(t_{\text{drift}} - t_0)}{\tau}\right), \quad (6.1)$$

where

$n_e(t_0)$ – Initial number of electrons

$n_e(t_{\text{drift}})$ – Number of electrons after a time $t_{\text{drift}} - t_0$

τ – Electron lifetime

The electron lifetime depends on the amount of electronegative contaminants present in the medium where higher electron lifetime signals low contamination levels. Figure 6.2 shows the effect of electron attenuation on final dQ/dx values.

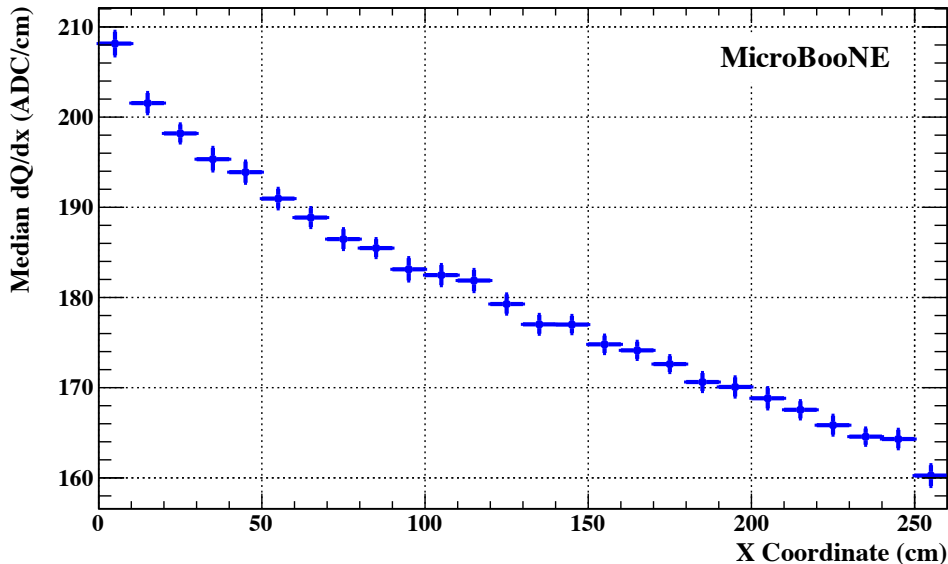


Figure 6.2: Plot of change of dQ/dx as a function of drift distance in low argon purity data run 5691 (03/31/2019)^[2]. Here median dQ/dx value is plotted for 10 cm wide bins in drift direction in the collection plane. The dQ/dx value drops from the anode to the cathode. This is due the fact that electronegative contaminants capturing ionization electrons.

6.2.5 Diffusion

The diffusion can be studied under two categories:

- Longitudinal diffusion.
- Transverse diffusion.

The cloud of ionization electrons tends to get smeared out in the direction of the drift because of the longitudinal diffusion. This could make the signal produced at longer drift distances wider and bias the reconstructed charge. On the other hand, due to transverse diffusion some of the charge can leak into the neighboring wires from the target wire. These diffusive processes can introduce a bias in reconstructing dQ/dx values.

6.2.6 Recombination

When a charged particle traverses the liquid argon, it produces both positive argon ions and ionization electrons. Some ionization electrons cannot completely liberate from their parent argon ions and recombine with parent ions to form neutral argon atoms again. This process is known as electron-ion recombination; a result of this effect is an underestimation of particle energy loss due to ionization, if no correction is made. As already mentioned in the Section 6.2.3, recombination is highly sensitive to the changes in the drift electric field.

6.2.7 Temporal Variations

The detector response can change over time because of effects such as drift of the electronics gains, changes of temperature, different running conditions, etc. Note the time referred to here is the calendar time, not to be confused with drift time in the TPC. The most significant time-dependent change affecting MicroBooNE calibrations are changes in purity.

6.2.8 dQ/dx Variation

Figure 6.3 shows the variation of detector response (dQ/dx) in YZ plane and in the drift direction X inside the TPC under the influence of various convoluted detector effects.

In the dQ/dx calibration of the detector, we aim to remove the aforementioned detector effects from the detector response. In other words, the dQ/dx calibration involves making the dQ/dx values uniform through out the detector and also in time. In this calibration process we use minimum ionizing cosmic muons as the standard candle for uniform energy deposition throughout the detector. These cosmic muons have typical momenta in the range of 4 GeV-5 GeV, and deposit ~ 1.7 MeV/cm. The dQ/dx calibration of the detector response is carried out in three separate steps:

- Calibration of the detector in the YZ plane.
- Calibration of the detector in the drift direction.

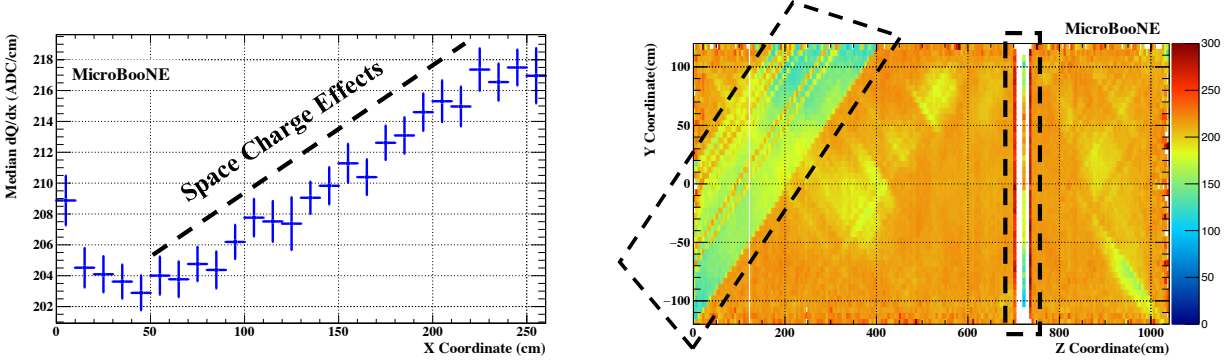


Figure 6.3: Plots of variation of dQ/dx in the drift direction (Left) and in the YZ plane (Right) in data due to various convoluted detector effects in the collection plane^[2]. In the right plot, the region inside the highlighted boundaries shows the effect of misconfigured or cross-connected TPC channels. The colors in the right plot represent the median dQ/dx value for a given $5\text{ cm} \times 5\text{ cm}$ cell in the YZ plane. Both plots are created using the collection plane information.

- Calibration of the detector in time.

Exact method used for dQ/dx calibration will be discussed in Section 6.5 in detail.

6.2.9 dE/dx Calibration

Once the detector response becomes uniform after the dQ/dx calibration, the absolute energy scale can be determined. To move from the calibrated dQ/dx to dE/dx , we use the modified box model^[96] for recombination as described in Equation 6.2.

$$\left(\frac{dE}{dx}\right)_{calibrated} = \frac{\exp\left(\frac{\left(\frac{dQ}{dx}\right)_{calibrated}}{C} \frac{\beta' W_{ion}}{\rho \mathcal{E}}\right) - \alpha}{\frac{\beta'}{\rho \mathcal{E}}}, \quad (6.2)$$

with

C – Calibration constant to convert ADC values to number of electrons

W_{ion} – 23.6×10^{-6} MeV/electron (work function of argon)

\mathcal{E} – 0.273 kV/cm (MicroBooNE drift electric field)

ρ – 1.38 g/cm^3 (liquid argon density at a pressure 18.0 psia)

β' – $0.212\text{ (kV/cm)(g/cm}^2\text{)/MeV}$

α – 0.93

The last two parameters in the Equation 6.2 were measured by the ArgoNeuT experiment^[96] at an operational electric field of 0.481 kV/cm. According to the above equation, precise determination of the calibration constant C which translates the **ADC/cm** to **number of electrons/cm** is important in determining the absolute energy scale. Here the goal of dE/dx calibration is to provide the calibration constant C . In this particular calibration scheme, we are using stopping muons as the standard candle, because they have a well-understood energy loss profile. The stopping muons could either be isolated from cosmic data or neutrino interactions. The exact method we are using for dE/dx calibration will be discussed in Section 6.5.4 in detail.

6.3 Event Selection

As described in Section 6.2, through-going cosmic muons are used for the dQ/dx calibration and stopping muons from neutrino interactions are used for the dE/dx calibration. Each muon in the selection is tagged with an initial time t_0 with respect to which the drift time is measured.

6.3.1 Selection Cuts (dQ/dx Calibration)

For the dQ/dx calibration of the detector, we chose to use the anode-cathode crossing muons. The main reason is that the anode-cathode crossing muons span over the whole drift distance, which make them the perfect sample to study any effects that depend on the drift distance. The crossing muons have a wide spatial but limited angular coverage. Figure 6.4 shows the presence of cosmic muons in our data.

The tracks used in the dQ/dx calibration should satisfy the following selection criteria.

- $250 \text{ cm} < \text{Track projected X length} < 270 \text{ cm}$: Any track that satisfies this selection cut is considered to be an anode-cathode crossing track. A 20 cm wide window is selected in order to account for imperfect reconstruction of track start and end positions.

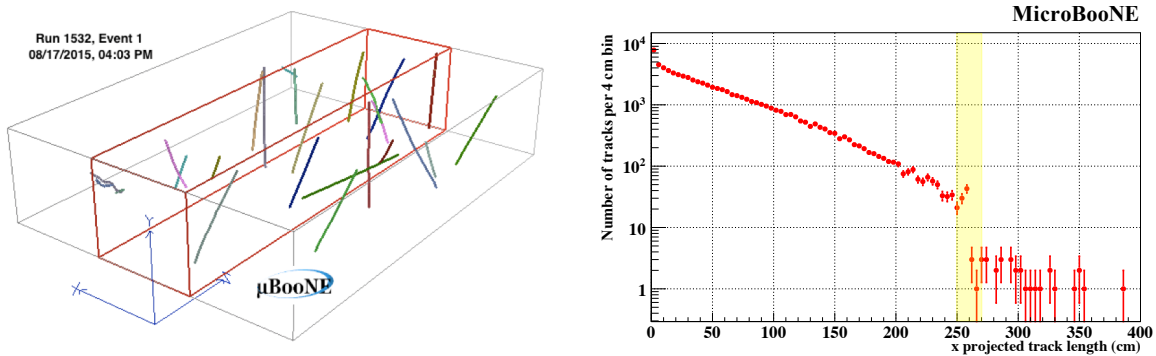


Figure 6.4: (Left) Presence of cosmic muons in MicroBooNE’s 4.8 ms wide read out window^[2]. The colored tracks are the cosmics. (Right) The color band shows the presence of anode-cathode crossing tracks in cosmic data^[2] (updated plot). It has been estimated in a ~ 5000 event cosmic data sample $\sim 0.13\%$ of the tracks are anode-cathode crossing tracks. The 20 cm window is selected to account for mis-reconstructions in track start and end points.

- Absolute value of track angle θ_{XZ} (See Figure 6.5) should not be in the region of 75° to 105° : This selection cut ensures that we are excluding the tracks, which are going into the wire planes (these tracks tend to be mis-reconstructed).
- Absolute value of track angle θ_{YZ} (See Figure 6.5) should not be in the region of 80° to 100° : This selection cut helps to remove tracks that are nearly parallel to the collection plane wires.

Figure 6.6 shows the excluded angular regions in the θ_{XZ} and θ_{YZ} space explained in the selection cuts. The difference between Monte Carlo and data in these figures is due to the fact that Monte Carlo is not simulating the effects such as SCE, field response, etc perfectly.

6.3.2 Selection Cuts (dE/dx Calibration)

In the dE/dx calibration of the detector, we employ stopping muons induced by the neutrino interactions. We use the following set of selection cuts to isolate these muons from Monte Carlo:

- $10 \text{ cm} < \text{reconstructed start (end) point X} < 250 \text{ cm}$, $-110 \text{ cm} < \text{reconstructed start(end) point Y} < 110 \text{ cm}$ and $10 \text{ cm} < \text{reconstructed start (end) point Z} < 1030$

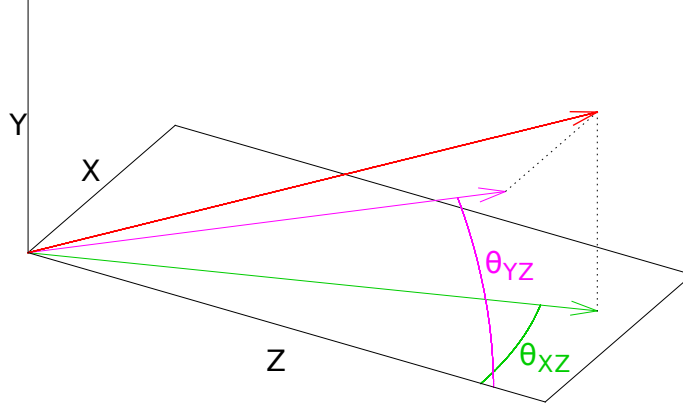


Figure 6.5: Definition of angle θ_{XZ} and θ_{YZ} ^[2].

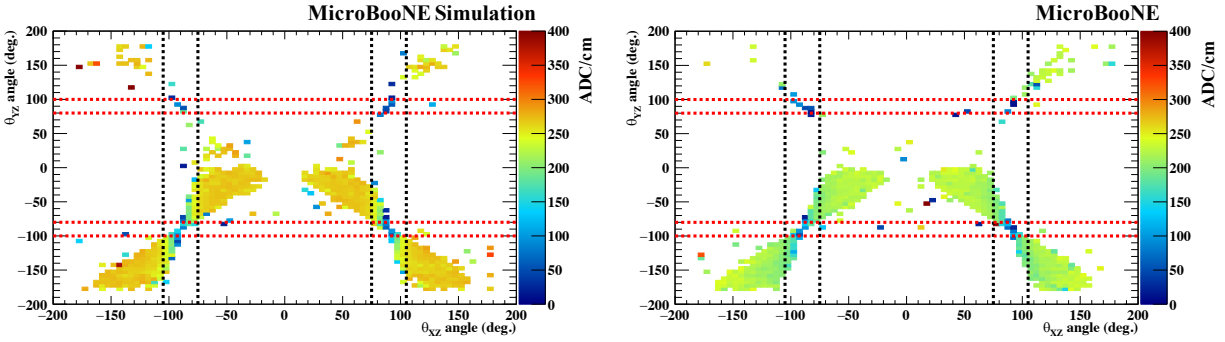


Figure 6.6: Plots of variation of average dQ/dx values in the phase space of θ_{XZ} and θ_{YZ} in the collection plane^[2]. The Z axis represents average dQ/dx for a track, which has a given θ_{XZ} and θ_{YZ} angular orientation. The units of the Z axis is in ADC/cm . The regions inside dashed lines show the angles excluded for crossing tracks discussed in Section 6.3.1 for the collection plane. (Left) Monte Carlo. (Right) Data.

cm: These selection cuts ensure that possible reconstructed muons are well contained within the TPC.

- Reconstructed track should match to a stopping muon, which comes from a neutrino interaction at truth level (this applies only to Monte Carlo).
- The distance between start (end) point of the true track and start(end) point of the reconstructed track < 5 cm: This cut further makes sure that we are getting the correct reconstructed muon track (this applies only to Monte Carlo).
- Absolute value of reconstructed track angle θ_{XZ} should not be in the region of 75° to 105° : This selection cut ensures that we are excluding the tracks which are going into

the wire planes.

- Absolute value of reconstructed track angle θ_{YZ} should not be in the region of 80° to 100° : This selection cut ensures that we are excluding the tracks, which are nearly parallel to the collection plane wires.

To isolate the stopping muons in data, the following selection criteria are applied:

- Run the CC Selection II Filter^[105] to isolate primary muons from charge current interaction.
- Use the same track containment and angular cuts as applied to the Monte Carlo sample.
- Calculate the median dQ/dx values of the track in the first and last 5 cm segments. If the ratio of the two median dQ/dx values in the last 5 cm segment and the first 5 cm segment is greater than 1.5, the track is selected as a stopping muon. This cut aims to find the Bragg peak and remove poorly reconstructed tracks. The cut value is determined from the Monte Carlo sample where well reconstructed stopping muons are selected.

6.4 Data Sample

The dQ/dx calibration of the detector is carried out using both data and Monte Carlo. For Monte Carlo, we use Corsika cosmic simulations^[106] overlaid with neutrino interactions to get the anode-cathode crossing cosmic muons while for data, we use the entire Run I data to get crossing muons. The time period of data used ranges from February to October of 2016. In both Monte Carlo and data, we use the *pandoraCosmicKalmanTrack*^[107] tracking algorithm to reconstruct particle tracks, which performs pattern recognition and a Kalman filter fit to the cosmic ray muon tracks.

The dE/dx calibration of the detector is also done for both Monte Carlo and data. For Monte Carlo, we use a cosmic overlaid neutrino sample to get stopping muons induced by the neutrino interactions where these stopping muons are reconstructed using the the

track algorithm *pandoraNu*^[107], which is optimized to reconstruct particles produced by the neutrino interactions with argon. In data, we apply the CC Selection Filter II over 5E19 run I unblinded dataset to get candidate muons from charged current interactions. A similar study was done using stopping cosmic ray muons^[108].

6.5 Analysis Method

The dQ/dx calibration of the detector is carried out in 3 separate steps for the collection plane.

- **Step 1:** Detector calibration in YZ plane - This step aims to remove the effects from space charge effects, misconfigured or cross-connected anode plane channels, and transverse diffusion.
- **Step 2:** Detector calibration in drift direction - This step aims to remove effects coming from electron attenuation, space charge effects, and longitudinal diffusion.
- **Step 3 :** Detector calibration in time - This step aims to remove any temporal variations in the detector response. This step is done only for data not for Monte Carlo since there is no time dependence in Monte Carlo simulation.

6.5.1 Detector Calibration in YZ Plane

Once we have a data sample consisting of anode-cathode crossing tracks, we use the following procedure to get the detector calibration factors in the YZ plane.

- Crossing tracks are isolated: The selection of crossing tracks is described in the Section 6.3.1.
- Filter out only the crossing tracks, which pass the angular cuts described in the Section 6.3.1.

- Starting time (t_0) of the track is calculated: For crossing muons, the minimum drift coordinate is supposed to correspond to t_0 .
- Once t_0 is known, the drift coordinate of each 3-D point of that track is corrected by the knowledge of t_0 .
- The YZ plane is segmented into 5 cm by 5 cm cells.
- Each 3-D point on a track is grouped into its relevant cell in YZ plane by looking into their Y and Z coordinates: Here we select only the points, which satisfy the conditions $0 \text{ cm} < X_{Corrected} < 260 \text{ cm}$, $-120 \text{ cm} < Y < 120 \text{ cm}$, and $0 \text{ cm} < Z < 1040 \text{ cm}$.
- Once looping over all the crossing tracks, we select only the cells, which have a population of more than five 3-D points.
- For each of the selected cells, we calculate the median dQ/dx value by considering charge information of all the 3-D points in that cell. The median dQ/dx of a given cell is called the *Local Median dQ/dx* of that cell.
- Once the local median dQ/dx values are calculated for all the cells in YZ plane, the *Global Median dQ/dx* is calculated by taking the median dQ/dx value from all the 3-D points coming from all crossing tracks.
- For each cell in YZ plane a correction factor $Corr(y, z)$ is defined using the Equation [6.3](#)

In data, we derive correction factors in YZ plane only for 3 separate time periods. Time period I is from 2016 February to 2016 May, time period II is from 2016 June to 2016 July, and time period III is from August 2016 to October 2016. The reason, we combine data for different times is due to the fact that the dominant contributor for YZ plane irregularities is from effects introduced by misconfigured or cross-connected TPC channels and these effects do not vary with time significantly. For Monte Carlo, we derived only a single set of YZ corrections for the collection plane.

$$Corr(y, z) = \frac{(dQ/dx)_{Global}}{(dQ/dx)_{Local}} \quad (6.3)$$

$(dQ/dx)_{Global}$ – Global median dQ/dx in the collection plane

$(dQ/dx)_{Local}$ – Local median dQ/dx for a given YZ plane cell in the collection plane

6.5.2 Drift Direction Calibration of the Detector

Once the calibration in YZ plane is done, we move to the drift direction calibration of the detector. The following set of points explain how this calibration procedure is carried out.

- Crossing tracks are isolated, which satisfy angular cut as explained in the procedure for YZ calibration.
- t_0 of the track is extracted and drift coordinates of all the 3-D points of the track are corrected by this t_0 .
- The charge information (dQ/dx) of each 3-D point is corrected using YZ correction factors derived in the previous step to remove the irregularities in YZ plane using the Equation 6.4. Here we select the 3-D points, which satisfy the conditions $0 \text{ cm} < X_{Corrected} < 260 \text{ cm}$, $-120 \text{ cm} < Y < 120 \text{ cm}$, and $0 \text{ cm} < Z < 1040 \text{ cm}$. Moreover, we look into the Y and Z coordinates of the 3-D points to decide as which YZ correction factor to use .
- The drift direction is segmented into 10 cm wide line segments in data and 5 cm wide line segments in Monte Carlo. The bin sizes are determined both in Monte Carlo and data so as to minimize the statistical fluctuations in correction factors.
- Each 3-D point of the tracks is grouped into the relevant drift direction line segment based on its corrected X coordinate.
- For each of the line segments in drift direction, which has more than five 3-D points, we define a local median dQ/dx as in the YZ calibration procedure.

- A global median dQ/dx is also defined as explained in the previous calibration procedure.
- Finally for each line segment in the drift direction, a correction factor $Corr(x)$ is defined using the Equation 6.5.

In data we derive drift direction correction factors daily as space charge effects and electron lifetime change significantly over time. To get a reliable set of correction factors, we need to have a data sample, which is rich in statistics. For this purpose, we derive correction factors in drift direction only for the days where there are more than 40 crossing tracks that leave hits in the collection plane after all the angular cuts. For Monte Carlo we derive only a single set of drift direction correction factors for the collection plane as there is no time variation of space charge effects and electron attenuation.

$$(dQ/dx)_{YZ_Corrected} = Corr(y, z) \cdot (dQ/dx)_{Reconstructed} \quad (6.4)$$

$(dQ/dx)_{YZ_Corrected}$ – Corrected (dQ/dx) value by $Corr(y, z)$ correction factor for irregularities in the YZ plane

$(dQ/dx)_{Reconstructed}$ – Uncorrected dQ/dx value

$$Corr(x) = \frac{(dQ/dx)'_{Global}}{(dQ/dx)'_{Local}} \quad (6.5)$$

$(dQ/dx)'_{Global}$ – Global median dQ/dx value after correcting for YZ plane irregularities by Equation 6.4 in the collection plane

$(dQ/dx)'_{Local}$ – Local dQ/dx median for the given X segment after correcting for YZ plane irregularities by Equation 6.4 in the collection plane

6.5.3 Time Dependent Calibration of the Detector

After step 1 and 2 we focus on the third step, which aims to remove any temporal variations in the detector response. The following set of steps explain how the detector calibration in

time is achieved.

- Crossing tracks, which satisfy the angular cuts are selected.
- All the 3-D points are corrected by t_0 for their drift coordinate.
- The dQ/dx value of each 3-D point is corrected using correction factors derived for YZ plane and drift direction using Equation 6.6: Only the 3-D points, which satisfy the conditions $0 \text{ cm} < X_{Corrected} < 260 \text{ cm}$, $-120 \text{ cm} < Y < 120 \text{ cm}$, and $0 \text{ cm} < Z < 1040 \text{ cm}$ are selected. Moreover, the relevant correction factor in YZ plane and drift direction for a given 3-D point is selected looking into its X,Y & Z coordinates.
- In the final step a global median dQ/dx value is defined in a way similar to step one and two. In the time calibration of the detector, we calculate this global median dQ/dx value on daily basis.
- The global median dQ/dx values are plotted against time to visualize the detector variations in time.
- By visually scanning the plots in the Figure 6.7, a reference value (210 ADC/cm) for the global median dQ/dx in the collection plane is chosen.
- A time dependent correction $Corr(t)$ is determined using the Equation 6.7 for each day: The corrections are derived for three planes separately.

$$(dQ/dx)_{XYZ_Corrected} = Corr(y, z) \cdot Corr(x) \cdot (dQ/dx)_{Reconstructed} \quad (6.6)$$

$(dQ/dx)_{XYZ_Corrected}$ – Corrected dQ/dx value for YZ plane and drift direction
irregularities in the collection plane
 $(dQ/dx)_{Reconstructed}$ – Uncorrected dQ/dx value in the collection plane

$$Corr(t) = \frac{(dQ/dx)_{Reference}}{(dQ/dx)_{Global}} \quad (6.7)$$

$(dQ/dx)_{Reference}$ – Reference dQ/dx value in the collection plane

$(dQ/dx)_{Global}$ – Global dQ/dx value in the anode wire plane after correcting for YZ plane and drift direction irregularities

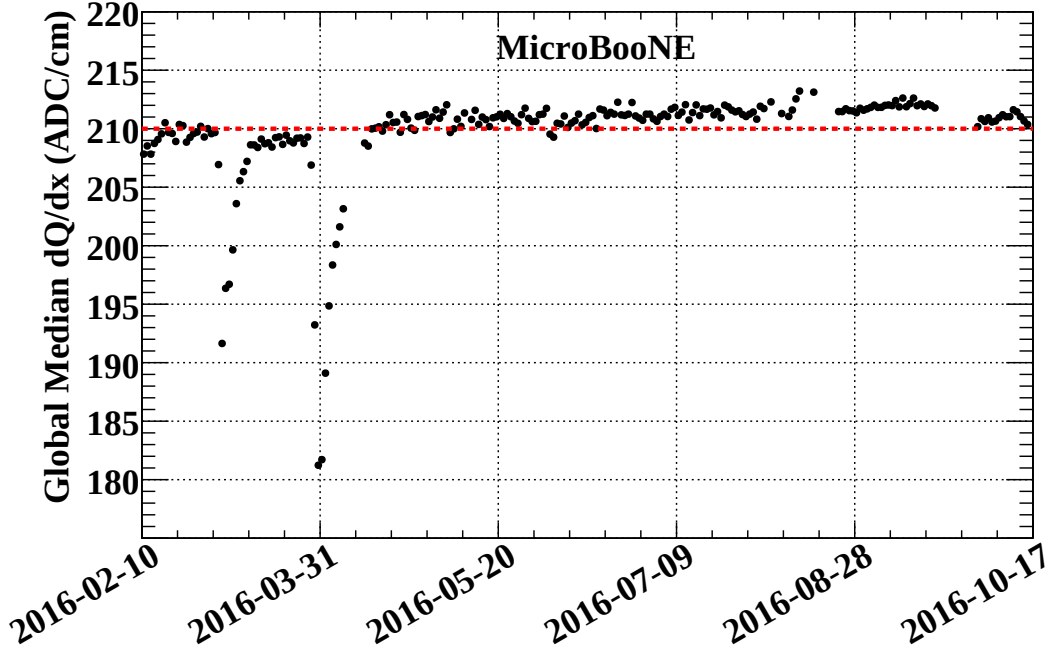


Figure 6.7: Plot of variation of the global median dQ/dx over time in the collection plane^[2]. The red lines drawn shows the reference value selected, which is 210 ADC/cm.

Once we are done with calibrating the detector in YZ plane, drift direction, and in time, we can use the Equation 6.8 and Equation 6.9 to get the calibrated dQ/dx values in data and Monte Carlo respectively.

$$(dQ/dx)_{XYZT_Corrected}^{data} = (dQ/dx)_{Reconstructed} \cdot Corr(y, z) \cdot Corr(x) \cdot Corr(t) \quad (6.8)$$

$(dQ/dx)_{XYZT_Corrected}^{data}$ – Corrected dQ/dx for YZ plane, drift direction irregularities and time variations in data in the collection plane

$(dQ/dx)_{Reconstructed}$ – Uncorrected dQ/dx in data in the collection plane

$$(dQ/dx)_{XYZ_Corrected}^{MC} = (dQ/dx)_{Reconstructed} \cdot Corr(y, z) \cdot Corr(x) \quad (6.9)$$

$(dQ/dx)_{XYZ_Corrected}^{MC}$ – Corrected dQ/dx for YZ plane and drift direction irregularities in Monte Carlo in the collection plane

$(dQ/dx)_{Reconstructed}$ – Uncorrected dQ/dx in Monte Carlo in the collection plane

6.5.4 dE/dx Calibration of the Detector

Once the dQ/dx calibration of the detector is done, we can move to get the correct particle energies. The following set of points explains the procedure, we adopt to do the dE/dx calibration both in Monte Carlo and data, which is the same method described in document^[108] except using stopping muons coming from the beam.

- Isolate the muon tracks coming from neutrino interactions, which satisfy the cuts explained in the Section 6.3.2 for the desired plane.
- The last 200 cm residual ranges of tracks are segmented into 5 cm wide bins, which leads to a total of 40 residual range bins: Here we select tracks which have a minimum track length of 150 cm.
- We loop over all the 3-D points of selected tracks and fill out the residual range bins with dE/dx values derived using the Equation 6.2 by setting the the calibration constant C to a particular value: Only the 3-D points that are inside the detector boundaries specified in the Section 6.5.1 are considered here as well. Moreover, here we consider only the 3-D points, which have a track pitch value in between 0.3 cm to 0.4 cm.
- After looping over all the tracks, we fit each of dE/dx distributions to a *Landau Convolved Gaussian* function^[109] to extract the Most Probable dE/dx Value (MPV) representing that particular residual range bin.
- We plot the MPV dE/dx values against kinetic energy of the particle: For each residual range bin, we take the middle bin value as the representative residual range value of that bin and transform that to kinetic energy using a cubic spline for the tabulated

data set in the Table 6.1. Here this reference dataset is representing the expected Kinetic energy vs Residual range profile for stopping muons in liquid argon.

- We compare the the curve generated in the previous step with the prediction made by the *Landau-Vavilov* function^[110] in the MIP region of the muons (250 MeV - 450 MeV) and χ^2 value is calculated using the Equation 6.10. The Landau-Vavilov function describes the energy loss probability distribution for a particle in a given medium. One of the striking features of this distribution is that the most probable energy loss of a particle is dependent on the thickness of the energy absorber. So here to get the predicted MPV dE/dx , we set the absorber thickness to be 0.35 cm.
- We iterate through the the same set of steps described above several times to generate tabulated set of data between a given calibration constant (C) and χ^2 value.
- In the final step, we plot the χ^2 values thus generated against calibration constants and fit that distribution with some polynomial (mostly second order) to get the calibration constant, which corresponds to the lowest χ^2 value. This method is known as the *Chi Squared Minimization*^[108] method.
- With the newly derived calibration constant (C), we calculate the dE/dx values using Equation 6.2 and using the calibrated dQ/dx values as the input.

After the dE/dx calibration, we compare the newly derived dE/dx values with uncorrected dE/dx values to see the effects of the new improvements (see Section 6.6).

$$\chi^2 = \Sigma \left(\frac{(MPV(dE/dx)_{prediction} - MPV(dE/dx)_{Measured})^2}{\sigma^2} \right) \quad (6.10)$$

Here we sum all the data points in the kinetic energy region of 250 MeV to 450 MeV.

For Monte Carlo,

$$\sigma^2 = \delta_{fit}^2 \quad (6.11)$$

where δ_{fit} is the uncertainty associated with the MPV dE/dx extracted by fitting a Landau convoluted Gaussian function to the energy distribution.

Residual range (cm)	Kinetic energy (MeV)
10	0.70437
14	1.27937
20	2.37894
30	4.72636
40	7.5788
80	22.0917
100	30.4441
140	48.2235
200	76.1461
300	123.567
400	170.845
800	353.438
1000	441.476

Table 6.1: Tabulated values of CSDA Residual range vs. Kinetic energy for stopping muons in liquid argon^[2] [111].

For data,

$$\sigma^2 = \delta_{fit}^2 + \delta_{recombination}^2 \quad (6.12)$$

where $\delta_{recombination}$ is the systematic error associated with recombination model uncertainties (here, we take the uncertainty to be 1.5% of the measured dE/dx)

Note the Monte Carlo sample was simulated and reconstructed with the same recombination model. Therefore, there is no systematic uncertainty associated with recombination model for Monte Carlo. See note^[108] for a detailed description of the above uncertainties.

6.6 Results

6.6.1 dQ/dx Calibration (Monte Carlo)

The dQ/dx calibration of the detector in Monte Carlo is done using a single large dataset described in Section 6.4. Figure 6.8 shows the variation of YZ and drift direction correction factors in the collection plane. Figure 6.9 shows the calibrated dQ/dx vs residual range for true stopping muons and stopping protons.

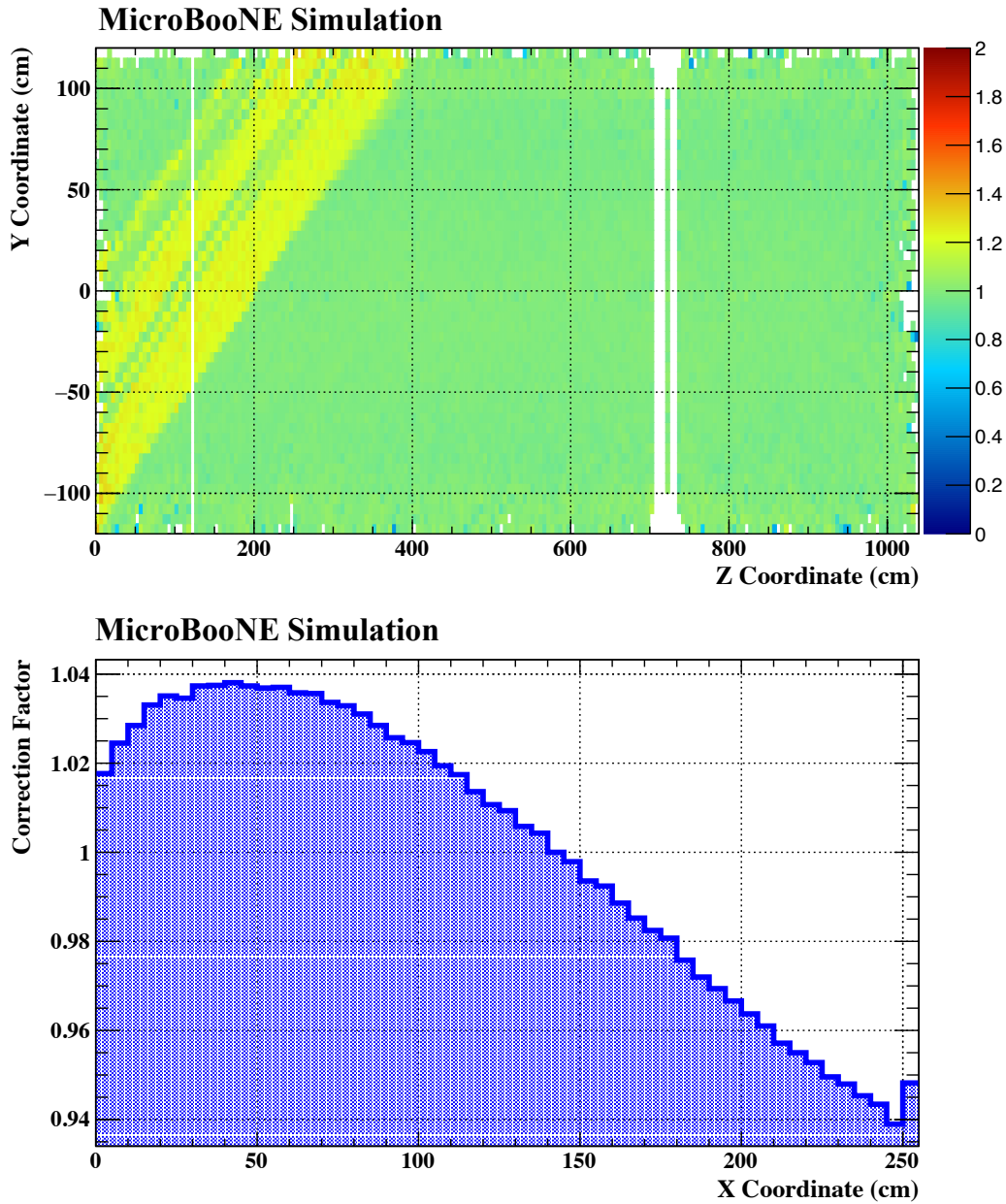


Figure 6.8: (Top) Plot of YZ correction factors in the collection plane in Monte Carlo^[2]. Here Z axis represents correction factors for a given $5\text{ cm} \times 5\text{ cm}$ cell in the YZ plane. (Bottom) Plot of drift direction correction factors in the collection plane in Monte Carlo^[2].

6.6.2 dQ/dx Calibration (Data)

YZ correction factors are derived for 3 separate data sets. In the first dataset, we have data combined between February and May; in the second one data from June and July are combined; and in the last dataset, data between August and October are combined. See

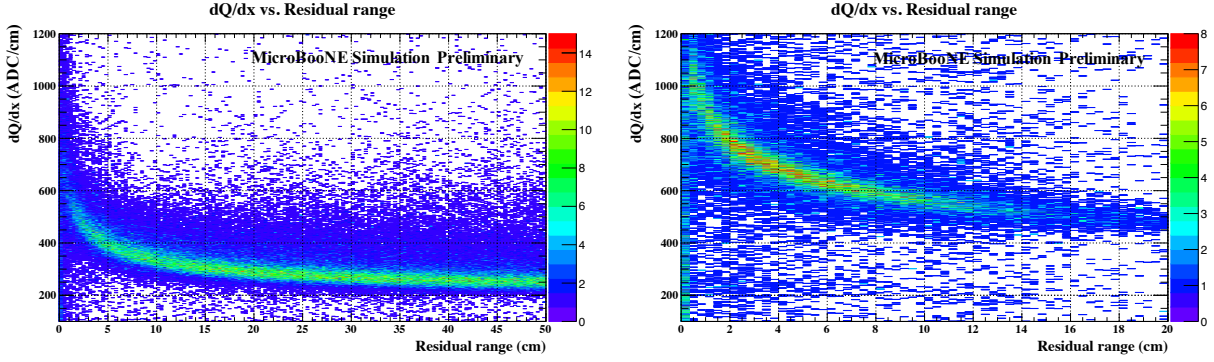


Figure 6.9: Calibrated dQ/dx vs residual range for true stopping muons^[2] (Left) and stopping protons^[2] (Right) using collection plane information.

Figure 6.10 for the variation of YZ correction factors in the collection plane for the first dataset. As there is no significant difference between YZ correction factors derived in 3 samples, only the results for the first dataset is shown here.

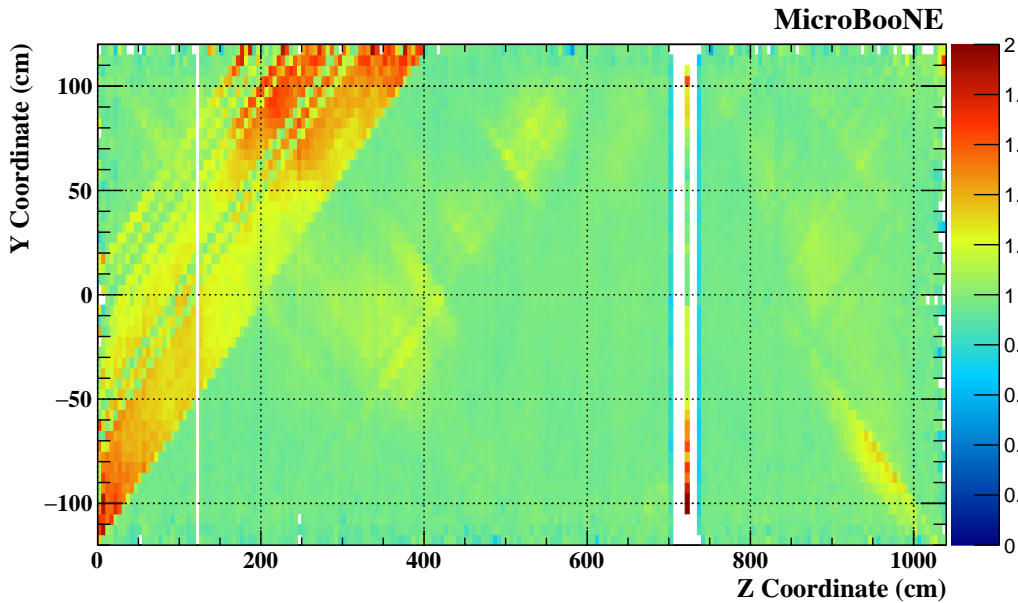


Figure 6.10: Plot of variation of YZ correction factors in the collection plane for the combined time period from February to May in 2016 in data^[2]. The Z axis represents correction factors for a given $5 \text{ cm} \times 5 \text{ cm}$ cell in the YZ plane.

The drift direction corrections factors and time corrections are derived for the time period starting from 02/10/2016 to 10/19/2016 on a daily basis. But due to lack of statistics, we are skipping some days. See Figure 6.11 for the variation of time correction over time.

Figure 6.12 shows the effect of dQ/dx calibration both in Monte Carlo and data. To create these comparison plots, anode-cathode crossing cosmic muons are used.

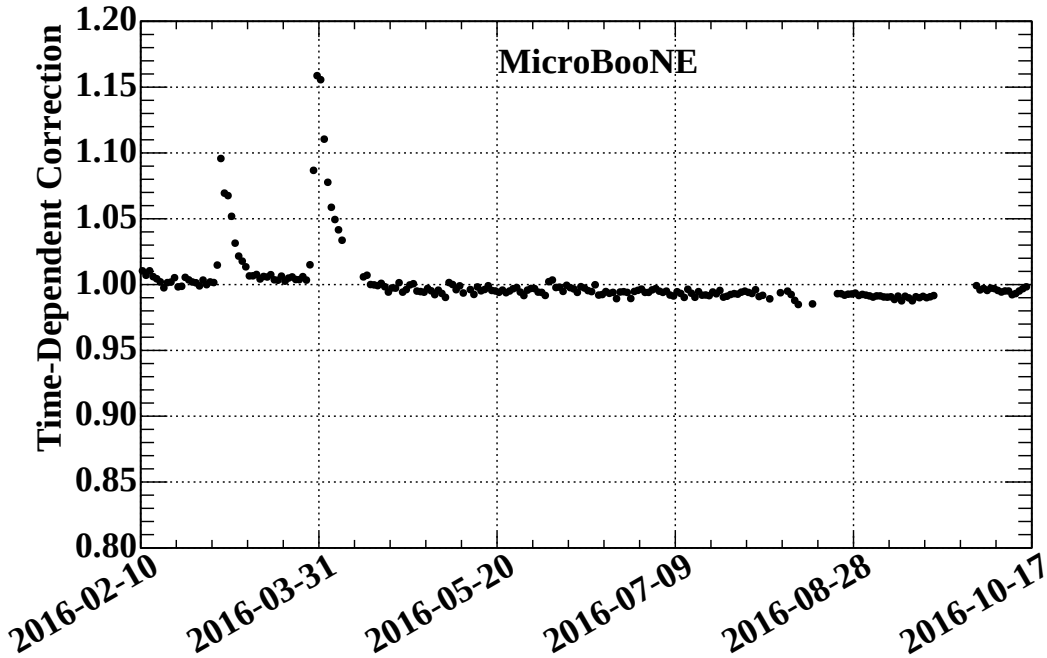


Figure 6.11: Plot of variation of the time correction $C(t)$ over time in the collection plane^[2].

6.6.3 dE/dx Calibration

The absolute calibration of the detector is done using both Monte Carlo and data. Figure 6.13 shows $\chi^2 - \chi_{Min}^2$ vs calibration constant C for the collection plane. The best fit value is the one that gives the minimal χ^2 . The uncertainty is determined by $\Delta\chi^2 = \chi^2 - \chi_{Min}^2 = 1$.

The calibration constants derived for the collection plane are shown in Table 6.2. The Monte Carlo calibration constant uncertainty is statistical only. The data calibration constant uncertainty include both the statistical uncertainty and the recombination uncertainty. Figure 6.14 shows the comparison between prediction and the measured MPV dE/dx with these calibration constants for stopping muons both in Monte Carlo and data.

Figure 6.15 shows the calibrated dE/dx vs residual range for the Monte Carlo true stopping muons and protons. The measured dE/dx profiles agree very well with the expectations.

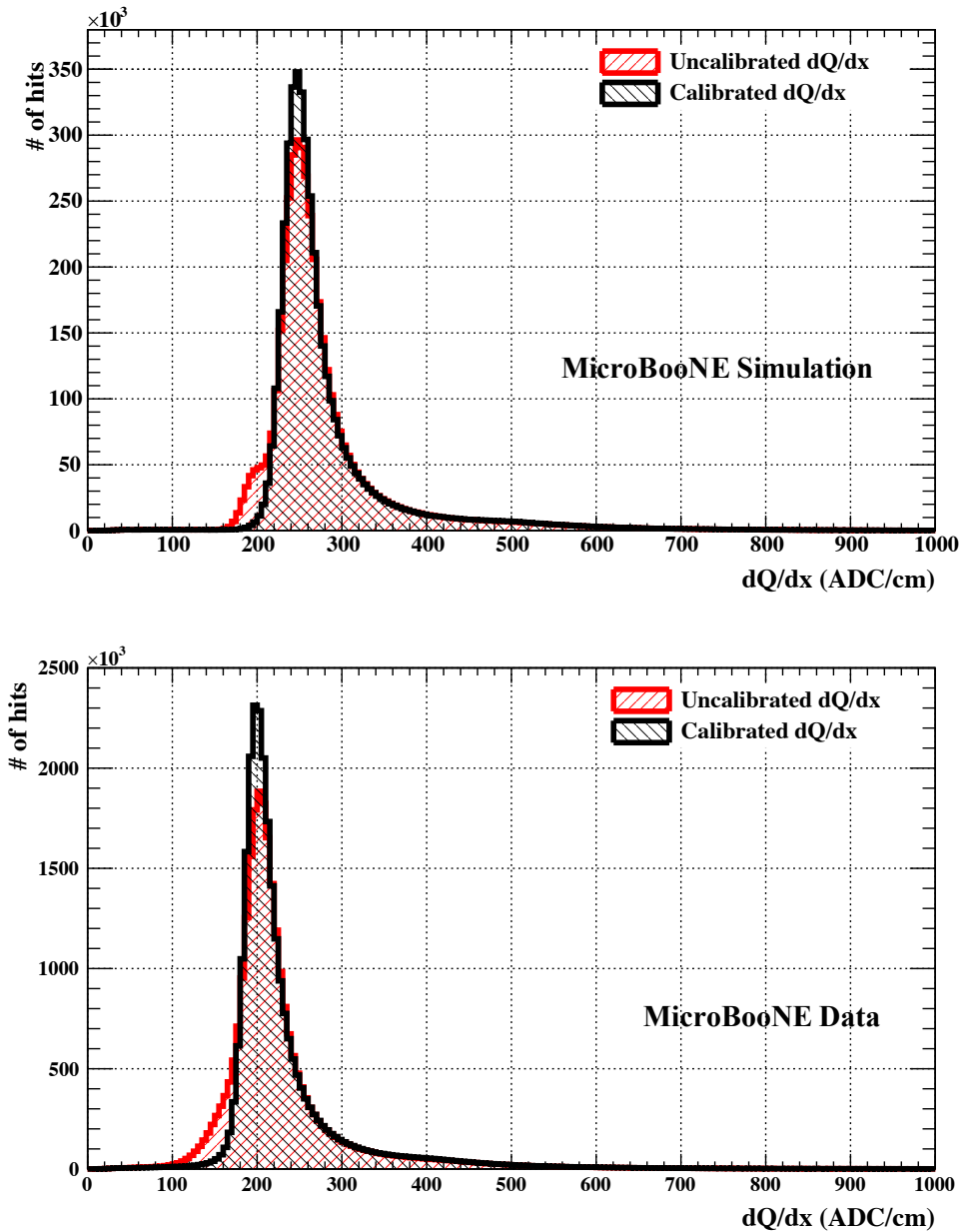


Figure 6.12: (Top) Plot of comparison of calibrated and uncalibrated dQ/dx in Monte Carlo using crossing muons in the collection plane^[2]. (Bottom) Plot of comparison of calibrated and uncalibrated dQ/dx in data using crossing muons in the collection plane^[2].

6.6.4 Validation of Calorimetric Energy Reconstruction

The absolute energy-scale calibration can be validated in a data-driven way by comparing the range-based energy to that obtained via calorimetry for selected stopping muon candidates in data and Monte Carlo. For each selected stopping muon track, the range vs calorimetric

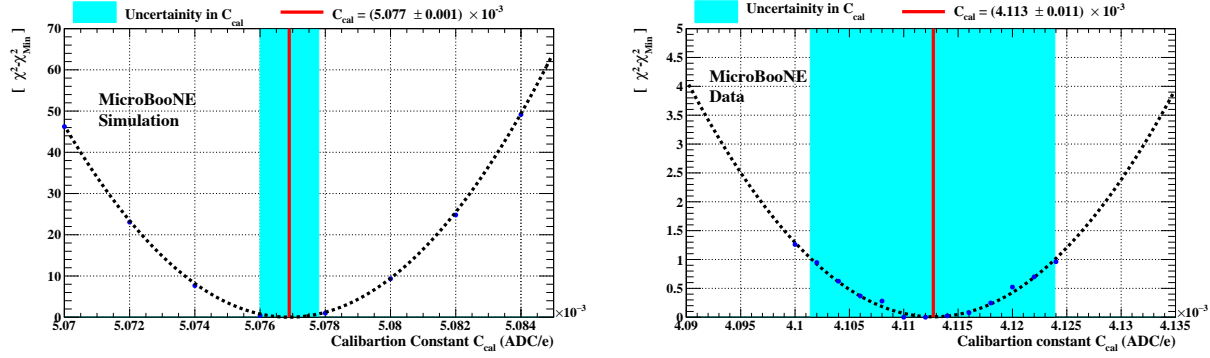


Figure 6.13: Distributions of $\chi^2 - \chi_{Min}^2$ vs calibration constant C for the collection plane^[2]. The color bands show the uncertainty associated with calibration constant C . The units of the X-axis is ADC per electron. (Left) Monte Carlo. (Right) Data.

	Monte Carlo (ADC/e)	Data (ADC/e)
Calibration Constant	$(5.076 \pm 0.001) \times 10^{-3}$	$(4.113 \pm 0.011) \times 10^{-3}$
$\chi_{Min}^2/d.o.f$	15.0/18 \sim 0.84	5.12/18 \sim 0.28

Table 6.2: Calibration constants and $\chi_{Min}^2/d.o.f$ for the collection plane in Monte Carlo and data^[2]. The units of the calibration constants are ADC per electron.

kinetic energy are computed, and the fractional difference between these methods is shown in Figure 6.16. The agreement between the two, approximately 3% (2% in Monte Carlo), gives confidence in the proper absolute energy-scale calibration to within this level of agreement, and provides a closure test for this calibration.

6.7 Angular Dependence Study

The calibration procedure described in the public note does not make any angular dependent corrections. The angular distributions of the anode-cathode crossing muons are shown in Figure 6.6. In order to study the angular dependence of the dQ/dx (relative) calibration, we divide the crossing muons into 4 angular bins:

- $0^\circ < |\theta_{xz}| < 50^\circ$
- $50^\circ < |\theta_{xz}| < 75^\circ$
- $105^\circ < |\theta_{xz}| < 130^\circ$

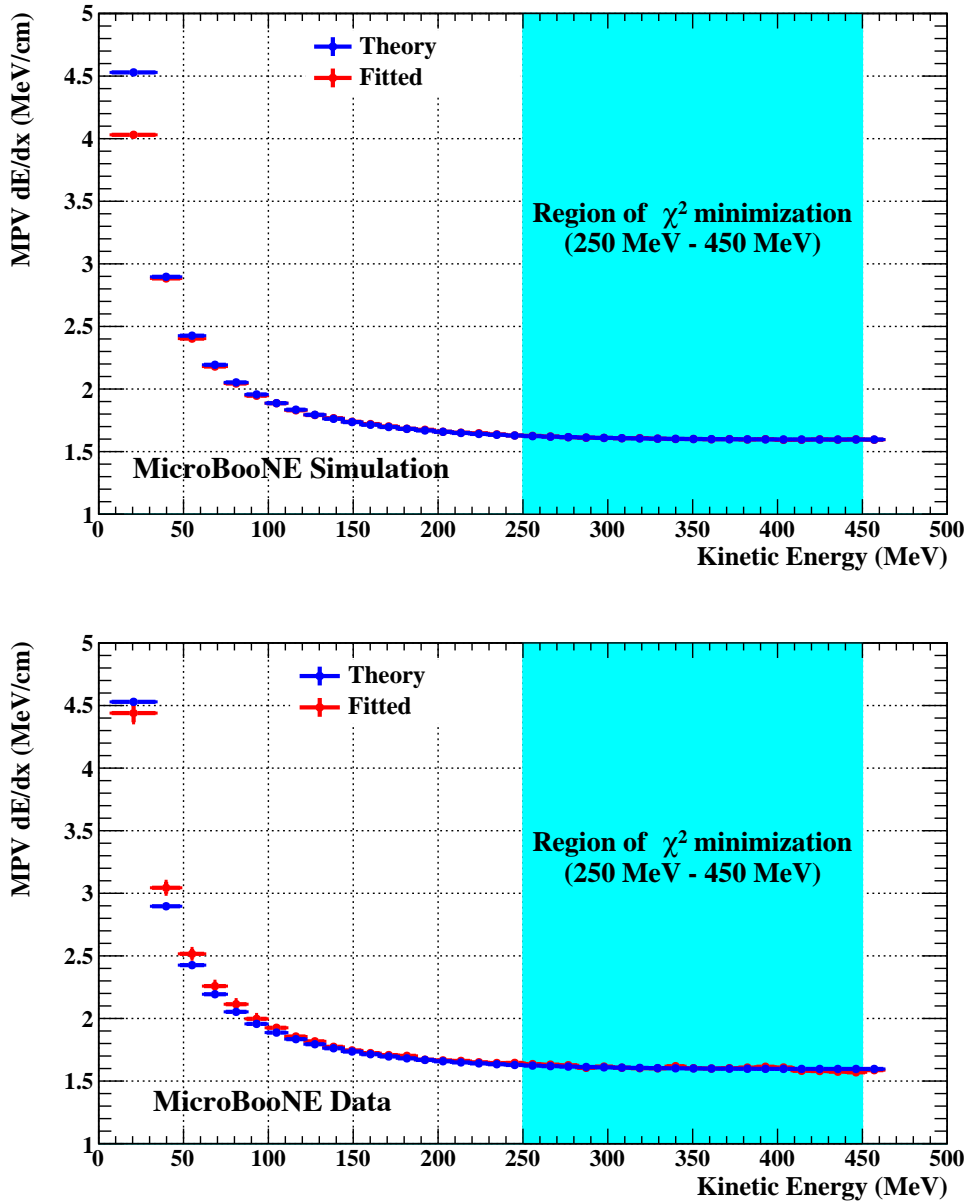


Figure 6.14: (Top) Plot of comparison between the prediction and the fitted MPV dE/dx for stopping muons in Monte Carlo in the collection plane^[2]. (Bottom) Plot of comparison between the prediction and the fitted MPV dE/dx for stopping muons in data in the collection plane^[2].

- $130^\circ < |\theta_{xz}| < 180^\circ$

and derive the YZ and X correction factors for each subsample following the same procedure described above. All the other selection criteria remain the same.

Figure 6.17 shows the percentage differences in YZ correction factors in all YZ cells

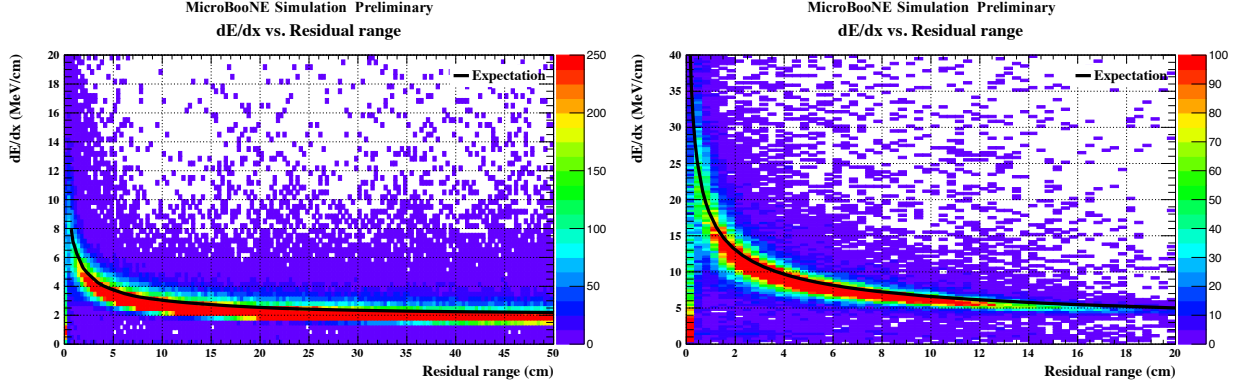


Figure 6.15: Calibrated dE/dx vs residual range for true stopping muons (Left)^[2] and protons (Right)^[2] in Monte Carlo using collection plane information. The overlaid curves are expected mean dE/dx vs. residual range.

between different subsamples and all samples combined for the collection plane. The shift of the mean of the distribution away from zero is indicative of the amount of bias observed in a given angular bin. There are more data tracks than MC tracks so the data distributions are narrower. The peaks of the four distributions all agree within 1%, which indicates the angular dependence of the YZ correction is small for collection plane.

Figure 6.18 shows the percentage differences in X correction factors between different subsamples and all samples combined for the collection plane. The collection plane shows very small angular dependence.

Based on the above studies, we assign 1% systematic error on the YZ correction and 1.5% systematic error on the X correction for the collection plane.

6.8 Conclusions

In this public note, we describe for the first time a method that calibrates a LArTPC using cosmic ray muons. We use through-going muons to remove spatial and temporal variations in the detector response. We use stopping muons to determine the absolute energy scale. The calibrated energy loss agrees very well with the expectation, which helps with the particle identification and energy reconstruction. This method can be used by other LArTPC experiments to calibrate their detectors. Here are a few observations we would like

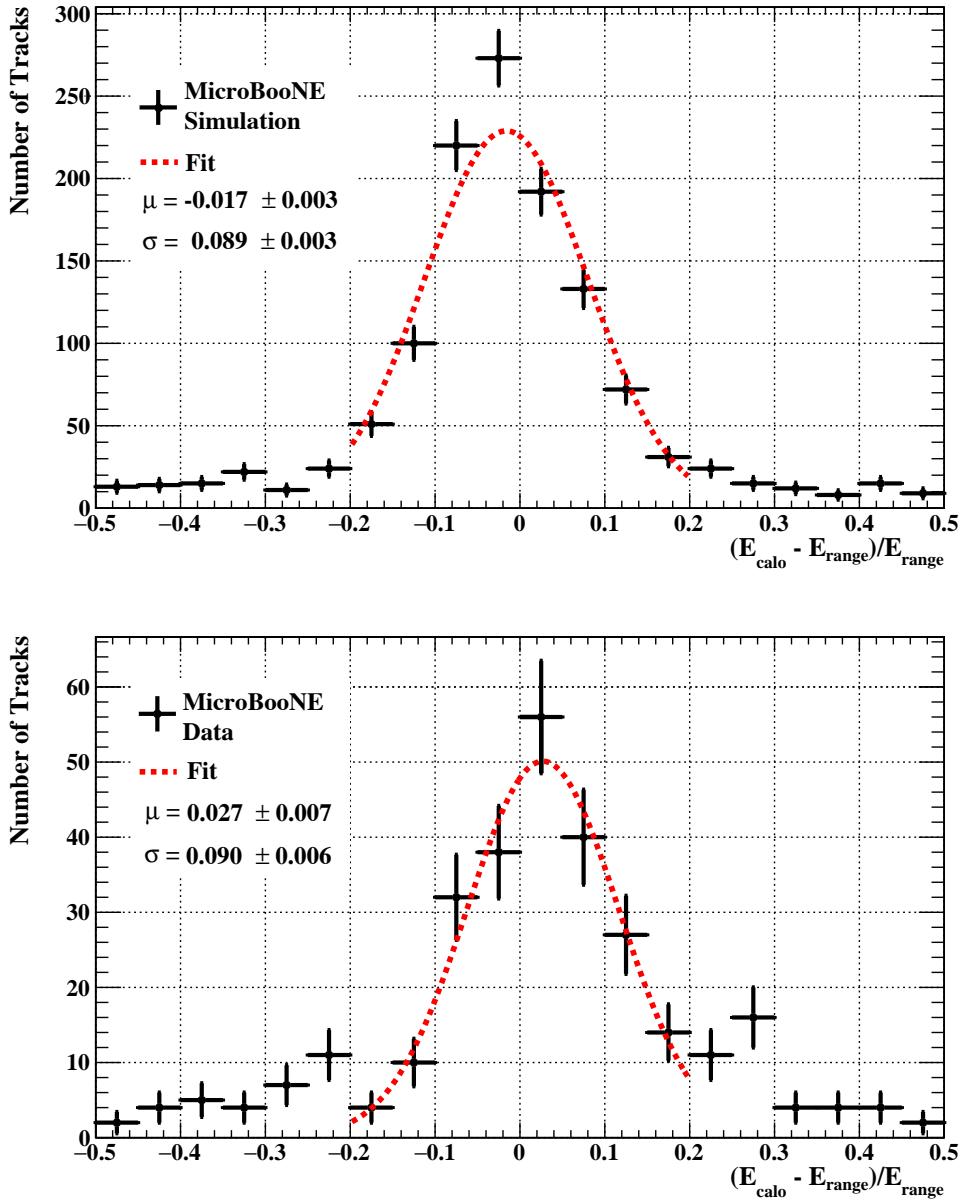
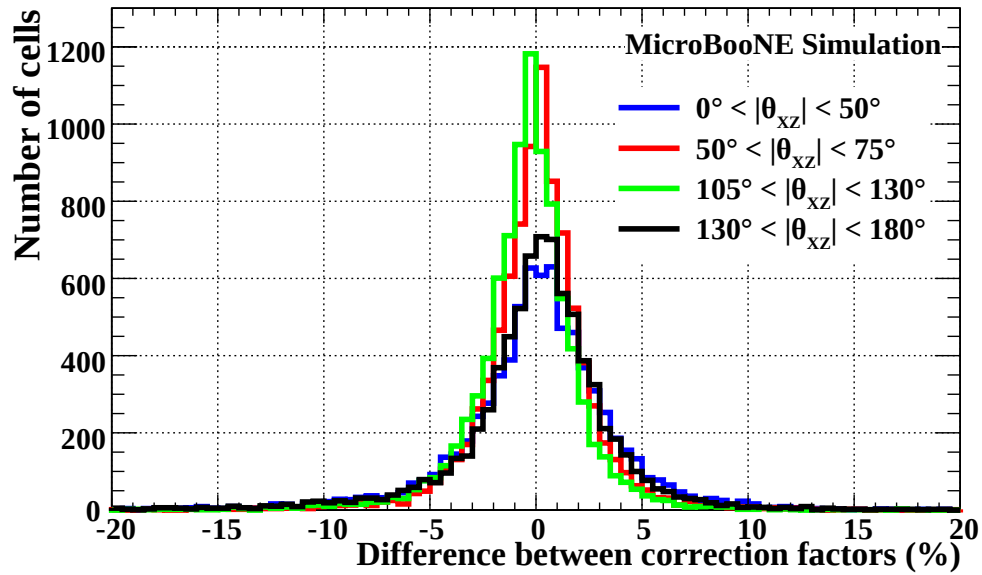


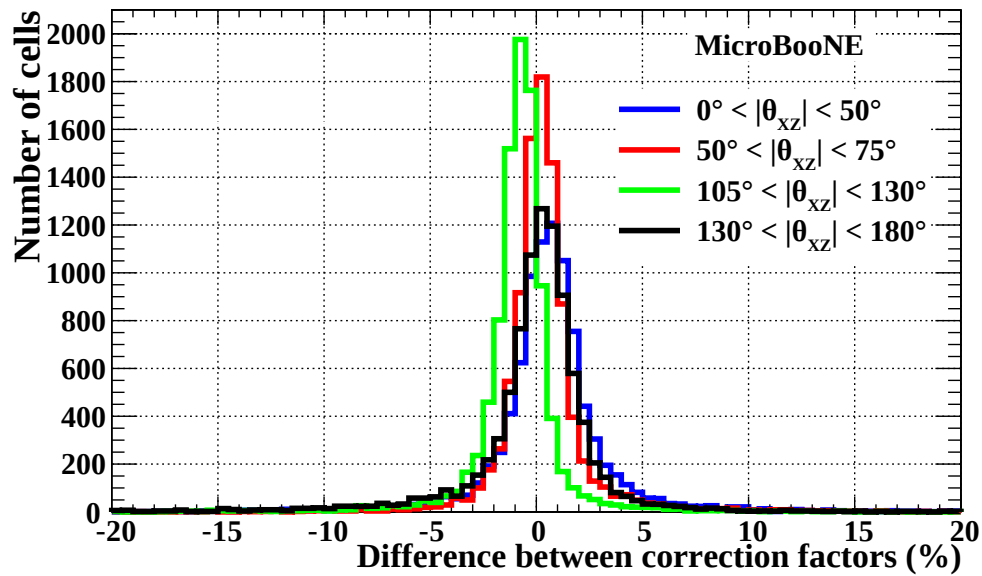
Figure 6.16: Plots of fractional difference in range vs. calorimetric kinetic energy for selected stopping muons^[2]. (Top) Monte Carlo. (Bottom) Data. The distributions are fitted to a Gaussian which returns a mean $\mu = -0.017 \pm 0.003$ and width $\sigma = 0.089 \pm 0.003$ for Monte Carlo. For data the mean $\mu = 0.027 \pm 0.007$ and width $\sigma = 0.090 \pm 0.006$.

to highlight.

- By looking at the YZ correction factors derived for data and Monte Carlo, the dQ/dx response seems uniform in the collection plane. See Figures 6.8 (Top) and 6.10. Moreover, we can see the same features in these plots indicating the simulations of the



(a) Collection plane, MC

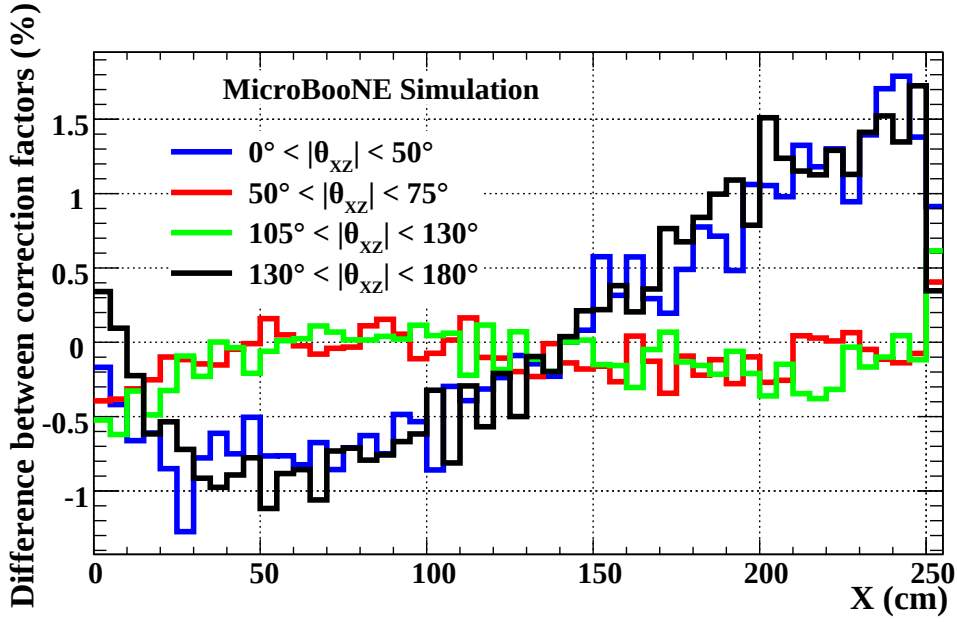


(b) Collection plane, data

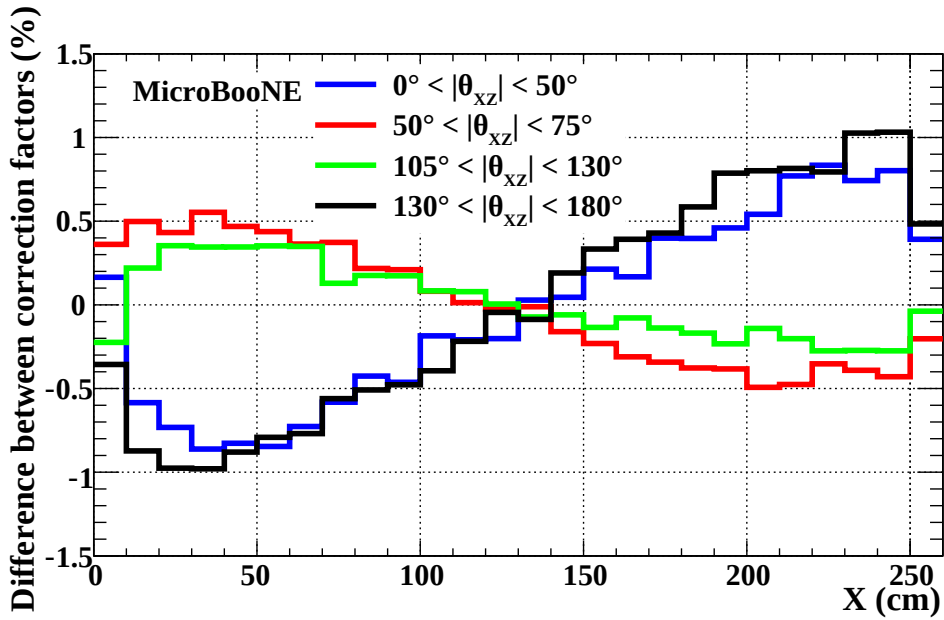
Figure 6.17: Plots of percentage differences in YZ correction factors in all YZ cells between different subsamples and all samples combined^[2]. (Top) Monte Carlo. (Bottom) Data.

collection plane are in agreement with data.

- The drift direction correction factors and time corrections are very uniform in time in the collection plane except for a few low purity datasets. See Figure 6.11. There is a



(a) Collection plane, MC



(b) Collection plane, data

Figure 6.18: Plots of percentage differences in X correction factors between different sub-samples and all samples combined^[2]. (Top) Monte Carlo. (Bottom) Data.

slight increase of detector response over time (Figure 6.7), which is being investigated.

- The effectiveness of the dQ/dx calibration is shown in Figure 6.12. Here it can be seen that the current dQ/dx calibration makes the distributions more sharply peaked

in the collection plane by minimizing the detector effects which smear out the dQ/dx spectrum.

- In Figure 6.14 we see a good agreement between the prediction and the measured dE/dx both in data and Monte Carlo for the given calibration constants. In data the measured dE/dx is slightly higher than theory at low kinetic energy. This is an indication of a mismodeling of the recombination effect.
- The calibration constant derived at Monte Carlo level is $(5.076 \pm 0.001) \times 10^{-3}$ ADC/e, which approximately matches with the input calibration constant of Monte Carlo 5×10^{-3} ADC/e. In data the calibration constant derived is $(4.113 \pm 0.011) \times 10^{-3}$ ADC/e. In addition, comparison between kinetic energies calculated using calorimetry after the dE/dx calibration and kinetic energies calculated using track range, agree within 3% in data and 2% in Monte Carlo. The bias in data is consistent with the discrepancy in the dE/dx measurement at low kinetic energy mentioned above.
- Figure 6.15 shows the calibrated dE/dx profiles for stopping muons and protons which agree with the expectation. This is crucial for the successful particle identification using calorimetric information.

Chapter 7

Neutrino Induced Kaons

In this chapter, we discuss about the strong interaction, the importance of neutrino induced kaon production, some beyond standard model physics (proton decay searches), different neutrino induced kaon production mechanisms, and current measurements of strange particle production. The most of the information mentioned in this chapter is based on the material listed in the References^{[22] [23] [43]}.

7.1 Strong Nuclear Force

It has already been mentioned in the Chapter 1 that kaons are produced as eigen states of the strong interaction Hamiltonian. The strong interaction is explained by the theory known as *Quantum Chromo Dynamics (QCD)*, which is analogous to the theory of *Quantum Electron Dynamics(QED)*, which explains the behavior of electromagnetic interaction. There are fundamental similarities and also some differences between two theories. As photon is the force carrier in the electromagnetic interaction the counterpart force carrier in the strong interaction is the *Gluon*. In total there exists eight gluons in QCD corresponding to the eight generators of the SU(3) local gauge symmetry. As the electromagnetic interaction is characterized by positive and negative charges, the strong interaction has its own version of charge known as the *Color Charge*. In QCD there exists three distinct color charges known

as r (Red), g (Green), and b (Blue). The gluons only interact with the objects, which have color charge. So as none of the fermions in the lepton family carry color charge, the strong interaction is only felt by the quarks, which carry non-zero color charges. Furthermore, it should be mentioned here that the coupling strength of the strong interaction is entirely independent of the color charge of the objects involved. The strong current in the QCD vertex can be parameterized in the following form.

$$j_q^\mu = \bar{u}(p_3)c_j^\dagger \left\{ -\frac{1}{2}ig_s\lambda^a\gamma^\mu \right\} c_i u(p_1) \quad (7.1)$$

γ - Gamma matrices, u and \bar{u} - Spinors, p_3 and p_1 - Four Momentum, g_s - Strong coupling constant, c_i and c_j - Color wave functions of quarks, λ^a - Three component color wave function.

As one of the underlying principles of the QCD is to conserve color charge in the interaction vertex, the mediating gluons should also carry color charge. This is one of the most striking differences between QCD and QED, which keeps two theories apart as the force carrier photons in QED are always neutral. Moreover, the mediating gluons in the strong interaction not only carry just color charge, but they carry combinations of both color and anti color charges (anti color charges are \bar{r} (Anti Red), \bar{g} (Anti Green), and \bar{b} (Anti Blue)). The color combinations of eight distinct gluons in the strong interaction are $r\bar{g}$, $g\bar{r}$, $r\bar{b}$, $b\bar{r}$, $g\bar{b}$, $b\bar{g}$, $\frac{1}{\sqrt{2}}(r\bar{r} - g\bar{g})$ and $\frac{1}{\sqrt{6}}(r\bar{r} + g\bar{g} - 2b\bar{b})$. One of the consequences of gluons themselves carrying color charges is that it allows for gluon-gluon interactions in the QCD, and this gluon-gluon self interaction ultimately leads to one of the nature's most fundamental phenomenon, known as *Color Confinement* (page 248-252^[23]) or also known as *Quark Confinement*.

The color confinement simply tells that individual quarks cannot be isolated in nature. So far all the quarks observed in nature are found in the form of hadrons, which are combinations of quarks forming a colorless bound state. The color confinement can be interpreted in terms of gluon-gluon interactions as follows. If we try to separate a pair of two quarks, which stay in some bound state, the gluons exchanged between two quarks try to keep them attracted to each other. Moreover, there are interactions between gluons as well. The more the separation

between quarks, the more the gluon-gluon interactions forcing the field lines emanating from two quarks to be squeezed to a tube like shape. At macroscopic distances the potential between these two quarks takes following functional form,

$$V(r) \sim \kappa r \tag{7.2}$$

r - Separation between quarks and $\kappa \sim 1 \text{ GeV/fm}$.

indicating that the more the separation is, the higher the energy stored in the strong field. So this means that it would take infinite amount of energy to separate out the two quarks. Thus, all the quarks found in nature manifests in the form of baryons (three quark combination) or mesons (two quark combinations), which form colorless objects. Moreover, this color confinement is also valid for gluons as well. Thus, no one will ever find a gluon in isolation in the nature. One of the direct consequence of this color confinement is the *Hadronization*, which basically refers to the formation of particle jets as a result of high energy particle collisions. When very high energy quarks are produced as a result of particle collisions as explained earlier, due to the action of gluons, there is lots of energy stored in the strong field produced in between these quarks. As these quarks are produced with lots of energy, the more they try to separate from each other, the more energy is stored in the strong field in between them. So there comes a moment that at a certain separation of the quarks, the energy of the strong field is enough to produce more quark anti quark pairs. These newly produced quark pairs also give birth to more quark and anti quark pairs as they try to separate from each other due to their high energy. This process cascades until the quarks do not have sufficient energy to produce more particles. In the final step all these quarks and anti quarks flock together to produce color neutral objects in the form of particle jets.

In the discussion of the strong force, one more important topic is the *Running of the α_S (Coupling Constant)* (page 253-254^[23]). This basically refers to the changing of the strength of the coupling constant with respect to the energy regime concerned. At the lower energy regime of $\sim 1 \text{ GeV}$, the strength of the α_S is of $O(1)$ whereas the in the higher

energy regime of energy > 100 GeV, the strength is ~ 0.1 . At the lower energy regime where α_S is comparatively larger, perturbation theory is not applicable and has to deploy novel computational techniques such as *Lattice QCD*^[112] to calculate low energy processes like bound hadronic states and hadronization. But to calculate the high energy processes such as high energy particle collisions at LHC, again we can go with the traditional perturbation theory, as the strength of the coupling constant is smaller. This particular nature of the QCD is famously known as the *Asymptotic Freedom*.

7.2 Neutrino Induced Kaons

There are several motivations behind the measurement of neutrino induced strange particle production. Among those,

- Helps to better model the background introduced by atmospheric neutrinos to the nucleon decay experiments.
- Allows for better estimation of neutrino oscillation parameters.
- Allows to have a better insight into the strange quark content of the nucleus in the few GeV energy regime and hence helps to better understand the behavior of weak current in the hadronic sector.
- Allows to better determine the weak form factors and axial form factors hence improve the current knowledge about V-A and Cabbibo theories for the weak interaction.

are of the most importance. As the current measurements for this particular channel are so sparse while most of the already existing measurement are coming from statistically limited bubble chamber data on very light nuclear targets like hydrogen and deuterium, any new information on complicated nuclear targets like argon would shed new lights into neutrino-nucleus interactions. In the context of neutrino induced kaon production, a discussion about neutrino-nucleus interactions is of very high importance. The neutrino-nucleus interactions

can separately be studied in the energy regions depending on the initial energy of the neutrinos. Primarily there exists three main energy regimes where neutrinos interact with the target nuclei with different characteristics.

- Low energy regime ($E_\nu \sim 1 \text{ MeV} - 100 \text{ MeV}$).
- Intermediate energy regime ($E_\nu \sim 0.1 \text{ GeV} - 20 \text{ GeV}$).
- High energy regime ($E_\nu \sim 20 \text{ GeV} - 500 \text{ GeV}$).

In the low energy regime, the neutrino interacts with the target nucleus coherently as the neutrino does not have enough energy to probe into the inner structure of the nucleus. This particular interaction shares mostly the same features of electron scattering interaction and has been already extensively studied. Some common examples for low energy neutrino interactions are inverse beta decay, neutron beta decay, and neutrino scattering on lighter nuclear targets such as hydrogen and deuterium.

When shifting to the intermediate energy regime, the neutrino acquires enough energy to interact with individual nucleons or constituent quarks of the nuclear target. The neutrino-nucleus interactions in the intermediate energy regime fall into three main categories namely,

- Elastic or quasi elastic scattering.
- Resonance.
- Deep inelastic scattering.

The Figure 7.1 shows the cross sections for different processes as a function of energy for the charged current interaction of neutrinos and anti neutrinos separately. As it is apparent in this figure when the neutrino energy is below $\sim 2 \text{ GeV}$, the neutrino interactions are dominated by the quasi elastic process, where the target neutron is transformed to a proton in the neutrino mode and target proton is transformed into a neutron in the anti neutrino mode (see Figure 7.2). In the neutral current mode the quasi elastic process becomes completely elastic as nothing is changed in the interaction except the exchange of kinetic energy. In the

early days, the QE interactions was heavily studied to determine the *Axial mass* (M_A) while early formulation of the quasi elastic interaction was pioneered by Llewellyn-Smith^[113] in 1972. The quasi elastic interaction plays a vital role in the modern day neutrino physics as most of the neutrino experiments are operating at ~ 2 GeV energy regime and hence their data set is vastly comprised of this particular interaction.

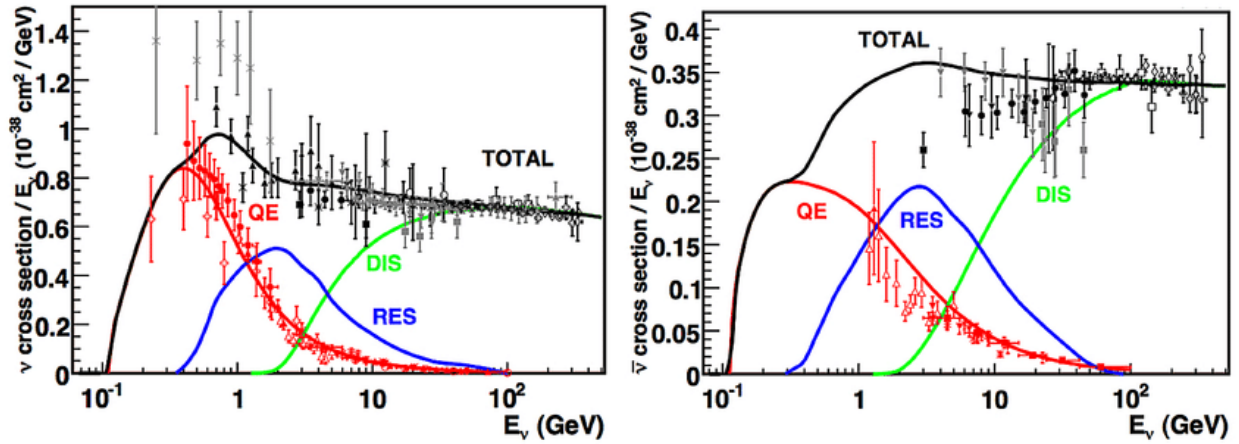


Figure 7.1: (Left) Neutrino cross sections per nucleon for different processes in the charged current interaction^[114]. (Right) Anti neutrino cross sections per nucleon for different processes in the charge current interaction^[114].

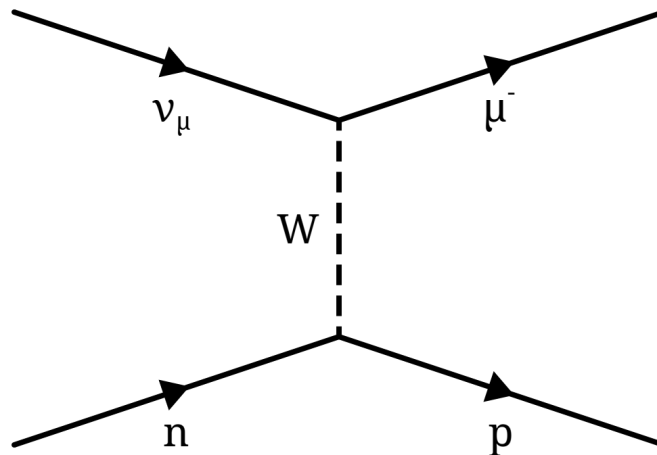


Figure 7.2: The Feynman diagram of QE interaction in the neutrino mode^[115]. Here the target neutron is transformed into a proton.

When the neutrinos have enough energy, sometimes they can interact with nucleons

themselves and excite them to unstable baryonic states, which ultimately decays to some nucleons and mesonic states. This particular production channel is referred to as the *Resonance*. Most of the time the intermediate baryonic resonant state is $\Delta(1232)$, which is a baryon made up of up and down quarks. In the resonance production, most of the time, the baryon decays to some nucleon and a single pion, although the other modes are possible with a little branching fraction. There exists a total of seven single pion production channels both in charged current and neutral current interaction in the resonance production as mentioned in the Table 7.1 (see Figure 7.3).

Charged Current Mode	Neutral Current Mode
$\nu_\mu + p \rightarrow \mu^- + p + \pi^+$	$\nu_\mu + p \rightarrow \nu_\mu + p + \pi^0$
$\nu_\mu + n \rightarrow \mu^- + p + \pi^0$	$\nu_\mu + p \rightarrow \nu_\mu + n + \pi^+$
$\nu_\mu + n \rightarrow \mu^- + n + \pi^+$	$\nu_\mu + n \rightarrow \nu_\mu + n + \pi^0$
	$\nu_\mu + n \rightarrow \nu_\mu + p + \pi^-$

Table 7.1: Different single pion production channels in the resonance production for neutral current interaction and charged current interaction^[43]. All these production channels are also valid for anti neutrino mode as well.

To describe these processes, the most commonly used model is the *Rein and Sehgal* model^{[116][117]}, which describes the behavior of both charged current and neutral current resonance productions accounting for the interferences between nearby resonances. The importance of any detailed study of these pion production channels is that on one hand, they introduced a significant background for any $\nu_\mu \rightarrow \nu_e$ oscillation search while at the same time impacting neutrino energy determination. In the early days, the pion production was studied on lighter nuclear targets to do the axial mass measurements described in the QE interaction. In the discussion of resonance pion production, one of the most important topic is the *Final State Interactions (FSI)*. The final state interactions basically describes, the possible interactions, a particle can undergo before it is emitted from the nucleus. For instance an original pion produced by resonance can undergo re-scattering, absorption or charge exchange inside the nucleus before it emerges out (see Figure 7.4). So what we observe may not be what has really happened in the original interaction. Therefore accounting for

these final state interactions is of utmost importance.

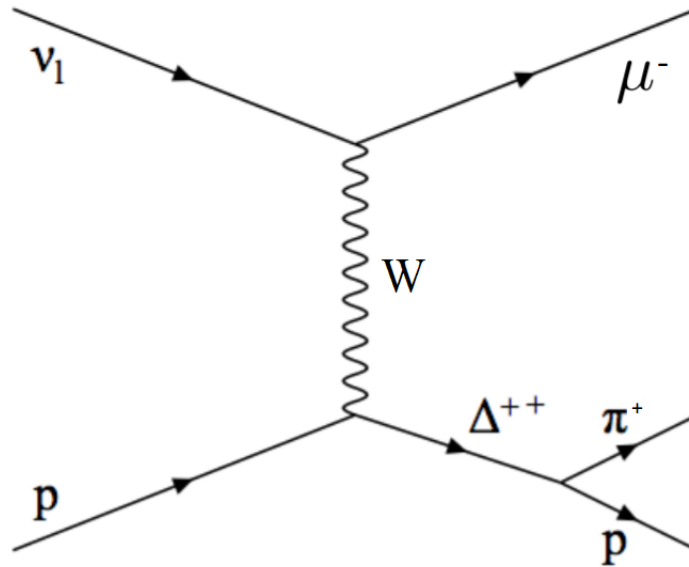


Figure 7.3: A Feynman diagram of single pion production by resonance in the charged current mode^[118]. The mother neutrino struck a proton and the proton is fluctuated into a Δ baryon, which ultimately decays giving birth to a single pion and a nucleon.

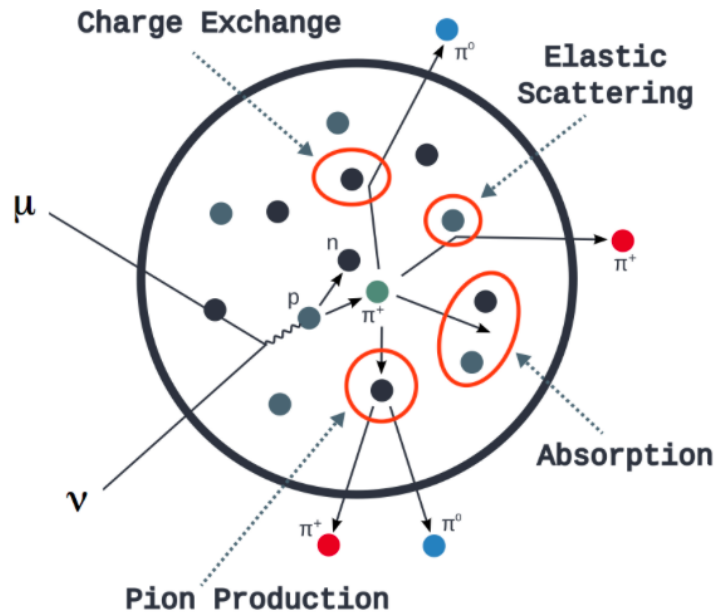


Figure 7.4: Possible final state interactions for pion produced in a neutrino interaction^[119]. In the FSI pion can scatter, charge exchange, be absorbed or produce more pions.

The other important possible production modes in the resonance are multi pion pro-

duction, single photon production and, strange particle production. The current existing measurements for multi pion production is so limited as reconstructing these events are so challenging. Chances of intermediate baryon decaying into a single photon is roughly $\sim 1\%$ where the production of strange particles are suppressed due to the higher masses of them and lack of any baryonic resonances.

Another possible pion production mechanism in this intermediate energy regime, other than the resonance, is *Coherent pion production*. Here due to the low momentum transferred by the neutrino, the target nucleus remain intact even after the interaction. The possible coherent single pion production modes in the charged current and the neutral current interactions are listed in the Table 7.2.

Charged Current Mode	Neutral Current Mode
$\nu_\mu + A \rightarrow \mu^- + A + \pi^+$	$\nu_\mu + A \rightarrow \nu_\mu + A + \pi^0$

Table 7.2: Coherent single pion production modes in the charged current and the neutral current interactions^[43]. Here A stands for the target nucleus. All these production modes are valid for anti neutrino mode as well.

The coherent pion production is not only restricted to the intermediate energy regime, but spreads across a broad energy range. Still, there is no proper model, which describes this particular production mode at all energies.

When we move to the high energy regime, due to the very high momentum transferred, the neutrino gets a chance to probe into the inner structure of the nucleons. These kinds of neutrino interactions with the constituent quarks of the nucleons are referred to as the *Deep Inelastic Scattering (DIS)*. The basic dynamics behind the deep inelastic scattering process is that, when a neutrino hits a quark in a nucleon, due to hadronization, a bunch of hadrons is produced in the final state. The deep inelastic scattering plays a major role in the particle physics in the sense that, it was helpful in understanding the nuclear structure, validating the standard model itself, determining electroweak parameters, measuring different coupling constants, and measuring cross sections for different particle productions. It should also be mentioned that both pion production and strange particle production is not only limited to

the resonance but also can happen through DIS in the intermediate energies.

Moving to the discussion of neutrino induced kaons, strange particles can be produced by both resonance and DIS mechanisms as already mentioned. Most of the time heavier resonances and strange resonances can produce multi pion systems and strange particles. For instance the lightest strange resonance $\Lambda(1405)$ decay produces a single pion and a Σ particle while much heavier strange resonances mostly decays to a nucleon and a K^- or \bar{K}^0 . The production of K^+ s are somewhat suppressed compared to the production of K^- s via resonance due the fact that K^+ is made up of an anti strange quark. In the DIS production, when a neutrino knocks off a quark in a nucleon, due to the hadronization, pairs of strange-anti strange quarks are popped up from gluons. The strange quarks, thus produced, get combined with up or down quarks and produce K^+ s and K^- s while the remaining make up the hyperons (see Figure 7.5).

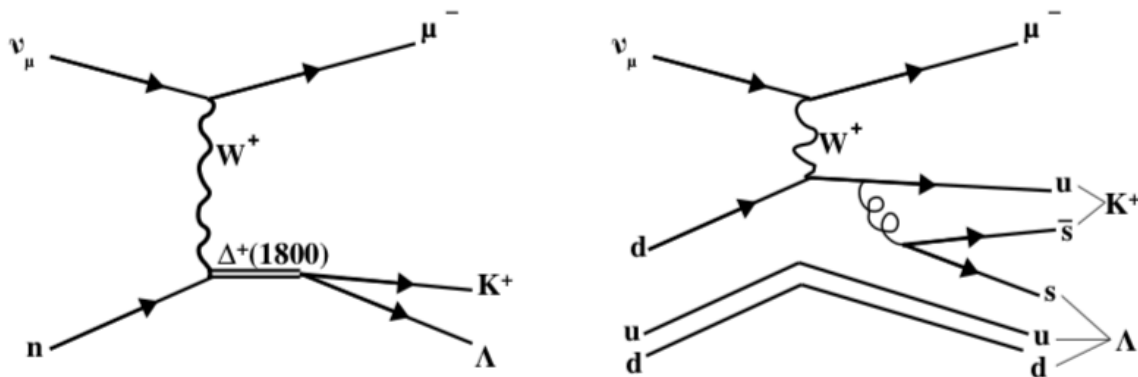


Figure 7.5: Feynman diagrams of neutrino induced kaon production^[22]. (Left) Neutrino induced kaon production through resonance. The heavy intermediate Δ resonance decay to kaon and a hyperon. (Right) Neutrino induced kaon production through DIS. The knocked off up quark combines with an anti strange quark to produce the K^+ while remaining up, down, and strange quarks form the hyperon.

Looking into the number of strange particles produced after the neutrino interaction, the kaon production mechanisms could be grouped into two categories namely, *Associated kaon production* and *Single kaon production*. In the associated kaon production, the kaon is always accompanied by another strange particle (another kaon or hyperon). As the strange quark

and the anti strange quark are shared in between the kaon and the hyperon, the associated kaon production is a $\Delta S = 0$ process where the threshold energy of this particular kaon production mode is 1.1 GeV. The Table 7.3 lists the possible associated kaon production channels in the charged current interaction and the neutral current interaction.

Charged Current Mode	Neutral Current Mode
$\nu_\mu + n \rightarrow \mu^- + K^+ + \Lambda^0$	$\nu_\mu + p \rightarrow \nu_\mu + K^+ + \Lambda^0$
$\nu_\mu + p \rightarrow \mu^- + K^+ + \Sigma^+$	$\nu_\mu + n \rightarrow \nu_\mu + K^0 + \Sigma^0$
$\nu_\mu + n \rightarrow \mu^- + K^+ + \Sigma^0$	$\nu_\mu + n \rightarrow \nu_\mu + K^+ + \Sigma^-$
$\nu_\mu + n \rightarrow \mu^- + K^0 + \Sigma^+$	$\nu_\mu + n \rightarrow \nu_\mu + K^- + \Sigma^+$

Table 7.3: Possible associated kaon production channels in both charged current interaction and neutral current interaction^[43].

In contrast to the associated kaon production, in the single kaon production, only a single kaon is produced after the neutrino interaction. Because of this, in the single kaon production, strangeness is no longer a conserved quantity having $\Delta S = 1$. At lower energies, single kaon production is dominated over associated kaon production as the threshold energy for this process is ~ 0.8 GeV (see Figure 7.6). But it should be noted that the single kaon production is a highly Cabbibo suppressed process. Table 7.4 lists all possible single kaon production channels while Figure 7.8 shows all its Feynman diagrams.

Charged Current Mode	Neutral Current Mode
$\nu_\mu + p \rightarrow \mu^- + K^+ + p$	
$\nu_\mu + n \rightarrow \mu^- + K^0 + p$	
$\nu_\mu + n \rightarrow \mu^- + K^+ + n$	

Table 7.4: Possible single kaon production channels in the charged current interaction^[43]. There are no neutral current production channels for this particular process.

There is a possibility that a single kaon being produced as a result of neutrino coherently interacting with the target nucleus. The coherent kaon production rate is very negligible compared to that of coherent pion production due to Cabbibo suppression and higher kaon mass. Here due to the low momentum transfer by the neutrino, the target nucleus remains

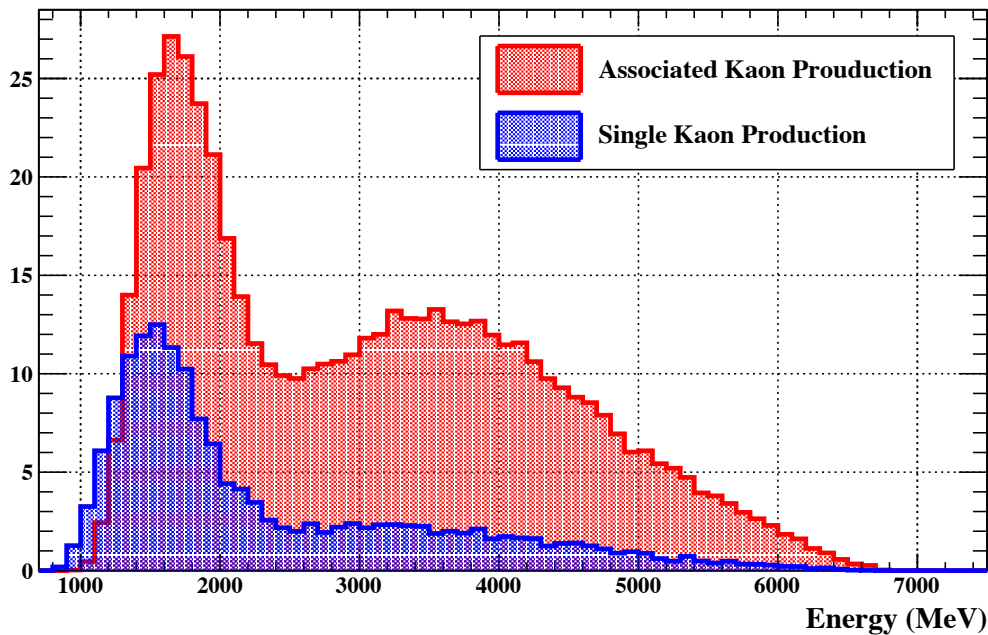


Figure 7.6: Energy distributions of neutrinos for different kaon production mechanisms using GENIE simulations in the MicroBooNE. For the associated kaon production the energy threshold is 1.1 GeV while for single kaon production 0.8 GeV. Here the two distributions are POT normalized to 6.6×10^{20} . 2/3 of the kaon events observed in the MicroBooNE simulations are from associated kaon production.

unharmful even after the interaction (see Figure 7.8).

When it comes to the final state interactions of kaons, one possibility is that the kaon being absorbed. But this absorption is only limited to K^- s where once absorbed the nucleus is transformed to a hyperon (Λ or Σ). The only possible final state interaction, a K^+ can undergo is the charge exchange where an original K^+ produced once inside the nucleus can emerge in the form of a neutral kaon. In addition, some models like Giessen Boltzman-Uehling-Uhlenbeck (GIBBU)^[122] discusses the possibility of rare final state processes like charge pion re-interacting with nucleons and producing strange particles ($\pi^+ + n \rightarrow K^+ + \Lambda$).

7.3 Proton Decay

In the discussion of neutrino induced kaon production, a topic that cannot be skipped is the *Proton decay*. One of the most fundamental laws of particle physics is the *Conservation*

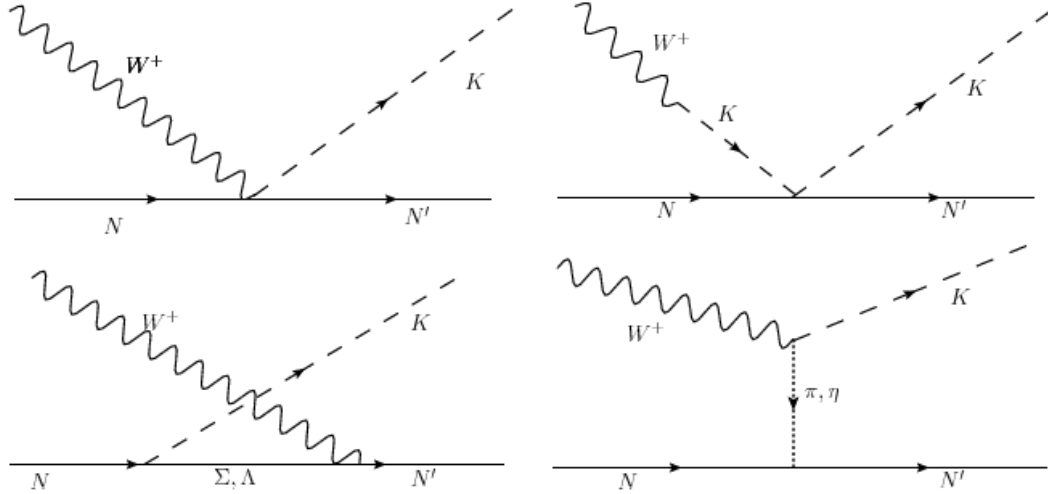


Figure 7.7: Feynman diagrams of for the generic channel $\nu_l + N \rightarrow l^- + N + K$ representing interactions listed in the Table 7.4 in the single kaon production^[120]. (Top Left) Contact term - The largest contributor for the single kaon production. (Top Right) Kaon pole term - Here W fluctuates to the kaon, which is brought on shell later by the interaction with some nucleon. The contribution to the total cross section from this process is minimal. (Bottom Left) this U channel process happens via an intermediate state involving Λ or Σ hyperons. No contribution from S channel due to the scarcity of hyperons having anti strange quarks in its procession. (Bottom Right) Meson in flight term - Kaon is produced by exchanging a pion or eta in the process.

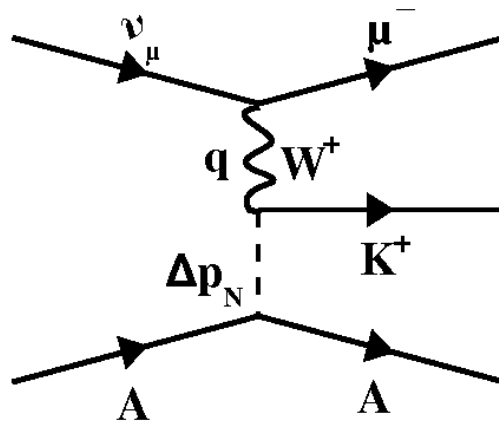


Figure 7.8: Feynman diagram for the charged current coherent kaon production $(\nu_\mu + A \rightarrow \mu^- + K^+ + A)$ ^[121]. Here A stands for target nucleus.

of baryon and leptons numbers in any of the particle interactions. So as proton being the lightest of all baryons, there is no chance for any proton to decay into any lighter decay products obeying the most sacred rules of particle physics. The same statement is true for the electron as well in the leptonic sector. But there is a little twist to this argument as

follows. We know that the neutron is similar to the proton in all possible aspects (the quark contents and masses are almost same). But still an isolated neutron cannot long last and within a few minutes, it decays to a proton by emitting a beta particle and a neutrino. Couldn't a proton also decay in the same manner? So far from the clues, we have found in nature, suggest that proton is a highly stable particle. For instance the matter in most of the galaxies exists in the form of hydrogen plasma, which consists of a soup of isolated protons and unattached electrons. If the protons are unstable, as neutrons then definitely these plasmas should vanish where this is not the case in reality. Then what about the possibility that protons actually do decay, but they do have a very high lifetime. With this particular argument, we have the chance to build up a coherent theory which explores the possibility of proton decay and at the same time explaining what we observe in nature. The *Grand Unified Theories (GUT)*^[123], which were formulated to unify electromagnetic, strong nuclear, and weak nuclear forces, suggested that in fact the proton has a finite lifetime. So the easiest way to validate any GUT model is to find evidences for proton decay, which would finally realize the physicist's dream of unifying everything. The earlier limits set on proton lifetime by old GUT models were ultimately ruled out by ongoing proton decay searches. But the new theories, which are basically hybrids of grand unification ideas and *Supersymmetry theory*, are pushing the limit on proton lifetime keeping the hope still alive for experiments to observe rare proton decay events. An example for such a theory, which shows lots of promise in the current era, is the $SO(10)$ ^[124]. This theory incorporates the ideas such as non-zero neutrino masses ... etc in its building blocks.

7.4 Proton Decay Searches

One of the most famous decay channels of proton in a number of GUT models is the $p \rightarrow e^+ + \pi^0$. This particular decay channel got the highest branching ratio in most of the models where a bound or free proton decays to a neutral pion and a positron. Once the proton decays, the energy of the proton manifests in the detector in the form of a positron induced shower and two back-to-back photons coming from π^0 decay. But, due to final

state interactions, the π^0 produced could sometimes be absorbed or charge-exchanged inside the nucleus. This particular decay topology is specially suited for proton decay searches in any water cherenkov detector like SuperK, as the topology is easy to be reconstructed (see Figures 7.9 and 7.10).

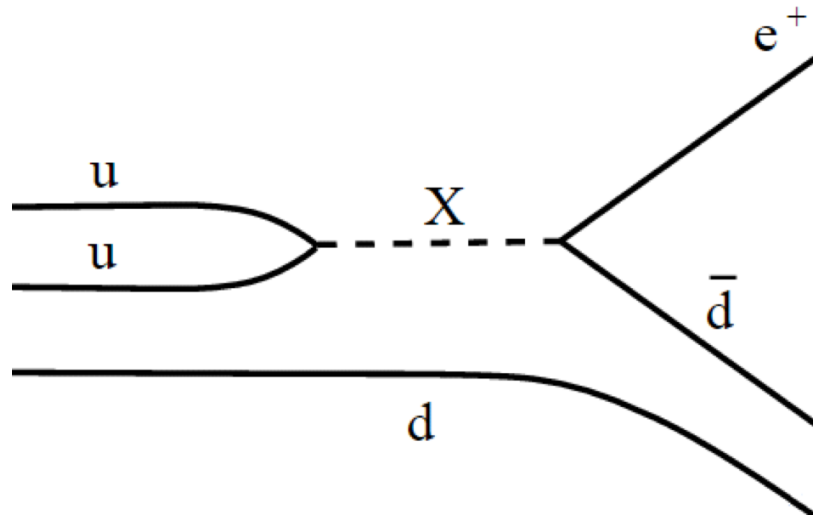


Figure 7.9: The Feynman diagram of $p \rightarrow e^+ + \pi^0$ in a non SUSY GUT model. Here an X boson is exchanged in the proton decay^[125].

The proton decay channel of importance having the highest branching ratio in most of the SUSY GUT hybrid models is the proton decaying into a kaon and a neutrino (see Figure 7.11 for $p \rightarrow K^+ + \nu$). This particular decay mode is ideal for proton decay experiments using LArTPC technology like the proposed DUNE experiment as most of the time the kaon does not exceed the cherenkov threshold to be registered in a water cherenkov detector. Figure 7.12 shows the variation of measured proton lifetime by SuperK against time in this particular decay mode. The kaon coming from proton decay could either decay into a muon and a neutrino ($K^+ \rightarrow \mu^+ + \mu_\nu$) with 63% branching ratio or charged pion and a neutral pion ($K^+ \rightarrow \pi^+ + \pi^0$) with a branching ratio of 20%. If the detector has very high resolution, even the michel electrons and muons coming from secondary particle decays could also be identified. Furthermore, as all these kaon decays are two body decays, the pions and muons coming from kaon decays (at rest) do have well-defined momenta and hence could easily be isolated from other topologies. The most common background for this proton

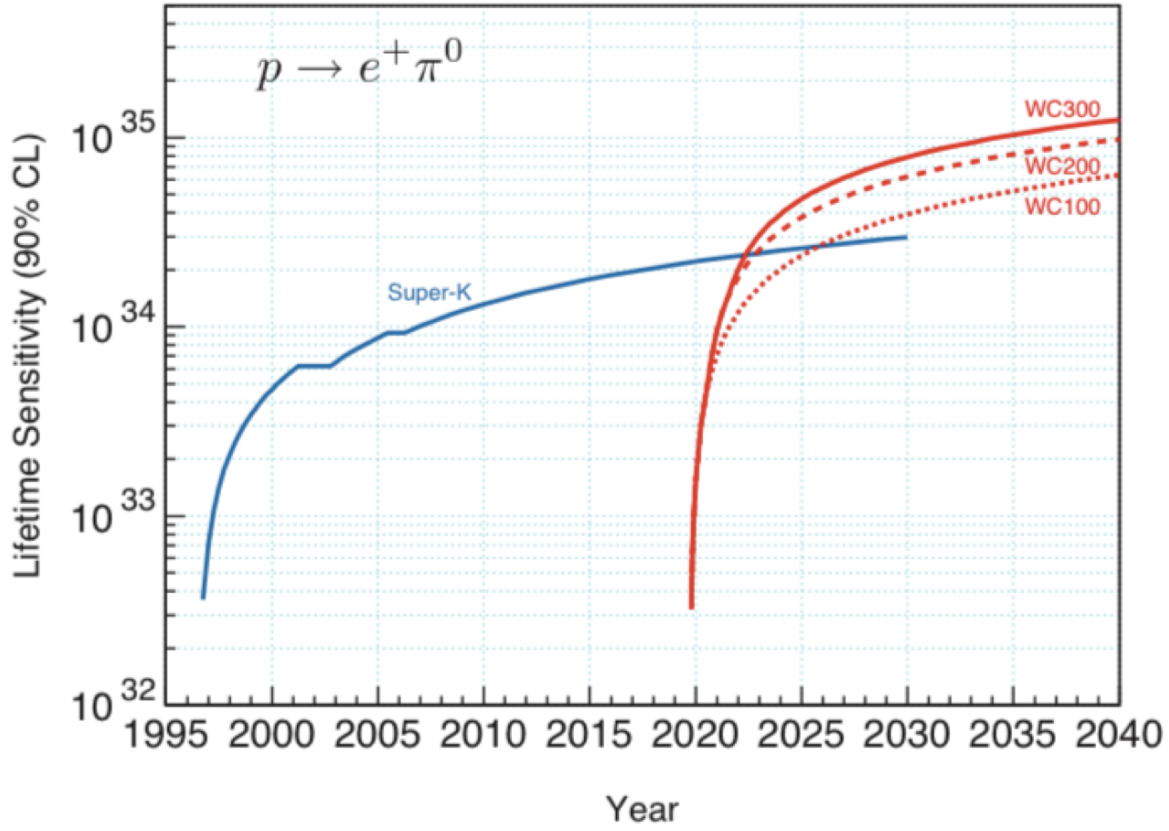


Figure 7.10: The limits set for proton lifetime by SuperK in the decay channel $p \rightarrow e^+ + \pi^0$ as a function of time^[126]. The red curves show the expected proton lifetime limits for the proposed 300 KT water cherenkov detector, which would start 2019. This new detector will be commissioned by three phases, 100 KT each year. The limits here shown are at 90% confidence level.

decay channel is an atmospheric neutrino producing a kaon by interacting with the detector medium. The other proton decay channels of interest, include, $p \rightarrow \mu^+ + \pi^0$, $p \rightarrow e^+ + \eta$... etc. Table 7.5 shows the upper limits set by SuperK experiment on different proton decay channels and Figure 7.13 shows the predicted proton lifetime by different models and constraints by different experiments.

7.5 Strange Particle Production (Early Measurements)

The work published in the Reference^[134] discusses the production of K^0 , Λ and $\bar{\Lambda}$ in the Big European Bubble Chamber (BEBC)^[135] at CERN. The detector medium consists of 1.1 tons

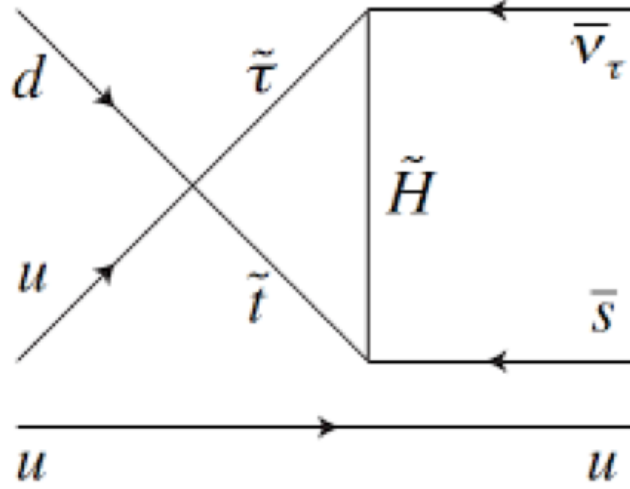


Figure 7.11: The Feynman diagram of $p \rightarrow K^+ + \nu$ with the participation of supersymmetric particles in SUSSY GUT models^[127]. The neutrino produced could either be a ν_τ or ν_μ .

Decay Mode	Lifetime (τ/B) with 90% C.L	Reference
$p \rightarrow e^+ + \pi^0$	$1.7 \times 10^{34} yrs.$	
$p \rightarrow \mu^+ + \pi^0$	$7.8 \times 10^{33} yrs.$	
$p \rightarrow \nu + K^+$	$6.6 \times 10^{33} yrs.$	[128]
$p \rightarrow \mu^+ + K^0$	$6.6 \times 10^{33} yrs.$	[129]
$p \rightarrow e^+ + \eta$	$4.2 \times 10^{33} yrs.$	[130]
$p \rightarrow \mu^+ + \eta$	$1.3 \times 10^{33} yrs.$	[130]
$p \rightarrow e^+ + \rho^0$	$7.1 \times 10^{32} yrs.$	[130]
$p \rightarrow \mu^+ + \rho^0$	$1.6 \times 10^{32} yrs.$	[130]
$p \rightarrow e^+ + \omega^0$	$3.2 \times 10^{32} yrs.$	[130]
$p \rightarrow \mu^+ + \omega^0$	$7.8 \times 10^{32} yrs.$	[130]
$p \rightarrow \nu + \pi^+$	$3.9 \times 10^{32} yrs.$	[131]
$p \rightarrow e^+ + \nu + \nu$	$1.7 \times 10^{32} yrs.$	[132]
$p \rightarrow \mu^+ + \nu + \nu$	$2.2 \times 10^{32} yrs.$	[132]

Table 7.5: Proton lifetime (lifetime is scaled over branching ration B) measured on different decay channels by SuperK experiment^[133].

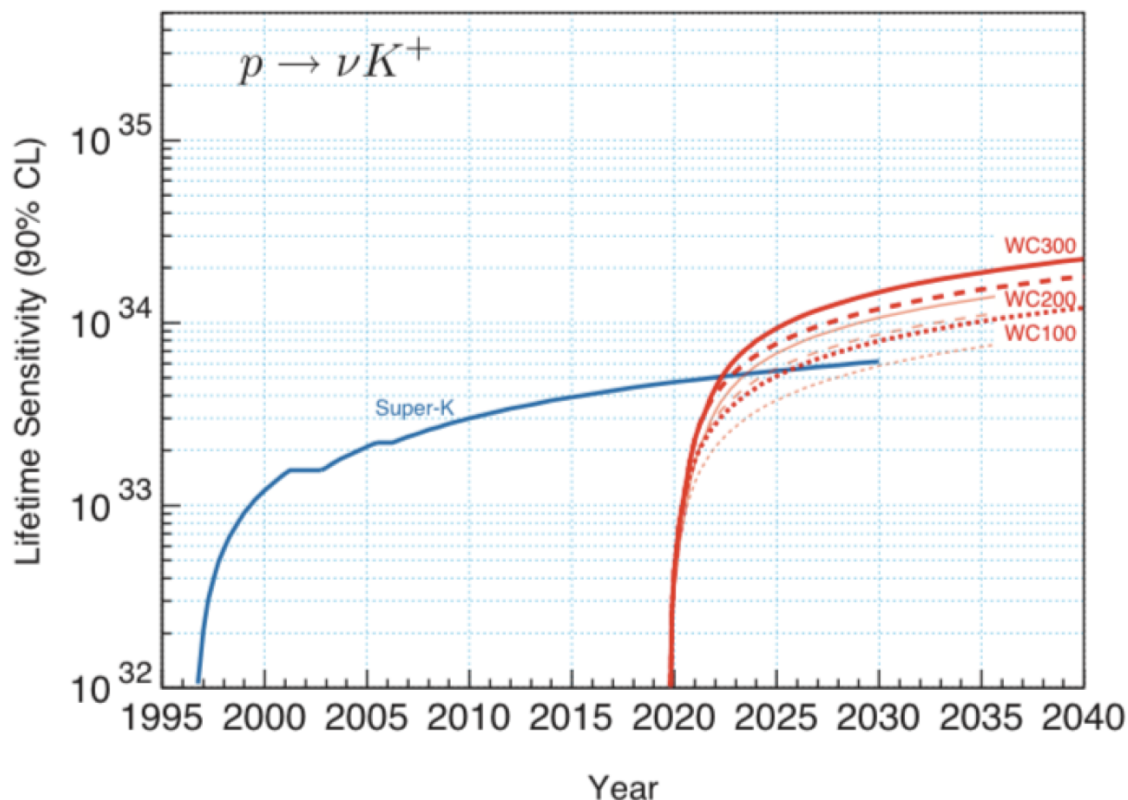


Figure 7.12: The limits set for proton lifetime by SuperK in the decay channel $p \rightarrow K^+ + \nu$ as a function of time^[126]. The red curves show the expected proton lifetime limits for the proposed 300 KT water cherenkov detector, which would start 2019. This new detector will be commissioned by three phases, 100 KT each year. Limits here shown are at 90% confidence level.

of liquid hydrogen and they made use of CERN’s SPS wide band neutrino beam to extract both neutrinos and anti neutrinos where the neutrinos are produced by hitting 400 GeV high energy protons on a beryllium target. This analysis is only restricted to the neutral strange particle production in the charged current mode. Final result reveals as listed in the Table 7.6,

The Reference^[136] reports about the inclusive neutral strange particle production rates (K^0 , Λ and $\bar{\Lambda}$) in the interaction types $\bar{\nu} - p$, $\bar{\nu} - n$, $\nu - p$, and $\nu - n$ at BEBC, CERN. The detector medium comprises deuterium where the neutrinos are extracted from the same beam structure explained earlier. Table 7.7 lists the final results.

The work published in the Reference^[137] discusses about the K^0 meson production and

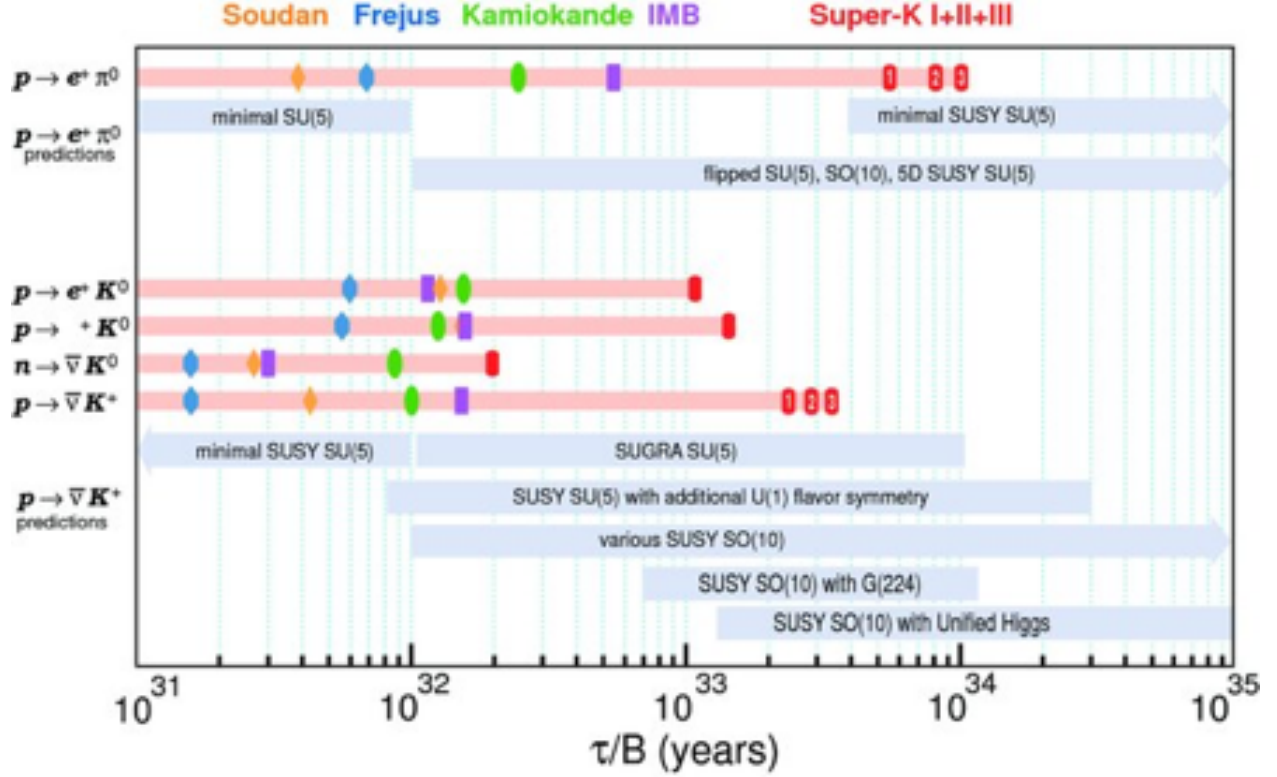


Figure 7.13: Constraints on proton lifetime by different experiments on different decay modes and predictions on proton lifetime by different GUT and SUSY GUT models^[126].

Particle Type	No. of events in the neutrino mode	No. of events in the anti neutrino mode
K^0	831	401
Λ	491	344
$\bar{\Lambda}$	27	9

Table 7.6: Number of events observed for different neutral strange particle species in the neutrino and anti neutrino modes. Here strange particles are produced in both associated and single particle production modes.

Particle Type	Production Rate (%)
K^0	21
Λ	7
$\bar{\Lambda}$	0.4

Table 7.7: Inclusive production rates observed for different neutral strange particle species in the interactions $\bar{\nu} - p$, $\bar{\nu} - n$, $\nu - p$, and $\nu - n$.

Λ hyperon production on a neon target. Here the data is collected in the BEBC at CERN where neutrinos and anti neutrinos are coming from parent protons having an energy of ~ 400 GeV. The analysis is focusing only on charged current interaction. The cross section ratios for different channels are,

$$\sigma(SP) = \frac{\nu N \rightarrow \mu^- + SP}{\nu N \rightarrow \mu^- + X} = (35.0 \pm 5.8)\%$$

$$\bar{\sigma}(SP) = \frac{\bar{\nu} N \rightarrow \mu^+ + SP}{\bar{\nu} N \rightarrow \mu^+ + X} = (23 \pm 12)\%$$

$$\sigma(SP) = (30.4 \pm 6.6)\%, (E_\nu < 100 GeV)$$

$$\sigma(SP) = (41.0 \pm 9.0)\%, (E_\nu > 100 GeV)$$

Where,

$$\sigma(SP) = 2[\sigma(\Lambda) + \sigma(K^0)] - 4[\sigma(K^0\Lambda) + \sigma(K^0\bar{K}^0)]$$

The publication cited in the Reference^[138] explains about neutral strange particle production in the anti neutrino-neon interaction. The data is again collected in the BEBC at CERN. This analysis only focuses on the charged current interaction and reveals the following production rates on individual strange particles (see Table 7.8).

The Reference^[139] describes the strange neutral particle production due to neutrino-neon

Particle Type	Production Rate (%)
K^0	15.7 ± 0.8
Λ	8.2 ± 0.5
$\bar{\Lambda}$	0.4 ± 0.2
σ^0	0.6 ± 0.3

Table 7.8: Different production rates for neutral strange particles, coming from anti neutrino-neon interactions in the charged current mode.

interactions in the charged current mode in the 15 ft bubble chamber at Fermilab^[140]. The neutrino energy spectrum peaks at ~ 23 GeV while the detector medium comprises heavy neon-hydrogen mixture. Table 7.9 shows their final results.

Particle Type	No. of particles	Production Rate (%)
K^0	2279	0.168 ± 0.012
Λ	1843	0.065 ± 0.005
$\bar{\Lambda}$	93	$(4.6 \pm 0.8) \times 10^{-3}$
Σ^0	94	0.011 ± 0.003
Ξ^-	4	$(5.8 \pm 3.6) \times 10^{-4}$

Table 7.9: Different production rates and number of events observed for strange particles coming from neutrino-neon interactions in the charged current mode at Fermilab bubble chamber.

The Reference^[141] reports about neutral strange particle production in the Fermilab bubble chamber at the average neutrino energy of ~ 150 GeV. The analysis focuses on neutrino and anti neutrino interactions on a $H_2 - Ne$ mixture in the charged current mode. Experiment reports following production rates (see Table 7.10).

The work published in the Reference^[142] reports the production of charged and neutral strange particles at the ANL (Argonne National Lab) 12-ft bubble chamber^[143] in both neutral current and charged current interactions. The energy spectrum of the neutrinos used here peaked less than 1 GeV. Here they study neutrino interactions on both deuterium and hydrogen. See Table 7.11. Figure 7.14 shows bubble chamber image of the reaction $\nu + n \rightarrow \nu + \Lambda + K^0$.

Particle Type	Production Rate in the ν mode (%)	Production Rate in the $\bar{\nu}$ mode (%)
K^0	40.8 ± 4.8	45.4 ± 7.8
Λ	12.7 ± 1.4	11.8 ± 1.9
$\bar{\Lambda}$	1.5 ± 0.5	1.0 ± 0.7
Σ^0	1.8 ± 1.1	-

Table 7.10: Different production rates for different individual strange particles at neutrino energies of 150 GeV on a $H_2 - Ne$ target at Fermilab bubble chamber. Rates are only for charged current interaction.

Interaction Type	No. of events
$\nu_\mu + d \rightarrow \nu_\mu + \Lambda + K_S^0$	1
$\nu_\mu + d \rightarrow \mu^- + \Lambda + K^+$	2
$\nu_\mu + d \rightarrow \mu^- + \pi^+ + \Lambda + K_L^0$	1
$\nu_\mu + p \rightarrow \mu^- + p + K + K_S^0 + \pi^0$	1
$\nu_\mu + d \rightarrow \mu^- + p + K_S^0$	1

Table 7.11: Number of events observed for different production channels listed in both charged current and neutral current interactions in the ANL bubble chamber. Here the neutrino interactions are studied on deuterium and hydrogen targets.

Moreover, the cross sections compared to pion production are,

$$\frac{\sigma(\nu + n \rightarrow \mu^- + \Lambda + K^+)}{\sigma(\nu + N \rightarrow \mu^- + N + m\pi)} = 0.04 \pm 0.03$$

$$\frac{\sigma(\nu + N \rightarrow \mu^- + p + K)}{\sigma(\nu + N \rightarrow \mu^- + N + m\pi)} = 0.03 \pm 0.03$$

and the neutral current to charge current cross section ratio is,

$$\frac{\sigma(\nu \Lambda K^0)}{\sigma(\mu^- \Lambda K^+)} = 1.5 \pm 1.5$$

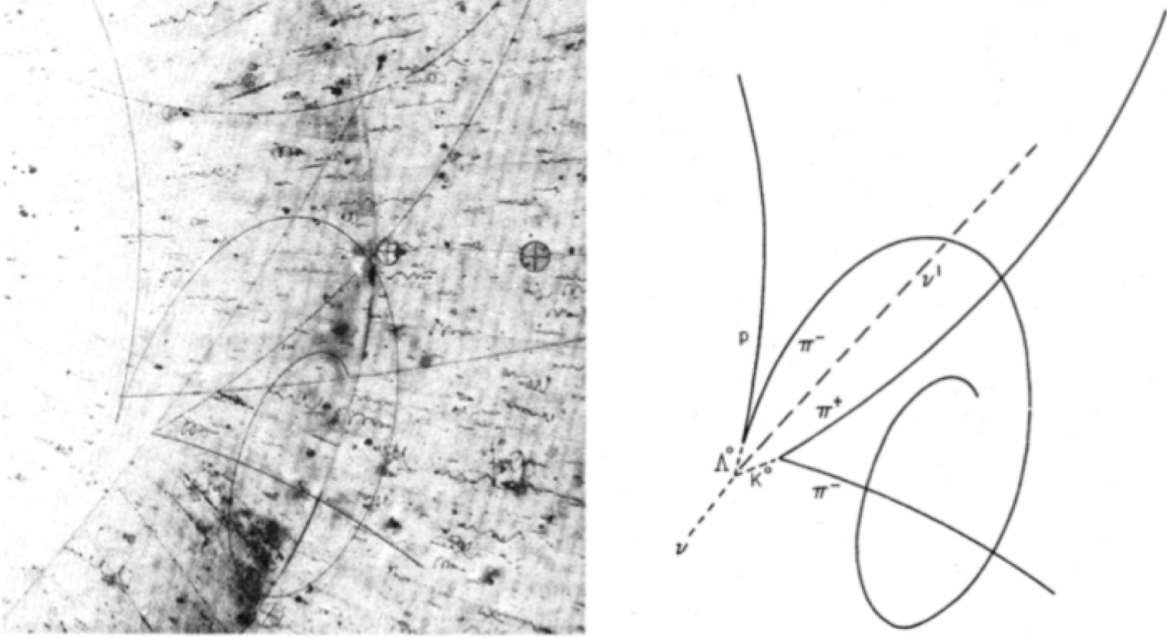


Figure 7.14: Bubble chamber image of the channel $\nu + n \rightarrow \nu + \Lambda + K^0$ [142].

The Reference [144] discusses the K meson production from the interaction of ν_μ -deuterium at ANL bubble chamber with the special purpose of evaluating background for nucleon decay experiments. The results reveal,

$$\frac{\sigma_{K^0 CC}}{\sigma_{SCC}} = 0.18 \pm 0.12$$

$$\frac{\sigma_{K^+ CC}}{\sigma_{SCC}} = 0.82 \pm 0.12$$

Here σ_{SCC} stands for the cross section if there is a K^+ or K^0 in the charged current interaction.

$$\frac{\sigma_{SCC}(\Delta S = 0)}{\sigma_{SCC}(\Delta S = 0) + \sigma_{SCC}(\Delta S = 1)} = 0.74 \pm 0.27$$

$$\frac{\sigma_{SNC}(\Delta S = 0)}{\sigma_{SCC}(\Delta S = 0) + \sigma_{SCC}(\Delta S = 1)} = 0.25 \pm 0.17$$

In this analysis the neutrino energy hovers in the region of $1 \text{ GeV} < E_\nu < 5 \text{ GeV}$. The final estimate is 6 ± 2 neutrino interactions producing strange particles in the final state inside one kiloton detector in an exposure time of one year.

The work published in the Reference^[145] describes the strange particle production at 7-ft bubble chamber^[146] at BNL (Brookhaven National Lab). Neutrino interactions are studied both on hydrogen and deuterium in the charged current and neutral current modes. They report an observation of 37 charged current and 9 neutral current events where strange particles are produced in the final state. The cross section results are,

$$\frac{\nu + d \rightarrow \mu^- + V^0 + \dots}{\nu + d \rightarrow \mu^- + \dots} = (4.2 \pm 1.0)\%, E_\nu > 1.5 \text{ GeV}$$

$$\frac{\nu + d \rightarrow \mu^- + K^0 + \dots}{\nu + d \rightarrow \mu^- + \dots} = (2.4 \pm 0.9)\%, E_\nu > 1.5 \text{ GeV}$$

The ratio between neutral current versus charged current reactions is,

$$\frac{\nu + d \rightarrow \nu + V^0 + \dots}{\nu + d \rightarrow \mu^- + V^0 + \dots} = 0.22 \pm 0.14$$

$$\frac{\sigma(\nu + K^+ + \Lambda)}{\sigma(\mu^- + K^+ + \Lambda) + \sigma(\mu^- + K^+ + \Lambda + X^0)} = 0.18 \pm 0.13$$

$$\frac{\sigma(\nu + K^0 + \Lambda)}{\sigma(\mu^- + K^+ + \Lambda) + \sigma(\mu^- + K^+ + \Lambda + X^0)} < 0.20$$

Here X^0 stands for undetected neutrals.

The work cited in the Reference^[147] explains the cross section for the reaction $\nu + n \rightarrow \mu^- + \Lambda + K^+$ for different neutrino energies at Fermilab bubble chamber. They observed a total of 21 events from this particular reaction and cross sections at different energies are listed in the Table 7.12.

Neutrino Energy Range	Cross Section ($\times 10^{-40} cm^2$)
$10 \text{ GeV} < E_\nu < 20 \text{ GeV}$	$4.7 \pm 1.8 \pm 1.0$
$20 \text{ GeV} < E_\nu < 30 \text{ GeV}$	$6.5 \pm 3.0 \pm 1.3$
$30 \text{ GeV} < E_\nu < 200 \text{ GeV}$	$5.8 \pm 3.0 \pm 1.2$
$E_\nu > 10 \text{ GeV}$	$5.5 \pm 1.3 \pm 1.1$

Table 7.12: Cross sections for the reaction $\nu + n \rightarrow \mu^- + \Lambda + K^+$ at different neutrino energies.

The publication^[148] reports about the strange particle production at the GARGAMELLE neutrino experiment^[30]. The detector is a bubble chamber filled with heavy freon and CF_3Br where energy of the neutrinos, which are responsible in producing strange particles in the final state are above 1 GeV. They report an interaction ratio between neutral current mode and charged current mode in the associated strange particle production to be,

$$\frac{SNC}{SCC} |_{\Delta S=0} = 0.34_{-0.09}^{+0.17}$$

Where $\Delta S = 0$ events include, strange particle pairs $K^+\Lambda, K^0\Lambda, K^+\bar{K}^0, K^0\bar{K}^0$.

The References cited in^{[149][150]} report the charged kaon production (K^+) in MINERVA experiment^[151]. Here the analysis is carried out in studying neutrino interactions on a carbon target in both charged current mode and neutral current mode. The neutrinos are extracted

from Fermilab NUMI beam. This is the first high statistic charged kaon production analysis on a complicated nuclear target, which simply dwarfs the previous measurements of charged kaon production at least by 50 times as far as the statistics are concerned. The analysis reports that they observed 885 charged kaon events in the charged current mode and 201 kaon events in the neutral current interaction. Figure 7.15 shows the single differential cross section of charged kaon production w.r.t kaon kinetic energy in both charged and neutral current modes. Figures 7.16 and 7.17 are event displays of kaon events, observed in MINERVA in charged current and neutral current modes respectively.

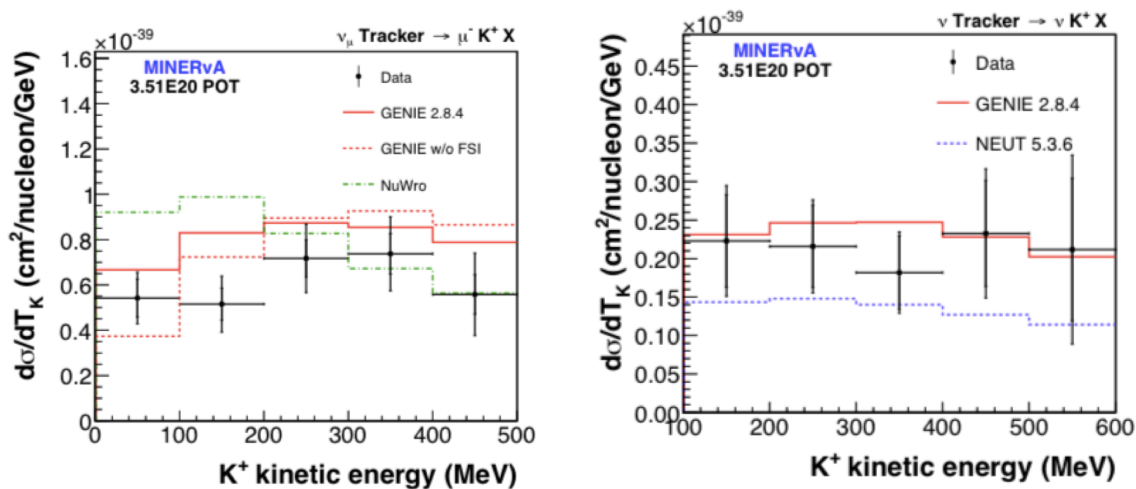


Figure 7.15: (Left) Differential cross section of charged kaon production in the charged current mode^[149]. Here comparison is made with NuWro and GENIE generators. The red dash line shows the prediction by GENIE with the FSI model turned off. (Right) Differential cross section of charged kaon production in the neutral current mode^[150]. Here the comparison is made with NEUT and GENIE generators.

The work published in the Reference^[121] reports about the presence of very rare single kaon coherent production in the charged current mode ($\nu_\mu + A \rightarrow \mu^- + K^+ + A$, A - Target nucleus). In the entire data set, they observed only six of these events (see Figure 7.18).

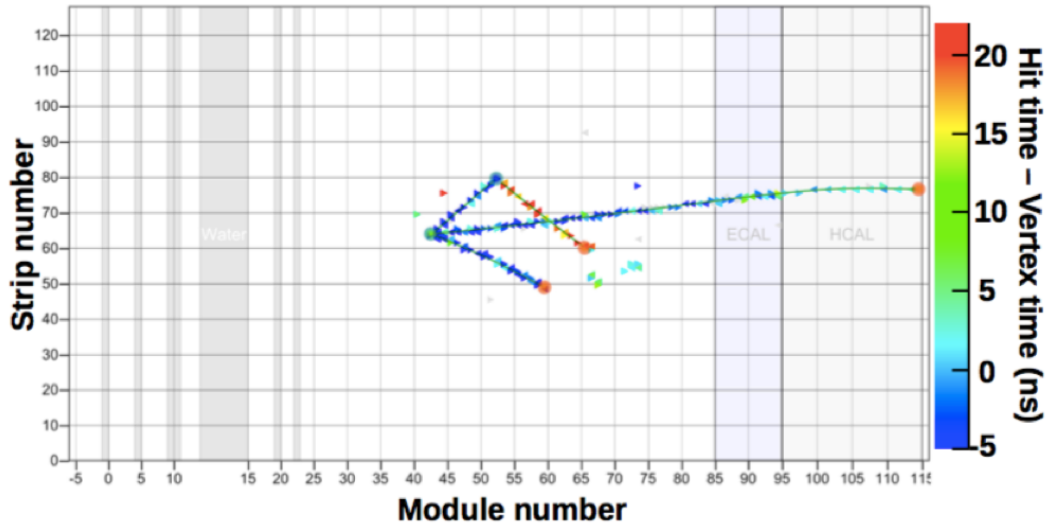


Figure 7.16: Charged current K^+ event observed in the MINERVA data^[149]. Here long track is the muon and kinked track is the K^+ decaying into μ^+ .

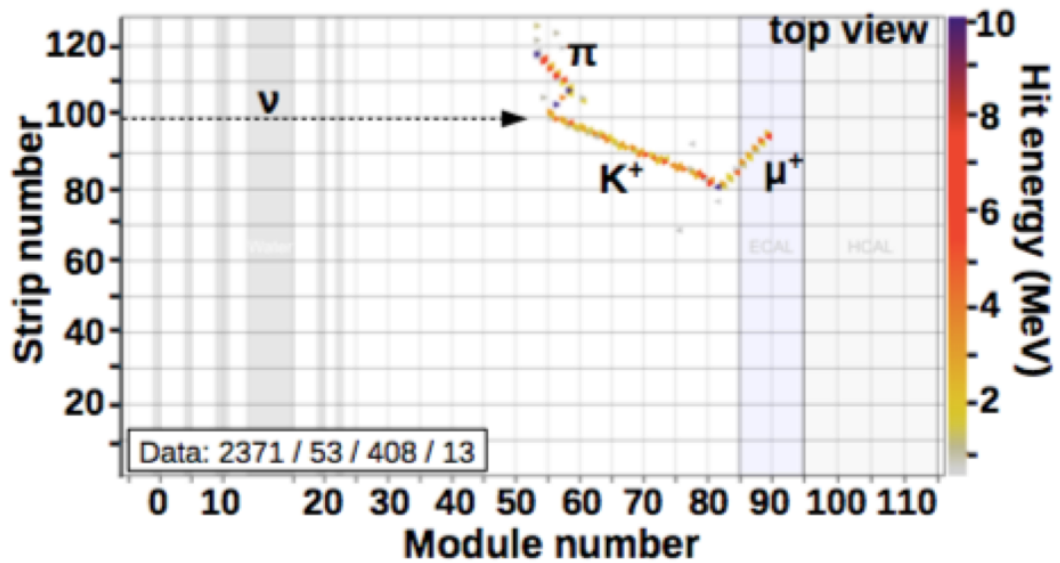


Figure 7.17: Neutral current K^+ event observed in the MINERVA data^[150].

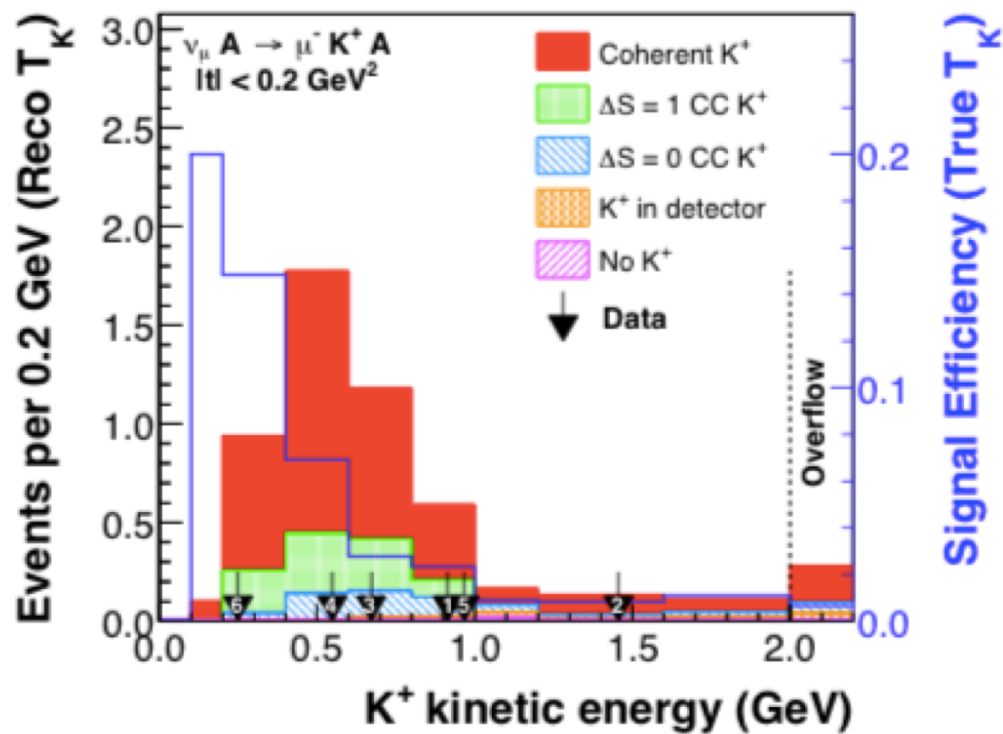


Figure 7.18: Kinetic energy of K^+ produced coherently in the interaction $\nu_\mu + A \rightarrow \mu^- + K^+ + A$ in the MINERVA detector^[121].

Chapter 8

Event Selection of Charged Current Neutrino Induced Kaon Events in MicroBooNE

In this chapter the discussion is about data samples used in this analysis, kaon production simulations, data reconstruction, calorimetry-based particle identification in MicroBooNE, event selection, background estimation, data-Monte Carlo comparisons, final results, and future plans.

8.1 MC and Data Samples

In this analysis, we used Monte Carlo, ON-Beam data, and OFF-Beam data. The Monte Carlo includes both neutrino and cosmic interactions. The cosmic interactions are simulated with the CORSIKA cosmic generator^[106]. Both Monte Carlo and data files are filtered using the CC Inclusive filter^[152] to isolate charged current neutrino interactions, and calibrated data products are saved (dQ/dx and dE/dx calibration schemes discussed in the Chapter 6 are applied). More details of these data sets can be found in the Table 8.1.

In the second and third data sets mentioned in Table 8.1, only neutrino induced associated

Data set name	Type	POT	# of Triggers
BNB plus cosmic	Monte Carlo	2.06712×10^{21}	-
Associated Kaons plus cosmic	Monte Carlo	1.48375×10^{23}	-
Single Kaons plus cosmic	Monte Carlo	6.31985×10^{22}	-
ON-Beam data	Data	1.595×10^{20}	35504733
OFF-Beam data	Data	-	21013851

Table 8.1: Data set information.

and single kaon events are simulated respectively in charged current mode. In all datasets, to reconstruct all types of particle tracks, the *Pandora* package^[107] is used.

The purpose of the first dataset in the table is to estimate the background introduced by events, which do not have a K^+ produced in the charged current interaction. In addition, the OFF-Beam dataset mentioned in the bottom of the table is also used to estimate the background due to cosmic interactions inside the detector in MicroBooNE data. The second and third datasets are used to estimate the Monte Carlo signal. When generating only charged current K^+ events in dataset 1 and 2, only the events having charged muon (μ^-) and K^+ at generator level are selected.

8.2 Simulation

In MicroBooNE, we are using the GENIE^[153] neutrino generator (Generates Events for Neutrino Interaction Experiments) to simulate neutrino interactions with argon (specific GENIE version used for this analysis is v2.12.2). GENIE uses Relativistic Fermi Gas (RFG) model^[154] to interpret the behaviour of nucleons inside the nucleus. The RFG model assumes nucleons are only affected by the mean field of the nucleus and independent of the other nucleons. The momentum of the nucleons inside the nucleus at any time is given by the Fermi distribution. GENIE produces neutrino induced K^+ both $\Delta S = 0$ (associated kaon production) and $\Delta S = 1$ (single kaon production) processes. But by default only $\Delta S = 0$ process is enabled in GENIE and $\Delta S = 1$ process should be turned on manually. The associated kaon production can happen via both baryonic resonances and Deep Inelastic

Scattering (DIS). In GENIE, only the baryonic resonances with hadronic invariant mass (W) $< 1.7 \text{ GeV}$ are simulated using the Rein-Sehgal model^[117]. So in this regime of hadronic invariant mass only the reaction $K^+\Lambda$ is allowed via resonance. To simulate DIS processes, GENIE is using the Bodek-Yang hadronization model^[155]. For the K^+ production via DIS in the energy regime of $1.7 \text{ GeV} < W < 2.3 \text{ GeV}$, GENIE is using a hadronization model based on the parameterization of the Koba-Nielsen-Olesen (KNO)^[156] scaling. The regime $2.3 \text{ GeV} < W < 3.0 \text{ GeV}$ is governed by the AGKY model^[157] while for $W > 3.0 \text{ GeV}$, it is PYTHIA6^[158]. All the parameters in these hadronization models are tuned in such a way that they agree with the observations of strange particle production in the Big European Bubble Chamber (BEBC) and Fermilab bubble chambers. To simulate final state interactions GENIE uses an effective cascade model named *hA*. When it comes to final state interactions undergone by K^+ , the *hA* model only simulates re-scattering of the kaon inside the nucleus, which ultimately results in a net loss of kinetic energy when the particle emerges out of the nucleus (We observe a maximum of $\sim 5\%$ momentum loss due to scattering of K^+ inside the argon nucleus.) The charged current single kaon production in GENIE is modeled using work done by Alam *et al*, which is documented in the Reference^[120]. The processes that can produce kaons in the single kaon production are discussed in detail in the Section 7.1 of Chapter 7.

8.3 Truth Level and Reconstructed Level Information

In the search for neutrino induced kaons, our signal is charged kaons produced in the charged current mode, which ultimately decay at rest to muons/pions. But from Monte Carlo truth level studies, we found that almost all of the K^- are captured before they decay. It is only the K^+ that decays giving birth to muons and pions. Figure 8.1 shows how a K^+ produced in the charged current interaction decays to a muon while Figure 8.2 is an event display showing how a K^+ produced in the charged current interaction decays to two pions. Table 8.2 summarizes the production rates of neutrino induced kaons in charged current mode in MicroBooNE according to truth level information at a POT equivalent to 6.6×10^{20} .

Here both single and associated kaon production modes are considered in estimating these rates while always the K^+ is assumed to have been confined in the TPC. Moreover, in these estimations, the neutrino interaction is always supposed to be contained within the fiducial volume defined in the Figure 8.3.

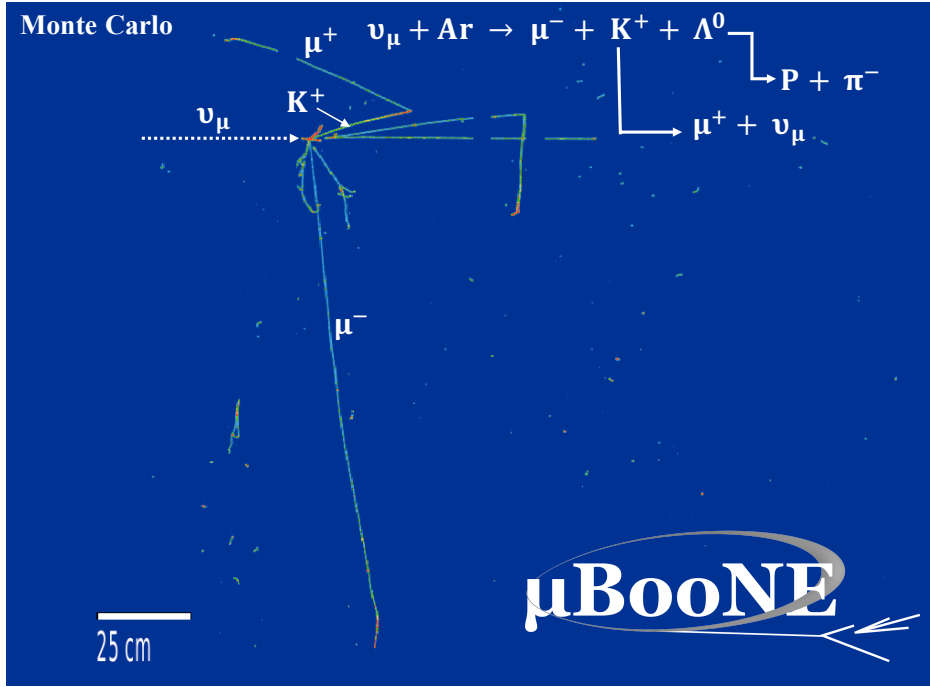


Figure 8.1: A Monte Carlo event display showing neutrino induced kaon decaying to muon.

Signal Type	# of events
All K^+	149.8
$K^+ \rightarrow$ All decay modes (Kinetic Energy of $K^+ < 30MeV$)	113.25
$K^+ \rightarrow \mu^+ + \nu_\mu$ (Kinetic Energy of $K^+ < 30MeV$)	71.54
$K^+ \rightarrow \pi^+ + \pi^0$ (Kinetic Energy of $K^+ < 30MeV$)	23.43
$K^+ \rightarrow \mu^+ + \nu_\mu$ (Kinetic Energy of $K^+ < 30MeV$ and both K^+ and μ^+ are contained in the TPC)	64.09
$K^+ \rightarrow \pi^+ + \pi^0$ (Kinetic Energy of $K^+ < 30MeV$ and both K^+ and π^+ are contained in the TPC)	22.79

Table 8.2: Kaon production rates of MicroBooNE at charged current mode by looking into truth level information at a POT equivalent to 6.6×10^{20} .

When identifying charged kaons inside the detector, the decay products of those kaons play a vital role. Most of the time when a charged kaon decays to a muon or a pion, a characteristic kinked track signature is produced, which easily distinguishes the kaon decay from other decay typologies as it can be seen in the two event displays in Figures 8.1 and 8.2.

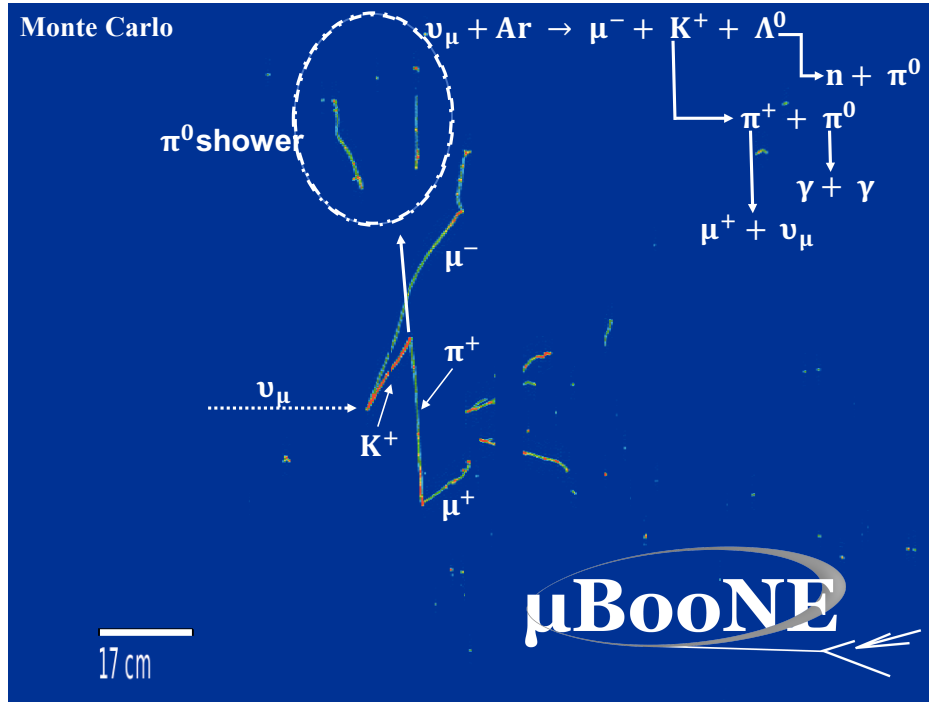


Figure 8.2: A Monte Carlo event display showing neutrino induced kaon decaying to pion in MicroBooNE.

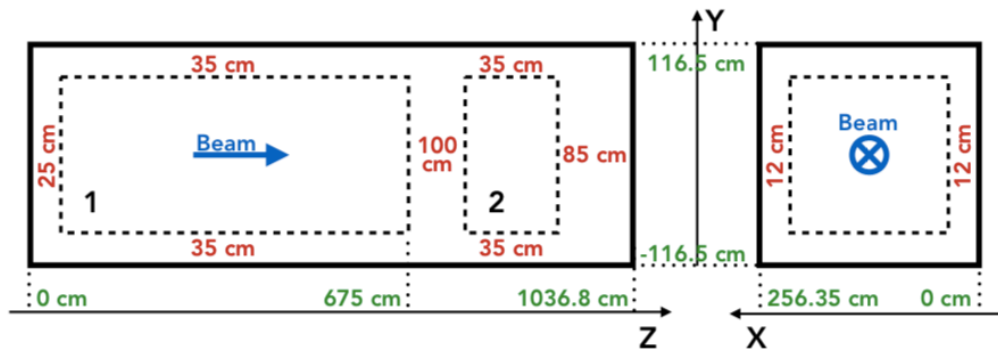


Figure 8.3: Fiducial volume defined within which all the neutrino interaction vertices are supposed to be contained. Here, the area within the dashed lines is the fiducial volume of interest. Image courtesy of Anne Schukraft and Marco Del Tutto.

Table 8.3 summarizes the branching fractions of the most dominant K^{+} decay modes. Here the first and second decay modes are of particular interest as these are two body decays, the pions and muons coming out of these decay modes have well defined kinetic energies (hence track lengths) always. Figure 8.4 shows the kinetic energies and track lengths of muons

and pions coming out of kaon decay at rest. This information is very helpful in mitigating background significantly in isolating K^+ events.

Decay Mode	Branching Fraction (%)
$K^+ \rightarrow \mu^+ + \nu_\mu$	63.56
$K^+ \rightarrow \pi^+ + \pi^0$	20.67
$K^+ \rightarrow \pi^+ + \pi^+ + \pi^-$	5.583
$K^+ \rightarrow \pi^0 + e^+ + \nu_e$	5.07
$K^+ \rightarrow \pi^0 + \mu^+ + \nu_\mu$	3.352
$K^+ \rightarrow \pi^+ + \pi^0 + \pi^0$	1.760

Table 8.3: The six most dominant K^+ decay modes and branching fractions.

From Figure 8.5 to 8.8 show the reconstructed information of different kinematic variables and respective reconstruction resolution of those variables for kaon tracks, which decay at rest to muons/pions. All these plots were generated using Monte-Carlo reconstructed level information, and resolutions were calculated using Equation 8.1.

$$Resolution = \frac{Reconstructed\ quantity - Truth\ level\ quantity}{Truth\ level\ quantity} \quad (8.1)$$

Figures 8.9 to 8.12 show the reconstructed information of different kinematic variables and respective reconstruction resolutions of those variables for muons coming from kaon decay at rest. Here again all the plots were generated using Monte-Carlo reconstructed level information and resolutions were calculated using Equation 8.1.

8.4 Calorimetry Based Particle Identification for Kaons/Muons

When a charged particle traverses through some medium the main source of energy loss is Ionization. Moreover, ionization energy loss is strongly correlated with the particles mass at low velocities for a given medium. So if a given particle is known to come to rest before

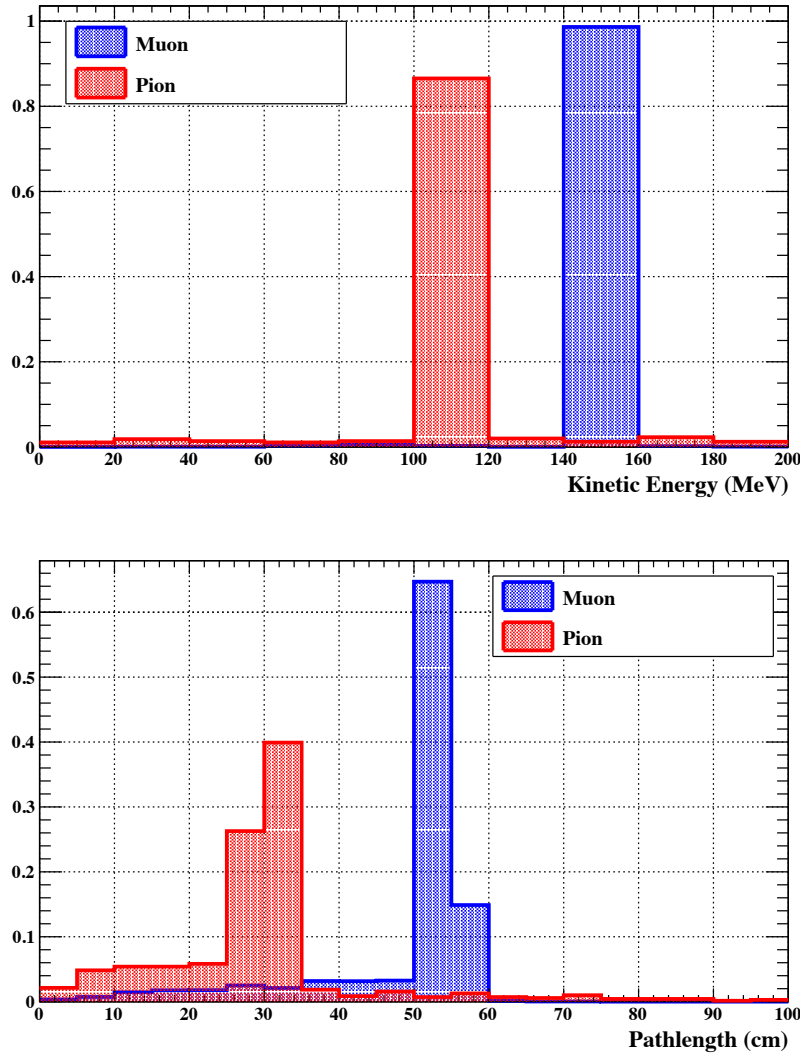


Figure 8.4: (Top) Kinetic energies of muons and pions coming from kaon decay at rest. (Bottom) Track lengths of muons and pions coming from kaon decay at rest. Both of these distributions were generated using Monte Carlo truth level information.

it undergoes any interaction, then the dE/dx (energy loss per unit length) profile of that particle can be used as a tool to find its identity.

In MicroBooNE we calculate a χ^2 value for each particle tracks under different particle hypothesis by comparing the particle's dE/dx profile with different standard dE/dx profiles of different particle types calculated using Bethe-Bloch formula in liquid argon. Figure 8.13 shows the standard dE/dx energy profiles for different particle types in liquid argon.

In this particular analysis, we found that χ^2 values calculated under both proton hypoth-

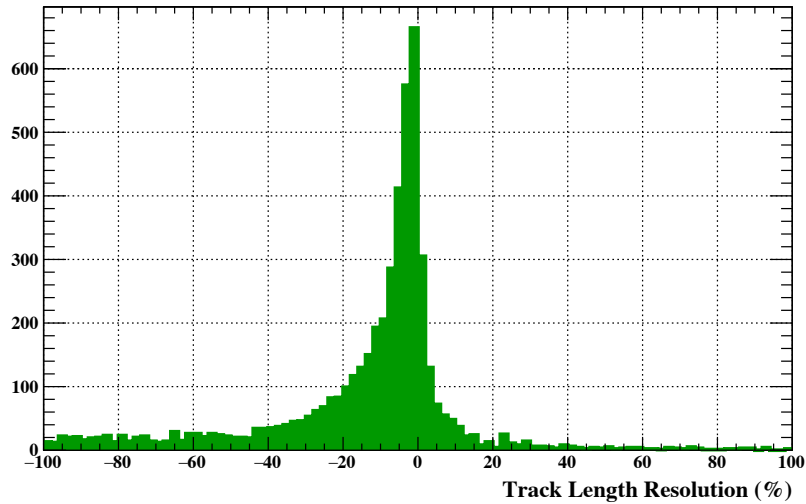
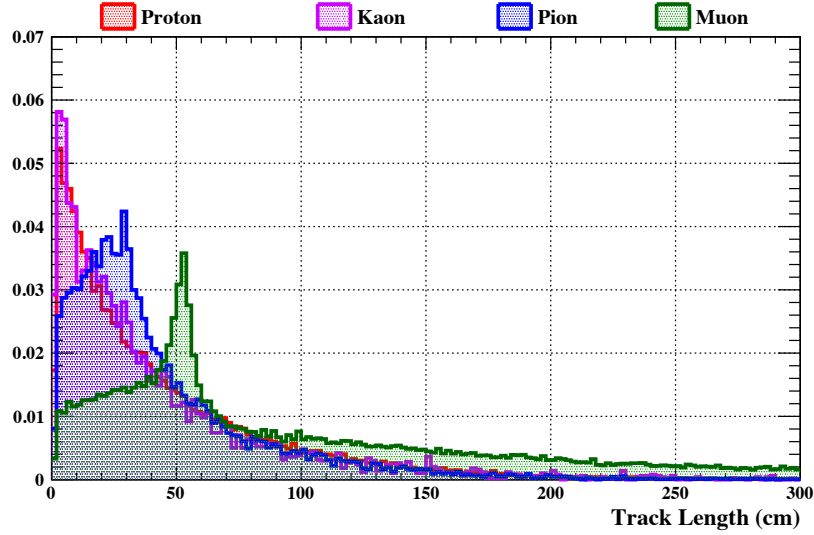


Figure 8.5: (Top) Comparison of reconstructed track length of kaons (decay at rest to pions/muons) with other particle types. (Bottom) Resolution of the track length of kaons, which decay at rest to pion/muons. All the distributions in the top plot were area normalized to 1.

esis and kaon hypothesis (χ_P^2 and χ_K^2) perform equally well in distinguishing kaons decaying at rest from other particle types (see Figure 8.14). Moreover, we also found that χ^2 value calculated under proton hypothesis is also working well in selecting the muons/pions coming out of kaons that decay at rest (see Figure 8.15).

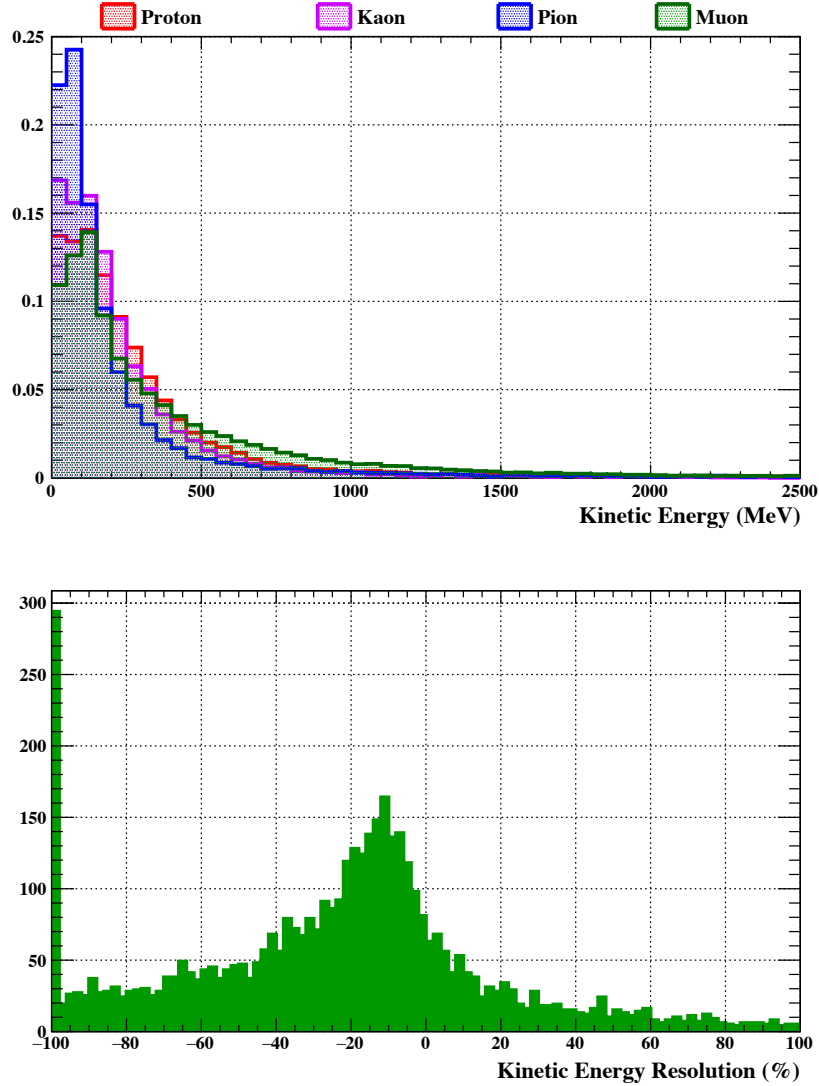


Figure 8.6: (Top) Comparison of reconstructed calorimetric kinetic energy of kaons (decay at rest to pions/muons) with other particle types. (Bottom) Resolution of the calorimetric kinetic energy of kaons, which decay at rest to pion/muons. All the distributions in the top plot were area normalized to 1.

8.5 Event Selection

By looking into the details of the Figures 8.5-8.8, 8.9-8.12, Figure 8.14, and Figure 8.15, we went on to define some selection cuts in order to isolate neutrino induced kaon events as described in the following steps.

In the first step we look for events, which have more than three tracks reconstructed.

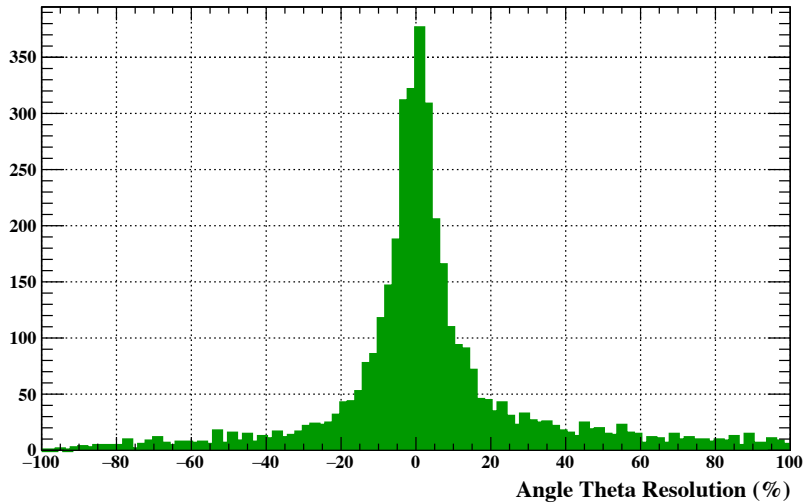
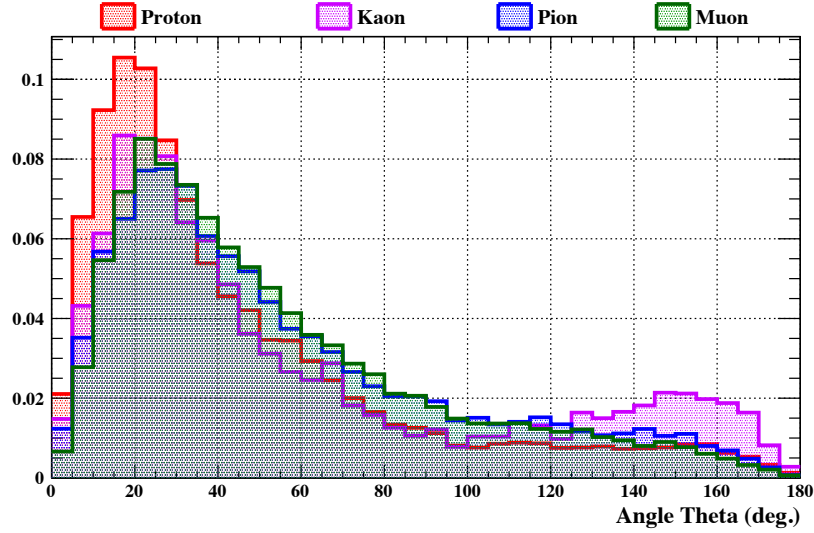


Figure 8.7: (Top) Comparison of reconstructed polar angle w.r.t beam direction (θ) of kaons (decay at rest to pions/muons) with other particle types. (Bottom) Resolution of the polar angle θ of kaons, which decay at rest to pion/muons. All the distributions in the top plot were area normalized to 1.

Here the three tracks serve as the candidates for charged current muon, neutrino induced kaon, and muon coming from kaon decay. Once an event contains more than three tracks reconstructed, we check whether that event contains two tracks originating within 7 cm from the neutrino vertex. The two tracks are supposed to be candidates for charged current muon and neutrino induced kaon. Then we move to get the kaon candidate tracks using the selection cuts listed in Table 8.4 from the events, which satisfy the above mentioned

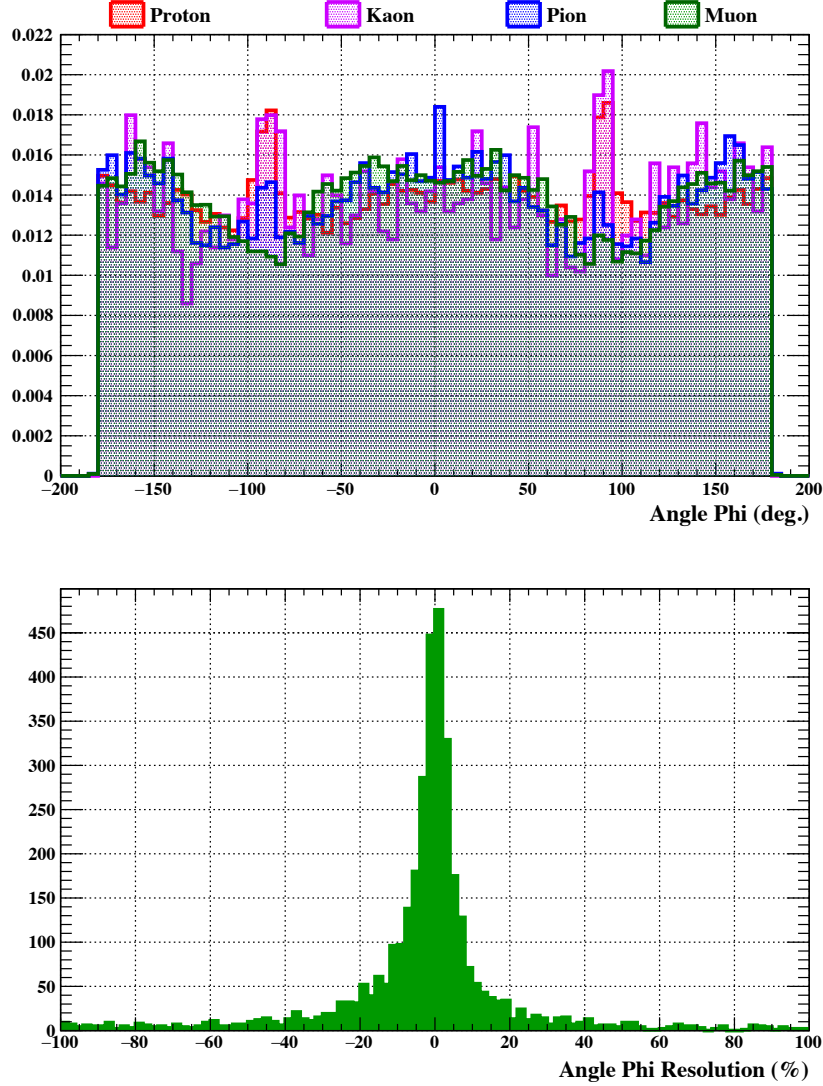


Figure 8.8: (Top) Comparison of reconstructed azimuth angle w.r.t beam direction (ϕ) of kaons (decay at rest to pions/muons) with other particle types. (Bottom) Resolution of the azimuth angle (ϕ) of kaons, which decay at rest to pion/muons. All the distributions in the top plot were area normalized to 1.

conditions.

To optimize the selection cuts on χ_P^2 and χ_K^2 variables of kaon candidate tracks listed at the bottom of the Table 8.4, the following procedure was adopted.

First we generated the $\chi_P^2 - \chi_K^2$ distributions for the tracks, which satisfy all the remaining selection cuts (except cuts on χ_P^2 and χ_K^2 variables) explained in the Table 8.4. The distributions were generated for the real kaon candidate tracks and other background tracks

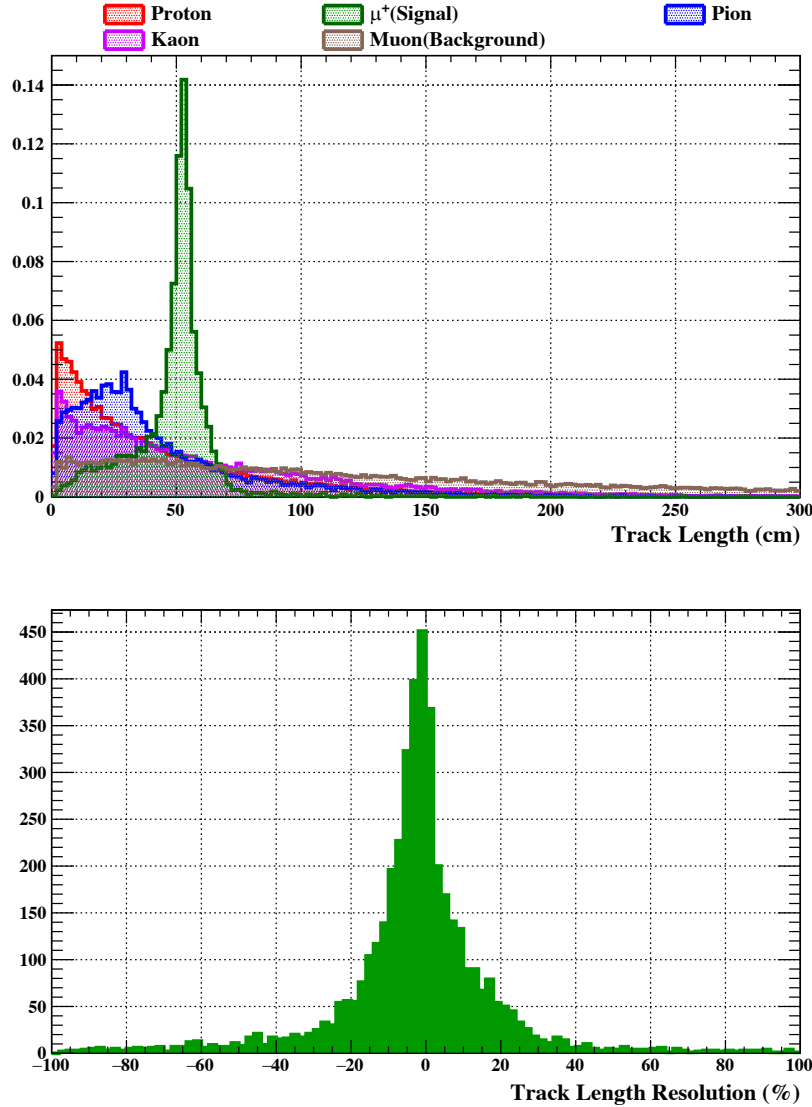


Figure 8.9: (Top) Comparison of reconstructed track length of muons coming from kaon decay at rest with other particle types. (Bottom) Resolution of the track length of muons coming from kaon decay at rest. All the distributions in the top plot were area normalized to 1.

separately. Then we counted the number of tracks bound by the curve, which is represented by the parametric Equation 8.2 for different combinations of the two free parameters A and B . This was done for signal events and background events separately. In the final step a signal to background ratio was calculated by taking the ratio between number of signal tracks to number of background tracks for a given combination of A and B values. The Figure 8.16 shows the signal to background ratio for different combinations of the two free

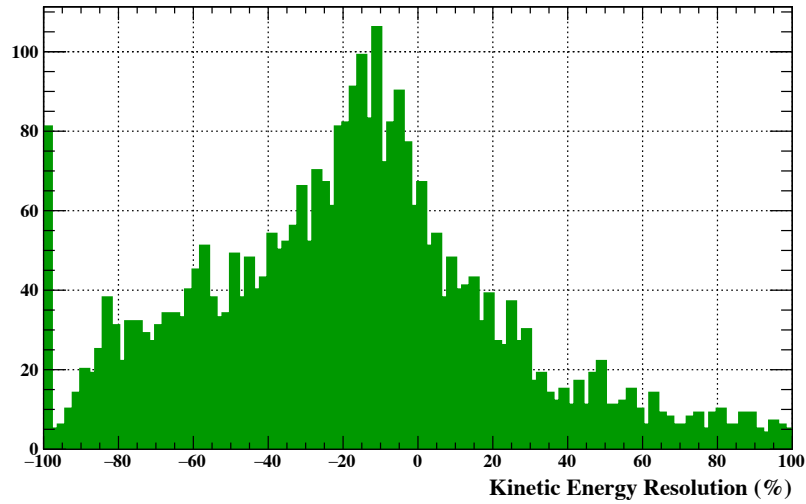
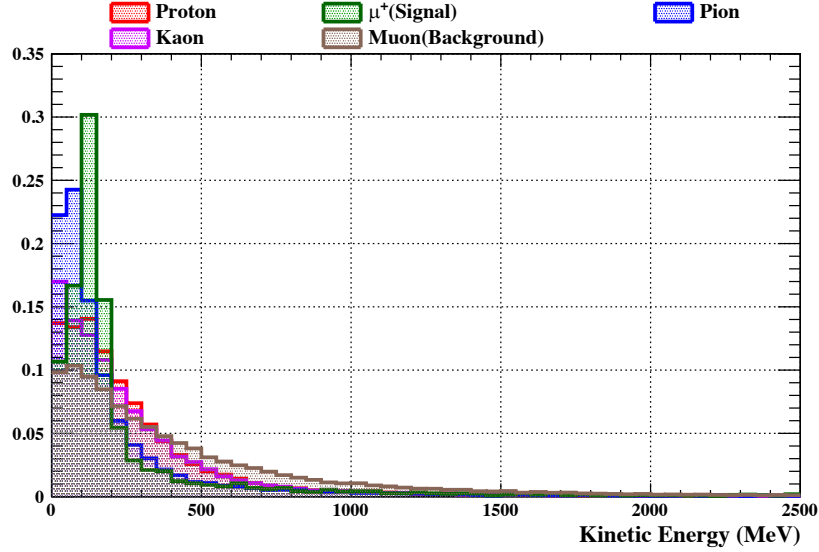


Figure 8.10: (Top) Comparison of reconstructed calorimetric kinetic energy of muons coming from kaon decay at rest with other particle types. (Bottom) Resolution of the calorimetric kinetic energy of muons coming from kaon decay at rest. All the distributions in the top plot were area normalized to 1.

parameters A and B shown in the Equation 8.2.

$$\frac{\chi_P^2}{A} + \frac{\chi_K^2}{B} = 1 \quad (8.2)$$

This equation represents a family of ellipses in the χ_P^2 - χ_K^2 phase space. The free parameter A is the intercept of the ellipse in the χ_P^2 axis and free parameter B is the intercept in the χ_K^2 axis.

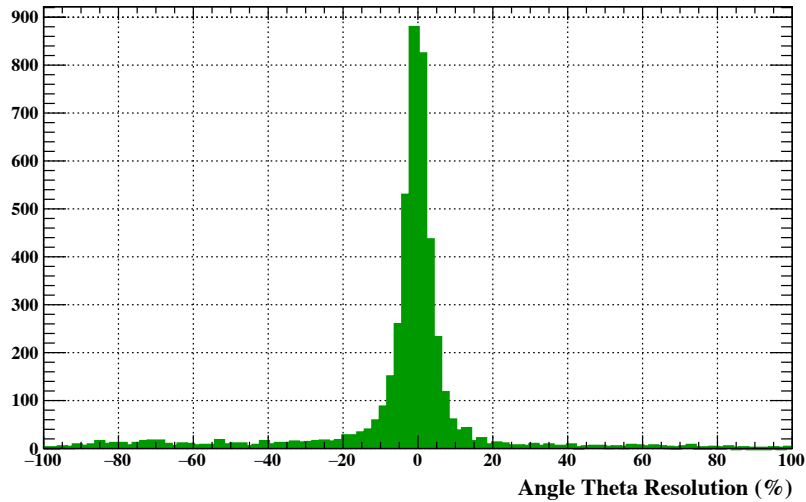
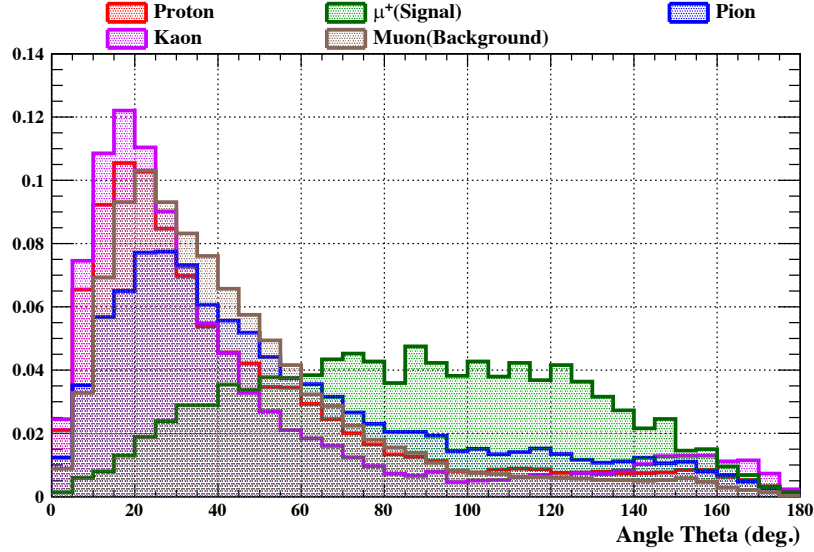


Figure 8.11: (Top) Comparison of reconstructed polar angle w.r.t beam direction (θ) of muons coming from kaon decay at rest with other particle types. (Bottom) The resolution of the polar angle θ of muons coming from kaon decay at rest. All the distributions in the top plot were area normalized to 1.

By looking into the Figure 8.16, the best signal to background ratios were observed for the two bounding curves determined by $A = 10$ & $B = 4$ and $A = 45$ & $B = 15$.

In the final step, Table 8.5 describes the selection cuts used to get muon candidate coming from kaon decay.

To determine the ideal selection cuts for muon candidate track length and χ^2_P variables, purity and efficiency curves shown in the Figure 8.18 were used. As the boundaries of the

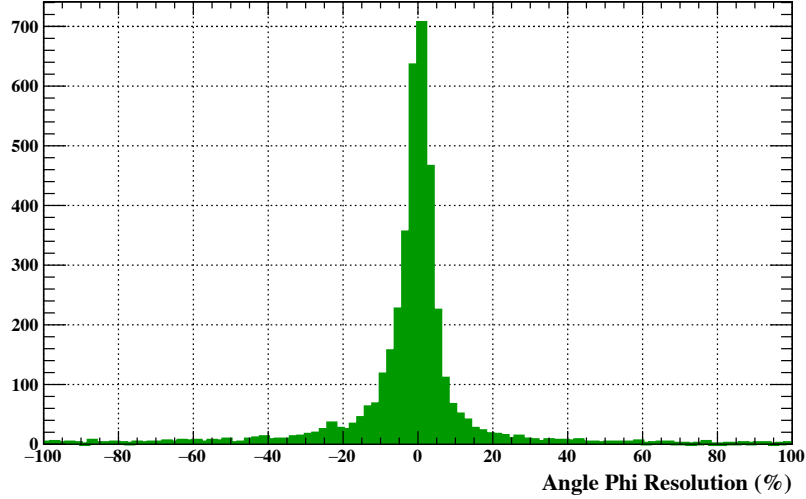
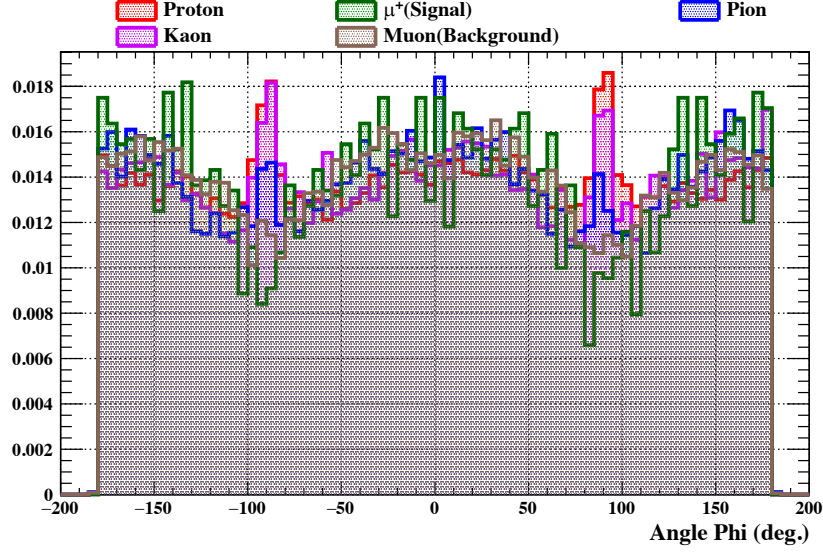


Figure 8.12: (Top) Comparison of reconstructed azimuth angle w.r.t beam direction (ϕ) of muons coming from kaon decay at rest with other particle types. (Bottom) The resolution of the azimuth angle ϕ of muons coming from kaon decay at rest. All the distributions in the top plot were area normalized to 1.

selection cuts for these variables, the points where $Efficiency \times Purity$ gets maximum were selected.

$$Efficiency(L) = \frac{\text{Total number of reconstructed events with variable value } X > a}{\text{Total number of signal events at truth level}} \quad (8.3)$$

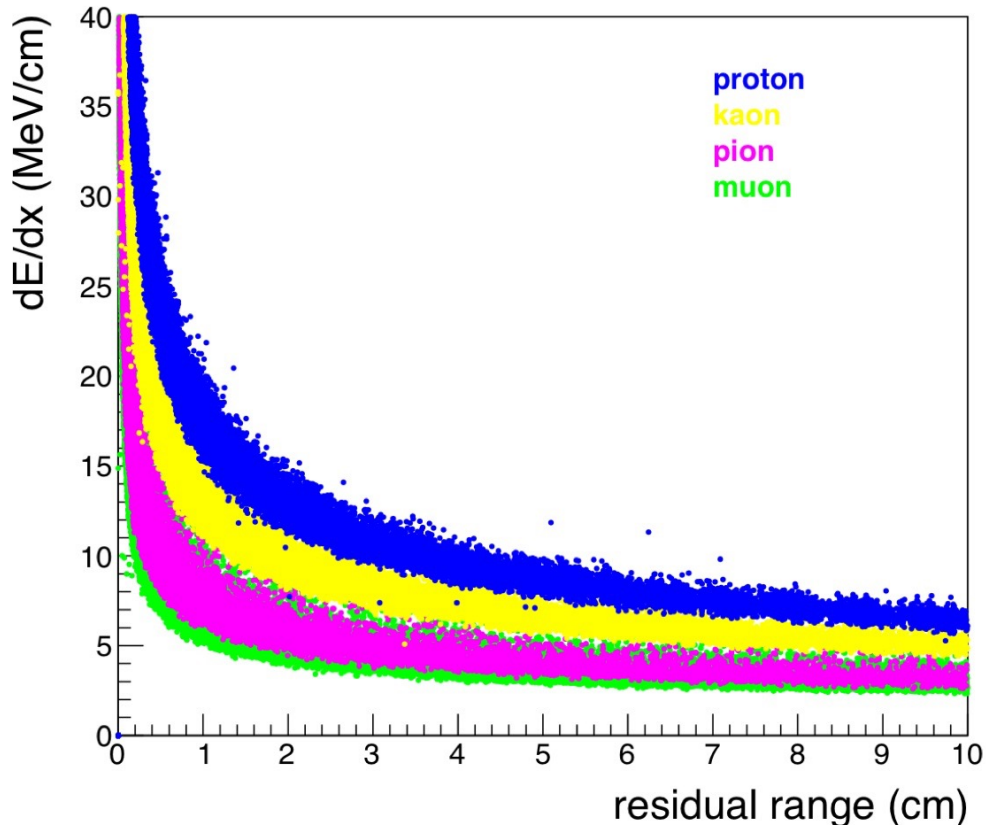


Figure 8.13: Standard dE/dx energy profiles for different particle types calculated using Bethe-Bloch formula in liquid argon.

Signal Variable	Selection Cut
Start X point of the track	$> 0 \text{ cm} \ \&\& \ < 256.35 \text{ cm}$
Start Y point of the track	$> -116.5 \text{ cm} \ \&\& \ < 116.5 \text{ cm}$
Start Z point of the track	$> 0 \text{ cm} \ \&\& \ < 1036.8 \text{ cm}$
End X point of the track	$> 0 \text{ cm} \ \&\& \ < 256.35 \text{ cm}$
End Y point of the track	$> -116.5 \text{ cm} \ \&\& \ < 116.5 \text{ cm}$
End Z point of the track	$> 0 \text{ cm} \ \&\& \ < 1036.8 \text{ cm}$
Closest distance to neutrino vertex	$< 7 \text{ cm}$
Start point of the track should be closer to the neutrino vertex than end point	
Track length	$> 5 \text{ cm}$
Number of hits, registered in the collection plane	> 5
χ_P^2 (χ^2 value using proton hypothesis)	Discussed bottom
χ_K^2 (χ^2 value using kaon hypothesis)	Discussed bottom

Table 8.4: Different selection cuts to isolate kaon tracks originating from neutrino interaction vertices.

$$Efficiency(R) = \frac{\text{Total number of reconstructed events with variable value } X < a}{\text{Total number of signal events at truth level}} \quad (8.4)$$

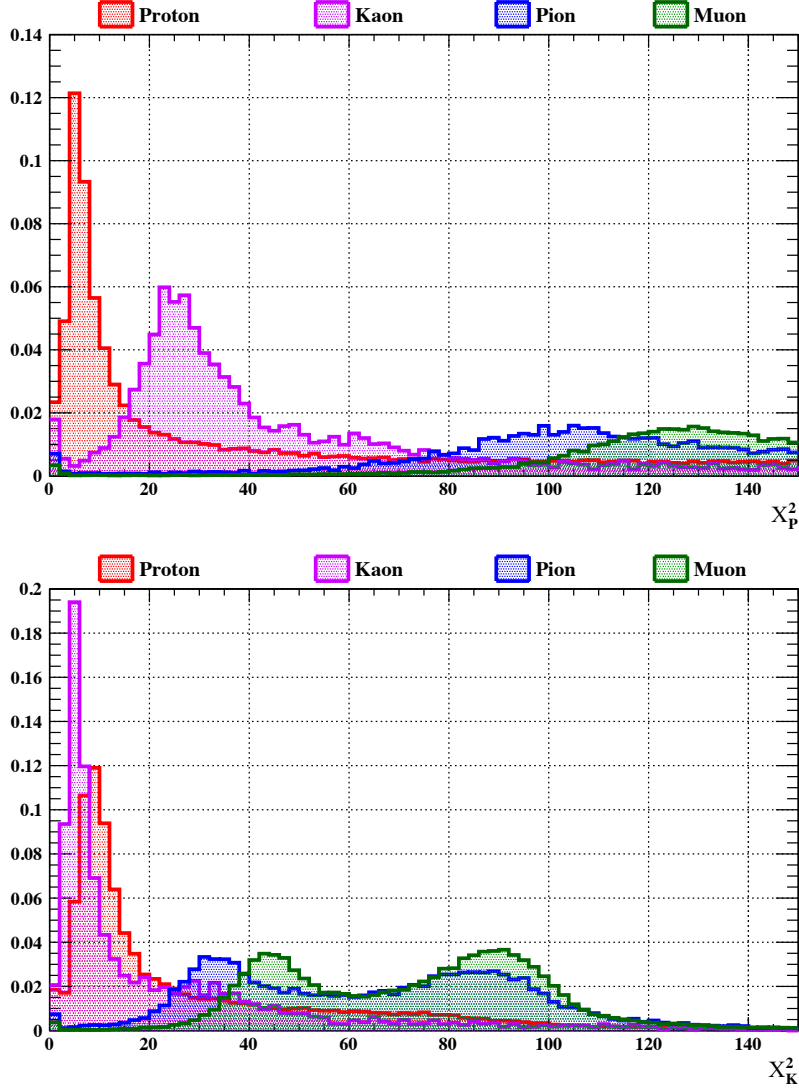


Figure 8.14: (Top) Comparison of χ^2 value calculated under proton hypothesis for kaon tracks that decay at rest with other particle tracks. (Bottom) Comparison of χ^2 value calculated under kaon hypothesis for kaon tracks that decay at rest with other particle tracks. All the distributions in both plots, here shown were area normalized to 1 and generated using Monte Carlo reconstructed information.

$$Purity(L) = \frac{\text{Total number of reconstructed signal events with variable value } X > a}{\text{Total number of reconstructed events with variable value } X > a} \quad (8.5)$$

$$Purity(R) = \frac{\text{Total number of reconstructed signal events with variable value } X < a}{\text{Total number of reconstructed events with variable value } X < a} \quad (8.6)$$

By incorporating all these selection cuts on kaon candidates and muon candidates, we wrote a filter to isolate charged current neutrino induced kaons, which ultimately decay

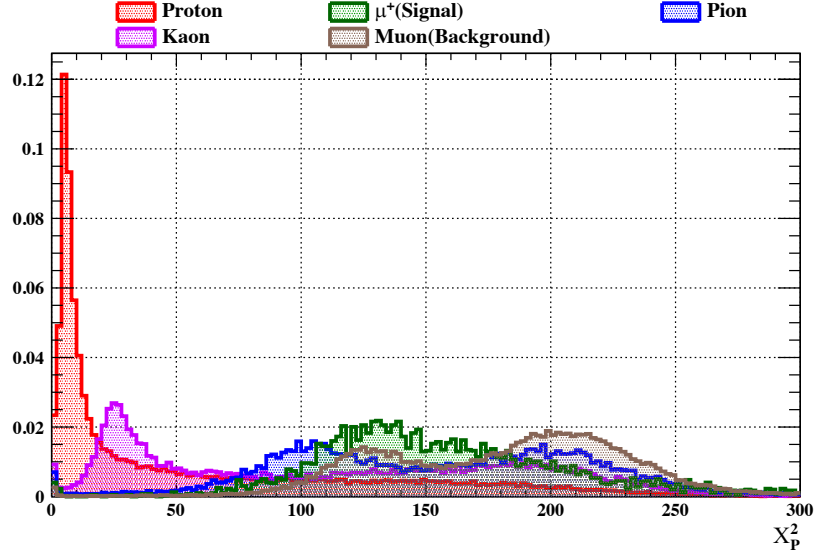


Figure 8.15: Comparison of χ^2 value calculated under proton hypothesis for muon tracks coming from kaon that decay at rest with other particle tracks. All the distributions in the plot were area normalized to 1 and generated using Monte Carlo reconstructed information.

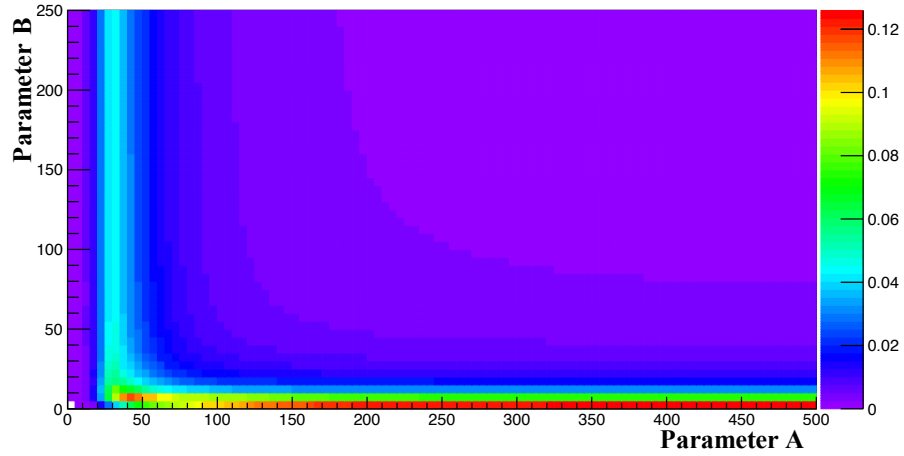


Figure 8.16: Signal/Background ratios for different combinations of the the two free parameters A and B in the Equation 8.2. Plot was generated by Jairo Rodriguez.

at rest to muons and pions. By running this filter on Monte Carlo (see Table 8.1 for a description of different data samples), we found that our filter can reach to an efficiency of 3% (from Equation 8.7) and a purity of 50% (from Equation 8.8).

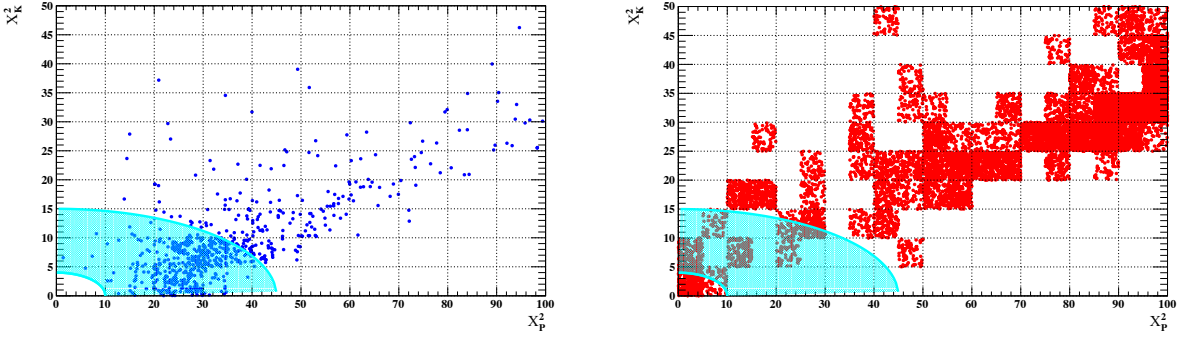


Figure 8.17: Distribution of signal and background events in the signal band of the $\chi_P^2 - \chi_K^2$ phase space. The cyan band in the plots shows the signal band defined, which is bound by the curves represented by parameter combinations $A = 10$ & $B = 4$ and $A = 45$ & $B = 15$. In the signal band we observed the highest signal to background ratio. (Left) Distribution of signal events in the $\chi_P^2 - \chi_K^2$ phase space. (Right) Distribution of background events in the $\chi_P^2 - \chi_K^2$ phase space.

Signal Variable	Selection Cut
Start X point of the track	$> 0 \text{ cm} \ \&\& \ < 256.35 \text{ cm}$
Start Y point of the track	$> -116.5 \text{ cm} \ \&\& \ < 116.5 \text{ cm}$
Start Z point of the track	$> 0 \text{ cm} \ \&\& \ < 1036.8 \text{ cm}$
End X point of the track	$> 0 \text{ cm} \ \&\& \ < 256.35 \text{ cm}$
End Y point of the track	$> -116.5 \text{ cm} \ \&\& \ < 116.5 \text{ cm}$
End Z point of the track	$> 0 \text{ cm} \ \&\& \ < 1036.8 \text{ cm}$
Closest distance to neutrino vertex	$> 5 \text{ cm}$
Track length	$> 30 \text{ cm} \ \&\& \ < 70 \text{ cm}$
Number of hits, registered in the collection plane	> 10
χ_P^2 (χ^2 value using proton hypothesis)	> 50
Closest distance to the kaon track	$< 4.5 \text{ cm}$

Table 8.5: Different selection cuts to isolate muon tracks coming from kaons that decay at rest.

$$Efficiency = \frac{\text{Total number of reconstructed signal events captured by the filter}}{\text{Total number of signal events at truth level}} \quad (8.7)$$

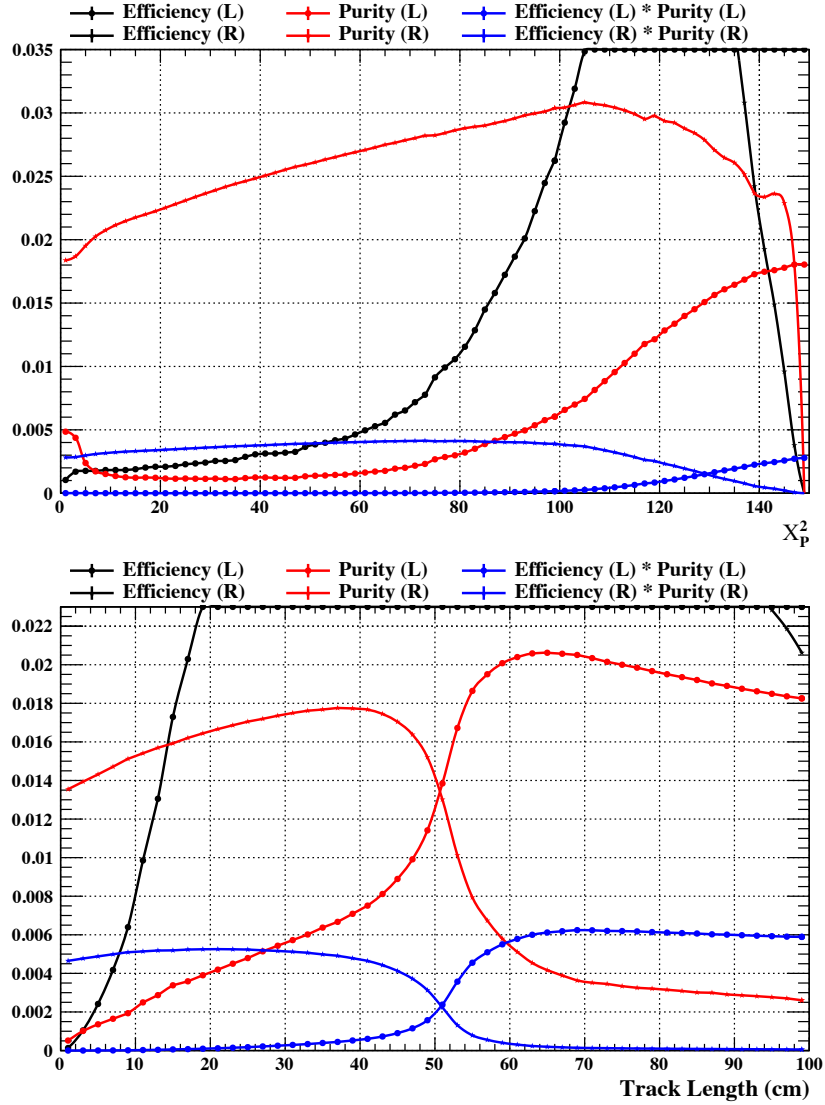


Figure 8.18: Purity and efficiency curves for muon candidate variables coming from kaon decay at rest. Here purities and efficiencies were calculated using the set of Equations 8.3 to 8.6. (Top) χ_P^2 variable. (Bottom) Track length variable.

$$Purity = \frac{\text{Total number of reconstructed signal events captured by the filter}}{\text{Total number of reconstructed events captured by the filter}} \quad (8.8)$$

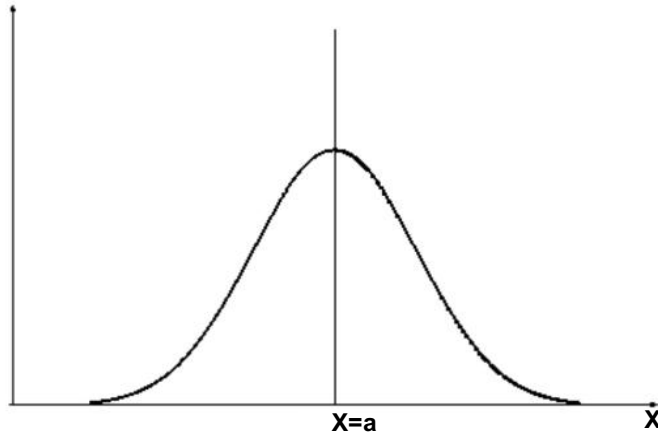


Figure 8.19: Schematic diagram showing the distribution of some arbitrary variable named \mathbf{X} to be used to define efficiencies and purities shown in the Figure 8.18.

8.6 Background Estimation

In this analysis, main sources of background include different particle scatterings such as proton-proton scattering and pion-pion scattering etc. Moreover, reconstruction inefficiencies such as getting the neutrino vertex wrong and broken tracks can also introduce significant amount of background contamination. Figures 8.20 to 8.23 are some event displays showing different background sources in Monte Carlo and data.

To estimate the background in a data-driven way, we performed a side band study in this analysis. We selected χ^2 variables calculated using proton hypothesis (χ^2_P) and kaon hypothesis (χ^2_K) of the kaon candidate as two ideal variables to perform this study. First we defined two upper side bands w.r.t the signal region as indicated in the Figures 8.24 and 8.25 (A lower side band cannot be defined due to the lack of statistics). The sizes of the side bands were determined in order to have enough statistics. Here on wards the side band closest to the signal band will be called the *Side band 1* and side band farther away from the signal band as *Side band 2*.

Figure 8.26 shows the comparison of kaon track length in Monte-Carlo and in data in side band 1 and side band 2. A ratio was calculated in each of these plots between *Monte-Carlo*

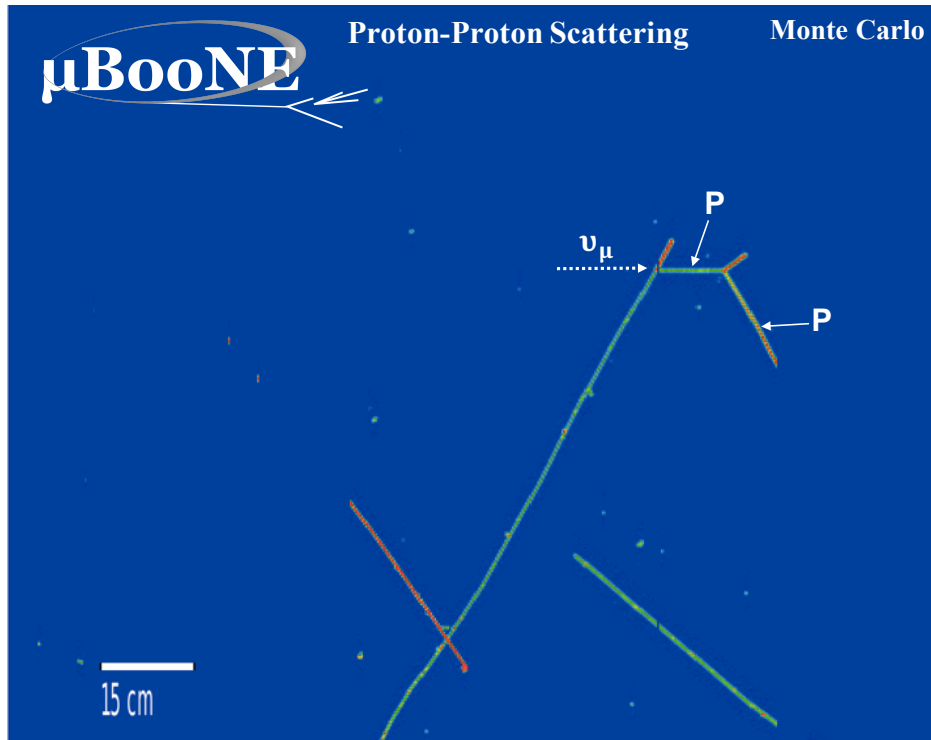


Figure 8.20: An event display showing proton-proton scattering event in Monte Carlo.

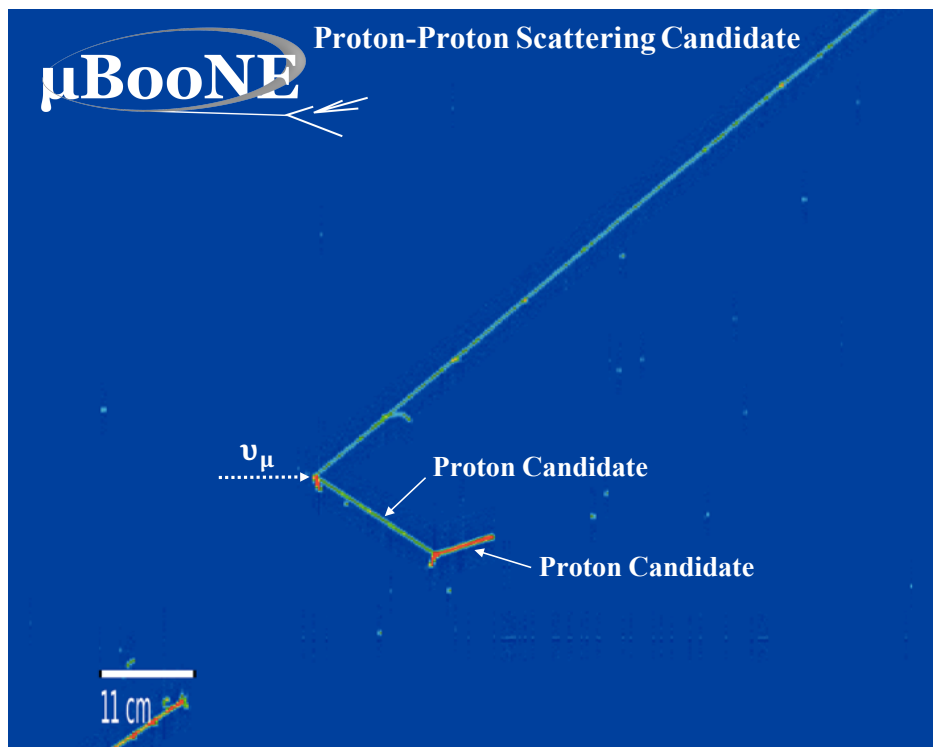


Figure 8.21: An event display found in data, which resembles proton-proton scattering event.

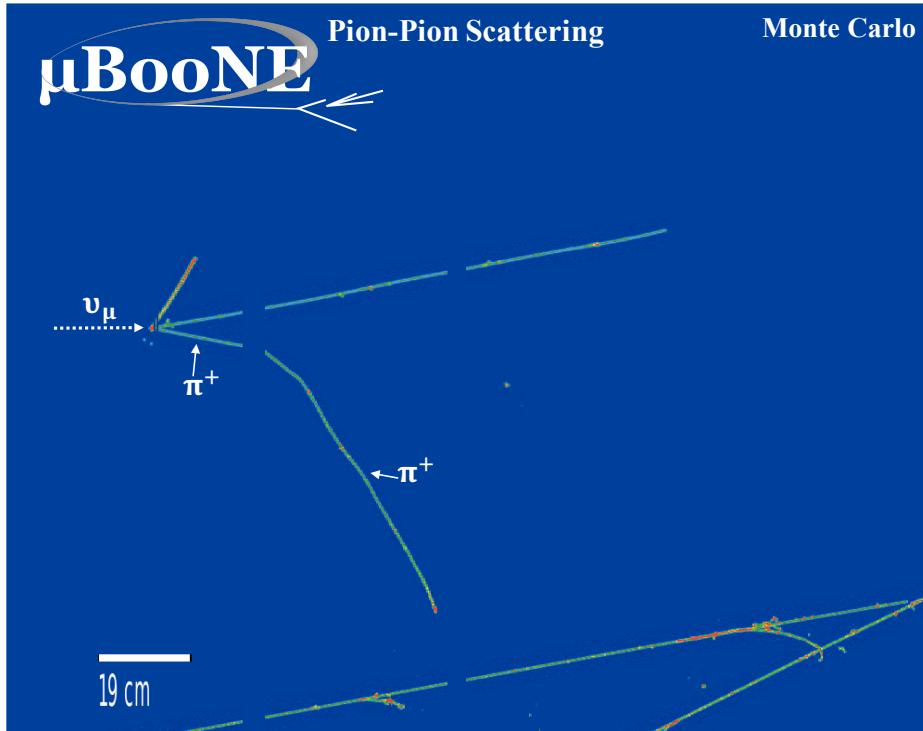


Figure 8.22: An event display showing pion-pion scattering event in Monte Carlo.

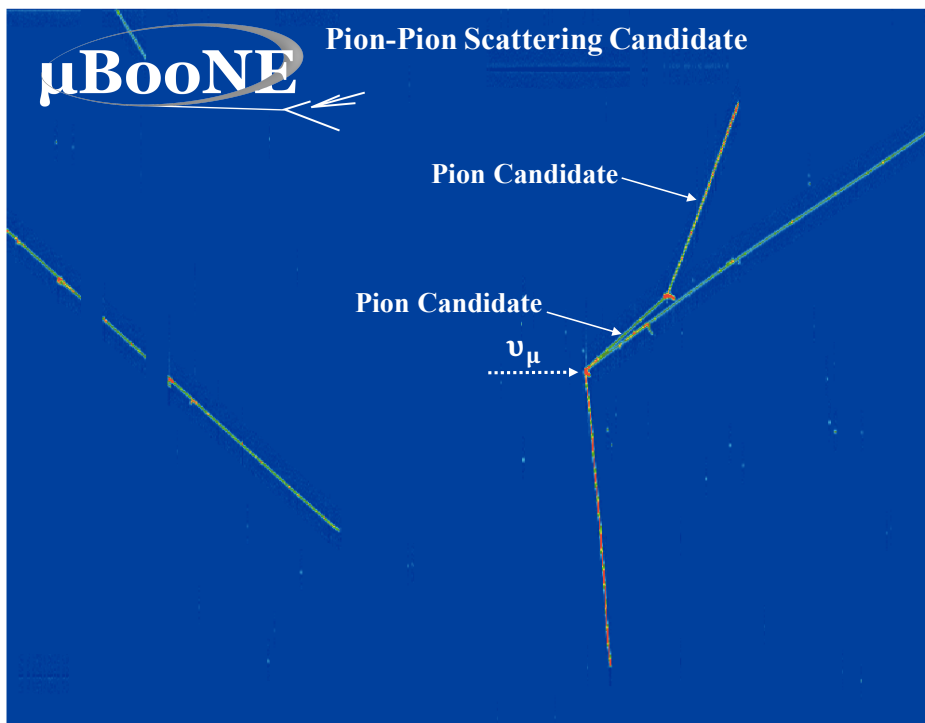


Figure 8.23: An event display found in data, which resembles pion-pion scattering event.

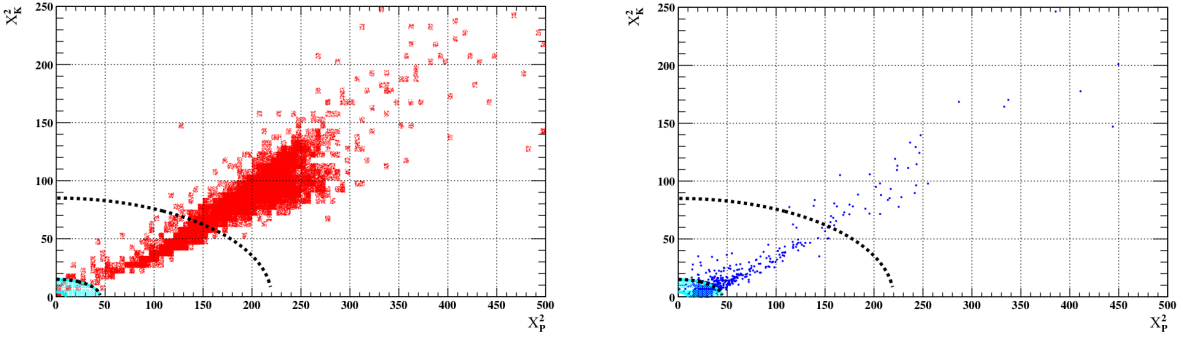


Figure 8.24: Distribution of signal and background kaon candidate events in the side band 1 in the phase space of χ_P^2 - χ_K^2 of kaon candidate tracks. The lower bounding curve is represented by the ellipse having $A = 45$ & $B = 15$ while upper bounding curve is represented by the ellipse having $A = 290$ & $B = 120$. The lower Cyan region is the signal region explained earlier. The kaon candidate events were selected using the selection cuts defined in the Tables 8.4 and 8.5 except cuts on χ_P^2 and χ_K^2 variables on kaon candidate tracks listed in the Table 8.4. (Left) Background events. (Right) Signal events.

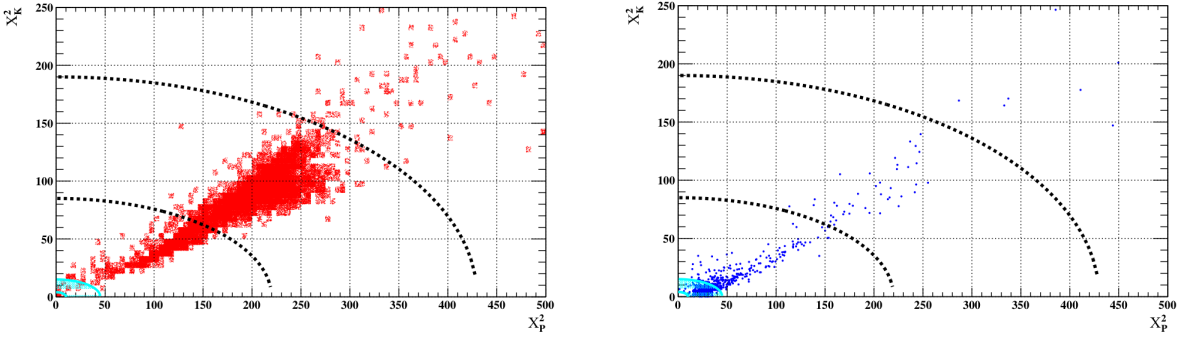


Figure 8.25: Distribution of signal and background kaon candidate events in the side band 2 in the phase space of χ_P^2 - χ_K^2 of kaon candidate tracks. The lower bounding curve is represented by the ellipse having $A = 290$ & $B = 120$ while upper bounding curve is represented by the ellipse having $A = 430$ & $B = 190$. The lower Cyan region is the signal region explained earlier. The kaon candidate events were selected using the selection cuts defined in the Tables 8.4 and 8.5 except the cuts on χ_P^2 and χ_K^2 variables on kaon candidate tracks listed in the Table 8.4. (Left) Background events. (Right) Signal events.

+ *OFF-Beam data to ON-Beam data.* The reason to add OFF-Beam data to Monte-Carlo is to better simulate the cosmic contamination in real data. Using these plots, we derived background scale factors ($W_i^{Background}$) for each bin to scale background predicted by Monte Carlo to match with data. Equation 8.9 shows, how these background scale factors were derived for each bin i in the plots coming from two side bands.

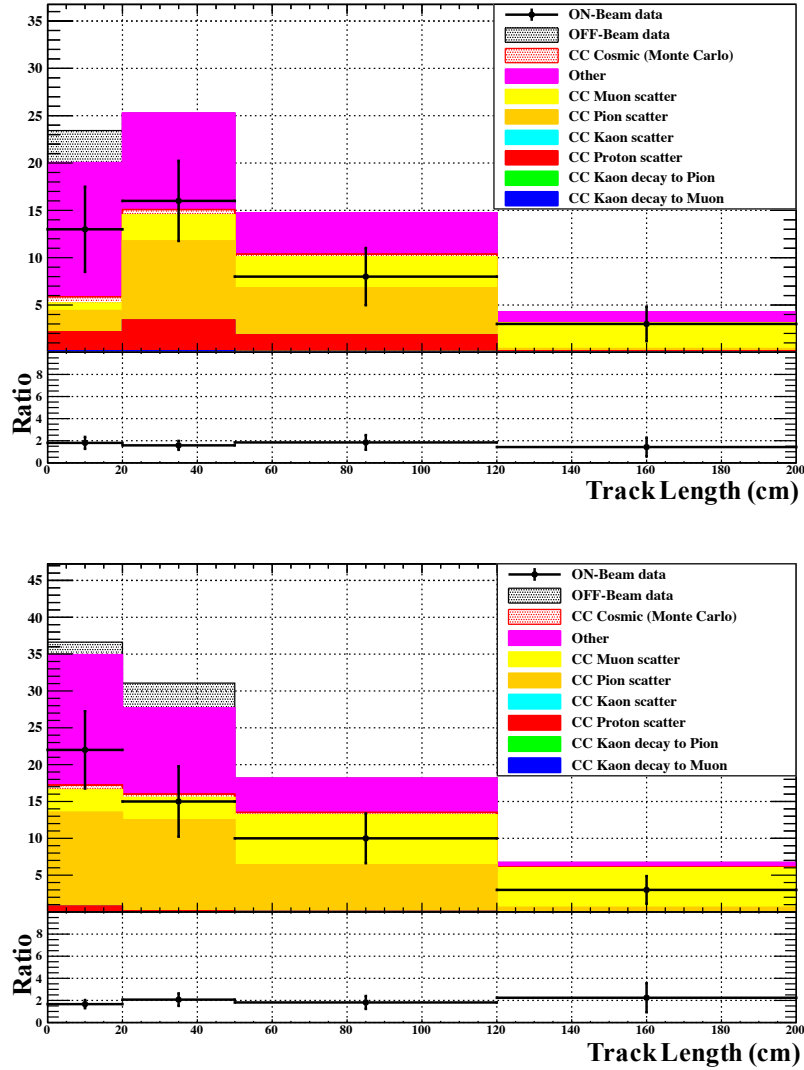


Figure 8.26: Data-Monte Carlo comparison of track length variable of kaon candidate tracks in side band 1 and side band 2 shown in the Figures 8.24 and 8.25. The kaon candidates tracks were selected using the selection cuts described in the Tables 8.4 and 8.5 except the cuts on χ_P^2 and χ_K^2 variables on kaon candidates. The plots here shown are POT normalized to a POT value equivalent to 1.595×10^{20} . The ratio is taken between (MC + OFF-Beam data)/ON-Beam data. The uncertainties shown are completely statistical. (TOP) Data-Monte Carlo comparison in the Side band 1. (Bottom) Data-Monte Carlo comparison in the side band 2.

$$W_i^{Background} = \frac{N_i^{ON-Beam\ data}}{N_i^{MC-Background} + N_i^{OFF-Beam\ data}} \quad (8.9)$$

- $W_i^{Background}$ – Background scale factor in the i th bin
- $N_i^{ON-Beam\ data}$ – Number of events in the i th bin in ON-Beam data
- $N_i^{MC-Background}$ – Number of background events in the i th bin in Monte Carlo
- $N_i^{OFF-Beam\ data}$ – Number of background events in the i th bin in OFF-Beam data

Figure 8.27 shows the background scale factors derived using the Equation 8.9 for each bin in the track length distributions. Here as the final scaling factor for a given bin, the average value of two scaling factors coming from two side bands was selected. Once the scaling factors were finalized, the Equation 8.10 was used to get the scaled Monte Carlo background.

$$MC_i^{Scaled-Background} = W_i^{Background} \times MC_i^{Unscaled-Background} \quad (8.10)$$

- $MC_i^{Scaled-Background}$ – Scaled Monte Carlo background in the i th bin
- $W_i^{Background}$ – Background scale factor in the i th bin
- $MC_i^{Unscaled-Background}$ – Unscaled Monte Carlo background in the i th bin

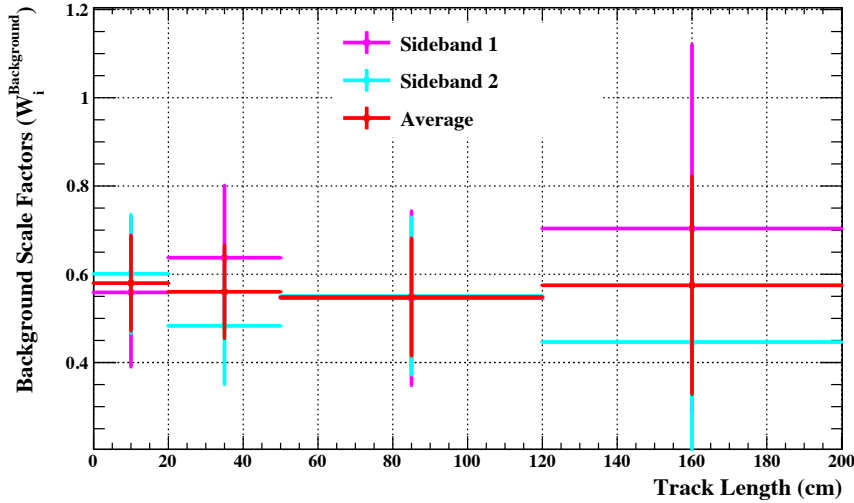


Figure 8.27: Background scale factors ($W_i^{Background}$) derived for each bin in kaon candidate track length distributions in side band 1 and 2. All the uncertainties here shown are completely statistical.

Track Length Range (Kaon Candidate)	Background Scale Factor ($W_i^{Background}$)
0 cm $>$ && $<$ 20 cm	0.580 ± 0.151
20 cm $>$ && $<$ 50 cm	0.560 ± 0.148
50 cm $>$ && $<$ 120 cm	0.548 ± 0.187
120 cm $>$ && $<$ 200 cm	0.575 ± 0.340

Table 8.6: Background scaling factors ($W_i^{Background}$) in different track length bins.

8.7 Data Monte Carlo Comparison

In this section we describe about the data-Monte Carlo comparisons of different kinematic variables performed for kaon candidates and muon candidates coming from kaon decay at rest. In getting the kaon and muon candidates from both Monte Carlo and data, we couldn't use the complete set of selection cuts described in the Section 8.5 as there are not many candidate events in both Monte Carlo and data. So we had to relax some of the selection cuts in order to get sufficient amount of statistics to perform these comparisons reliably. The first set of bullet points shows the relaxed cuts to get kaon candidates from data and Monte Carlo.

- Track should be completely confined within the TPC as described in the first six entries of the Table 8.4.
- Closest distance to the neutrino vertex should be less than 7 cm.
- Start point of the track should be closer to the neutrino vertex than the end point of the track.
- There should be a track attached to the end point of the track within 4.5 cm radius.
- The attached track should have a track length in the range of 20 cm to 70 cm.
- The second track should also be completely confined within the TPC as described in the first six entries of the Table 8.5.

Here the second attached track described in the second and third bullet points serve as the muon track coming from kaon decay.

The following set of points describes, how we found muon candidates coming from kaons that decay.

- Track should be completely confined within the TPC as described in the first six entries of the Table 8.5.
- To the start point of the track, there should be a second track attached within 4.5 cm radius.
- The second track should be within 7 cm of the neutrino vertex and the start point should always be closer to the neutrino vertex than the end point.
- The second track should be completely confined within the TPC as described in the first six entries of the Table 8.4
- The second track should have a minimum track length of 5 cm.
- The second track should have a χ^2 value calculated under proton hypothesis in the range of 10 to 100.

Here the second attached track described in the third bullet point onward serves as the mother kaon. The distributions from Figure 8.28 to 8.34 show the data-Monte Carlo comparisons for different kinematic variables of kaon and muon candidates selected using above mentioned cuts. In these plots all the individual distributions were POT normalized to a POT value equivalent to 1.595×10^{20} except the distribution shown in dashed lines. The distributions in dashed line are the scaled signal distributions. The signal had to be scaled by several factors (scaled by a factor of 100) in order to be visible as there are not many kaon candidate events in both Monte Carlo and data. Furthermore, in all of these plots Monte Carlo and OFF-Beam background were scaled according to the Equation 8.10.

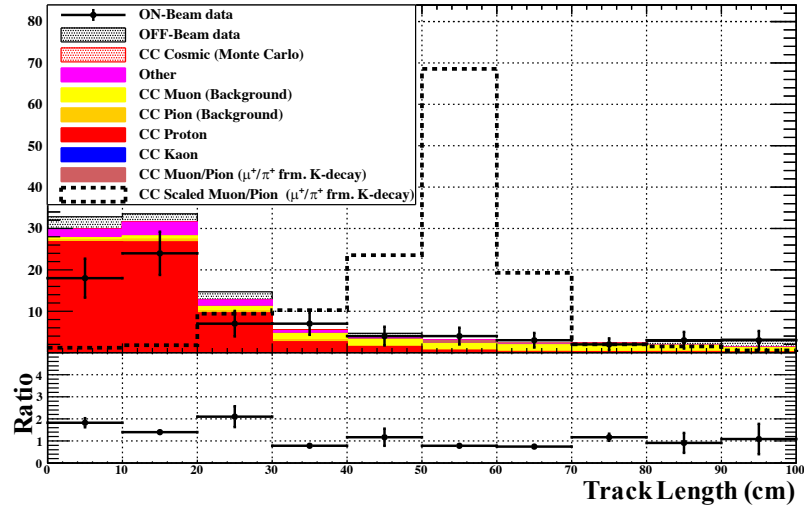
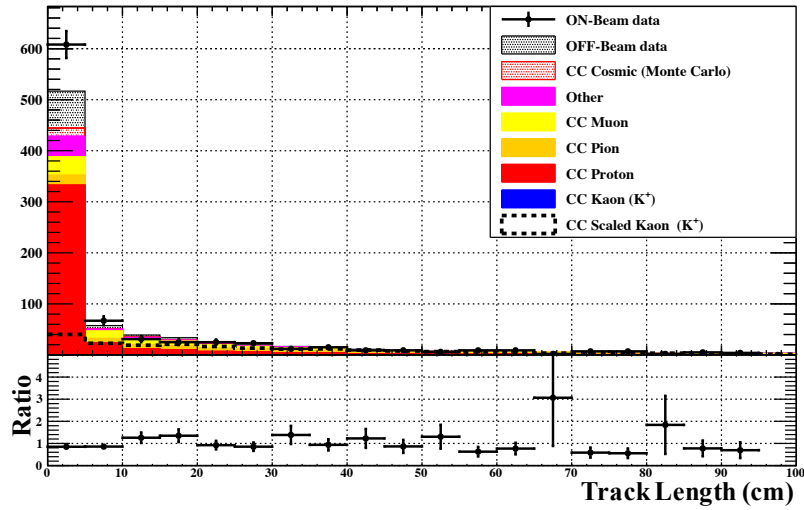


Figure 8.28: (Top) Data-Monte Carlo comparison for the track length of kaon candidates. (Bottom) Data-Monte Carlo comparison for the track length of muon candidates coming from kaon decay. The ratios shown in both plots were taken between (MC + OFF-Beam data)/ON-Beam data. All the uncertainties are completely statistical.

8.8 Kaon Candidate Events in MicroBooNE Data

By running the kaon filter on an ON-Beam data sample, which has a POT equivalent to 1.595×10^{20} , we found two kaon candidate events in the MicroBooNE data as shown in the Figures 8.35 and 8.36.

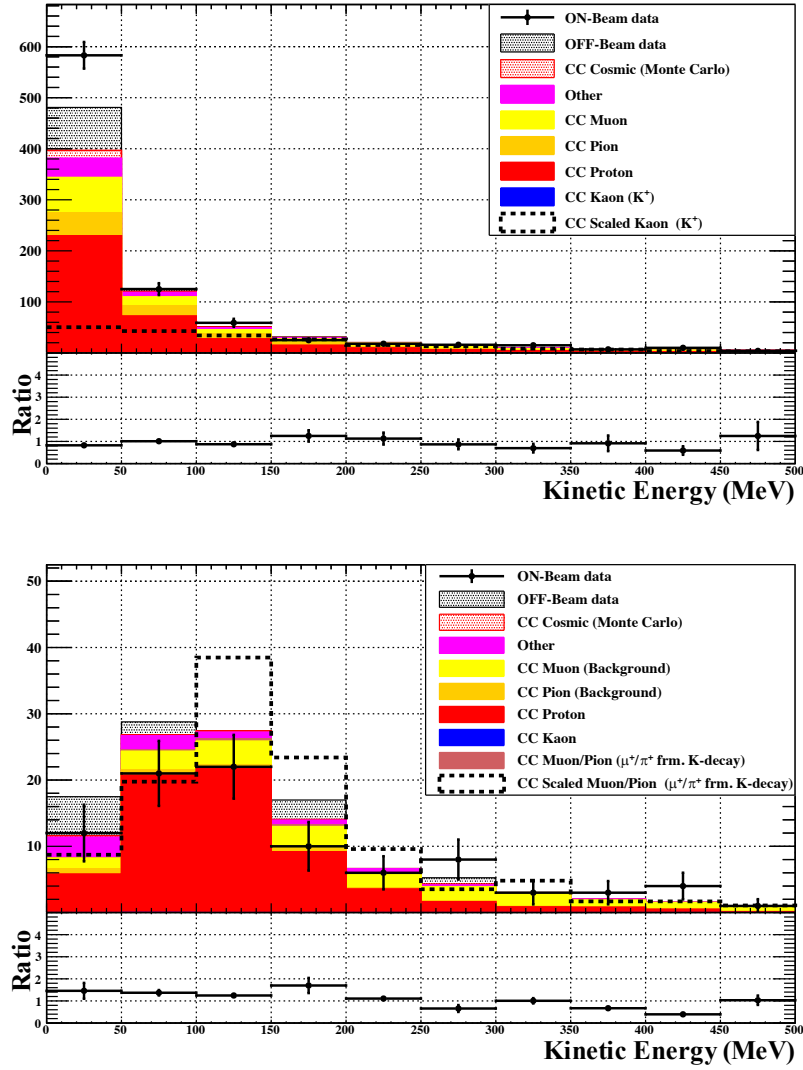


Figure 8.29: (Top) Data-Monte Carlo comparison for the calorimetric kinetic energy of kaon candidates. (Bottom) Data-Monte Carlo comparison for the calorimetric kinetic energy of muon candidates coming from kaon decay. The ratios shown in both plots were taken between (MC + OFF-Beam data)/ON-Beam data. All the uncertainties are completely statistical.

8.9 Cross Section

we calculated a neutrino flux integrated cross section for the neutrino induced charged kaon (K^+) production at charged current mode on argon using the Equation 8.11.

$$\sigma = \frac{N - B}{\epsilon N_T \Phi_{\nu_\mu}} \quad (8.11)$$

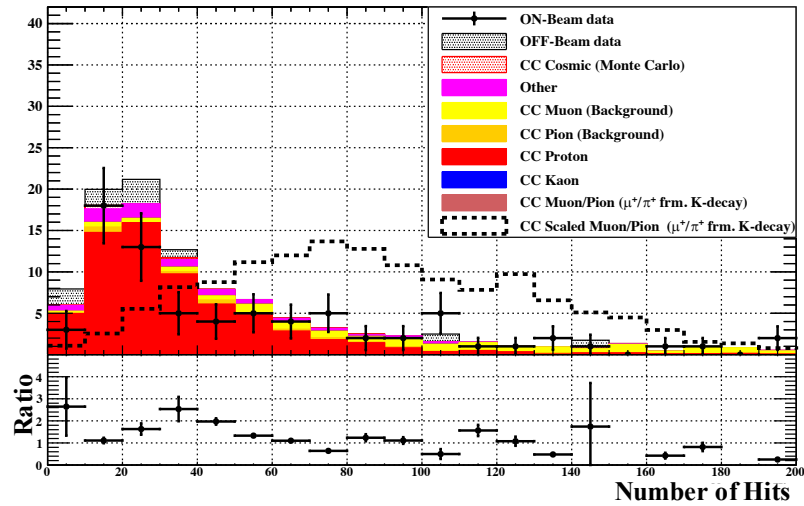
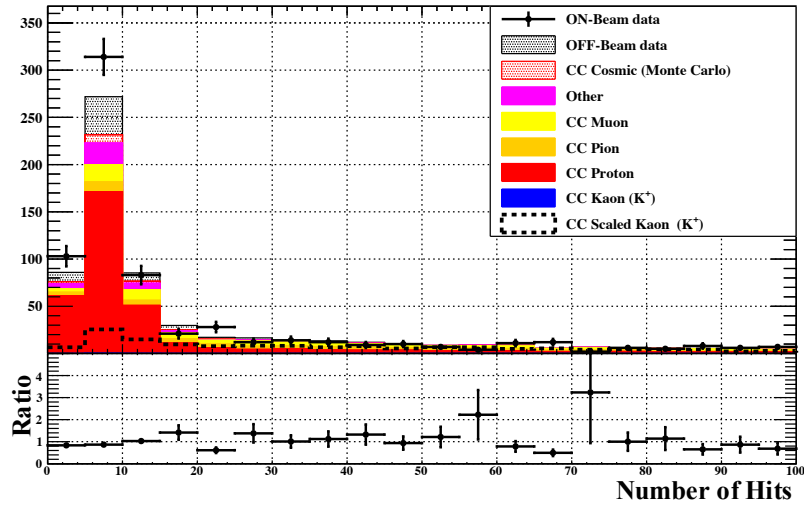


Figure 8.30: (Top) Data-Monte Carlo comparison for the number of hits registered in the collection plane of kaon candidates. (Bottom) Data-Monte Carlo comparison for the number of hits registered in the collection plane of muon candidates coming from kaon decay. The ratios shown in both plots were taken between (MC + OFF-Beam data)/ON-Beam data. All the uncertainties are completely statistical.

σ - Cross section

N - Number of selected events by kaon filter in ON-Beam neutrino data

B - Weighted number of selected background events by kaon filter in Monte Carlo

ϵ - Kaon filter efficiency (0.0301 ± 0.0012 (Stat.))

N_T - Number of target nucleons in the fiducial volume defined in the Figure (no statistical uncertainties while any systematic uncertainties due to pressure and temperature variations)

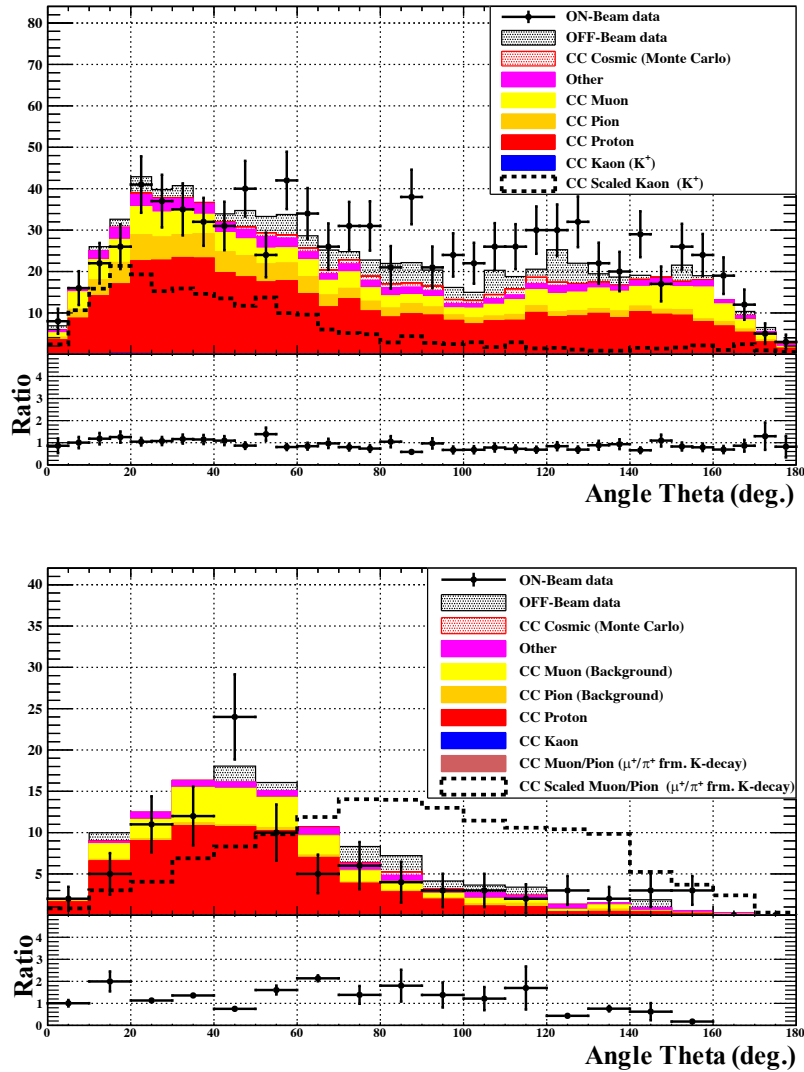


Figure 8.31: (Top) Data-Monte Carlo comparison for the angle θ (polar angle of the track w.r.t beam direction) of kaon candidates. (Bottom) Data-Monte Carlo comparison for the angle θ of muon candidates coming from kaon decay. The ratios shown in both plots were taken between (MC + OFF-Beam data)/ON-Beam data. All the uncertainties are completely statistical.

inside the detector are deemed to be minimal)

$\Phi_{\nu_\mu} - \nu_\mu$ flux integrated over all neutrino energies for the given POT of the dataset (only systematic uncertainties)

The number of target nucleons (N_T) was calculated using the Equation 8.12.

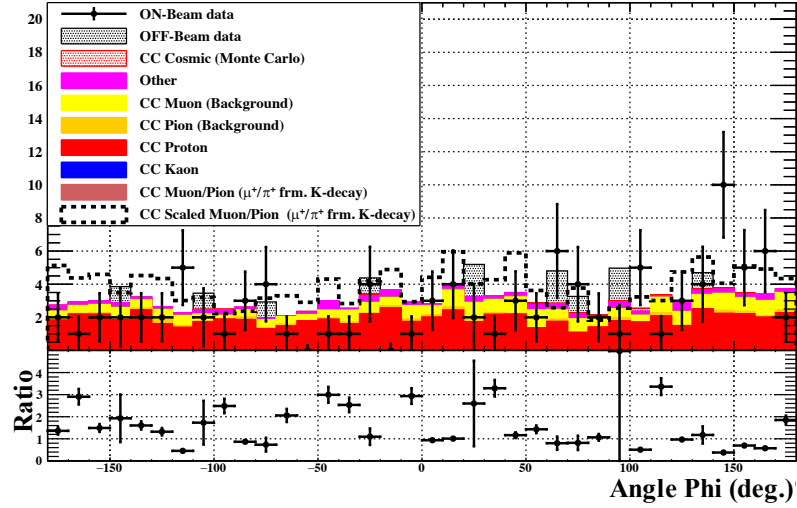
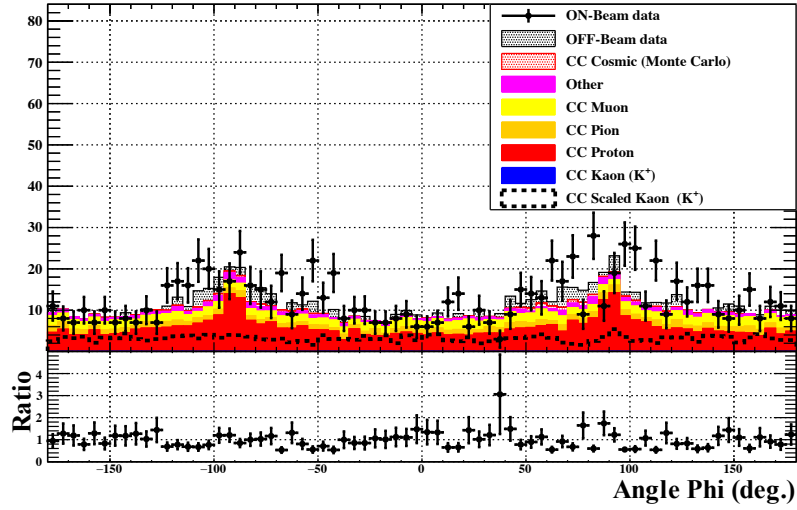


Figure 8.32: (Top) Data-Monte Carlo comparison for the angle ϕ (azimuth angle of the track w.r.t beam direction) of kaon candidates. (Bottom) Data-Monte Carlo comparison for the angle ϕ of muon candidates coming from kaon decay. The ratios shown in both plots were taken between (MC + OFF-Beam data)/ON-Beam data. All the uncertainties are completely statistical.

$$N_T = \frac{\rho_{Ar} V N_A N_{nucleons}}{m_{mol}} \quad (8.12)$$

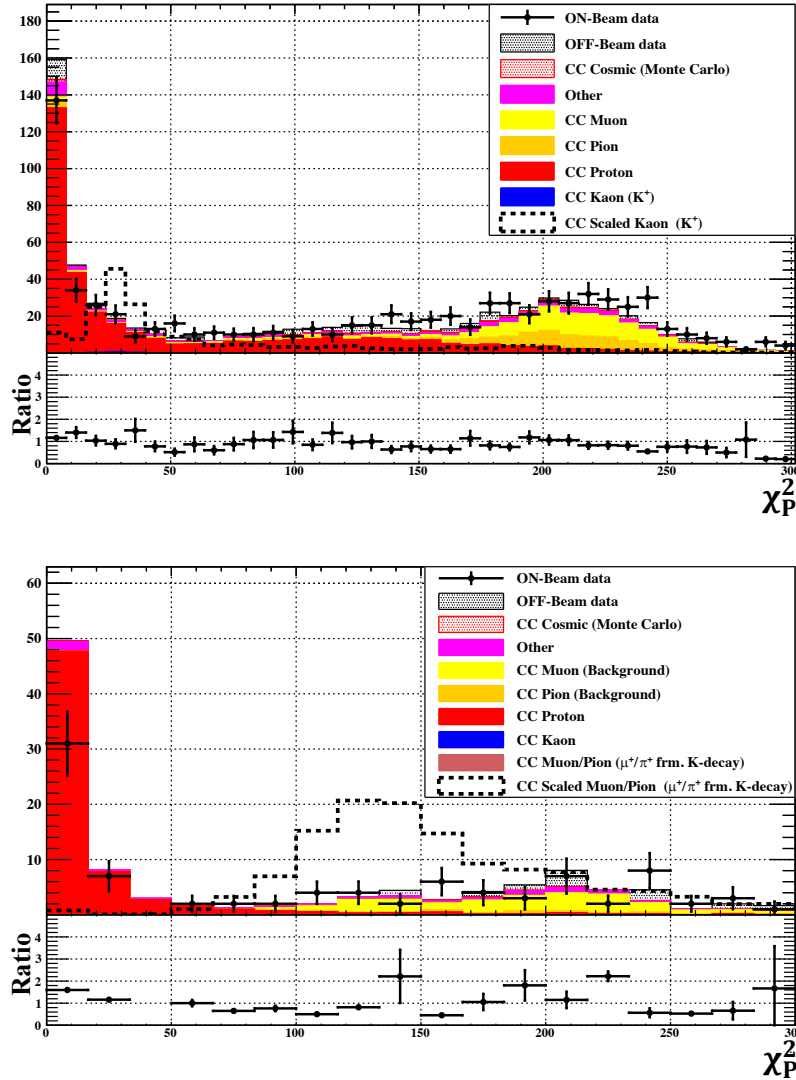


Figure 8.33: (Top) Data-Monte Carlo comparison for the variable χ_P^2 (χ^2 value calculated under proton hypothesis) of kaon candidates. (Bottom) Data-Monte Carlo comparison for the variable χ_P^2 (χ^2 value calculated under proton hypothesis) of muon candidates coming from kaon decay. The ratios shown in both plots were taken between (MC + OFF-Beam data)/ON-Beam data. All the uncertainties are completely statistical.

ρ_{Ar} – Liquid argon density (1.3836 g/cm³)

V – Fiducial volume defined where all neutrino interaction vertices are supposed to be contained (see Figure 8.3)

N_A – Avagadro Number ($6.02214085774 \times 10^{23}$ atoms/mol)

$N_{nucleons}$ – Number of nucleons per argon nucleus (40)

m_{mol} – Number of grams per mole of argon (39.95 g/mol)

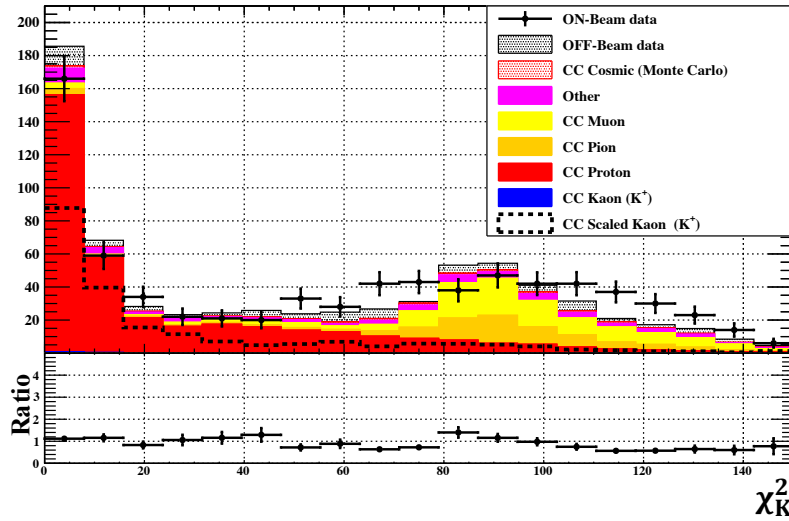


Figure 8.34: Data-Monte Carlo comparison for the variable χ_K^2 (χ^2 value calculated under kaon hypothesis) of kaon candidates. The ratio shown in the plot was taken between (MC + OFF-Beam data)/ON-Beam data. All the uncertainties are completely statistical.

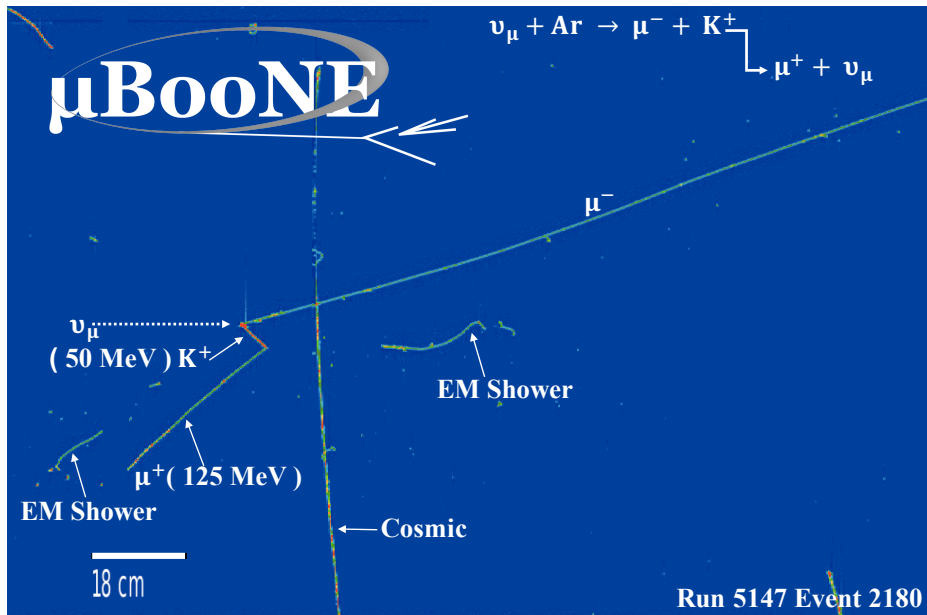


Figure 8.35: An event display showing charged current neutrino induced kaon candidate event in MicroBooNE data.

The motivation of using different POT values in Table 8.7 and 8.8 is to illustrate the importance of improved statistics to get rid of large statistical uncertainties on cross section numbers as this is a statistically constrained rare process. One notable observation by

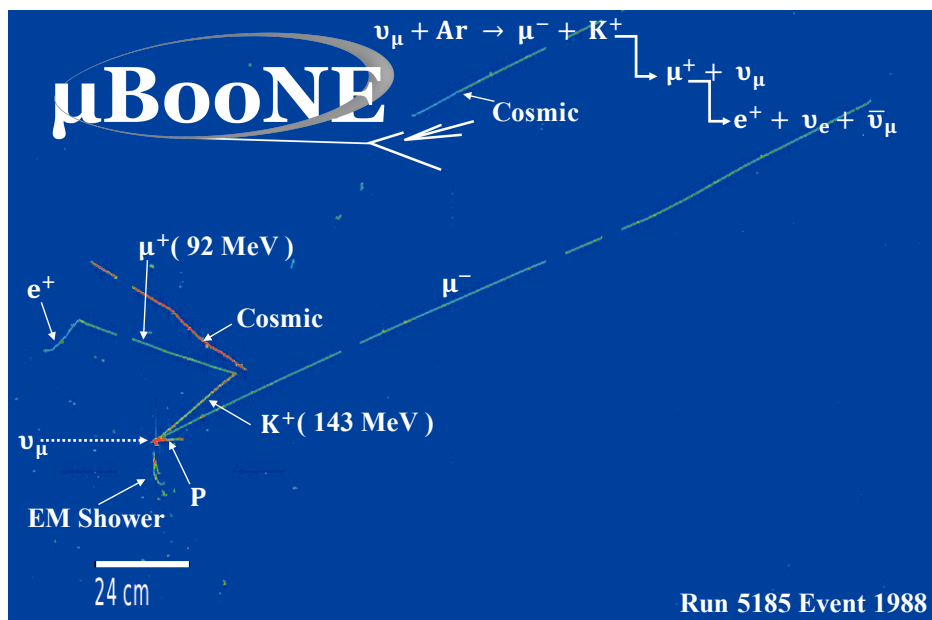


Figure 8.36: An event display showing charged current neutrino induced kaon candidate event in MicroBooNE data.

POT ($\times 10^{20}$)	ν_μ flux ($\times 10^{11}$)	N - B	$\sigma \times 10^{-40} (cm^2/nucleon)$
1.595	1.172	1.64 ± 1.42 (Stat.)	0.18 ± 0.15 (Stat.)
6.6	4.851	6.78 ± 2.93 (Stat.)	0.18 ± 0.08 (Stat.)
13.2	9.702	13.57 ± 4.23 (Stat.)	0.18 ± 0.06 (Stat.)

Table 8.7: Cross section calculated using ON-Beam data for different datasets having different POT numbers. All the uncertainties shown in the table are completely statistical.

POT ($\times 10^{20}$)	ν_μ flux ($\times 10^{11}$)	N - B	$\sigma \times 10^{-40} (cm^2/nucleon)$
1.595	1.172	0.91 ± 1.19 (Stat.)	0.10 ± 0.12 (Stat.)
6.6	4.851	3.78 ± 2.42 (Stat.)	0.10 ± 0.06 (Stat.)
13.2	9.702	7.55 ± 3.42 (Stat.)	0.10 ± 0.04 (Stat.)

Table 8.8: Cross section calculated using Monte-Carlo for different datasets having different POT numbers. All the uncertainties shown in the table are completely statistical.

comparing Monte Carlo cross section with data-driven cross section is that, in data we found more kaon candidate events than predicted by Monte Carlo.

8.10 Future Plans

As neutrino induced charged kaon production is a very rare process in MicroBooNE low neutrino energies, the next immediate plan is to use a larger dataset having more statistics. This will improve the statistical uncertainties of the cross section numbers shown in the Tables [8.7](#) and [8.8](#). Moreover, systematic study will also be performed by considering various biases introduced by different detector effects, neutrino flux uncertainties, etc.

Bibliography

- [1] MicroBooNE. A measurement of the attenuation of drifting electrons in the microboone lartpc, 2017. URL <https://microboone.fnal.gov/wp-content/uploads/MICROBOONE-NOTE-1026-PUB.pdf>. online; accessed 10-Jan-2019.
- [2] MicroBooNE. Detector calibration using through going and stopping muons in the microboone lartpc, 2018. URL <https://microboone.fnal.gov/wp-content/uploads/MICROBOONE-NOTE-1048-PUB.pdf>. online; accessed 15-Jan-2019.
- [3] C. Rubbia. The Liquid Argon Time Projection Chamber: A New Concept for Neutrino Detectors. 1977.
- [4] D. R. Nygren. The Time Projection Chamber: A New 4 pi Detector for Charged Particles. *eConf*, C740805:58, 1974.
- [5] S. E. Derenzo, A. R. Kirschbaum, P. H. Eberhard, R. R. Ross, and F. T. Solmitz. Test of a Liquid Argon Chamber with 20-Micrometer RMS Resolution. *Nucl. Instrum. Meth.*, 122:319, 1974. doi: 10.1016/0029-554X(74)90495-9.
- [6] S. Amerio et al. Design, construction and tests of the ICARUS T600 detector. *Nucl. Instrum. Meth.*, A527:329–410, 2004. doi: 10.1016/j.nima.2004.02.044.
- [7] C. Anderson et al. The ArgoNeuT Detector in the NuMI Low-Energy beam line at Fermilab. *JINST*, 7:P10019, 2012. doi: 10.1088/1748-0221/7/10/P10019.
- [8] R. Acciarri et al. Design and Construction of the MicroBooNE Detector. *JINST*, 12(02):P02017, 2017. doi: 10.1088/1748-0221/12/02/P02017.
- [9] M. Antonello et al. A Proposal for a Three Detector Short-Baseline Neutrino Oscillation Program in the Fermilab Booster Neutrino Beam. 2015.

- [10] B. Abi et al. The DUNE Far Detector Interim Design Report, Volume 2: Single-Phase Module. 2018.
- [11] Jonathan Asadi. Liquid argon time projection chambers, 2017. URL https://npc.fnal.gov/wp-content/uploads/2017/06/NuPhysSymposium_Asaadi.pdf. online; accessed 08-Jan-2019.
- [12] Bo Yu. Tpc design concept: From microboone to lar20. URL <https://slideplayer.com/slide/8458229/>. online; accessed 08-Jan-2019.
- [13] Syracuse University. Scientists work on the microboone, 2015. URL http://thecollege.syr.edu/news/2015/mitch_soderberg_fermilab.html. online; accessed 08-Jan-2019.
- [14] Andrzej Szlec. Microboone, 2013. URL https://microboone-exp.fnal.gov/public/talks/uboone_win_talk_szlec.pdf. online; accessed 08-Jan-2019.
- [15] Mike Zuckerbrot. Microboone cryogenic system. URL https://indico.cern.ch/event/335453/contributions/1724151/attachments/655338/901044/uBoone_Cryogenic_System.pdf. online; accessed 08-Jan-2019.
- [16] Reidar Hahn. Microboone photomultiplier, 2015. URL <http://news.fnal.gov/2015/07/microboone-photomultiplier/>. online; accessed 08-Jan-2019.
- [17] R. Acciarri et al. Summary of the Second Workshop on Liquid Argon Time Projection Chamber Research and Development in the United States. *JINST*, 10(07):T07006, 2015. doi: 10.1088/1748-0221/10/07/T07006.
- [18] Michael Mooney. The MicroBooNE Experiment and the Impact of Space Charge Effects. In *Proceedings, Meeting of the APS Division of Particles and Fields (DPF 2015): Ann Arbor, Michigan, USA, 4-8 Aug 2015*, 2015.
- [19] Shanshan Gao. Cold electronics for protodune-sp lar tpc, 2016. URL <https://indico.>

- ihep.ac.cn/event/6156/session/3/contribution/65/material/slides/0.pdf.
online; accessed 08-Jan-2019.
- [20] David Caratelli. *Study of Electromagnetic Interactions in the MicroBooNE Liquid Argon Time Projection Chamber*. PhD thesis, Columbia U., 2018. URL <http://lss.fnal.gov/archive/thesis/2000/fermilab-thesis-2018-02.pdf>.
- [21] Aguilar-Arevalo et al. Neutrino flux prediction at miniboone. *Phys. Rev. D*, 79:072002, Apr 2009. doi: 10.1103/PhysRevD.79.072002. URL <https://link.aps.org/doi/10.1103/PhysRevD.79.072002>.
- [22] Christopher Marshall. *Measurement of charged kaon production by neutrinos at MINERvA*. PhD thesis, U. Rochester, 2016. URL <http://lss.fnal.gov/archive/thesis/2000/fermilab-thesis-2016-12.pdf>.
- [23] Mark Thomson. *Modern particle physics*. Cambridge University Press, New York, 2013. ISBN 9781107034266. URL <http://www-spires.fnal.gov/spires/find/books/www?cl=QC793.2.T46::2013>.
- [24] 2018 Conference on the “History of the Neutrinos”, Paris. History of the neutrino, 2019. URL <https://neutrino-history.in2p3.fr>. online; accessed 10-Jan-2019.
- [25] Warwick University. Neutrino oscillations, 2015. URL https://warwick.ac.uk/fac/sci/physics/staff/academic/boyd/stuff/lec_oscillations.pdf. online; accessed 10-Jan-2019.
- [26] Yan-Rui Liu, Hua-Xing Chen, Wei Chen, Xiang Liu, and Shi-Lin Zhu. Pentaquark and Tetraquark states. *Prog. Part. Nucl. Phys.*, 107:237–320, 2019. doi: 10.1016/j.pnpnp.2019.04.003.
- [27] Wikipedia. Standard model, 2019. URL https://en.wikipedia.org/wiki/Standard_Model. online; accessed 10-Jan-2019.

- [28] Fred L. Wilson. Fermi's Theory of Beta Decay. *Am. J. Phys.*, 36(12):1150–1160, 1968. doi: 10.1119/1.1974382.
- [29] Samoil M. Bilenky and J. Hosek. GLASHOW-WEINBERG-SALAM THEORY OF ELECTROWEAK INTERACTIONS AND THE NEUTRAL CURRENTS. *Phys. Rept.*, 90:73–157, 1982. doi: 10.1016/0370-1573(82)90016-3.
- [30] M. Haguenaer. "Gargamelle" Experiment. In *High energy physics. Proceedings, 17th International Conference, ICHEP 1974, London, England, July 01-July 10, 1974*, pages IV.95–100, 1974.
- [31] C. S. Wu, E. Ambler, R. W. Hayward, D. D. Hoppes, and R. P. Hudson. Experimental test of parity conservation in beta decay. *Phys. Rev.*, 105:1413–1415, Feb 1957. doi: 10.1103/PhysRev.105.1413. URL <https://link.aps.org/doi/10.1103/PhysRev.105.1413>.
- [32] Bayes et al. Experimental constraints on left-right symmetric models from muon decay. *Phys. Rev. Lett.*, 106:041804, Jan 2011. doi: 10.1103/PhysRevLett.106.041804. URL <https://link.aps.org/doi/10.1103/PhysRevLett.106.041804>.
- [33] C. Jarlskog. Cabibbo theory. *J. Phys. Colloq.*, 32(C3):17–25, 1971. doi: 10.1051/jphyscol:1971303.
- [34] Luciano Maiani. The GIM Mechanism: origin, predictions and recent uses. In *Proceedings, 48th Rencontres de Moriond on Electroweak Interactions and Unified Theories: La Thuile, Italy, March 2-9, 2013*, pages 3–16, 2013.
- [35] Dylan Harries. *Aspects of E_6 Inspired Supersymmetric Models*. PhD thesis, Adelaide U., 2017. URL <https://digital.library.adelaide.edu.au/dspace/handle/2440/114067>.
- [36] Marko Petric and Prof. Peter Krizan. Flavour-changing neutral currents, 2008. URL http://mafija.fmf.uni-lj.si/seminar/files/2007_2008/petricflavour.pdf. online; accessed 10-Jan-2019.

- [37] C. L. Cowan, F. Reines, F. B. Harrison, H. W. Kruse, and A. D. McGuire. Detection of the free neutrino: A Confirmation. *Science*, 124:103–104, 1956. doi: 10.1126/science.124.3212.103.
- [38] G. Danby, J. M. Gaillard, Konstantin A. Goulianos, L. M. Lederman, Nari B. Mistry, M. Schwartz, and J. Steinberger. Observation of High-Energy Neutrino Reactions and the Existence of Two Kinds of Neutrinos. *Phys. Rev. Lett.*, 9:36–44, 1962. doi: 10.1103/PhysRevLett.9.36.
- [39] K. Kodama et al. Observation of tau neutrino interactions. *Phys. Lett.*, B504:218–224, 2001. doi: 10.1016/S0370-2693(01)00307-0.
- [40] S. Schael et al. Precision electroweak measurements on the Z resonance. *Phys. Rept.*, 427:257–454, 2006. doi: 10.1016/j.physrep.2005.12.006.
- [41] Valery A. Rubakov and Dmitry S. Gorbunov. *Introduction to the Theory of the Early Universe*. World Scientific, Singapore, 2017. ISBN 9789813209879, 9789813209886, 9789813220058. doi: 10.1142/10447. URL <http://www.DESY.ebib.com/patron/FullRecord.aspx?p=737614>.
- [42] M. G. Aartsen et al. First observation of PeV-energy neutrinos with IceCube. *Phys. Rev. Lett.*, 111:021103, 2013. doi: 10.1103/PhysRevLett.111.021103.
- [43] J. A. Formaggio and G. P. Zeller. From eV to EeV: Neutrino Cross Sections Across Energy Scales. *Rev. Mod. Phys.*, 84:1307–1341, 2012. doi: 10.1103/RevModPhys.84.1307.
- [44] Stephen Parke. Neutrinos: Theory and Phenomenology. *Phys. Scripta*, T158:014013, 2013. doi: 10.1088/0031-8949/2013/T158/014013.
- [45] Adrin-Martnez et al. Letter of intent for KM3NeT 2.0. *Journal of Physics G: Nuclear and Particle Physics*, 43, 2016. doi: 10.1088/0954-3899/43/8/084001.

- [46] John N. Bahcall, Aldo M. Serenelli, and Sarbani Basu. New solar opacities, abundances, helioseismology, and neutrino fluxes. *Astrophys. J.*, 621:L85–L88, 2005. doi: 10.1086/428929.
- [47] IAS. Solar neutrino spectrum, 2002. URL <http://www.sns.ias.edu/~jnb/SNviewgraphs/SNspectrum/neutrinospectrum.pdf>. online; accessed 13-May-2019.
- [48] Y. Fukuda et al. The Super-Kamiokande detector. *Nucl. Instrum. Meth.*, A501:418–462, 2003. doi: 10.1016/S0168-9002(03)00425-X.
- [49] A. Y. Smirnov. The Mikheyev-Smirnov-Wolfenstein (MSW) Effect. In *International Conference on History of the Neutrino: 1930-2018 Paris, France, September 5-7, 2018*, 2019.
- [50] B. T. Cleveland, Timothy Daily, Raymond Davis, Jr., James R. Distel, Kenneth Lande, C. K. Lee, Paul S. Wildenhain, and Jack Ullman. Measurement of the solar electron neutrino flux with the Homestake chlorine detector. *Astrophys. J.*, 496:505–526, 1998. doi: 10.1086/305343.
- [51] J. N. Abdurashitov et al. Solar neutrino flux measurements by the Soviet-American Gallium Experiment (SAGE) for half the 22 year solar cycle. *J. Exp. Theor. Phys.*, 95:181–193, 2002. doi: 10.1134/1.1506424. [Zh. Eksp. Teor. Fiz.122,211(2002)].
- [52] W. Hampel et al. GALLEX solar neutrino observations: Results for GALLEX IV. *Phys. Lett.*, B447:127–133, 1999. doi: 10.1016/S0370-2693(98)01579-2.
- [53] Talk given by Georg G. Raffelt from Max-Planck-Institut für Physik München. Sn 1987a 30 years later, 2017. URL https://sciencedocbox.com/Space_and_Astronomy/68817190-Supernova-1987a-and-the-birth-of-neutrino-astronomy.html. online; accessed 13-May-2019.
- [54] J. Boger et al. The Sudbury neutrino observatory. *Nucl. Instrum. Meth.*, A449:172–207, 2000. doi: 10.1016/S0168-9002(99)01469-2.

- [55] Bahcall-Serenelli. Total rates: Standard model vs. experiment, 2005. URL <http://www.sns.ias.edu/~jnb/SNviewgraphs/snviewgraphs.html>. online; accessed 13-May-2019.
- [56] M. Tanabashi et al. Review of Particle Physics. *Phys. Rev.*, D98(3):030001, 2018. doi: 10.1103/PhysRevD.98.030001.
- [57] M. G. Aartsen et al. The IceCube Neutrino Observatory Part V: Neutrino Oscillations and Supernova Searches. In *Proceedings, 33rd International Cosmic Ray Conference (ICRC2013): Rio de Janeiro, Brazil, July 2-9, 2013*, 2013.
- [58] Y. Fukuda et al. Evidence for oscillation of atmospheric neutrinos. *Phys. Rev. Lett.*, 81:1562–1567, 1998. doi: 10.1103/PhysRevLett.81.1562.
- [59] R. Acquafredda et al. The OPERA experiment in the CERN to Gran Sasso neutrino beam. *JINST*, 4:P04018, 2009. doi: 10.1088/1748-0221/4/04/P04018.
- [60] K. Eguchi et al. First results from KamLAND: Evidence for reactor anti-neutrino disappearance. *Phys. Rev. Lett.*, 90:021802, 2003. doi: 10.1103/PhysRevLett.90.021802.
- [61] Gregory Pawlosky. The NOvA Experiment. *PoS*, NEUTEL2015:037, 2015. doi: 10.22323/1.244.0037.
- [62] Gregory Pawloski. The MINOS experiment. *PoS*, HQL2016:004, 2017. doi: 10.22323/1.274.0004.
- [63] K. Abe et al. The T2K Experiment. *Nucl. Instrum. Meth.*, A659:106–135, 2011. doi: 10.1016/j.nima.2011.06.067.
- [64] P. Adamson et al. Measurement of Neutrino and Antineutrino Oscillations Using Beam and Atmospheric Data in MINOS. *Phys. Rev. Lett.*, 110(25):251801, 2013. doi: 10.1103/PhysRevLett.110.251801.
- [65] K. Abe et al. Combined Analysis of Neutrino and Antineutrino Oscillations at T2K. *Phys. Rev. Lett.*, 118(15):151801, 2017. doi: 10.1103/PhysRevLett.118.151801.

- [66] Ko Abe et al. Measurement of Muon Antineutrino Oscillations with an Accelerator-Produced Off-Axis Beam. *Phys. Rev. Lett.*, 116(18):181801, 2016. doi: 10.1103/PhysRevLett.116.181801.
- [67] B. Aharmim et al. Combined Analysis of all Three Phases of Solar Neutrino Data from the Sudbury Neutrino Observatory. *Phys. Rev.*, C88:025501, 2013. doi: 10.1103/PhysRevC.88.025501.
- [68] T. Araki et al. Measurement of neutrino oscillation with KamLAND: Evidence of spectral distortion. *Phys. Rev. Lett.*, 94:081801, 2005. doi: 10.1103/PhysRevLett.94.081801.
- [69] A. Gando et al. Constraints on θ_{13} from A Three-Flavor Oscillation Analysis of Reactor Antineutrinos at KamLAND. *Phys. Rev.*, D83:052002, 2011. doi: 10.1103/PhysRevD.83.052002.
- [70] F. Ardellier et al. Double Chooz: A Search for the neutrino mixing angle θ_{13} . 2006.
- [71] Jun Cao and Kam-Biu Luk. An overview of the Daya Bay Reactor Neutrino Experiment. *Nucl. Phys.*, B908:62–73, 2016. doi: 10.1016/j.nuclphysb.2016.04.034.
- [72] F. P. An et al. New measurement of θ_{13} via neutron capture on hydrogen at Daya Bay. *Phys. Rev.*, D93(7):072011, 2016. doi: 10.1103/PhysRevD.93.072011.
- [73] J. K. Ahn et al. RENO: An Experiment for Neutrino Oscillation Parameter θ_{13} Using Reactor Neutrinos at Yonggwang. 2010.
- [74] C. Jollet. The JUNO experiment. *Nuovo Cim.*, C39(4):318, 2017. doi: 10.1393/ncc/i2016-16318-6.
- [75] C Athanassopoulos et al. The Liquid scintillator neutrino detector and LAMPF neutrino source. *Nucl. Instrum. Meth.*, A388:149–172, 1997. doi: 10.1016/S0168-9002(96)01155-2.

- [76] A. Aguilar-Arevalo et al. Evidence for neutrino oscillations from the observation of anti-neutrino(electron) appearance in a anti-neutrino(muon) beam. *Phys. Rev.*, D64: 112007, 2001. doi: 10.1103/PhysRevD.64.112007.
- [77] Division of Nuclear Physics. Evidence for neutrino oscillations from the lsnd experiment, 2019. URL <https://www.aps.org/units/dnp/research/lsnd.cfm>. online; accessed 14-May-2019.
- [78] E. Church et al. A Letter of intent for an experiment to measure muon-neutrino \rightarrow $\bar{\nu}_e$ electron-neutrino oscillations and muon-neutrino disappearance at the Fermilab booster (Boone). 1997.
- [79] A. A. Aguilar-Arevalo et al. The MiniBooNE Detector. *Nucl. Instrum. Meth.*, A599: 28–46, 2009. doi: 10.1016/j.nima.2008.10.028.
- [80] A. A. Aguilar-Arevalo et al. A Combined $\nu_\mu \rightarrow \nu_e$ and $\bar{\nu}_\mu \rightarrow \bar{\nu}_e$ Oscillation Analysis of the MiniBooNE Excesses. 2012. URL <http://lss.fnal.gov/archive/2012/pub/fermilab-pub-12-394-ad-ppd.pdf>.
- [81] A. A. Aguilar-Arevalo et al. Significant Excess of ElectronLike Events in the MiniBooNE Short-Baseline Neutrino Experiment. *Phys. Rev. Lett.*, 121(22):221801, 2018. doi: 10.1103/PhysRevLett.121.221801.
- [82] R. Acciarri et al. First Observation of Low Energy Electron Neutrinos in a Liquid Argon Time Projection Chamber. *Phys. Rev.*, D95(7):072005, 2017. doi: 10.1103/PhysRevD.95.072005.
- [83] Fermilab. Particle physics, 2019. URL <https://strategicplan.fnal.gov/particle-physics/>. online; accessed 14-May-2019.
- [84] Fermilab. Dune, 2019. URL <https://www.dunescience.org>. online; accessed 14-May-2019.

- [85] E. Buckley et al. A Study of Ionization Electrons Drifting Over Large Distances in Liquid Argon. *Nucl. Instrum. Meth.*, A275:364–372, 1989. doi: 10.1016/0168-9002(89)90710-9.
- [86] A. Bettini et al. A Study of the factors affecting the electron lifetime in ultrapure liquid argon. *Nucl. Instrum. Meth.*, A305:177–186, 1991. doi: 10.1016/0168-9002(91)90532-U.
- [87] MicroBooNE. Measurement of the electronegative contaminants and drift electron lifetime in the microboone experiment, 2016. URL <https://microboone.fnal.gov/wp-content/uploads/MICROBOONE-NOTE-1003-PUB.pdf>. online; accessed 10-Jan-2019.
- [88] S. Amoruso et al. Analysis of the liquid argon purity in the ICARUS T600 TPC. *Nucl. Instrum. Meth.*, A516:68–79, 2004. doi: 10.1016/j.nima.2003.07.043.
- [89] A. Ereditato, C. C. Hsu, S. Janos, I. Kreslo, M. Messina, C. Rudolf von Rohr, B. Rossi, T. Strauss, M. S. Weber, and M. Zeller. Design and operation of ARGONTUBE: a 5 m long drift liquid argon TPC. *JINST*, 8:P07002, 2013. doi: 10.1088/1748-0221/8/07/P07002.
- [90] M. Antonello et al. Experimental observation of an extremely high electron lifetime with the ICARUS-T600 LAr-TPC. *JINST*, 9(12):P12006, 2014. doi: 10.1088/1748-0221/9/12/P12006.
- [91] Sigma-aldrich, p.o. box 14508, st. louis, mo 63178 usa.
- [92] Basf corp., 100 park avenue, florham park, nj 07932 usa.
- [93] Eric D. Church. LArSoft: A Software Package for Liquid Argon Time Projection Drift Chambers. 2013.
- [94] R. Acciarri et al. Noise Characterization and Filtering in the MicroBooNE Liquid Argon TPC. *JINST*, 12(08):P08003, 2017. doi: 10.1088/1748-0221/12/08/P08003.

- [95] C Anderson et al. Analysis of a large sample of neutrino-induced muons with the ArgoNeuT detector. *Journal of Instrumentation*, 7(10):P10020, 2012. URL <http://stacks.iop.org/1748-0221/7/i=10/a=P10020>.
- [96] R. Acciarri et al. A study of electron recombination using highly ionizing particles in the ArgoNeuT Liquid Argon TPC. *JINST*, 8:P08005, 2013. doi: 10.1088/1748-0221/8/08/P08005.
- [97] MicroBooNE. Study of space charge effects in microboone, 2016. URL <https://microboone.fnal.gov/wp-content/uploads/MICROBOONE-NOTE-1018-PUB.pdf>. online; accessed 10-Jan-2019.
- [98] C. Bromberg et al. Design and operation of LongBo: a 2 m long drift liquid argon TPC. *Journal of Instrumentation*, 10(07):P07015, 2015. URL <http://stacks.iop.org/1748-0221/10/i=07/a=P07015>.
- [99] The DUNE 35 ton Prototype Collaboration. Evidence of impurity stratification in the dune 35 ton prototype cryostat, fermilab-tm-2642-nd (2017), 2017.
- [100] The ICARUS Collaboration. Measurement of the μ decay spectrum with the icarus liquid argon tpc. *The European Physical Journal C - Particles and Fields*, 33:233–241, 2004. ISSN 1434-6052. doi: 10.1140/epjc/s2004-01597-7. URL <https://doi.org/10.1140/epjc/s2004-01597-7>.
- [101] A. Ereditato, I. Kreslo, M. Lthi, C. Rudolf von Rohr, M. Schenk, Thomas Strauss, M. Weber, and M. Zeller. A steerable UV laser system for the calibration of liquid argon time projection chambers. *JINST*, 9(11):T11007, 2014. doi: 10.1088/1748-0221/9/11/T11007.
- [102] C. Adams et al. Ionization electron signal processing in single phase LArTPCs. Part I. Algorithm Description and quantitative evaluation with MicroBooNE simulation. *JINST*, 13(07):P07006, 2018. doi: 10.1088/1748-0221/13/07/P07006.

- [103] C. Adams et al. Ionization electron signal processing in single phase LArTPCs. Part II. Data/simulation comparison and performance in MicroBooNE. *JINST*, 13(07):P07007, 2018. doi: 10.1088/1748-0221/13/07/P07007.
- [104] Jeffrey J. Hartnell. Measurement of the calorimetric energy scale in minos. 1 2005. doi: 10.2172/875528.
- [105] MicroBooNE. Selection and kinematic properties of numu charged-current inclusive events in 5e19 pot of microboone data, 2016. URL <https://microboone.fnal.gov/wp-content/uploads/MICROBOONE-NOTE-1010-PUB.pdf>. online; accessed 15-Jan-2019.
- [106] D. Heck, J. Knapp, J. N. Capdevielle, G. Schatz, and T. Thouw. CORSIKA: A Monte Carlo code to simulate extensive air showers. 1998.
- [107] R. Acciarri et al. The Pandora multi-algorithm approach to automated pattern recognition of cosmic-ray muon and neutrino events in the MicroBooNE detector. *Eur. Phys. J.*, C78(1):82, 2018. doi: 10.1140/epjc/s10052-017-5481-6.
- [108] The MicroBooNE Collaboration. Calibration of the microboone tpc’s energy response with cosmic-ray stopping muons (tech note-9149-v5), 2018. online; accessed 15-Jan-2019.
- [109] ROOT-CERN. Convolutd landau and gaussian fitting function. URL <https://root.cern.ch/root/html/tutorials/fit/langaus.C.html>.
- [110] K.A. Olive and Particle Data Group. Review of Particle Physics, 2014. URL <http://stacks.iop.org/1674-1137/38/i=9/a=090001>.
- [111] Donald E. Groom, Nikolai V. Mokhov, and Sergei I. Striganov. Muon stopping power and range tables 10-MeV to 100-TeV. *Atom. Data Nucl. Data Tabl.*, 78:183–356, 2001. doi: 10.1006/adnd.2001.0861.

- [112] P. Hasenfratz. Lattice QCD. *Acta Phys. Austriaca Suppl.*, 25:283–356, 1983. doi: 10.1007/978-3-7091-7651-1_9.
- [113] C. H. Llewellyn Smith. Neutrino Reactions at Accelerator Energies. *Phys. Rept.*, 3: 261–379, 1972. doi: 10.1016/0370-1573(72)90010-5.
- [114] P. Kyberd et al. nuSTORM - Neutrinos from STORed Muons: Letter of Intent to the Fermilab Physics Advisory Committee. 2012.
- [115] Daniel Ivan Scully. *Neutrino Induced Coherent Pion Production*. PhD thesis, Warwick U., 2013. URL <http://www.t2k.org/docs/thesis/038>.
- [116] D. Rein. Angular Distribution in Neutrino Induced Single Pion Production Processes. *Z. Phys.*, C35:43–64, 1987. doi: 10.1007/BF01561054.
- [117] Dieter Rein and Lalit M. Sehgal. Neutrino Excitation of Baryon Resonances and Single Pion Production. *Annals Phys.*, 133:79–153, 1981. doi: 10.1016/0003-4916(81)90242-6.
- [118] TEX. Resonance pion production in feynmf, 2019. URL <https://tex.stackexchange.com/questions/446144/resonance-production-in-feynmf>. online; accessed 15-May-2019.
- [119] Sowjanya Gollapinni. Neutrino Cross section Future. In *Proceedings, Prospects in Neutrino Physics (NuPhys2015): London, UK, December 16-18, 2015*, 2016.
- [120] M. Rafi Alam, I. Ruiz Simo, M. Sajjad Athar, and M. J. Vicente Vacas. Weak Kaon Production off the Nucleon. *Phys. Rev.*, D82:033001, 2010. doi: 10.1103/PhysRevD.82.033001.
- [121] Z. Wang et al. First evidence of coherent K^+ meson production in neutrino-nucleus scattering. *Phys. Rev. Lett.*, 117(6):061802, 2016. doi: 10.1103/PhysRevLett.117.061802.
- [122] U. Mosel, O. Lalakulich, and K. Gallmeister. Reaction mechanisms at MINER?A. *Phys. Rev.*, D89(9):093003, 2014. doi: 10.1103/PhysRevD.89.093003.

- [123] Graham G. Ross. *GRAND UNIFIED THEORIES*. 1985.
- [124] Nobuhiro Maekawa and Toshifumi Yamashita. Flipped SO(10) model. *Phys. Lett.*, B567:330–338, 2003. doi: 10.1016/j.physletb.2003.06.054.
- [125] John Rennie. Proton lifetime, 2015. URL <https://physics.stackexchange.com/questions/224920/is-there-any-stable-hadron>. online; accessed 15-May-2019.
- [126] T. Akiri et al. The 2010 Interim Report of the Long-Baseline Neutrino Experiment Collaboration Physics Working Groups. 2011.
- [127] Ed Kearns (Boston University). Feynman diagram for susy-mediated proton decay, 2019. URL <https://www.sheffield.ac.uk/physics/research/pppa/nugroup/dune/nudune-phys>. online; accessed 15-May-2019.
- [128] K. Abe et al. Search for proton decay via $p \rightarrow \nu?K^+$ using 260 kilotonyear data of Super-Kamiokande. *Phys. Rev.*, D90(7):072005, 2014. doi: 10.1103/PhysRevD.90.072005.
- [129] C. Regis et al. Search for Proton Decay via $p \rightarrow \mu^+K^0$ in Super-Kamiokande I, II, and III. *Phys. Rev.*, D86:012006, 2012. doi: 10.1103/PhysRevD.86.012006.
- [130] H. Nishino et al. Search for Nucleon Decay into Charged Anti-lepton plus Meson in Super-Kamiokande I and II. *Phys. Rev.*, D85:112001, 2012. doi: 10.1103/PhysRevD.85.112001.
- [131] K. Abe et al. Search for Nucleon Decay via $n \rightarrow \bar{\nu}\pi^0$ and $p \rightarrow \bar{\nu}\pi^+$ in Super-Kamiokande. *Phys. Rev. Lett.*, 113(12):121802, 2014. doi: 10.1103/PhysRevLett.113.121802.
- [132] V. Takhistov et al. Search for Tripleton Nucleon Decay via $p \rightarrow e^+\nu\nu$ and $p \rightarrow \mu^+\nu\nu$ in the Super-Kamiokande Experiment. *Phys. Rev. Lett.*, 113(10):101801, 2014. doi: 10.1103/PhysRevLett.113.101801.

- [133] Volodymyr Takhistov. Review of Nucleon Decay Searches at Super-Kamiokande. In *Proceedings, 51st Rencontres de Moriond on Electroweak Interactions and Unified Theories: La Thuile, Italy, March 12-19, 2016*, pages 437–444, 2016.
- [134] G. T. Jones, R. W. L. Jones, B. W. Kennedy, S. W. O’Neale, O. Villalobos-Baillie, H. Klein, D. R. O. Morrison, P. Schmid, H. Wachsmuth, D. B. Miller, M. M. Mobayyen, S. Wainstein, M. Aderholz, D. Hantke, U. F. Katz, J. Kern, N. Schmitz, W. Wittek, H. P. Borner, G. Myatt, D. Radojicic, F. W. Bullock, and S. Burke. Neutral strange particle production in neutrino and antineutrino charged current interactions on protons. *Zeitschrift fur Physik C Particles and Fields*, 57:197–209, June 1993. doi: 10.1007/BF01565049.
- [135] Laura Weiss. The construction of cern’s first hydrogen bubble chambers, 1988. URL <https://cds.cern.ch/record/194093/files/CERN-CH-26.pdf>. online; accessed 28-June-2019.
- [136] D. Allasia et al. Production of Neutral Strange Particles in $\bar{\nu}_\mu d^{-2}$ and $\nu_\mu d^{-2}$ Charged Current Interactions. *Nucl. Phys.*, B224:1, 1983. doi: 10.1016/0550-3213(83)90309-7.
- [137] P. Bosetti et al. Strange Particle Production in Neutrino and Anti-neutrino Neon Interactions. *Nucl. Phys.*, B209:29–44, 1982. doi: 10.1016/0550-3213(82)90100-6.
- [138] S. Willocq et al. Neutral strange particle production in anti-neutrino - neon charged current interactions. *Z. Phys.*, C53:207–218, 1992. doi: 10.1007/BF01597556.
- [139] N. J. Baker et al. Strange Particle Production in Neutrino - Neon Charged Current Interactions. *Phys. Rev.*, D34:1251–1264, 1986. doi: 10.1103/PhysRevD.34.1251.
- [140] Charles Baltay et al. Reflections on the 15-Foot Bubble Chamber at Fermilab. 1989. doi: 10.2172/1155197.
- [141] D. DeProspero et al. Neutral strange particle production in neutrino and anti-neutrino charged current interactions on neon. *Phys. Rev.*, D50:6691–6703, 1994. doi: 10.1103/PhysRevD.50.6691.

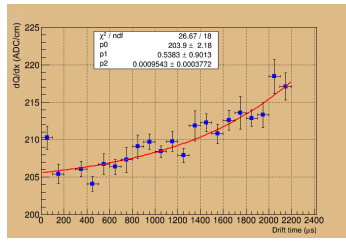
- [142] S. J. Barish et al. Strange-Particle Production in Neutrino Interactions. *Phys. Rev. Lett.*, 33:1446, 1974. doi: 10.1103/PhysRevLett.33.1446.
- [143] Argonne National Laboratory K, JAEGGER. Performance of the argonne 12-foot bubble chamber. track sensitive target construction and operating conditions, 1974. URL <https://www.osti.gov/servlets/purl/4324156>. online; accessed 28-June-2019.
- [144] W. A. Mann, T. Kafka, M. Derrick, B. Musgrave, R. Ammar, D. Day, and J. Gress. K Meson Production by ν_μ - Deuterium Reactions Near Threshold: Implications for Nucleon Decay Searches. *Phys. Rev.*, D34:2545–2553, 1986. doi: 10.1103/PhysRevD.34.2545.
- [145] N. J. Baker, P. L. Connolly, S. A. Kahn, H. G. Kirk, M. J. Murtagh, R. B. Palmer, N. P. Samios, and M. Tanaka. Strange Particle Production from Neutrino Interactions in the BNL 7-Ft Bubble Chamber. *Phys. Rev.*, D24:2779–2786, 1981. doi: 10.1103/PhysRevD.24.2779.
- [146] J. E. Jensen. THE BROOKHAVEN NATIONAL LABORATORY 80-INCH LIQUID HYDROGEN BUBBLE CHAMBER. In *Proceedings, 1964 Cryogenic Engineering Conference (CEC 1964): Philadelphia, Pennsylvania, August 18-21, 1964*, 1964. doi: 10.2172/4011747.
- [147] D. Son et al. Quasielastic Charmed Baryon Production and Exclusive Strange Particle Production by High-energy Neutrinos. *Phys. Rev.*, D28:2129, 1983. doi: 10.1103/PhysRevD.28.2129.
- [148] H. Deden et al. Strange Particle Production and Charmed Particle Search in the Gargamelle Neutrino Experiment. *Phys. Lett.*, 58B:361–366, 1975. doi: 10.1016/0370-2693(75)90674-7.
- [149] C. M. Marshall et al. Measurement of K^+ production in charged-current ν_μ interactions. *Phys. Rev.*, D94(1):012002, 2016. doi: 10.1103/PhysRevD.94.012002.

- [150] C. M. Marshall et al. Measurement of neutral-current K^+ production by neutrinos using MINERvA. *Phys. Rev. Lett.*, 119(1):011802, 2017. doi: 10.1103/PhysRevLett.119.011802.
- [151] L. Aliaga et al. Design, Calibration, and Performance of the MINERvA Detector. *Nucl. Instrum. Meth.*, A743:130–159, 2014. doi: 10.1016/j.nima.2013.12.053.
- [152] MicroBooNE. First muon-neutrino charged-current inclusive differential cross section measurement for microboone run 1 data, 2018. URL <https://microboone.fnal.gov/wp-content/uploads/MICROBOONE-NOTE-1045-PUB.pdf>. online; accessed 16-Jan-2019.
- [153] C. Andreopoulos et al. The GENIE Neutrino Monte Carlo Generator. *Nucl. Instrum. Meth.*, A614:87–104, 2010. doi: 10.1016/j.nima.2009.12.009.
- [154] R. A. Smith and E. J. Moniz. NEUTRINO REACTIONS ON NUCLEAR TARGETS. *Nucl. Phys.*, B43:605, 1972. doi: 10.1016/0550-3213(75)90612-4,10.1016/0550-3213(72)90040-5. [Erratum: Nucl. Phys.B101,547(1975)].
- [155] Arie Bodek, Inkyu Park, and Un-ki Yang. Improved low Q^2 model for neutrino and electron nucleon cross sections in few GeV region. *Nucl. Phys. Proc. Suppl.*, 139:113–118, 2005. doi: 10.1016/j.nuclphysbps.2004.11.208. [,113(2004)].
- [156] Z. Koba, Holger Bech Nielsen, and P. Olesen. Scaling of multiplicity distributions in high-energy hadron collisions. *Nucl. Phys.*, B40:317–334, 1972. doi: 10.1016/0550-3213(72)90551-2.
- [157] T. Yang, C. Andreopoulos, H. Gallagher, K. Hoffmann, and P. Kehayias. A Hadronization Model for Few-GeV Neutrino Interactions. *Eur. Phys. J.*, C63:1–10, 2009. doi: 10.1140/epjc/s10052-009-1094-z.
- [158] Torbjorn Sjostrand, Stephen Mrenna, and Peter Z. Skands. PYTHIA 6.4 Physics and Manual. *JHEP*, 05:026, 2006. doi: 10.1088/1126-6708/2006/05/026.

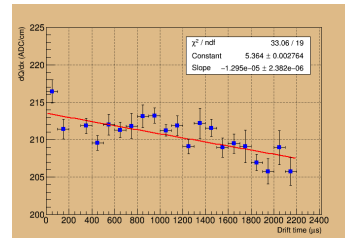
Appendix A

Electron Attenuation

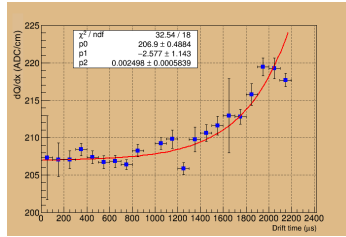
Studies described in this chapter are derived from the MicroBooNE public note^[1], which I co-authored. The dQ/dx vs drift time plots for all 56 data runs explained in the Chapter 5, Section 5.3 before and after the space charge corrections are shown here. The left column is electron attenuation before space charge correction and the right column is electron attenuation after space charge correction.



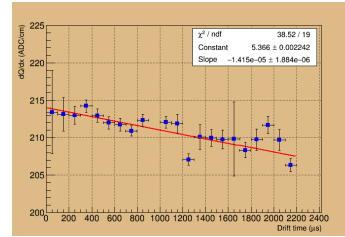
(a) Run 5025 (before)



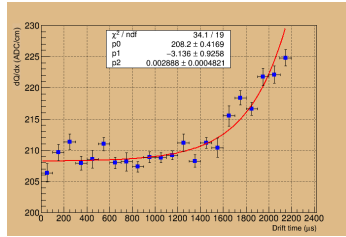
(b) Run 5025 (after)



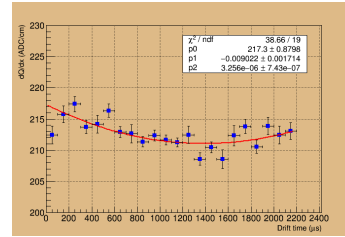
(c) Runs 5039,5041 (before)



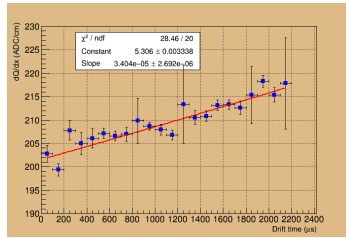
(d) Runs 5039,5041 (after)



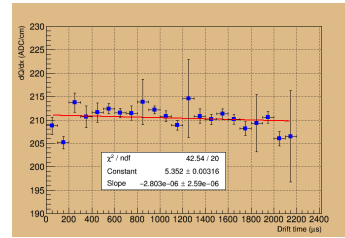
(e) Run 5051 (before)



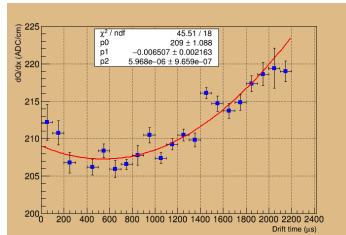
(f) Run 5051 (after)



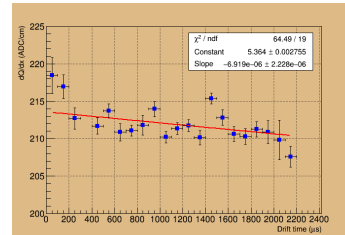
(g) Run 5068 (before)



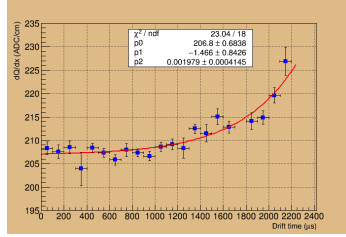
(h) Run 5068 (after)



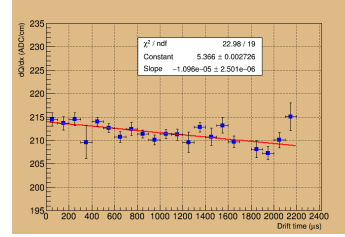
(i) Runs 5077,5078 (before)



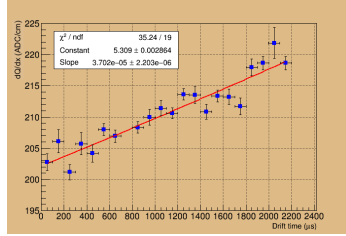
(j) Runs 5077,5078 (after)



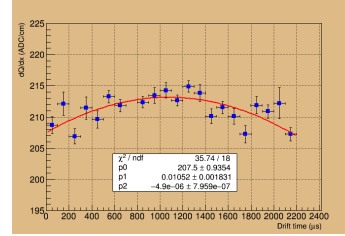
(a) Run 5092 (before)



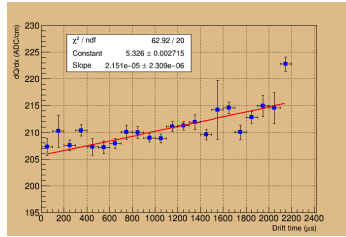
(b) Run 5092 (after)



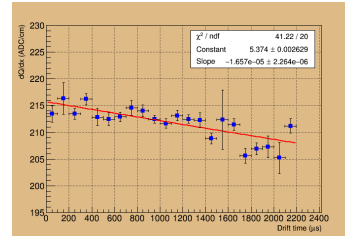
(c) Runs 5099,5100 (before)



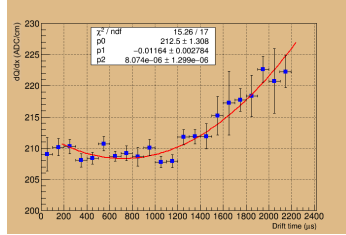
(d) Runs 5099,5100 (after)



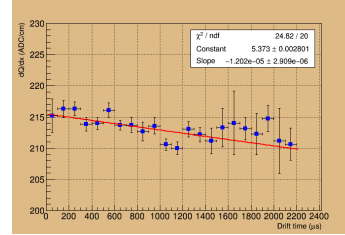
(e) Runs 5109,5110 (before)



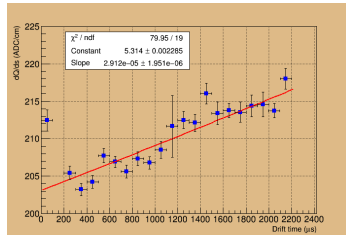
(f) Runs 5109,5110 (after)



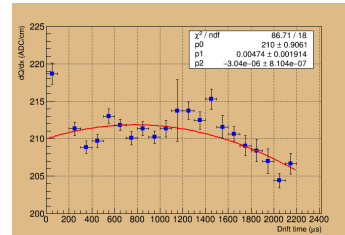
(g) Run 5130 (before)



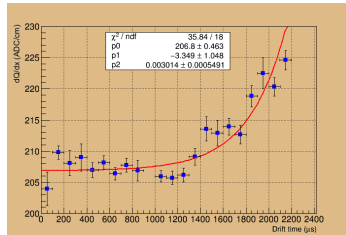
(h) Run 5130 (after)



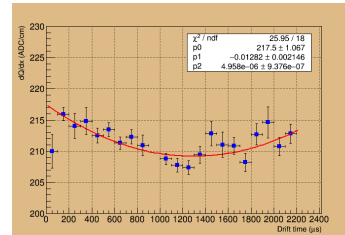
(i) Run 5151 (before)



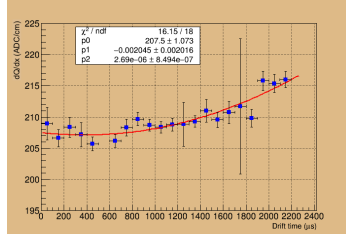
(j) Run 5151 (after)



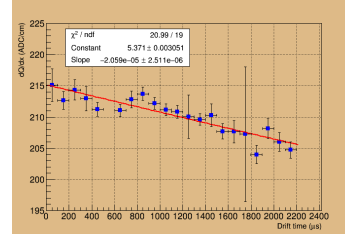
(k) Run 5157 (before)



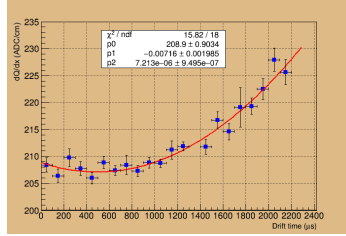
(l) Run 5157 (after)



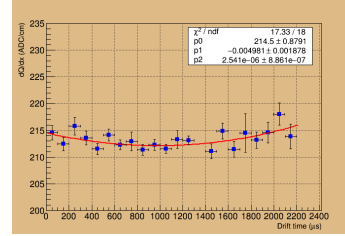
(a) Run 5179 (before)



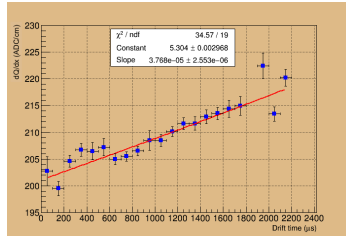
(b) Run 5179 (after)



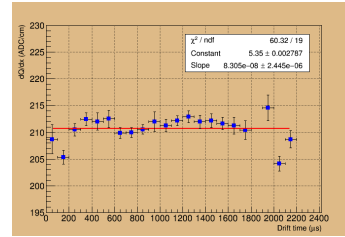
(c) Run 5191 (before)



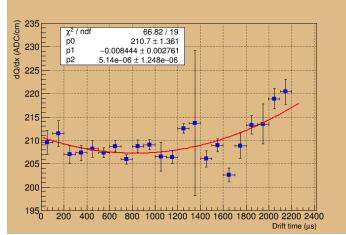
(d) Run 5191 (after)



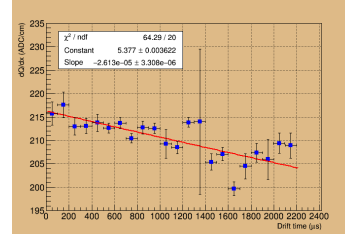
(e) Run 5204 (before)



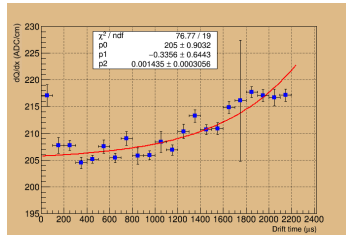
(f) Run 5204 (after)



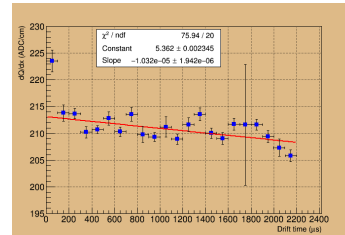
(g) Run 5217 (before)



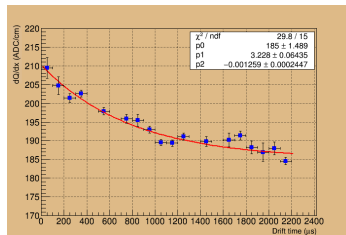
(h) Run 5217 (after)



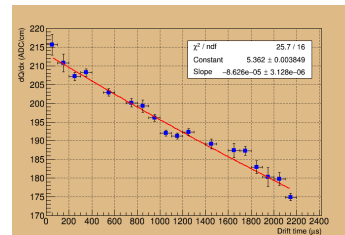
(i) Runs 5235,5237 (before)



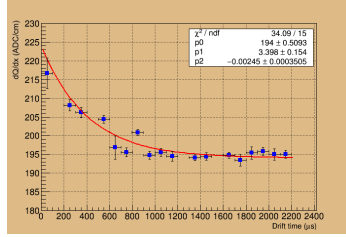
(j) Runs 5235,5237 (after)



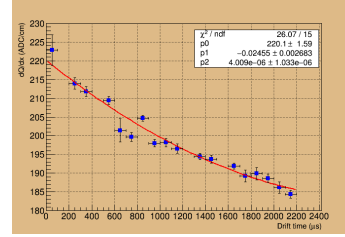
(k) Run 5265 (before)



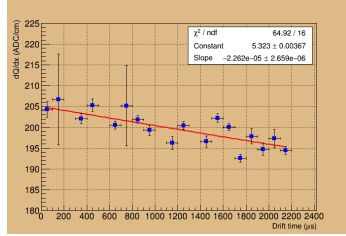
(l) Run 5265 (after)



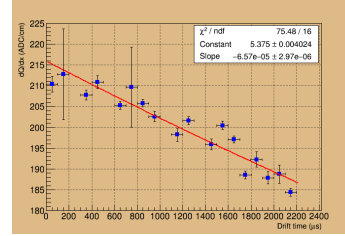
(a) Run 5278 (before)



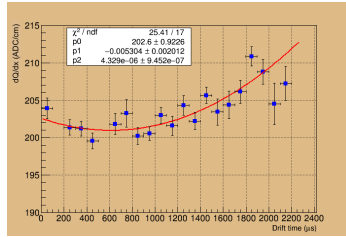
(b) Run 5278 (after)



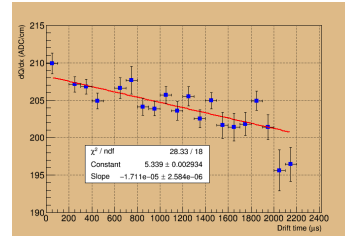
(c) Run 5326 (before)



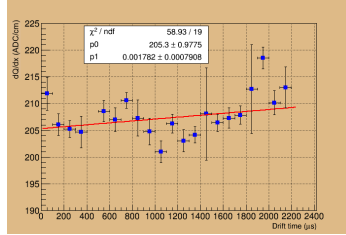
(d) Run 5326 (after)



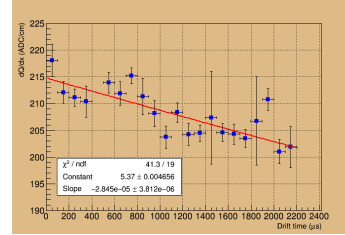
(e) Run 5337 (before)



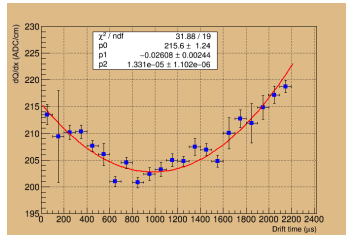
(f) Run 5337 (after)



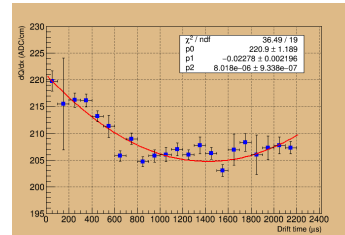
(g) Runs 5343,5344 (before)



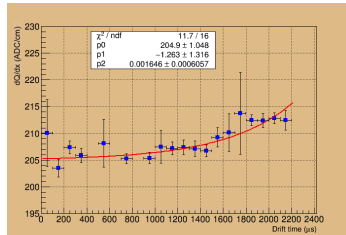
(h) Runs 5343,5344 (after)



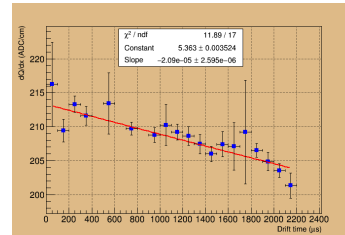
(i) Run 5364 (before)



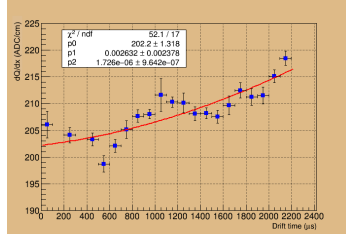
(j) Run 5364 (after)



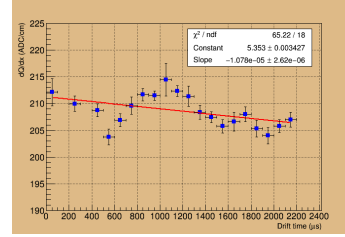
(k) Runs 5374,5375 (before)



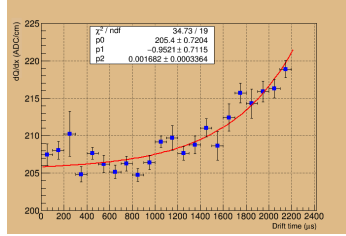
(l) Runs 5374,5375 (after)



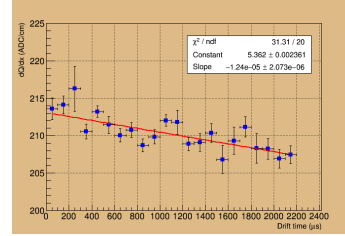
(a) Run 5385 (before)



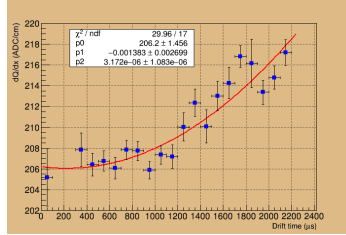
(b) Run 5385 (after)



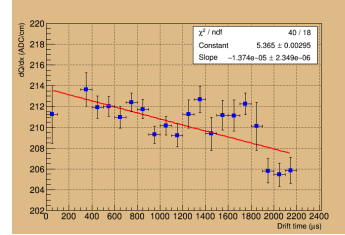
(c) Runs 5393,5394 (before)



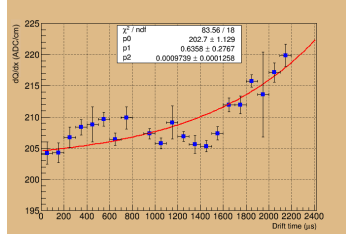
(d) Runs 5393,5394 (after)



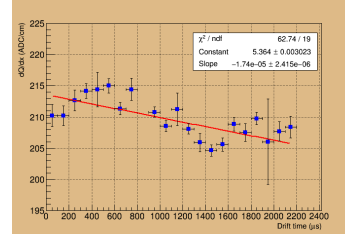
(e) Run 5411 (before)



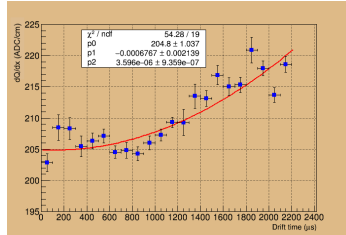
(f) Run 5411 (after)



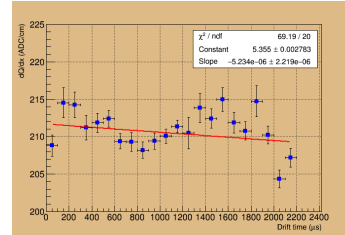
(g) Runs 5425,5427 (before)



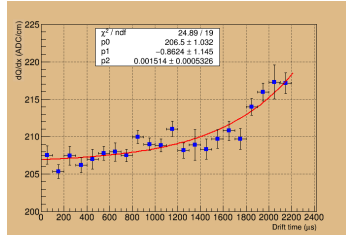
(h) Runs 5425,5427 (after)



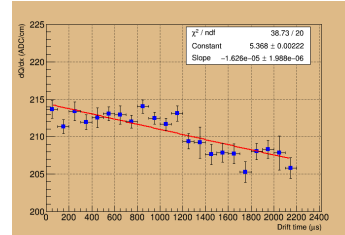
(i) Run 5441 (before)



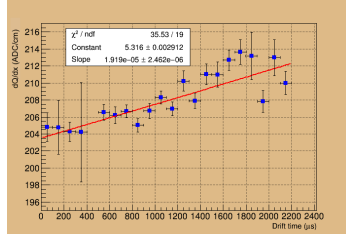
(j) Run 5441 (after)



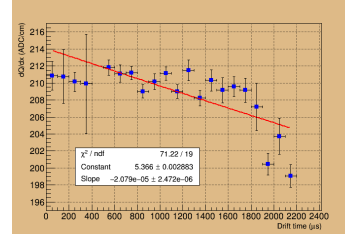
(k) Run 5455 (before)



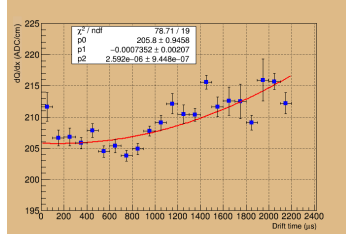
(l) Run 5455 (after)



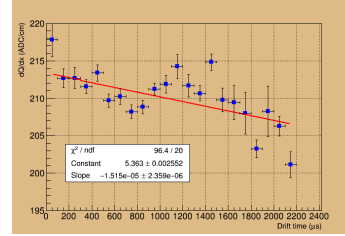
(a) Run 5600 (before)



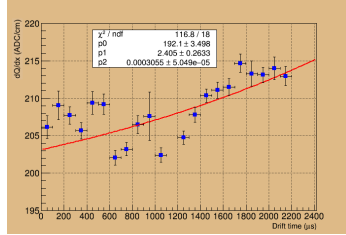
(b) Run 5600 (after)



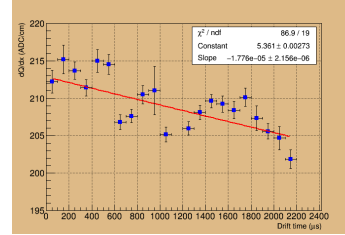
(c) Run 5606 (before)



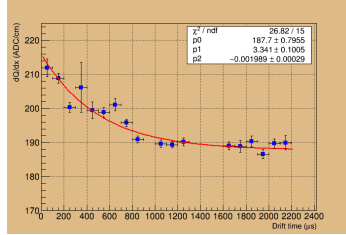
(d) Run 5606 (after)



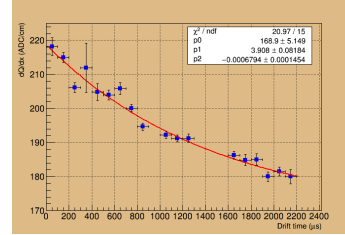
(e) Runs 5622,5624 (before)



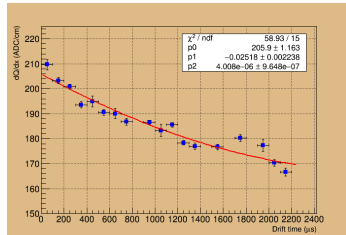
(f) Runs 5622,5624 (after)



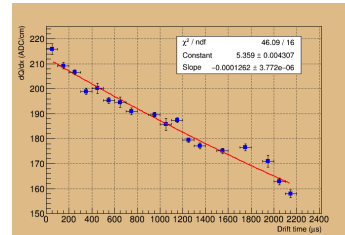
(g) Run 5637 (before)



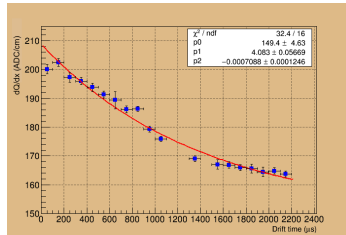
(h) Run 5637 (after)



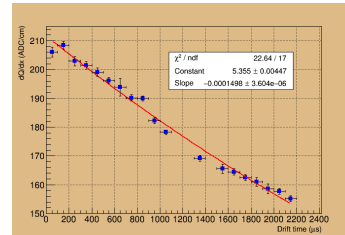
(i) Runs 5653,5654 (before)



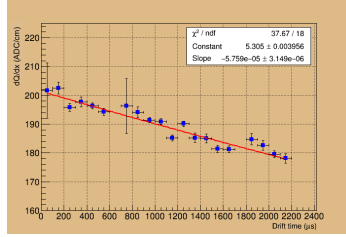
(j) Runs 5653,5654 (after)



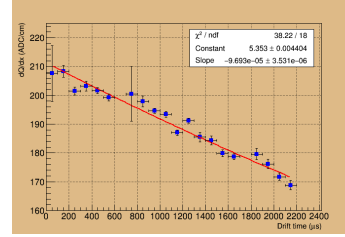
(k) Run 5691 (before)



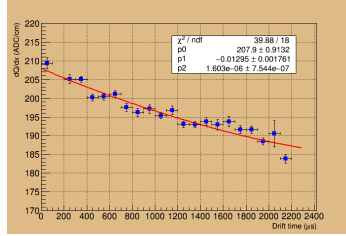
(l) Run 5691 (after)



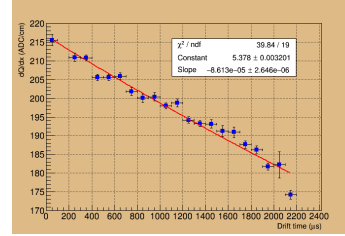
(a) Run 5709 (before)



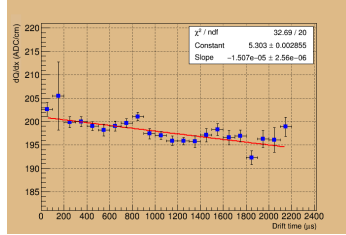
(b) Run 5709 (after)



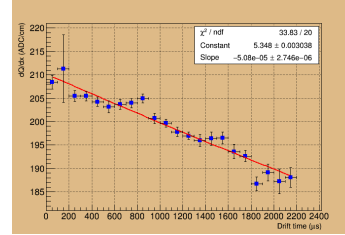
(c) Run 5725 (before)



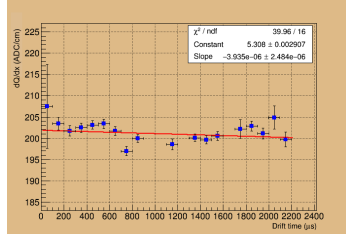
(d) Run 5725 (after)



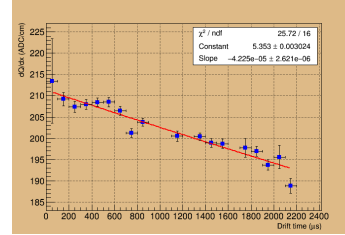
(e) Run 5733 (before)



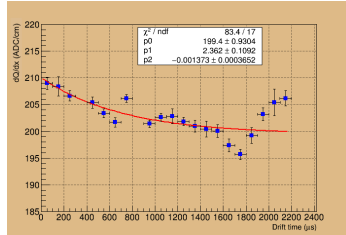
(f) Run 5733 (after)



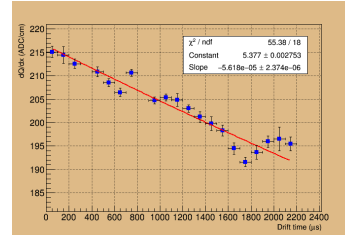
(g) Run 5758 (before)



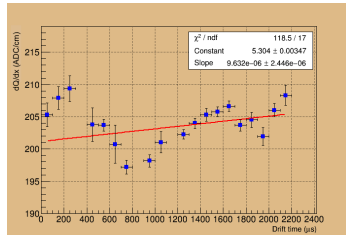
(h) Run 5758 (after)



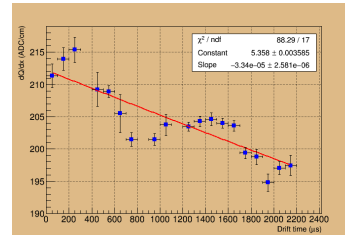
(i) Runs 5768,5769 (before)



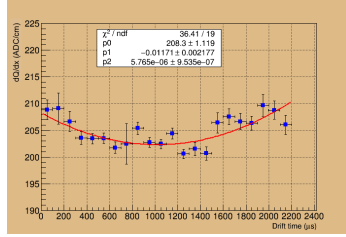
(j) Runs 5768,5769 (after)



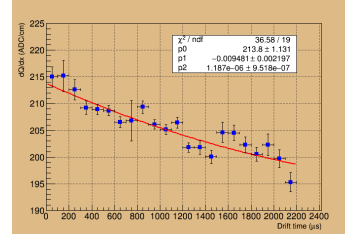
(k) Run 5783 (before)



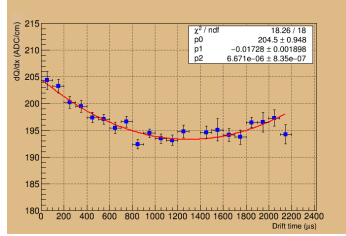
(l) Run 5783 (after)



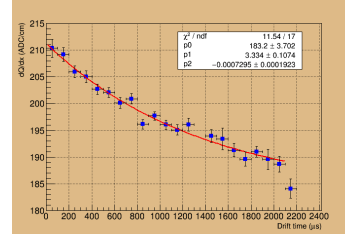
(a) Run 5808 (before)



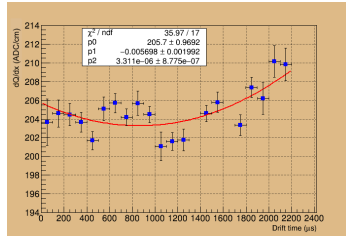
(b) Run 5808 (after)



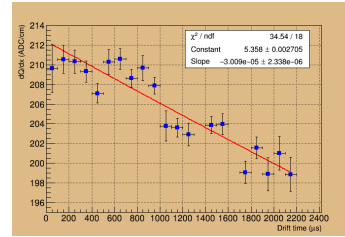
(c) Run 5823 (before)



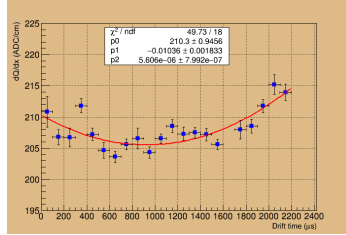
(d) Run 5823 (after)



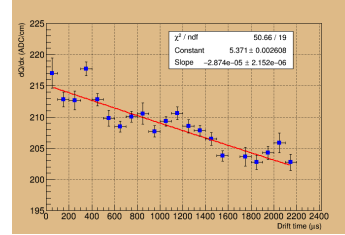
(e) Run 5833 (before)



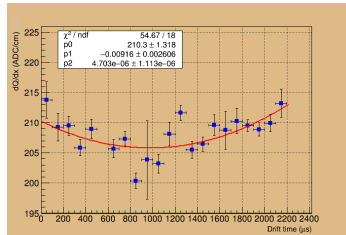
(f) Run 5833 (after)



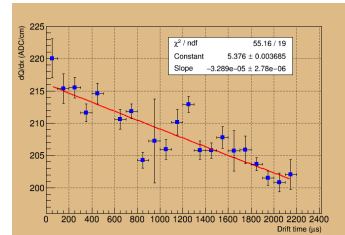
(g) Runs 5844,5845 (before)



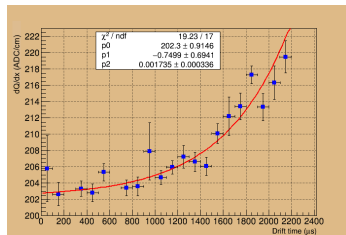
(h) Runs 5844,5845 (after)



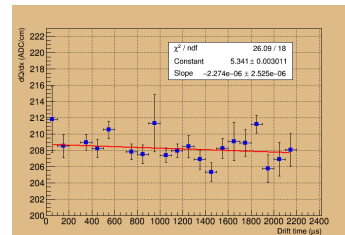
(i) Run 5854 (before)



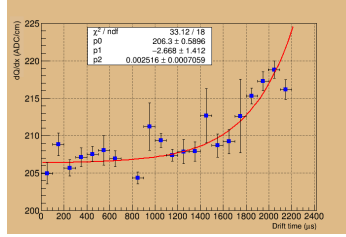
(j) Run 5854 (after)



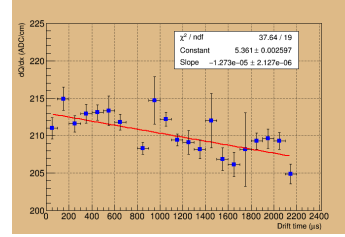
(k) Run 5875 (before)



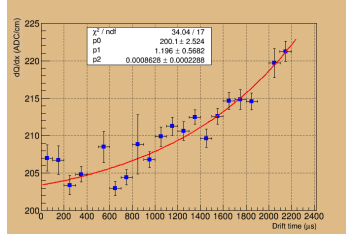
(l) Run 5875 (after)



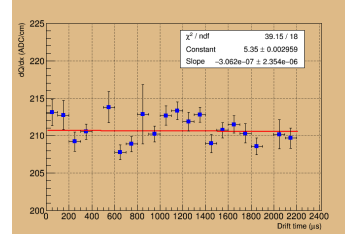
(a) Runs 5896,5897 (before)



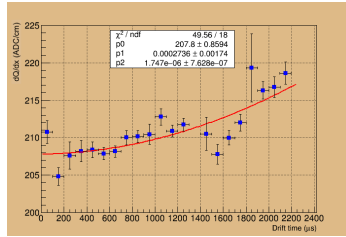
(b) Runs 5896,5897 (after)



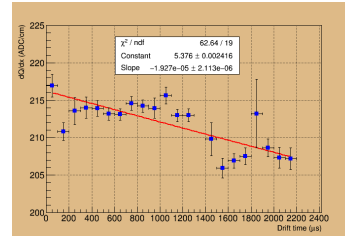
(c) Run 5910 (before)



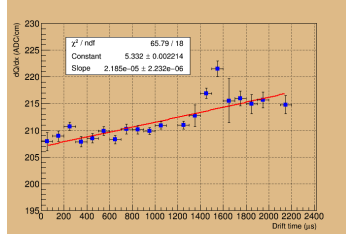
(d) Run 5910 (after)



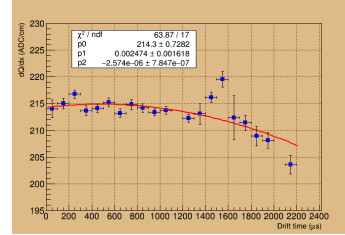
(e) Run 5921 (before)



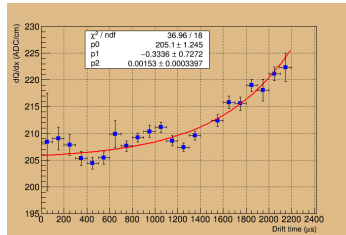
(f) Run 5921 (after)



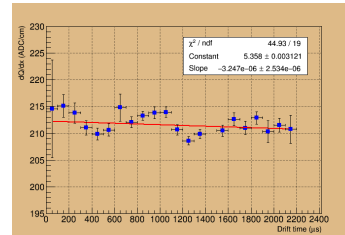
(g) Run 5933 (before)



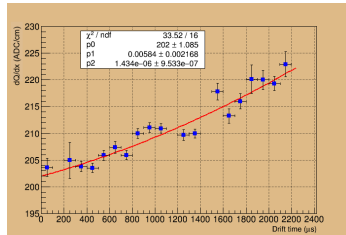
(h) Run 5933 (after)



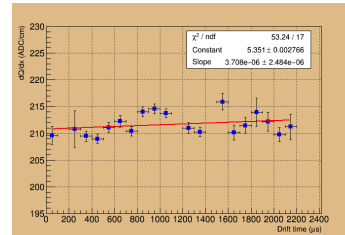
(i) Run 5947 (before)



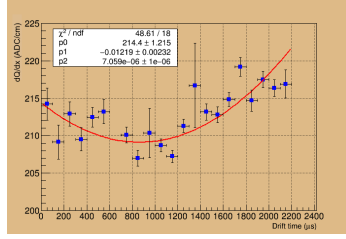
(j) Run 5947 (after)



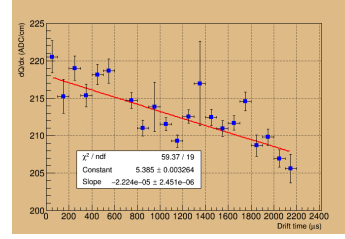
(k) Run 5966 (before)



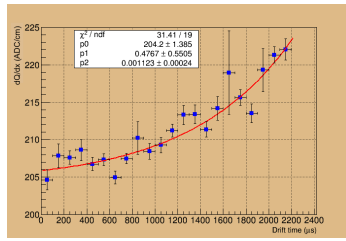
(l) Run 5966 (after)



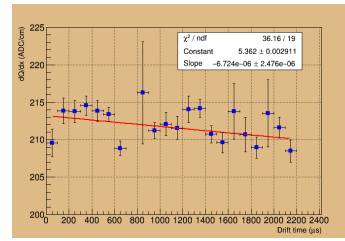
(a) Run 5979 (before)



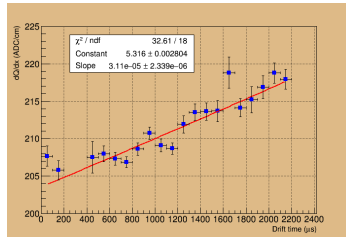
(b) Run 5979 (after)



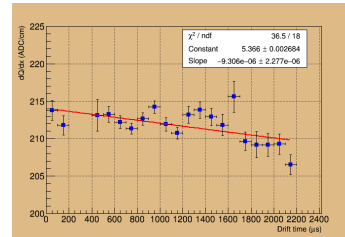
(c) Runs 5990,5996 (before)



(d) Runs 5990,5996 (after)



(e) Run 6011 (before)



(f) Run 6011 (after)

Figure A.10: Plots of dQ/dx Vs. drift time for all 56 days of data analyzed in the electron attenuation measurement. (Left) before space charge correction applied. (Right) after space charge correction applied.

Appendix B

Event Selection of Charged Current Neutrino Induced Kaon Events in MicroBooNE

Area normalized distributions of data-Monte Carlo comparisons made for different kinematics of kaon candidates and muon candidates coming from kaon decay at rest explained in the Chapter [8](#), Section [8.7](#).

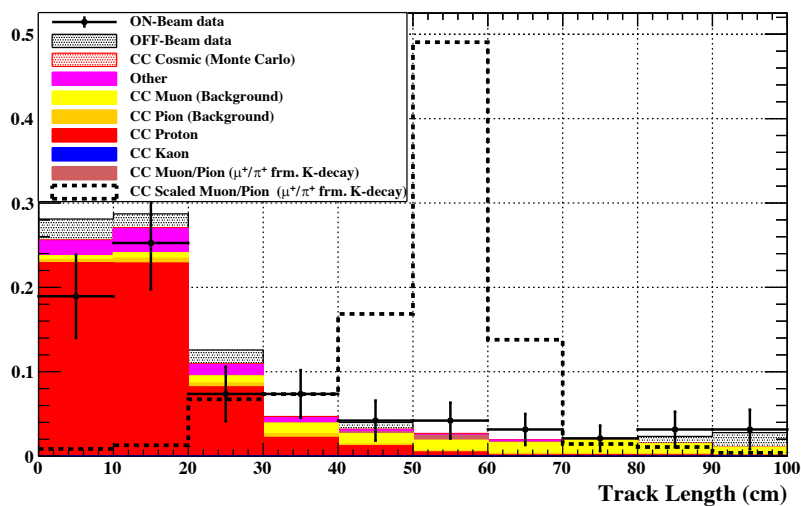
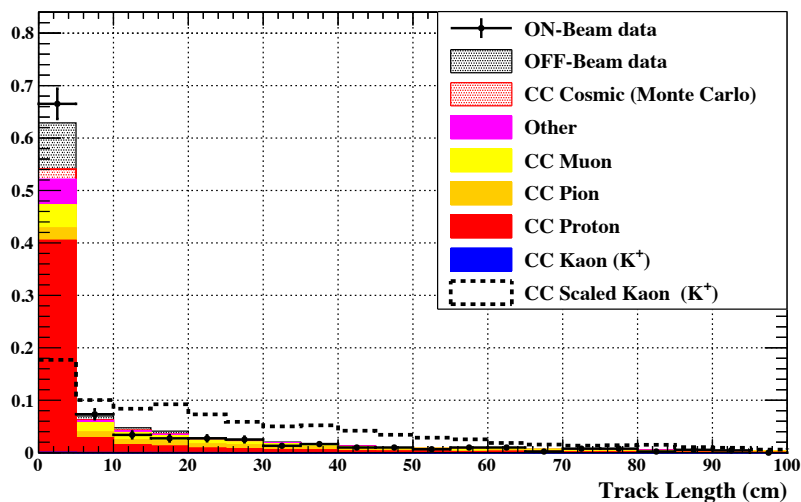


Figure B.1: (Top) Data-Monte Carlo comparison for the track length of kaon candidates. (Bottom) Data-Monte Carlo comparison for the track length of muon candidates coming from kaon decay at rest. Here all the distributions were area normalized to 1 except the signal distributions. The signal distributions were scaled by a factor of 100. All the uncertainties in both plots are completely statistical.

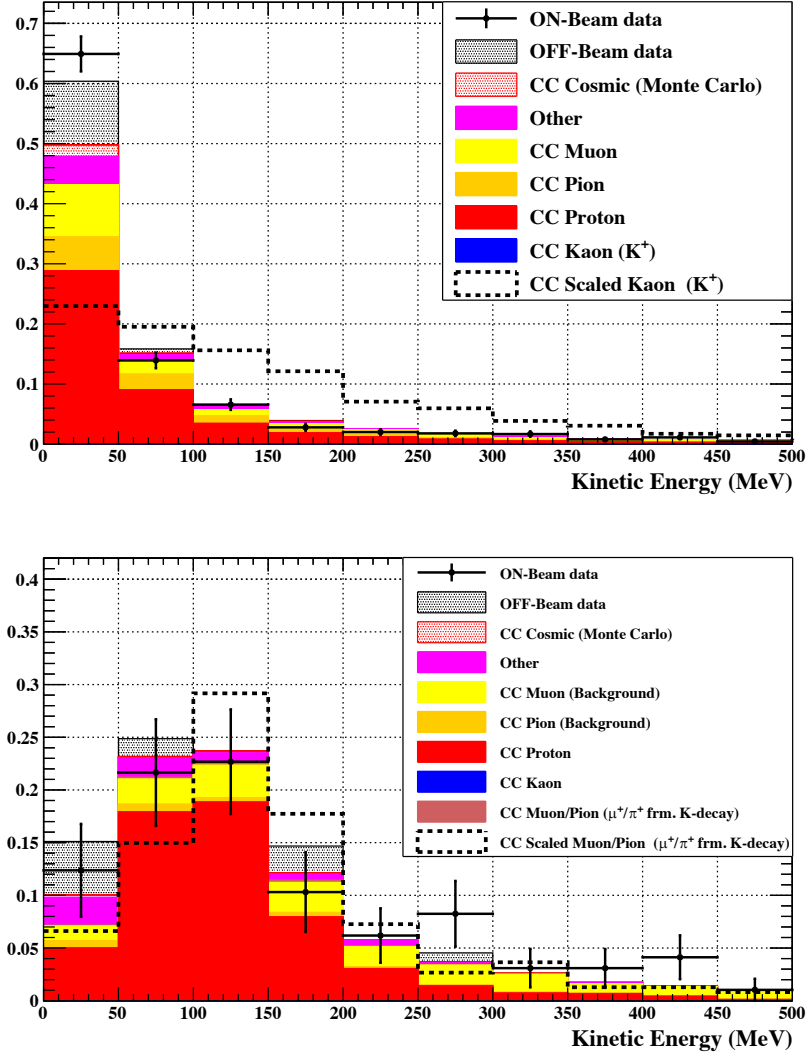


Figure B.2: (Top) Data-Monte Carlo comparisons for the calorimetric kinetic energy of kaon candidates. (Bottom) Data-Monte Carlo comparisons for the calorimetric kinetic energy of muon candidates coming from kaon decay. Here all the distributions were area normalized to 1 except the signal distributions. The signal distributions were scaled by a factor of 100. All the uncertainties in both plots are completely statistical.

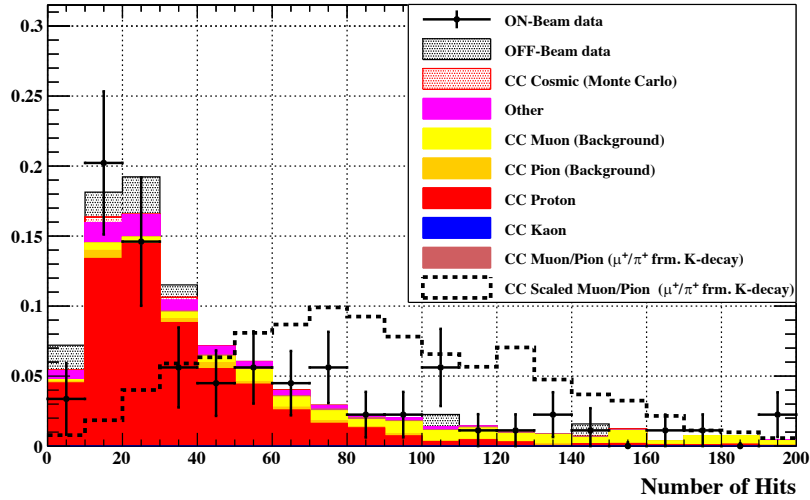
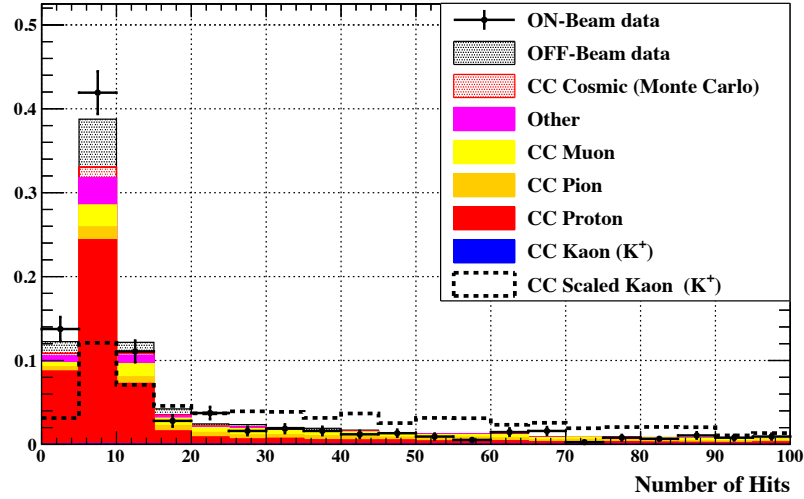


Figure B.3: (Top) Data-Monte Carlo comparison for the number of hits registered in the collection plane of kaon candidates. (Bottom) Data-Monte Carlo comparison for the number of hits registered in the collection plane of muon candidates coming from kaon decay. Here all the distributions were area normalized to 1 except the signal distributions. The signal distributions were scaled by a factor of 100. All the uncertainties in both plots are completely statistical.

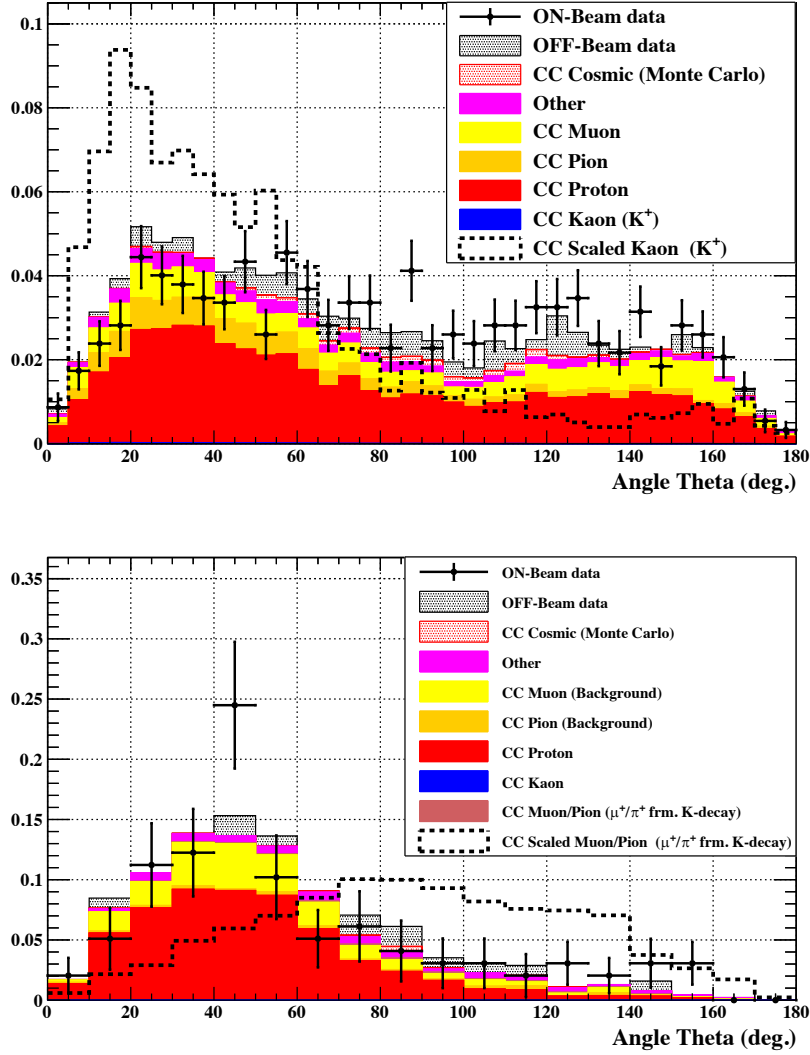


Figure B.4: (Top) Data-Monte Carlo comparison for the angle θ (polar angle of the track w.r.t beam direction) of kaon candidates. (Bottom) Data-Monte Carlo comparison for the angle θ of muon candidates coming from kaon decay. Here all the distributions were area normalized to 1 except the signal distributions. The signal distributions were scaled by a factor of 100. All the uncertainties in both plots are completely statistical.

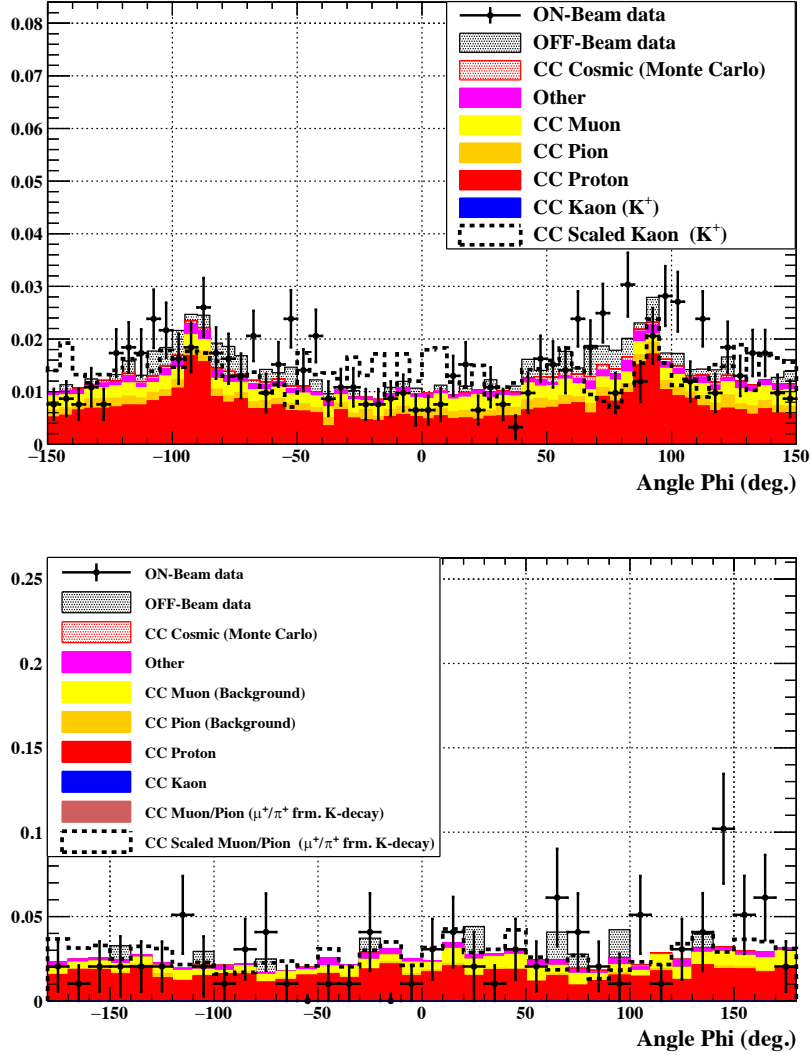


Figure B.5: (Top) Data-Monte Carlo comparison for the angle ϕ (azimuth angle of the track w.r.t beam direction) of kaon candidates. (Bottom) Data-Monte Carlo comparison for the angle ϕ of muon candidates coming from kaon decay. Here all the distributions were area normalized to 1 except the signal distributions. The signal distributions were scaled by a factor of 100. All the uncertainties in both plots are completely statistical.

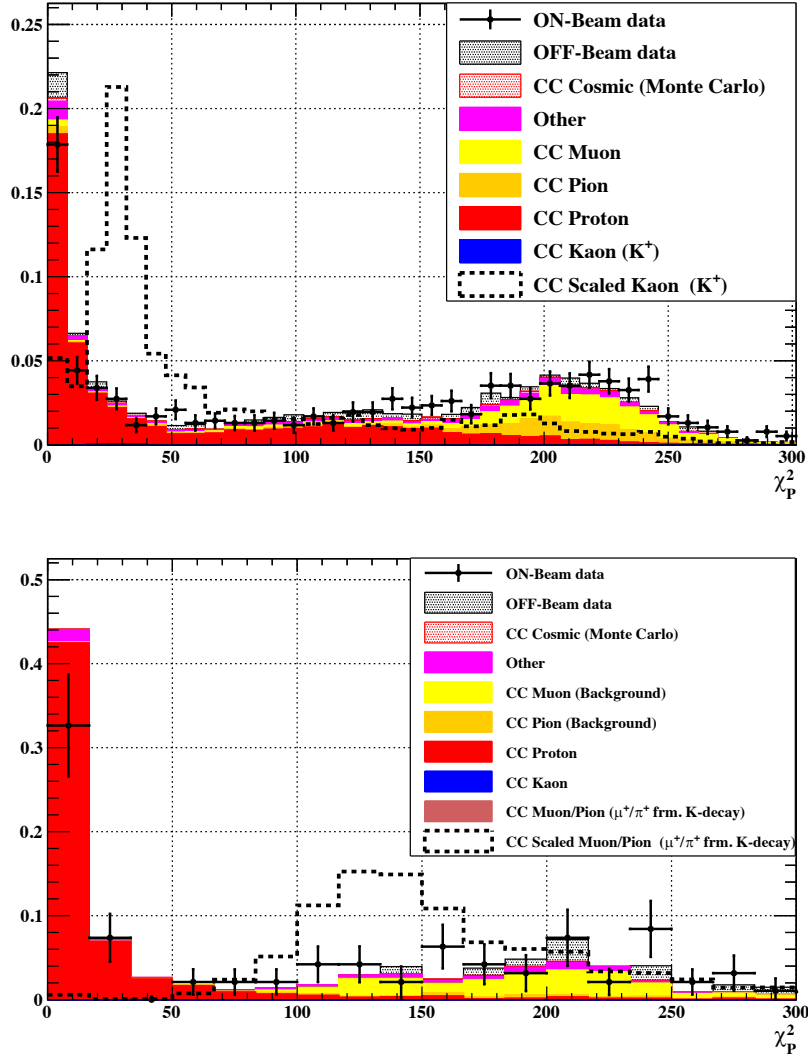


Figure B.6: (Top) Data-Monte Carlo comparison for the variable χ^2_P (χ^2 value calculated under proton hypothesis) of kaon candidates. (Bottom) Data-Monte Carlo comparison for the the variable χ^2_P (χ^2 value calculated under proton hypothesis) of muon candidates coming from kaon decay. Here all the distributions were area normalized to 1 except the signal distributions. The signal distributions were scaled by a factor of 100. All the uncertainties in both plots are completely statistical.

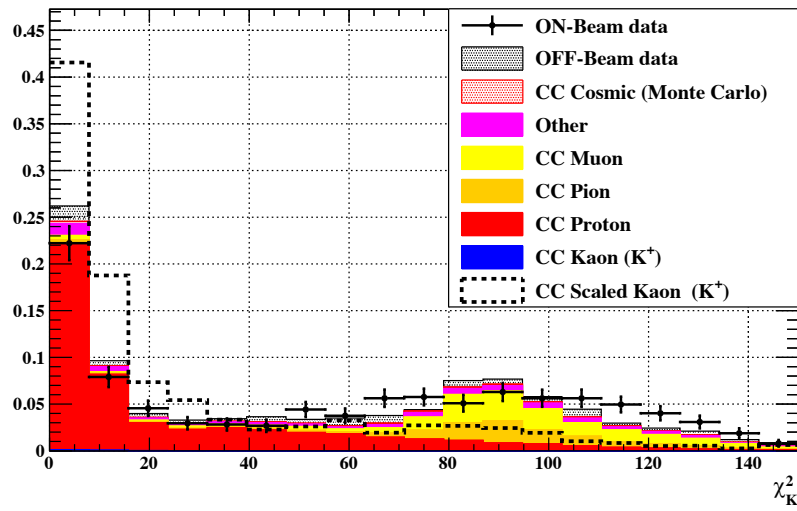


Figure B.7: Data-Monte Carlo comparison for the variable χ_K^2 (χ^2 value calculated under kaon hypothesis) of kaon candidates. Here all the distributions were area normalized to 1 except the signal distribution. The signal distributions was scaled by a factor of 100. All the uncertainties shown are completely statistical.